

Alma Mater Studiorum – Università di Bologna

**DOTTORATO DI RICERCA IN
INGEGNERIA ENERGETICA, NUCLEARE E DEL
CONTROLLO AMBIENTALE**

Ciclo XXIII

Settore scientifico-disciplinare di appartenenza: ING-IND/11 FISICA TECNICA AMBIENTALE

**DYNAMIC THERMAL PERFORMANCE OF BUILDING
COMPONENTS AND APPLICATION TO THE
EXPERIMENTAL AND THEORETICAL ANALYSIS OF A
VENTILATED FACADE**

Presentata da: Cosimo Marinosci

Coordinatore Dottorato

Prof. Antonio Barletta

Relatore

Prof. Alessandro Cocchi

ESAME finale 2011

ABSTRACT

The general aim of this work is to contribute to the energy performance assessment of ventilated façades by the simultaneous use of experimental data and numerical simulations.

A significant amount of experimental work was done on different types of ventilated façades with natural ventilation. The measurements were taken on a test building.

The external walls of this tower are rainscreen ventilated façades. Ventilation grills are located at the top and at the bottom of the tower.

In this work the modelling of the test building using a dynamic thermal simulation program (ESP-r) is presented and the main results discussed.

In order to investigate the best summer thermal performance of rainscreen ventilated skin façade a study for different setups of rainscreen walls was made. In particular, influences of ventilation grills, air cavity thickness, skin colour, skin material, orientation of façade were investigated.

It is shown that some types of rainscreen ventilated façade typologies are capable of lowering the cooling energy demand of a few percent points.

Keywords: Ventilated façade, Rainscreen wall, Modelling and Simulation, Test cell, Energy demand, Periodic thermal transmittance.

This work could not have been completed without the support and help of many people and institutions, for which I am very grateful.

I am especially grateful to Professor Gian Luca Morini for enabling me to carry out the present work and for his encouragement over the years. He inspired, motivated, and challenged me throughout the course of my studies.

I would like to thank Prof. Sylvie Lorente and Dr. Arjan Frijns who - as foreign members of the award committee - reviewed and commented the drafts for this dissertation.

I also gratefully acknowledge ESRU, University of Strathclyde for cooperation regarding ESP-r use and in particular Prof. J. A. Clarke, P. Strachan and J. Hand.

Many thanks to the staff at the DIENCA (Dipartimento di Ingegneria Energetica e del Controllo Ambientale) for creating a stimulating and positive atmosphere. I would especially like to thank Stefania Falcioni, Carmen Auricchio, Luca Barbaresi, Mirco Magnini, Dario Fattori, for many interesting conversations, and especially Dario D'Orazio for his support, and outings to the pub.

I wish to express the sincerest gratitude to Giovanni Semprini as my local thesis supervisor and further Prof. Alessandro Cocchi as my thesis supervisor.

Special thanks to Marco Lorenzini, who took the time to review and comment on sections of the manuscript.

I never thought of writing this thesis without the help of my parents. They taught me the value of education and work hard, and raised to believe more in myself.

Finally, and most importantly, I wish to express my warmest appreciation and love for my wife, Filomena Fiore. I could not have accomplished my goal without her support, encouragement, and inspiration. During the past months, she stood by me despite my mind was elsewhere. She also selflessly accepted my lack of attention and time. I dedicate this work to her with all my love.

TABLE OF CONTENTS

ABSTRACT.....	I
TABLE OF CONTENTS.....	III
LIST OF SIMBOLS.....	VI
INTRODUCTION.....	1
CHAPTER 1: VENTILATED FAÇADE WALLS	
1.1 Introduction.....	3
1.2 Definition.....	3
1.3 Typology.....	5
1.3.1 Airflow origin.....	6
1.3.2 Driving force.....	6
1.4 External skin materials and examples.....	7
1.5 About Trombe-walls and solar chimneys.....	9
1.6 Performance assessment.....	9
1.7 Technical Standards.....	10
1.8 Envelope performances.....	10
1.9 Conclusion.....	12
CHAPTER 2: VENTILATED FAÇADE - THEORETICAL ANALYSIS	
2.1 Introduction.....	13
2.2 Heat balance for ventilated façades.....	13
2.2.1 Heat balance for the external skin façade.....	13
2.2.2 Heat balance for the air cavity.....	17
2.2.3 Heat balance for the internal wall.....	21
2.3 Convective heat transfer.....	23
2.3.1 Definition.....	23
2.3.2 Convection configurations.....	24
2.3.3 Dimensionless numbers.....	24
2.3.4 Ventilated cavities.....	26
2.3.5 Convective heat transfer coefficient equations.....	27
2.3.6 Convection with surroundings.....	30
2.4 Heat transfer correlation methods.....	31
2.5 Evaluation of steady-state thermal transmittance (U-value).....	33
2.5.1 U-value: classical steady state method.....	33
2.5.2 U-value: evaluation with European standard EN ISO 6946.....	33
2.6 Conclusions.....	34

CHAPTER 3: RAINSCREEN VENTILATED SKIN FAÇADE - ENERGY SIMULATION MODEL

3.1 Introduction.....	35
3.2 History about building simulation tools.....	35
3.3 Thermal model.....	36
3.3.1 Finite-difference control-volume heat-balance approach.....	36
3.3.2 Heat balance for intra-constructional nodes.....	37
3.3.3 Heat balance for internal surface nodes.....	39
3.3.4 Heat balance for air-point nodes.....	42
3.4 Modelling setup of rainscreen ventilated skin façades with ESP-r.....	45
3.5 Conclusions	48

CHAPTER 4: RAINSCREEN VENTILATED SKIN FAÇADE - EXPERIMENTAL SETUP

4.1 Introduction.....	49
4.2 The test building.....	49
4.3 Measurement sensors.....	52
4.4 Analysis of the local weather data (winter period)	54
4.5 Monitoring measurements: Winter period.....	57
4.6 Analysis of measurements of rainscreen ventilated skin façades in winter period.....	65
4.6.1 Cavity air temperature.....	65
4.6.2 Temperatures in the wall.....	68
4.6.3 Cavity air velocity.....	70
4.6.4 Comparison of the heat transfer correlations with measurements.....	72
4.6.5 Evaluation of U-value of the ventilated façade in the winter period.....	74
4.7 Analysis of the local weather data (summer period).....	77
4.8 Monitoring measurements: Summer period.....	82
4.9 Analysis of measurements of rainscreen ventilated skin façades in summer period.....	87
4.9.1 Influence of the local weather data on the cavity air velocity.....	89
4.9.2 Influence of the thickness of the air cavity.....	92
4.9.3 Influence of patterns setup on measured parameters.....	92
4.10 Conclusions.....	100

CHAPTER 5: EMPIRICAL VALIDATION MODELLING VENTILATED RAINSCREEN IN WINTER PERIOD

5.1 Introduction.....	103
5.2 Model validation (winter period)	103
5.3 Comparison with monitored data (winter period).....	109
5.4 Remarks.....	113
5.5 Conclusions.....	113

CHAPTER 6: EMPIRICAL VALIDATION MODELLING VENTILATED RAINSCREEN IN SUMMER PERIOD

6.1 Introduction.....	115
6.2 Upgrade for the test cell in summer period.....	115
6.3 Modelling setup for the summer period.....	116
6.4 Model validation (summer period)	118
6.5 Comparison with monitored data (summer period)	121
6.6 Remarks and conclusions.....	123

CHAPTER 7: DYNAMIC THERMAL PERFORMANCE OF THE VENTILATED RAINSCREEN FAÇADE

7.1 Introduction.....	125
7.2 Summer thermal performance.....	125
7.2.1 Periodic thermal transmittance.....	126
7.2.2 Comparison of periodic thermal transmittance of analyzed summertime patterns....	127
7.3 Analysis of dynamic thermal performance.....	133
7.3.1 Influence of ventilation grills.....	134
7.3.2 Influence of air cavity thickness.....	135
7.3.3 Influence of the skin's colour.....	137
7.3.4 Influence of the skin's material.....	138
7.3.5 Influence of the façade's orientation.....	140
7.4 Conclusions.....	141

CHAPTER 8: ENERGY PERFORMANCE: A CASE STUDY

8.1 Introduction.....	143
8.2 Simulation.....	143
8.2.1 Simulation results for a single room.....	143
8.2.2 Simulation results for a whole building.....	147
8.3 Conclusion.....	154

CONCLUSIONS.....	157
------------------	-----

LIST OF PUBLICATIONS.....	161
---------------------------	-----

REFERENCES.....	163
-----------------	-----

LIST OF SYMBOLS

This list of symbols is not exhaustive. Symbols that appear only “locally” in the text, and are not important to understand the other parts of the work, are not included here.

Roman symbols

A	area [m^2]
B	width [m]
C	thermal conductance [Wm^2K]
C_d	discharge coefficient [-]
c_p	specific heat [$Jkg^{-1}K^{-1}$]
C_p	surface wind pressure coefficient [-]
D_h	hydraulic diameter [m]
DMIN	minimum difference [K]
DMAX	maximum difference [K]
E	energy demand [kWh]
g	gravitational acceleration [ms^{-2}]
h	convective heat transfer coefficient [$Wm^{-2}K^{-1}$]
h_r	radiative heat transfer coefficient [$Wm^{-2}K^{-1}$]
H	height of a vertical surface [m]
I	solar radiation [Wm^{-2}]
L	depth [m]
\dot{m}	mass flow rate [$kg s^{-1}$]
MEANDT	average difference [K]
M_t	measured value at hour t [-]
\bar{M}	mean values of the measured values [-]
n	number of total hours in the period selected [-]
p	pressure [Pa]
q	heat flow rate [W]
Q	heat flow rate [Wm^{-2}].
q'''	heat flow rate [Wm^{-3}].
R	thermal resistance [m^2KW^{-1}]
RSQMEANDT	root mean square difference [K]
R^2	pearson coefficient [-]
s	thickness [cm or m]
t	time [s]
T	temperature [K or °C]
T_m	cross-section averaged mean temperature [K]
T_∞	free stream temperature [K]
U	steady state thermal transmittance [$Wm^{-2}K^{-1}$]
U_p	absolute value of the periodic thermal transmittance [$Wm^{-2}K^{-1}$]
v	velocity [ms^{-1}]
V	volume [m^3]
X	hydraulic entrance length [m]
X_T	thermal entrance length [m]
X_t	predicted value at hour t [-]
\bar{X}	mean values of the predicted values [-]
Y	periodic thermal transmittance [-]
Z	complex number
x,y,z	cartesian coordinates [m]

Dimensionless numbers

Gr	Grashof number [-]
Nu	Nusselt number [-]
Pr	Prandtl number [-]
Ra	Rayleigh number [-]
Re	Reynolds number [-]

Greek symbols

A	absorption coefficient [-]
β	coefficient of volumetric thermal expansion [K^{-1}]
δ	wind boundary layer thickness [m]
ε	emissivity [-]
λ	thermal conductivity [$Wm^{-1}K^{-1}$]
μ	dynamic viscosity [sPa]
ν	kinematic viscosity [m^2s^{-1}]
ρ_a	air density [kgm^{-3}]
σ	Stefan–Boltzmann constant [$Wm^{-2}K^{-4}$]
$\Delta x, \Delta y, \Delta z$	Width, depth, and height of a control volume

Subscripts

a	air
ac	cavity air
avg	average
buoy	buoyancy
c	convection
<i>cas-rad</i>	radiant energy from casual sources
<i>cas-conv</i>	convective energy from casual sources
ce	external cover
ci	internal cover
cond	conduction
d	diffuse solar radiation
dp	dew point
e	exterior
enth	enthalpy
eq	equivalent
fd	fully developed
g	global
grd	ground
i	interior
<i>l</i>	state at node under consideration
<i>l-1, l+1</i>	state at neighbouring nodes
inf	infiltration
int-zone	internal zone
J	internal zone node
lw	long wave
max	maximum
met	meteorological
min	minumum
nat	natural
o	outdoor

LIST OF SYMBOLS

<i>plant</i>	plant interaction
r	radiation
s	surface
si	internal surface
sol-air	sol-air
<i>solar</i>	solar gain
sky	sky
st	storage
sur	surround
T	total
V	ventilation
w	wall
wi	internal wall
we	external wall

Superscripts

t	Value of a variable at the beginning of a simulation time-step
$t+\Delta t$	Value of a variable at the end of a simulation time-step
\wedge	complex number

Abbreviations

ARH	ambient relative humidity [%]
AT	ambient temperature [K or °C]
CAV	cavity air velocity [ms^{-1}]
HGSR	horizontal global solar radiation [Wm^{-2}]
RVF	rainscreen ventilated façade
VF	ventilated façade
VGSR	vertical global solar radiation [Wm^{-2}]
WS	wind speed [ms^{-1}]
WD	wind direction [-]

INTRODUCTION

Background

Efficient energy use is quickly becoming a pressing concern both in developed and developing countries, owing to the dwindling supplies of traditional energy sources and to the impact that energy wastes have on the environment. Building energy consumption is an important portion of the energy demand of a country, and an important portion of the building energy consumption is due to heating, ventilation and air conditioning. As a consequence, research and development of natural methods for conditioning are gaining importance in modern building in order to achieve substantial energy savings.

Decades of research have generated a significant fundamental knowledge in the area of building envelope performance. Building envelopes have evolved from monolithic mass type designs to multi-layered lightweight systems. Today, building envelopes are complex to assemble, sophisticate, and require considerable fine tuning for good performance.

Parallel to the development of constructive solution, the need for energy conservation and sustainable design in buildings is awakening renewed interest towards passive solar systems, which are perceived as able to provide free energy for the conditioning needs of the building. Among them, ventilated façades have proven themselves to be extremely attractive and promising.

Ventilated façade design is not a new topic - the implementation of ventilated façades in buildings has been an object of broad application especially in recent years when the design of buildings having low energy consumption has become a priority. In addition, this kind of component attracts designers and architects because of aesthetic reasons, of good noise insulation and of improved indoor conditions. In regions with high levels of solar radiation, ventilated structures keep the temperature of the inner shell of single or double-skin buildings at a temperature close to that of the outdoors, significantly reducing the impact of incident radiation on the indoor environment. Ventilating walls, façades and roofs, if well designed, can help to considerably reduce the summer thermal loads due to direct solar radiation. Moreover, ventilated structures can be extremely useful for the installation of photovoltaic panels in order to increase their cooling and, as a consequence, their efficiency.

Aim and scope of this work

The goal of this thesis is to contribute to the energy performance assessment of ventilated façades by the simultaneous use of experimental data and numerical simulations. To attain this result, the following steps were followed.

Firstly, a significant amount of experimental work was done on different types of ventilated façades with natural ventilation. The measurements were taken on a test building.

The purpose of the measurements is twofold. On one hand, the experiments offer insight into the complex behaviour of ventilated façades. On the other, the measurements provide data to validate the numerical models by means of dynamic simulation software (ESP-r).

The numerical simulation program requires a certain degree of complexity to achieve reliable energy simulations. However, this complexity must also be controlled in order to keep computation time within reasonable bounds.

Finally, an ideal office building is modelled with several kinds of ventilated façades to assess its energy performance. The results are compared to a traditional façade solution.

Outline of the thesis

Five main parts can be identified in this work: first (Chapter 1), a general introduction on ventilated façades is presented, followed (Chapters 2 and 3) by the theoretical analysis of ventilated walls and building energy simulation are treated. After this, the experimental setup on the test building is described and the measured data are commented (Chapter 4). The next part (Chapters 5 and 6) presents the empirical validation and modelling of the ventilated façade in the winter and the summer period respectively. The final part of this work (Chapters 6 and 7) is devoted to the analysis of the thermal and energy performance of several types of ventilated façades.

The contents of the chapters are summarized in the following.

Chapter 1 gives definitions and different typologies of ventilated façades. Next, an overview of the external skin's materials is given with a brief description of other ventilated systems such as Trombe-walls and solar chimneys. The final section makes some design considerations on the envelope performances and the main technical Standards of ventilated façade system are illustrated.

Chapter 2 gives an overview of the basic theoretical analysis for naturally ventilated façades. A simple comparison of the heat transfer correlations and the steady-state thermal transmittance with measurements is given. Chapter 3 describes ESP-r's thermal simulation methodology, and the modelling setup of rainscreen ventilated skin façades with the program.

Chapter 4 deals with the measurements carried out on a rainscreen ventilated skin façade on a test building located in San Mauro Pascoli (Italy). The measurement set-up is used to extend the knowledge on the thermal behaviour of the rainscreen ventilated façades. Climate measurements of the local zone both for winter and summer are described, as well as the horizontal and vertical temperature gradients inside ventilated walls. In order to investigate the summer thermal performance of the rainscreen wall component a series of tests are performed through twelve different patterns of ventilated façade.

Chapter 5 and 6 constitute the core of this work. The thermal behaviour of a rainscreen ventilated façade is numerically investigated both in the winter and summer period. The modelling of the test building using a dynamic thermal simulation program (ESP-r) is presented and the main results discussed. In order to study the rainscreen ventilated façade three different multi-zone models are defined and comparison with the experimental results is made in order to select the best ESP-r air flow network for the modelling of this kind of envelope component.

The summer thermal performance of the rainscreen ventilated façade is illustrated in Chapter 7. A study on the summer thermal performance by means of dynamic parameters for different configurations of the setup of rainscreen walls is made. In particular influences of ventilation grills, air cavity thickness, skin's colour, skin's material, orientation of façade are investigated. Chapter 8 reports the assessment of the energy performance of different ventilated façades and their bearing on the energy performance on a whole building. To this aim, the building energy simulation program ESP-r is on four types of envelope façades. Two traditional Italian masonry (with and without thermal insulation) and two naturally RVFs are studied. Sensible energy demand for space heating and cooling of office buildings is determined.

Finally, conclusions are drawn and recommendations for future research are presented.

CHAPTER 1

VENTILATED FAÇADE WALLS

1.1 Introduction

This chapter starts with a general definition of ventilation façades is presented. The section thereafter describes the different typologies from an operational point of view. The origin and the driving force of the airflow characterise the main principles of ventilation modes. An overview of different materials for the external skin is then given followed by a brief description of other ventilated system such us Trombe-wall and solar chimney.

The final section gives an overview of the design considerations and envelope performance, main technical Standards on ventilated façade systems, while in the last section some consideration on energy performance are illustrated.

1.2 Definition

The Ventilated Façade (VF) is multiple layer construction with an external skin (either transparent or opaque), an intermediate space (generally air) and an internal wall (either transparent or opaque) while constitute the outer envelope of outside modern buildings.

In this work, the expression “ventilated façade” is used as a general term to cover all possible typologies. Instead “ventilated opaque façades” are defined by the following description:

“A ventilated opaque façade is an envelope construction, which consists of one external opaque skin separated by an air cavity from the internal opaque wall”.

Usually, at the top and at the bottom of this wall ventilation grills are located. In Figure 1.01 a typical of ventilated opaque façade section is depicted in detail.

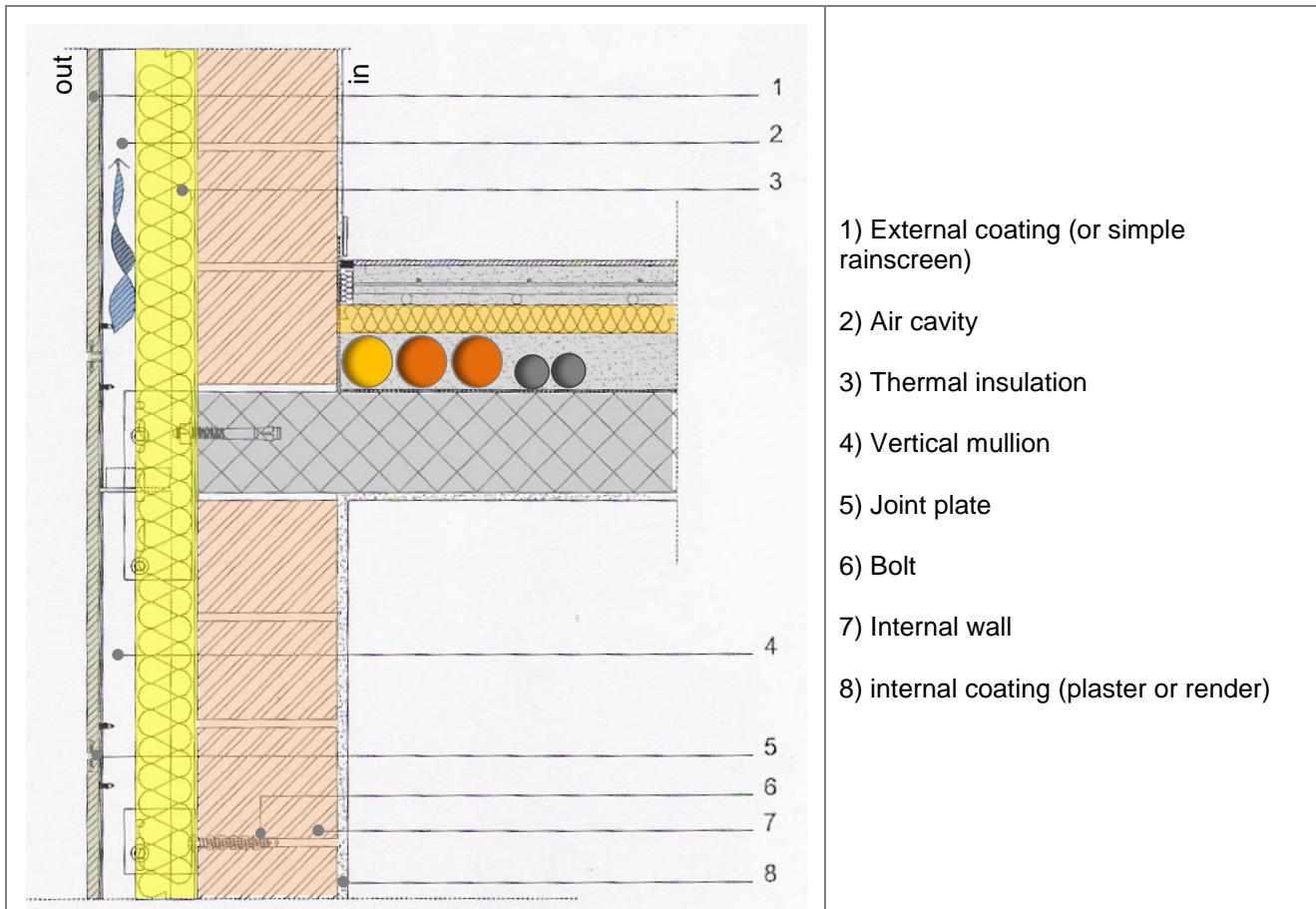


Figure 1.01: Ventiladed opaque façade (vertical section)

Beside its aesthetics, the VF can collect or expel the solar radiation absorbed by the external skin façades and realize natural ventilation in the building’s envelope, thereby improving the thermal comfort while saving energy for heating and cooling.

In fact, energy consumption of buildings with VF strictly depends on their thermal performances, especially the thermal heat transfer and solar heat gain which vary with seasons and location. VFs are in fact becoming an important and widely used architectural element in office buildings, as they can provide numerous advantages beyond their good aesthetics.

The external façade layer provides protection against the weather and improved acoustic insulation against external noise.

In general terms, the main purpose of one ventilated opaque wall is not to reduce the thermal load of the hot surface during the summer period but rather to inhibit moisture transport through the wall and protect from weathering. The reduction of heat gains in the summer period through ventilation in the channel is very low. If the external thermal insulation layer is present then the influence of ventilation on the expulsion of the heat is still more limited. One of the aims of this work is to investigate on above mentioned energy performance of one typical ventilated façade.

Air cavities in the building envelope can also be found in old typical buildings to protect the external walls from weathering, and in this case they are separated from the external layers of coating [Torricelli et al, 2001]. Moreover, different layers in building structures, with external coating (that would feature decorative function) was a good practice already common in Roman architecture during the late Republican period (II-I century BC) [Acocella, 2000].

1.3 Typology

A vast amount of possibilities exists to construct ventilated façades. In the literature, a multitude of definitions, descriptions and synonyms are employed to designate ventilated façades. For example the lists below sums up a variety of terms both for VFs [Poirazis, 2006] and ventilate opaque façades:

- Double-Skin Façade
- Active Façade (usually when the air cavity ventilation is mechanical)
- Passive Façade (usually when the air cavity ventilation is natural)
- Double Façade
- Double Envelope (Façade)
- Dual-Layered Glass Façade
- Dynamic Façade
- Wall-Filter Façade
- Environmental Second Skin System
- Energy Saving Façade
- Ventilated Façade
- Energy Saving Façade
- Environmental Façade
- Multiple-Skin Façades
- Intelligent Glass Façade
- Second Skin Façade/System
- Airflow Window
- Supply Air Window
- Exhaust Window/Façade
- Double Skin Curtain Wall
- Twin Skin Façade
- Curtain wall
- Rainscreen ventilated skin façade
- Ventilated opaque façade

The ventilated opaque façades can be classified according to the typology (nature, type and size), building materials used for exterior coating and also the systems to fix the coating to the wall structure [Bondielli, 2000]. Further, the structure of the ventilated roof is similar to that of ventilated façades, except for the inclusion of a waterproof layer in order to protect from weathering. The external coating layer, for both ventilated façades and roof, has the function to mark the cavity and protect the internal building structure component weathering.

Regardless of the many characteristics from associated with VFs, two parameters adequately characterise the major working principles:

- The origin of the airflow
- The driving force of the airflow

1.3.1 Airflow origin

The origin of the airflow is an important characteristic because it largely influences the average cavity temperature. Three airflow concepts are possible [terminology after Park et al., 1989]:

- *supply*: fresh outside air flows through the cavity into the building (Figure 1.3a).
- *exhaust*: inside air flows through the cavity to the outside (Figure 1.3b).
- *air curtain*: the air leaves the cavity from the same side it came in: there is no air exchange between the inside and outside through the multiple-skin façade. There are two possibilities: (1) an air curtain with exterior air, common for natural ventilation (Figure 1.02c) and (2) an air curtain with interior air, normally combined with mechanical ventilation (Figure 1.02d).

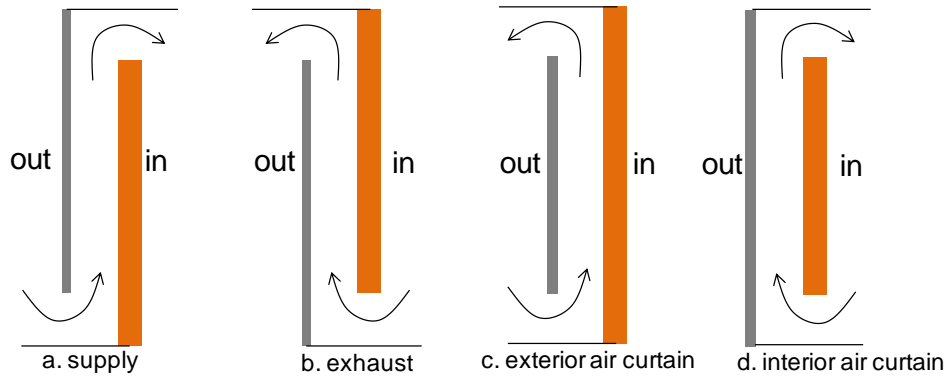


Figure 1.02: Diagram of the different options regarding the origin of the air flowing through ventilated façade. The direction of the airflow is illustrative.

In this work only configuration 1.02c is analysed.

1.3.2 Driving force

The cavity can either be *mechanically* or *naturally* ventilated. The knowledge of the driving force is important to determine the convection regime which should be used to calculate the convective heat transfer (see Chapter 2). Furthermore the driving force determines the continuity and controllability of the airflow. In the first option, fans generate the airflow. Usually, mechanically ventilated façades are incorporated for the HVAC-system, but examples with small built-in fans exist as well. The airflow in mechanically VF is much more controllable than in the naturally ventilated variants.

The driving forces behind naturally ventilated façades are thermal buoyancy and wind pressure differences. As a result, the airflow rate is no longer a known quantity but depends on climatic conditions. Naturally ventilated façades are either applied as supply windows in naturally ventilated offices or as air curtain envelopes in fully conditioned offices.

1.4 External skin materials and examples

Among the external coating systems, one can distinguish between "traditional" materials, including the wood and stone, and "innovative" materials: metals (e. g. aluminium, stainless steel, copper, titanium), plastics (HPL melamine) and concrete (fibrocement) [Ferrario and Gregato, 2001; Lucchini, 2000]. Traditional materials with innovative systems have also been employed recently such as ceramics (porcelain stoneware tile and natural stones) and clay bricks (Figures 1.02a and 1.02b).

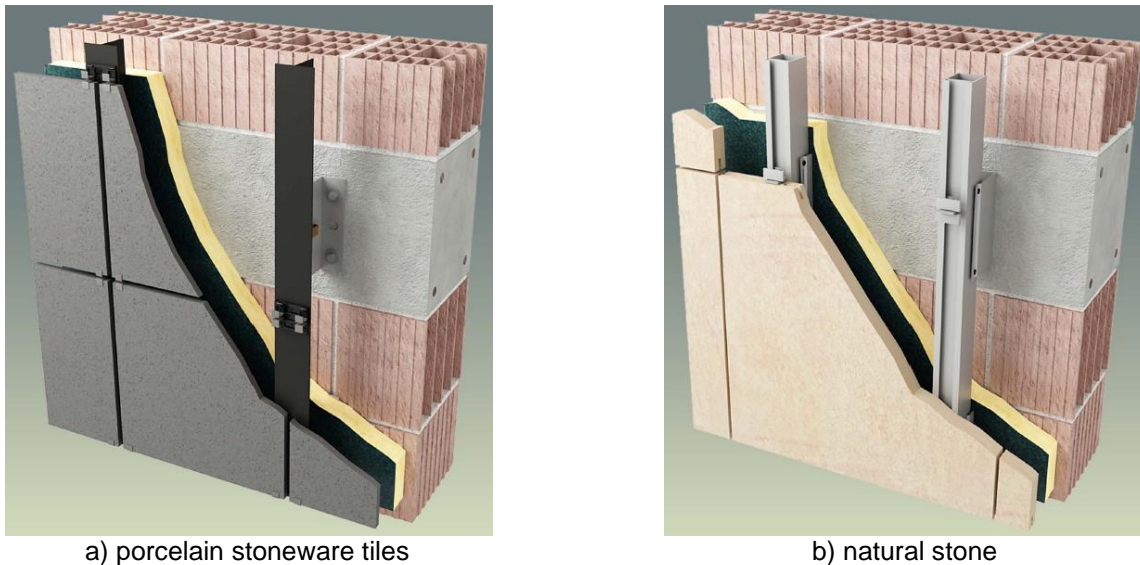


Figure 1.03: Rainscreen ventilated skin façade (source Aliva s.r.l.)

Usually, the external coating materials are pre-assembled panels of various sizes which are fixed to the anchor substructure and spaced appropriately to create continuous joints between panels. Joints are functionally necessary to allow free thermal expansion of slabs, caused by variations in temperature or any structural adjustment thus can be either "closed" (2 to 3 mm) or open (Figure 1.04) (6 to 7 mm, up to 1.5 cm).

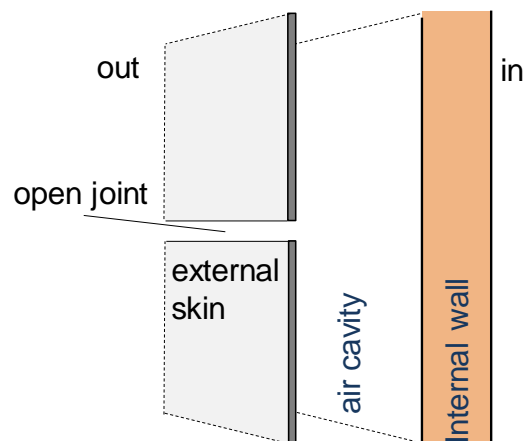


Figure 1.04: Open joints in external skin of ventilated opaque façade.

The brick façade is also utilised as external coating even for pre-assembled modular panels or in building's roofs with elements in roof tiles of various shapes and sizes. The use of brick on façades keeps traditional aspects of brick facing (recurrent in some areas of Italy). An example of brick façade building is given in Figure 1.05a.

External coverings with ceramic tiles can be made with porcelain stone cladding due its high of mechanical strength. The use of modular tiles of white porcelain is present, for example, in Meier's architecture (Figure 1.05b).

The coating in metal claddings (slabs of special shapes and sizes) has a growing tendency, such as for example Libeskind's Jewish Museum (Figure 1.05c) and Gehry's Guggenheim Museum (Bilbao, 1997). The materials used for metal cladding are usually aluminium, galvanized and painted steel, stainless steel, zinc, copper, titanium, for use in both façades and roofs.



Figure 1.05: Examples of realised building with ventilated façade system

1.5 About Trombe-walls and solar chimneys

An analogue thermal buoyancy mechanism can be obtained by other ventilated component such Trombe walls, solar chimneys and double ventilated façades. Examples of experimental and numerical studies of Trombe walls include the work by Warrington and Ameal [1995], Pitts and Craigen [1996], Borgers and Akbari [1984], Chaturvedi [1992] and Gan [1998]. Solar chimneys have been investigated by a number of researchers for providing a comfortable living environment in buildings [Barozzi et al 1992, Bansal et al 1994, Bouchair 1994, Gan and Riffat 1998]. Investigations into the thermal performance of double façades have also been carried out for preheating incoming air or ventilation of façade interior or as an exhaust duct for mechanical ventilation of buildings [van Paassen and Stec 2000, di Maio and van Paassen 2000, Hensen et al 2002, Stec et al 2005] or even for air conditioning using the hot air from façade-integrated solar thermal and electricity [Eicker et al 1999].

A Trombe wall is a south-facing thermal storage wall made of concrete or masonry blackened and covered on the exterior by glazing. The storage wall collects and stores solar energy to provide room heating in winter or facilitate room ventilation in summer. Trombe-wall (TW) have been used for decades as an efficient and durable solar heating method. The TW comprises a massive thermal wall and a clear glazing cover with an air duct in between.

A solar chimney has a similar structure and working mechanism to a TW but is mainly used for enhancing natural ventilation of a building.

Solar chimneys are natural ventilation systems which can contribute to improve the energy efficiency of buildings, and it is therefore necessary to investigate their behaviour from the energy point of view. Those building components conditioning which use natural ventilation take advantage of solar radiation to generate convective air flows, which pull air out of the interior of the building, replacing it with air from outside. In this case the parameters of interest for bioclimatic construction are the air flow rate through these systems, and the amount of energy which they supply to the building.

The first studies about solar chimneys began with Bansal et al. [1993] which developed a mathematical model for a steady state of a solar chimney consisting of a conventional chimney connected to a solar air collector. Khedari et al. [1999] showed the experimental results of natural ventilation effect by a solar chimney in the temperature and air renovation in a school. Afonso and Oliveira [2000], published the results of a solar chimney compared with a conventional chimney. They proposed a non-steady model of heat transfer in a single horizontal dimension, applying a model based on finite differences. In this model, the coefficients of heat transfer vary throughout the day according to temperatures. The measurements on air flow were made with tracer gas techniques that agreed with the results of the simulation. Ong [2003] proposed a mathematical model of steady state heat transfer for a solar chimney, and applied it to a real solar chimney [Ong and Chow 2003].

When photovoltaic (PV) cells/modules are integrated into the outer skin of the façade [Eicker 1999], heat absorption by the skin would become pronounced and consequently the flow behaviour in the façade would be similar to that in a solar chimney. Use can then be made of the PV façade for ventilation cooling of the building as well as the façade cavity and PV cells.

1.6 Performance assessment

Like any façade, ventilated façades have to comply with a variety of envelope requirements. It is therefore helpful to identify and to assess the pros and cons of ventilated façades.

The advantages resulting from the ventilated wall compared to a traditional one are:

- elimination of the risk of cracked cover;
- elimination of the risk of detachment from the wall;
- protection of the façade against the direct action of atmospheric agents;
- elimination of heat bridges leading to energy saving;
- elimination of surface condensation (the presence of an air gap facilitates evacuation of water vapour from the interior and promotes the removal of possible moisture);
- lasting efficiency of the outer insulating material, which is kept dry thanks to the ventilation;
- easy ventilated wall installation regardless of the climatic conditions;
- maintenance and work can be carried out on individual porcelain tiles;
- creation of a technical workspace for pipe and duct housing.

As stated in the previous section, the modes of ventilation in the cavity of a ventilated opaque façade could be natural, forced or mixed. The natural ventilation of the VF is based on the thermal buoyancy produced by the temperature difference between the exterior and interior cavity, while is

increased by the asymmetric solar radiation on and transmittance through the façades. Wind pressure can also influence the natural ventilation in the cavity [Gratia and Herde 2007a, 2007b].

Therefore the airflow is not easy to control nor is it continuous since it depends on weather conditions. Ventilation behind the cladding can be an important means of both drying and avoiding inward vapour drive wetting. In fact, a lack of ventilation may be the reason inward vapour driven problems in filled-cavity walls [Straube and Burnett 1997]. Very small air flows can, however, transport significant quantities of moisture if they act for long enough. Because the air space in any wall is usually warmer and contains more moisture than the outdoor air, even small ventilation flows over many days have the potential to remove significant amounts of moisture.

Ventilation flow is driven by a combination of wind pressure differences, thermal buoyancy and moisture buoyancy. The provision of vent openings at both the top and bottom of the air space will generally induce the best ventilation because these vent locations take advantage of both buoyancy forces and wind pressure. This was demonstrated by field monitoring of a test building (see Straube and Burnett 1995). The primary function of the air cavity behind the cladding is to provide a capillary break and drainage for accidental inflows of entered rainwater or condensation. Extensive research has been carried out on evaluating the airflow rate in the air cavity and the moisture removal by cavity ventilation through laboratory testing, field measurements, and simulations (Bassett and Mcneil 2005a, 2005b; Hansen et al. 2002; Hazleden 2001; Straube and Burnett 1995; VanStraaten and Straube 2004; Onysko 2003).

The ventilated wall, despite its many advantages, has some drawbacks too. The critical issues are control technology in the design phase and during installation works. The main drawbacks, especially for the existing buildings include for example unevenness of the coating, impact resistance, limitations in the form of building volumes, bad acoustic behaviour concerning wind impact, rain and hail and also higher cost of installation than traditional solutions.

1.7 Technical Standards

The Italian Standards do not address the ventilated wall system in detail, but there are many technical recommendations on classification and characteristics of materials used for external cladding and mechanical anchor systems. Among the main Standards on the classification and criteria for quality product may be mentioned, for example, for stone materials UNI EN 12670:2003, UNI EN 12057:2005, UNI EN 12058:2005 and for ceramic tiles, the Standards UNI EN 14411, 2007 and UNI EN ISO 10545-1, 2000. Further, there are also the standard UNI 9811:1991 on the metal expansion anchors and Directive ICITE -1992 on the anchor bolts. The most important Italian Standard regarding the ventilated walls system is the UNI 11018 [2003].

The UNI 11018/2003 standard has been published as part of a project on “Cladding with synthetic materials”, “Cladding with metal materials” as well as “Cladding with stone and ceramic materials”. It is divided into 10 chapters and has been drafted to provide basic information for operators (designers, fitters, testers, maintenance persons or manufacturers); it is applied to the following conditions: installation of opaque protective or decorative surfaces as outer cladding of vertical, outer walls; cladding of new buildings; design of cladding as components of microventilated and ventilated façades; construction of cladding with mechanical installation systems. The standard does not apply to the following cases: supporting structures made of stone or brick; cladding realised by means of slabs secured in place by adhesion or of slabs applied with mixed systems, such as mortar and anchorage plates; systems in which the cladding is used as disposable formwork for concrete or for prefabricated panels or in which any type of external cladding is mechanically fixed or glued to profiles for doors and windows; systems using light multilayer prefabricated panels for external insulation, without ventilation. After providing a complete list of standards relating to the matters dealt with, the UNI 11018/2003 provides 96 definitions of technical terms for ventilated façade systems envisaging the use of stone or ceramic material. In the paragraph called “Materials and components”, basic information is given concerning the

products used for anchorage and cladding systems. The subsequent section, "Equipment", provides a list of tools, equipment and machines, which are used for securing the cladding material. Given the importance of the project and in particular of the construction principles, in the section "Instructions for design" references are given concerning the choice and size of the main components, as well as guidelines for development of the project, along with a list of typical mistakes to avoid when constructing a ventilated façade with mechanical fixing elements and stone or ceramic cladding materials. Inside the "Instructions for construction and quality control" you will find the guidelines for the project with examples of instructions for assembly along with tolerance ratings.

Concerning the international legal standards, it seems appropriate to recall the ASTM C1242, BS 8298 [1994], CSTB [1999] and DIN 18516/3 [1990] containing guidelines for design and installation of ventilated walls, accompanied by examples and technical details. However, except for the French Standard CSTB [1999] on the general rules for light ventilated skin systems, the Standards mentioned above treat only the case of stone cladding and its anchorage systems.

Concerning the thermal resistance of ventilated walls and roofs the international standard UNI EN ISO 6946 [2007] provides useful indications on design in several cases in which the gap is not ventilated (unventilated air layer), slightly and well ventilated air layer. More information details are indicated in Chapter 2. Further, a short information for ventilated air cavity is present in the Standard EN ISO 13792 [2005] regarding a simplified method to calculate internal temperatures of a room in summer period without mechanical cooling.

1.8 Envelope performance

Opaque ventilated façade systems are increasingly used in buildings, even though their effects on the overall thermal performance of buildings have not yet been fully understood. The only way to estimate the building envelope energy efficiency at the design stage is through energy simulations, which quantitatively represent a system without actually building it. Currently not all the types of building envelope can be accurately described and simulated due to the lack of available data and software tools, for instance the ventilated façade has no certified performance, and needs to be tested to understand how it affects energy savings.

This thesis is consequently focusing on a characterization an energy simulation methodology able to asses performance of the ventilated opaque façade and investigate its effectiveness.

In the design phase of a building equipped with a ventilated façade, it is essential to be able to predict its energy performance and this for different design possibilities of the façade. The possibility of modelling the façade (and the building) with simulation programs can play an important role from this point of view and allows to compare different possible design concepts.

The prediction of the energy performance of a ventilated double façade is a complex matter. The thermal process and the airflow process interact. These processes depend on the geometric, thermo-physical, optical and aerodynamic properties of the various components of the ventilated façade.

The aim of this work is also to explain how the thermal and solar performances of ventilated façades and of buildings equipped with this kind of façades can be predicted by simulation.

The energy savings achievable with the use of ventilated walls depend in general on environmental factors (site and climatic conditions), and geometric characteristics construction of the wall. In some works [Brunello and Peron, 1996; Ciampi and Tuoni 1995, 1998; Fracastoro *et al.*, 1997; Torricelli, 2000; Zannoni, 1996; Bartoli *et al* 1997a, 1997b], in the case of natural ventilation, the air cavity velocity (typically ranging from 0.4-1.2 ms⁻¹) relates with the air flow and the height of the channel.

The air flow will also depend on pressure drop, due to the anchoring systems and the presence of openings in the façade (windows) and roof (skylights), and the wind speed near the upper and lower ventilation grills [Brinkworth et al., 2000]. Recent studies [Naboni, 2007] demonstrate that the energy saving cooling for summer may reach about 6-8% with a ventilated wall solution in comparison a traditional solution (without ventilated air cavity).

1.9 Conclusion

In this chapter, a definition of ventilated façades is given, the typology and different external skin's material is outlined. The typology is based on the origin and the driving force of the airflow of the façade. The presented typology allows to describe the operation of a ventilated façade.

Such performance assessment allows to put this research in a broader perspective. It demonstrates that although energy performance is an important issue, there are several other reasons to chose for ventilated façades. Nevertheless, it is shown that an energy performance assessment interferes with a large number of these reasons.

CHAPTER 2

VENTILATED FAÇADE - THEORETICAL ANALYSIS

2.1 Introduction

There are many published works on the thermal behaviour of ventilated façades, Trombe-Michel walls and solar chimneys. A large number of them is concerned with the numerical simulation of such components by using Computational Fluid Dynamics (CFD) and Building energy Simulation (BS). For example, Smolec and Thomas [1991] determined the air temperature distribution through a Trombe wall by using a thermal model having a network structure in order to take into account all the heat fluxes occurring in this component and they compared the results with experimental data. Mootz and Bezian [1996] performed a numerical study of a ventilated façade panel structured like a composite Trombe-Michel wall. Gan [1998] carried out the numerical simulation of a Trombe wall for summer cooling by using the CFD technique and investigated the effect of the distance between the wall and glazing, wall height, glazing type, and wall insulation on the thermal performance of a Trombe wall.

Other authors highlighted important aspects such as changing density on buoyancy forces [Rodrigues et al. 2000, Stovall 2004], convective moisture transport [Davidovic et al. 2006], mechanical ventilation on active transparent façades [Serra et al. 2010, Coussirat et al 2008] and also the pressure coefficient in building energy simulation [Costola et al. 2009, and Nore et al. 2010].

In this Chapter an overview of the basic theoretical analysis for naturally Ventilated Façades (VF) is given. Section 2.2 presents the heat balance for VF with the description of the different types of heat fluxes involved, continuing the Section 2.3 is devoted to convective heat transfer; further a simple comparison of the heat transfer correlations with measurements is given. In the last Section 2.4 the steady-state thermal transmittance of analysed Rainscreen Ventilated Façade (RVF) wall in winter period for southern and western façade is determined. Results based on the average method [ISO 9869 1994] and compared with the standard method [EN ISO 6946 2007].

2.2 Heat balance for ventilated façades

This section presents the fundamental heat balance for ventilated façades starting from the external skin façade, continuing with the heat balance for the air cavity and ending with that for the inner wall. The following equations are valid for the 1-dimensional approximation.

2.2.1 Heat balance for the external skin façade

As known, at the exterior surface (labeled with “ce” in Figure 2.01) the heat exchange with the environment per unit of surface area (Q_e) is a combination of convection and long-wave radiation:

$$Q_e = Q_{h,ce} + Q_{lw,ce} \quad (Wm^{-2}) \quad [2.01]$$

The convection with outdoor air can be described by means:

$$Q_{h,ce} = h_{ext}(T_e - T_{ce}) \quad (Wm^{-2}) \quad [2.02]$$

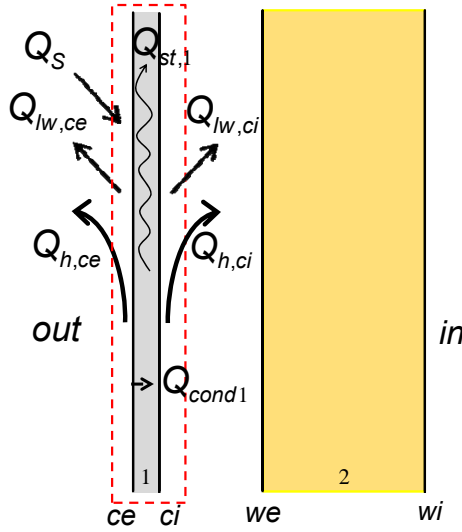


Figure 2.01: Heat balance for the skin façade

where h_{ext} is the convection coefficient at the exterior surface ($Wm^{-2}K^{-1}$) (see Section 2.3.6), $(T_e - T_{ce})$ is the temperature difference between the exterior ambient and the skin surface (K).

The heat transfer Q_e usually depends on the wind velocity or sky temperature but if this information is not available, the heat transfer to the environment can be described by a combined surface film coefficient (h_e ($Wm^{-2}K^{-1}$))) and an equivalent exterior or “sol-air” temperature ($T_{sol-air}$ ($^{\circ}C$)):

$$Q_{h,ce} = h_e(T_{sol-air} - T_{ce}) \quad (Wm^{-2}) \quad [2.03]$$

The value of the surface film coefficient is standardized. In Italy it amounts to $h_e = 25 Wm^{-2}K^{-1}$ considering specific input such as a wind speed of $4 ms^{-1}$, a long-wave emissivity of the surface ε of 0.9 and a external surface temperature evaluated at $10^{\circ}C$ [UNI EN ISO 6946, 2008].

The long-wave length radiation exchange with the outdoor landscape surface and with the sky can be described by the Equation 2.04. In other words the net long-wave radiation exchange at some exposed external building surface is given as the difference between the emitted and received flux. If the surroundings are represented by some equivalent temperature, T_{eq} then the net exchange can be expressed as:

$$Q_{lw,ce} = \varepsilon_{ce} \cdot \sigma \cdot (T_{eq}^4 - T_{ce}^4) \dots (Wm^{-2}) \quad [2.04]$$

where ε_{ce} is the long-wave emissivity of the external surface, σ is the Stefan-Boltzmann constant ($W m^{-2} K^{-4}$), T_{ce} and T_{sur} are the absolute temperatures of the external surface and the equivalent respectively.

The equivalent temperature is a function of the temperatures of the sky, ground and surroundings:

$$T_{eq}^4 = f_s \cdot T_{sky}^4 + f_g \cdot T_{grd}^4 + f_u \cdot T_{sur}^4 \quad (K) \quad [2.05]$$

where f_s , f_g and f_u are view factors to the sky, ground and surroundings respectively. Table 2.01 [Clarke, 2001] gives some values.

Table 2.01: Representative values of sky, ground and obstructions view factors.

Location	f_s	f_g	f_u
City centre: surrounding buildings at same height, vertical surface	0.36	0.36	0.28
City centre: surrounding buildings higher, vertical surface	0.15	0.33	0.52
Urban site: vertical surface	0.41	0.41	0.18
Rural site: vertical surface	0.45	0.45	0.10
City centre: sloping roof	0.50	0.20	0.30
Urban site: sloping roof	0.50	0.30	0.20
Rural site: isolated	0.50	0.50	0.00

As an alternative the long-wave radiation exchange with the exterior can approximately be described by:

$$Q_{lw,ce} = \frac{\epsilon_{ce} \cdot \sigma}{2} \cdot \left[(T_{sky}^4 - T_{ce}^4) + (T_{sur}^4 - T_{ce}^4) \right] \quad (W m^{-2}) \quad [2.06]$$

In this case the surroundings and the sky are assumed to be black bodies and the surface can be considered as a diffuse grey surface.

In the following simple sky temperature estimation will be described.

The fictive sky temperature used to calculate the long-wave radiation exchange to the sky depends on ambient temperature, ambient humidity, cloudiness factor of the sky and local atmospheric pressure. For a partially overcast sky it may be estimated by [Cole, 1976]:

$$T_{sky} = T_e \cdot [\epsilon_0 + 0.84 \cdot c \cdot (1 - \epsilon_0)]^{0.25} \quad (K) \quad [2.07]$$

where T_e is the exterior air temperature (K), ϵ_0 is the emissivity of the clear sky and c is the cloudiness factor ($c = 0$ defines a clear sky). Berdahl and Martin [1984] proposed the following relationship to calculate the emissivity of the clear sky:

$$\epsilon_0 = 0.711 + 0.005 \cdot T_{dp} + 7.3 \cdot 10^{-5} \cdot T_{dp}^2 + 0.013 \cdot \cos\left(2\pi \frac{h}{24}\right) + 12 \cdot 10^{-5} (p_{atm} - p_0) \quad (-) \quad [2.08]$$

where T_{dp} is the exterior air dew-point temperature ($^{\circ}C$), h is the hour of the day (h), p_{atm} is the atmospheric pressure (Pa) and p_0 is the atmospheric pressure at sea level (Pa). If the cloudiness factor is not included in the weather data, it can be estimated by a formula proposed by Kasten and Czeplak [1980]:

$$c = \left(1.4286 \frac{I_d}{I_g} - 0.3 \right)^{0.5} \quad (-) \quad [2.09]$$

where I_d and I_g are the horizontal diffuse and the global horizontal solar radiation respectively. This relationship predicts physical impossible values in the absence of direct radiation (for $I_{d,h} = I_h$, $c > 1$). The relationship can be used with the constraint $0 \leq c \leq 1$. During night time, a corrective factor averaged over the afternoon may be applied. As an alternative to overcome the absence of the cloudiness factor, the sky temperature can be calculated as [Bliss, 1961]:

$$T_{sky} = T_e \cdot \left[0.8 + \frac{T_{dp} - 273}{250} \right]^{0.25} \quad (K) \quad [2.10]$$

where T_e and T_{dp} are the exterior air and dew-point temperature (K) respectively.

The simplest method to estimate the temperature of the ground and surrounding is to use the concept of sol-air temperature with the simple relationship:

$$T_{grd} = T_e + \frac{(\alpha_{grd} \cdot I_g - Q_{lw})}{R_{sg}} \quad (K) \quad [2.11]$$

where T_e is the air temperature, α_{grd} the ground absorptivity, I_g the total solar irradiance (Wm^{-2}), Q_{lw} the net long-wave radiation exchange (Wm^{-2}) and R_{sg} the combined convective/radiative ground surface layer resistance (m^2KW^{-1}). Application of this expression will require, firstly, that the long-wave exchange term be evaluated. This, in turn, will require knowledge of the temperatures of the sky and obstructions. If the influence of the vertical surface on the temperature distribution on the ground is ignored, the ground temperature can be calculated from a two surface radiation model. As an example, this was done with a fully coupled transient one-dimensional ground slab model [Janssen, 2002] taking into account solar and long-wave radiation and the heat loss to the soil. However, calculating the ground temperature requires a substantial computational effort. As a simplification, the ambient air temperature is used as surrounding temperature.

The absorbed solar energy (Q_s) is calculated as:

$$Q_s = \alpha_{ce} \cdot I_{g,t} \quad (Wm^{-2}) \quad [2.12]$$

Where α_{ce} is absorption coefficients for global solar radiation (-), $I_{g,t}$ is global solar irradiation (Wm^{-2}) on the vertical surface.

Q_{cond1} in Figure 2.01 is the conductive heat transfer into external skin of the façade. The thermal conductivity of the layer material is assumed to be constant. The thermal capacitance of the layer is examined not to be negligible. In this case, the conductive heat transfer between external surface (ce) and internal surface (labeled with "ci" in Figure 2.01) may then be estimated by the Fourier law of conduction:

$$Q_{cond1}(x) = -\lambda_1 \cdot \frac{\partial T_1(x,t)}{\partial x} \quad (Wm^{-2}) \quad [2.13]$$

where λ_1 and T_1 are respectively the thermal conductivity and the temperature of the skin façade material.

Of course also the heat storage in the external skin of the façade ($Q_{st,1}$) will be considered:

$$Q_{st1} = \rho_1 \cdot c_{p1} \cdot B \cdot \frac{\partial T_1(x,t)}{\partial t} \quad (Wm^{-2}) \quad [2.14]$$

where ρ_1 (kgm^{-3}) is the density of the skin façade material, c_{p1} ($Jkg^{-1}K^{-1}$) the specific heat at constant pressure and B is the length of the wall.

Equation 2.13 and 2.14 can be solved with control volume method [Clarke, 2001], for more details see the Section 3.2.2.

In Figure 2.01 it possible to notice also the convective heat transfer ($Q_{h,ci}$). The convective heat transfer ($Q_{h,ci}$) depends on the nature of the airflow, the airflow rate and the temperature difference between the surface and the fluid. If the horizontal temperature gradient is small, it possible to use a mixed temperature to represent the air control volume. The heat transfer from the surface to the fluid can then be calculated as:

$$Q_{h,ci} = h_{ci}(T_{ci} - T_{ac}) \quad (Wm^{-2}) \quad [2.15]$$

where h_{ci} is the convective heat transfer coefficient ($Wm^{-2}K^{-1}$) and $(T_{ci} - T_{ac})$ is the temperature difference between the surface and the air in the cavity. The relationships used to determine the convective heat transfer coefficient depend on the nature of the airflow and are summarized in Section 2.3.

Another important contribution on the total heat is radiation heat transfer ($Q_{lw,ci}$). As a first approach, the radiation heat transfer can approximately be described by:

$$Q_{lw,ci} = \frac{\sigma(T_{we}^4 - T_{ci}^4)}{\frac{1}{\epsilon_{we}} + \frac{1}{\epsilon_{ci}} - 1} \quad (Wm^{-2}) \quad [2.16]$$

where σ is the Stefan-Boltzmann constant ($Wm^{-2}K^{-4}$), ϵ_{we} and ϵ_{ci} are the long-wave surface emissivity on the external wall and internal skin façade respectively while T_{we} and T_{ci} are the absolute surface temperature (K) of external wall and internal skin façade (K). A more accurate model uses the net-radiation method [Hottel, 1954] to evaluate the radiation heat transmission in the cavities. For each surface in the cavity the net radiation is given by the difference between the outgoing and incoming radiation. The outgoing flux is composed of directly emitted and reflected radiation. The incoming flux consists of the sum of the outgoing fluxes of all other surfaces multiplied by the view-factor between the surfaces.

Finally the equation for the heat balance for the surface of the skin façade could be becomes:

$$Q_{h,ce} + Q_{lw,ce} + Q_S + Q_{cond}|_{ce} + Q_{cond}|_{ci} + Q_{h,ci} + Q_{hrci} = Q_{st1} \quad (Wm^{-2}) \quad [2.17]$$

2.2.2 Heat balance for the air cavity

Basically heat transfers in the air cavity are convective heat transfers for each internal surface of the channel and enthalpy flow. In Figure 2.02 one can see the convective heat transfer ($Q_{h,ci}$ and $Q_{h,we}$) and the enthalpy flow (Q_{enth}).

The convective heat transfer ($Q_{h,we}$) of course depends on the nature of the airflow, the airflow rate and the temperature difference between the surface and the fluid.

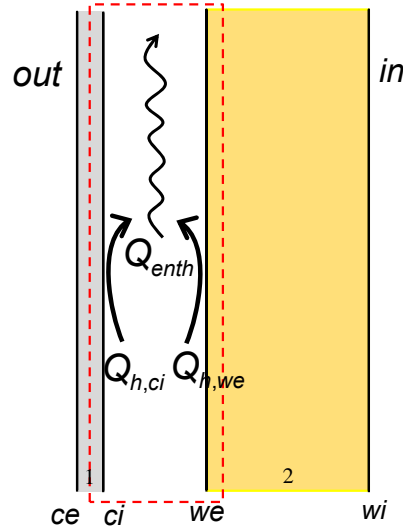


Figure 2.02: Heat balance for the air cavity

The heat transfer from the surface to the fluid can be described as:

$$Q_{h,we} = h_{we}(T_{ac} - T_{we}) \quad (Wm^{-2}) \quad [2.18]$$

where h_{we} is the convective heat transfer coefficient ($Wm^{-2}K^{-1}$) and $(T_{ac} - T_{we})$ is the temperature difference between the external surface of the wall and the air of the cavity.

Besides, the enthalpy flow (Q_{enth}) depends of the airflow through the cavity. The enthalpy flow is given by:

$$Q_{enth} = \rho_{air} \cdot c_{p,air} \cdot v_{ac} \cdot (T_{ac} - T_e) \quad (Wm^{-2}) \quad [2.19]$$

where ρ_{air} is the air density (kgm^{-3}), $c_{p,air}$ is the specific heat capacity ($Jkg^{-1}K^{-1}$), v_{ac} is the air velocity and $(T_{ac} - T_e)$ is the temperature difference between cavity air temperature and ambient temperature.

The air velocity and the temperature profiles in the naturally VF are mutually dependent and hence the thermal system must be solved iteratively. The air velocity depends from the equilibrium between the pressure difference between the inlet and outlet and the pressure characteristic of skin façade. For naturally ventilated skin façades, the pressure difference between the inlet and outlet is generated by thermal buoyancy (ΔP_{buoy}) and wind pressure differences (ΔP_{wind}):

$$\Delta P = \Delta P_{buoy} + \Delta P_{wind} \quad (Pa) \quad [2.20]$$

The pressure difference due to thermal buoyancy can be evaluated either by Archimedes principle or as [Liddament, 1996]:

$$\Delta P_{buoy} = \rho_e \cdot g \cdot H \cdot \left(\frac{T_{ac}}{T_e} - 1 \right) \quad (Pa) \quad [2.21]$$

with ρ_e is the outdoor air density (kgm^{-3}), g is the gravitational acceleration (ms^{-2}), H is the cavity height (m), T_{ac} is the absolute average cavity air temperature (K) and T_e is the absolute ambient temperature (K).

As a first estimate, the wind pressure difference (ΔP_{wind}) may be evaluated from the free field variation of the wind velocity with height and the Bernoulli equation:

$$\rho_v = \frac{\rho_e \cdot v_h^2}{2} \quad (\text{Pa}) \quad [2.22]$$

where ρ_e is the outdoor air density (kgm^{-3}) and v_h is the approach wind speed at height h (ms^{-1}). The wind speed as function of the height can be estimated by a power law function:

$$v_h = v_{met} \left(\frac{\delta_{met}}{h_{met}} \right)^{a_{met}} \cdot \left(\frac{h}{\delta} \right)^a \quad (\text{ms}^{-1}) \quad [2.23]$$

where δ is the wind boundary layer thickness (m), h is the height above ground level of the inlet grid (m) and “a” is the local terrain exponent. The subscript “met” means the values of the meteorological station. Values for the wind boundary layer thickness (δ) and the local terrain exponent (a) are available from ASHRAE [1997]. In the area considered of this study the wind boundary layer thickness is estimated to be $\delta = 370$ m while the local terrain exponent a is equal to 0.22. Both values are representative of suburban terrain [ASHRAE 1997].

Combining the two Equations, the wind pressure difference for a VF with height H can be described by:

$$\Delta P_{wind} = \left[\frac{\rho_e}{2 \cdot \delta^{2a}} \cdot \left(\frac{\delta_{met}}{h_{met}} \right)^{2a_{met}} \cdot (h^{2a} - H^{2a}) \right] \cdot v_{met}^2 \quad (\text{Pa}) \quad [2.24]$$

An alternative approach estimates the wind pressure difference from the local wind pressure coefficient (C_p) on the building surface. The local pressure on a building surface (p_s) can be calculated as:

$$p_s = C_p \cdot \rho_v \quad (\text{Pa}) \quad [2.25]$$

where ρ_v is usually calculated from Equation 2.22, with the wind velocity at roof height as a reference. The main problem is the determination of the distribution of local wind pressure coefficients (C_p) over the building surface. The values for C_p depend on the shape of the building, the wind direction, the nearby buildings and the terrain features. Values of C_p can be gained from wind tunnel tests or numerical simulations. C_p values as a function of the wind direction can be found in Davenport and Hui [1982] for high, tall buildings and in Holmes [1986] for low-rise buildings. Numerically determined values are for example available from Murakami and Mochida [1988], Zhou and Stathopoulos [1996] and Tsuchiya et al. [1997].

A local heat balance equation for air at a certain area with an infinitesimal length dy , located at a height y above the channel entry, relates the local air temperature variation, dT , to the heat exchange by convection with each of the adjacent surfaces (c_i and w_e in figure 2.02):

$$dQ_{enth} = \rho_{ac} \cdot c_{p,a} \cdot v_{ac} \cdot s1 \cdot dT_{ac}(y) \quad (Wm^{-1}) \quad [2.26]$$

$$dQ_{h,we} = h_{we}(T_{we} - T_{ac})dy \quad (Wm^{-1}) \quad [2.27]$$

$$dQ_{h,ci} = h_{ci}(T_{ci} - T_{ac})dy \quad (Wm^{-1}) \quad [2.28]$$

$$dQ_{enth} = dQ_{h,we} + dQ_{h,ci} \quad (Wm^{-1}) \quad [2.29]$$

$$\rho_{ac} \cdot c_{p,a} \cdot v_{ac} \cdot s1 \cdot dT_{ac}(y) = h_{we}(T_{we} - T_{ac})dy + h_{ci}(T_{ci} - T_{ac})dy \quad [2.30]$$

$$dT_{ac}(y) = \frac{h_{we}(T_{we} - T_{ac}) + h_{ci}(T_{ci} - T_{ac})}{\rho_{ac} \cdot c_{p,a} \cdot v_{ac} \cdot s1} dy \quad (K) \quad [2.31]$$

If is to assume that the average values of the convection coefficients, h_{we} and h_{ci} and the cross-section average velocity, v_{ac} are known, integrating between 0 and y , the result is the expression for the temperature at height y :

$$T_{ac}(y) = \frac{h_{we} \cdot T_{we} + h_{ci} \cdot T_{ci}}{h_{we} + h_{ci}} - \frac{h_{we}(T_{we} - T_{inlet}) + h_{ci}(T_{ci} - T_{inlet})}{h_{we} + h_{ci}} \cdot e^{-\frac{h_{we} + h_{ci}}{\rho_{ac} \cdot c_{p,a} \cdot v_{ac} \cdot s1} y} \quad (K) \quad [2.32]$$

where T_{inlet} is the air inlet grid temperature. In the equation 2.32 it possible to introduce an equivalent temperature (T_{ac}^*) of the air cavity defined as:

$$T_{ac}^* = \frac{h_{we} \cdot T_{we} + h_{ci} \cdot T_{ci}}{h_{we} + h_{ci}} \quad (K) \quad [2.33]$$

With this parameter Equation 2.32 becomes:

$$T_{ac}(y) = T_{ac}^* - (T_{ac}^* - T_{inlet}) \cdot e^{-\frac{h_{we} + h_{ci}}{\rho_{ac} \cdot c_{p,a} \cdot v_{ac} \cdot s1} y} \quad (K) \quad [2.34]$$

which is similar to the typical expression for the evolution of the fluid temperature in internal pipe flow. More information about the typical solution procedure and mathematical model can be found in [Ciampi et al., 2003].

Finally the equation for the heat balance for the air cavity of ventilated façade becomes:

$$Q_{h,ci} + Q_{h,we} = Q_{enth} \quad (Wm^{-2}) \quad [2.35]$$

2.2.3 Heat balance for the inner wall

Starting from the heat exchange with the interiors, as for the exterior surface, the heat exchange with the internal environment per unit of façade width (Q_i) is a combination of convection $Q_{h,wi}$ and long-wave radiation $Q_{lw,wi}$ as depicted in Figure 2.03:

$$Q_i = Q_{h,wi} + Q_{lw,wi} \quad (\text{Wm}^{-2}) \quad [2.36]$$

Convection with indoor air it has the following expression:

$$Q_{h,wi} = h_{\text{int}}(T_i - T_{wi}) \quad (\text{Wm}^{-2}) \quad [2.37]$$

where h_{int} is the convection coefficient at the interior surface ($\text{Wm}^{-2}\text{K}^{-1}$) (see Section 2.3.6), $(T_i - T_{wi})$ is the temperature difference between the interior ambient and the skin surface (K).

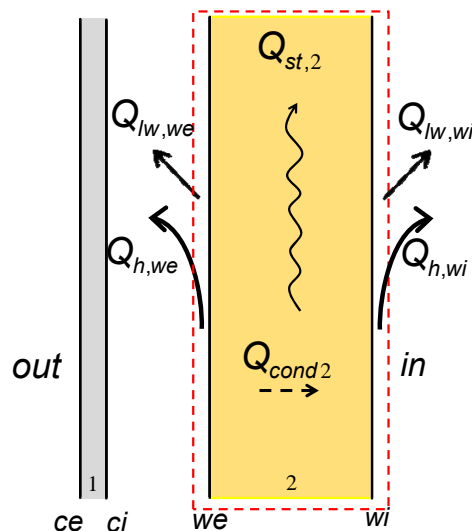


Figure 2.03: Heat balance for the inner wall

If the interior surface temperatures are known, the long-wave radiation ($Q_{lw,wi}$) can be calculated with the net-radiation method described in the Section 2.2.1.

Alternately, the heat transfer to the interior (Q_i) can be described by combine surface film coefficients h_{int} ($\text{Wm}^{-2}\text{K}^{-1}$) and h_r ($\text{Wm}^{-2}\text{K}^{-1}$).

As for the external surface film coefficient, the value of the surface film coefficient h_i is also standardized. In Italy, it mainly depends for the direction of flow. In Table 2.02 main internal surface film coefficient h_i are summarized.

Table 2.02: conventional surface film coefficient h_{int}

h_{int}	Direction flow
$5.0 \text{ W m}^{-2} \text{ K}^{-1}$	Upwards
$2.5 \text{ W m}^{-2} \text{ K}^{-1}$	horizontal
$0.7 \text{ W m}^{-2} \text{ K}^{-1}$	Downwards

The value of the surface film coefficient h_r is obtained by:

$$h_r = \varepsilon h_{r0} \quad (W m^{-2} K^{-1}) \quad [2.38]$$

$$h_{r0} = 4\sigma T_m^3 \quad (W m^{-2} K^{-1}) \quad [2.39]$$

where ε is the hemispherical emissivity of the surface (-), h_{r0} is the radiative coefficient for a black-body surface ($W m^{-2} K^{-1}$), σ is the Stefan-Boltzmann constant ($5.67 \times 10^{-8} W m^{-2} K^{-4}$) and T_m is the average temperature between the surface and its surroundings absolute temperature (K).

The surface film coefficient h_{int} of Equation 2.37 is calculated for a surface emissivity ε of 0.9 and with h_{r0} equal to $5.7 W m^{-2} K^{-1}$ ($T_m = 293 K$) [EN ISO 6946, 2007]

In Figure 2.03 Q_{cond2} is the conductive heat transfer in the internal wall of the façade. The thermal conductivity of the layer material is assumed to be constant. The thermal capacitance of layer is supposed to be non negligible. In this case the conductive heat transfer between external surface of the wall (w_e) and internal surface (w_i) may then be estimated by the Fourier law of conduction:

$$Q_{cond2}(x) = -\lambda_2 \cdot \frac{\partial T_2(x,t)}{\partial x} \quad (W m^{-2}) \quad [2.40]$$

where λ_2 and T_2 are the thermal conductivity and the temperature of the skin façade material respectively (see Figure 2.03).

The heat storage in the internal wall of the façade ($Q_{st,2}$) is obtained by:

$$Q_{st2} = \rho_2 \cdot c_{p2} \cdot B \cdot \frac{\partial T_2(x,t)}{\partial t} \quad (W m^{-2}) \quad [2.41]$$

where ρ_2 ($kg m^{-3}$) is the density of the internal layer, c_{p2} ($J kg^{-1} K^{-1}$) its specific heat at pressure constant and B is the length of the wall.

Equation 2.40 and 2.41 can be solved with control volume method [Clarke, 2001].

Finally the equation for the heat balance for the surface of the skin façade becomes:

$$Q_{h,we} + Q_{lw,we} + Q_S + Q_{cond}|_{w_e} + Q_{cond}|_{w_i} + Q_{h,wi} + Q_{lw,wi} = Q_{st2}$$

2.3 Convective heat transfer in an air cavity

2.3.1 Definition

Convection is the heat transfer phenomenon caused by fluid flow [see e.g. Bejan, 1993]. In particular, it refers to the heat transfer from a bounding surface to the fluid in motion. In general, the heat transfer rate from the bounding surface to the fluid is described by Newton's law of cooling:

$$Q_s = h_c(T_s - T_{ac}) \quad (\text{Wm}^{-2}) \quad [2.42]$$

where Q_s is the convective body-to-stream heat transfer rate (Wm^{-2}), h_c is the convective heat transfer coefficient ($\text{Wm}^{-2}\text{K}^{-1}$), T_s is the temperature of the exposed boundary surface ($^{\circ}\text{C}$) and T_{ac} is a characteristic fluid temperature ($^{\circ}\text{C}$) (Figure 2.04).

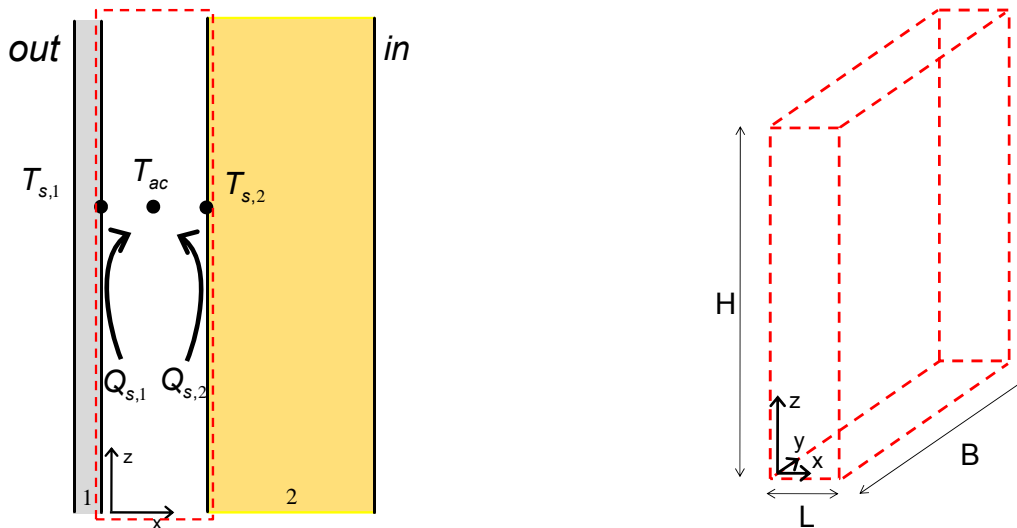


Figure 2.04: Basic definitions for convection analysis in ventilated façades.

In external or unbounded flow configurations the characteristic temperature is the fluid temperature far away into the stream: the free-stream temperature T_{∞} . If the surface surround on the flow (e.g. flow in tubes, channels, etc.), the flow configuration is called internal or bounded. A cross-section averaged mean or bulk temperature, identified as T_m replaces the free-stream temperature:

$$T_m = \frac{1}{U_l A} \int_A u_l T dA \quad (\text{K}) \quad [2.43]$$

where U_l is the average longitudinal velocity (ms^{-1}), A is the cross-sectional area (m^2), u_l is the local longitudinal velocity (m s^{-1}) and T is the local fluid temperature (K).

Since the fluid velocity at the surface is zero, the heat transfer there is governed by conduction. Therefore, we may apply Fourier's law of heat conduction to the infinitesimally small layer:

$$Q_s = -\lambda \left(\frac{\partial T}{\partial x} \right) \quad (\text{Wm}^{-2}) \quad [2.44]$$

Combining Newton's cooling law (Eq. 2.42) and Fourier's law of heat conduction (Eq. 2.44) we obtain a relationship for calculating the heat transfer coefficient:

$$h_c = -\frac{\lambda}{T_s - T_{ac}} \left(\frac{\partial T}{\partial x} \right) \quad (Wm^{-2}K^{-1}) \quad [2.45]$$

The fundamental problem in convective heat transfer consists of determining the heat transfer coefficient h_c .

2.3.2 Convection modes

In Table 2.03 it possible to distinguished three conventional different convection modes. Usually this distinction between the modes is not always sharp defined.

Table 2.03: Classification of the main convection modes

1. external versus internal flow	in between: entrance region problems
2. forced versus natural or free convection	in between: mixed convection
3. laminar versus turbulent flow	in between: transition

Beyond external or unbounded flow and internal or bounded flow a group of intermediate flow problems, which are neither external nor internal, exists. A typical example is the entrance region of the flow in a tube. In this case, distinction is usually made between developing flow and fully developed flow.

A second differentiation can be made according to the origin of the motion. In forced convection, the flow is generated by an external force over the bounding surface. In the case of ventilated façades, this external force may be the pressure difference caused by a fan or wind pressure. In free or natural convection, the fluid motion occurs without external mechanism. Sometimes both mechanisms are present. In mixed-convection regimes (Table 2.03), both forced and natural convection occur simultaneously.

The distinction between laminar and turbulent flows refers to the different types of fluid motion. Laminar flow is smooth and can be identified by non-intersecting streamlines in which the fluid particle velocity equals the flow velocity. Turbulent flows are characterised by eddies of different sizes and intersecting streamlines. The flow properties in turbulent flows are not constant with time and place but change irregularly. Turbulent motion is extremely complicated and difficult to explain. When the flow changes from a laminar to a turbulent regime, the flow is said to be in a transition regime. In some configurations, both laminar and turbulent flow regimes coexist in the same flow field, further complicating the problem.

2.3.3 Dimensionless numbers

There are many dimensionless parameters literature in about convection which are used to characterise its manifestations. In this section the dimensionless numbers which are necessary to describe convection in ventilated façades are described. For more details information of the physical nature of the different dimensionless numbers the reader is referred to the specialised literature, such as Bejan [1984].

The Nusselt number

The Nusselt number defines the ratio between the convective heat transfer and pure conduction between fluid and solid. From the Nusselt number, the heat transfer coefficient h_c can be obtained.

$$Nu_l = \frac{Q_s}{\Delta T} \frac{l}{\lambda} = \frac{h_c l}{\lambda} \quad (-) \quad [2.46]$$

where Q_s is the wall heat flux (Wm^{-2}), ΔT is the temperature difference between the wall and the fluid (K), h_c is the convective heat transfer coefficient ($Wm^{-2}K^{-1}$), λ is the fluid conductivity ($Wm^{-1}K^{-1}$) and l is a characteristic length (m). For external flows, the characteristic length l in the local Nusselt number is usually defined as the position along the wall x or the wall height H . For internal flows, the cavity thickness L , the height H or the hydraulic diameter D_h are chosen. The hydraulic diameter is defined as:

$$D_h = \frac{4A}{P} \quad (m) \quad [2.47]$$

where A is the cross-sectional area (m^2) and P is the wetted perimeter (m). The local Nusselt number in cavities is often a function of the position along the height of the cavity and may vary locally due to a complex inlet geometry [Dyer, 1978] or the presence of obstacles [Hung and Shiau, 1988; Said and Krane, 1990; and Tanda, 1997] and shading devices.

The Reynolds number

The Reynolds number is defined as:

$$Re_l = \frac{U_l l}{\nu} \quad (-) \quad [2.48]$$

where U_l is the average velocity of the fluid (ms^{-1}), l is a characteristic length (m) and ν is the kinematic viscosity (m^2s^{-1}). The Reynolds number is a measure for the ratio between the momentum transfer by eddy diffusion and the momentum by molecular transport.

The Prandtl number

The Prandtl number is defined as the ratio between the kinematic viscosity ν (m^2s^{-1}) and the thermal diffusivity α (m^2s^{-1}). The Prandtl number compares the momentum diffusivity with the thermal diffusivity and connects the temperature to the velocity boundary layer.

$$Pr = \frac{\nu}{\alpha} \quad (-) \quad [2.49]$$

The Prandtl number of air in building engineering applications is often assumed constant: $Pr_{air} = 0.72$ ($-50 < \theta < 30^\circ C$, [Bejan 1993, Yunus A.Çengel 1997]).

The Grashof number

For free convection, the Grashof number replaces the Reynolds number. It is defined as:

$$Gr_l = \frac{\beta g l^3 \Delta T}{\nu^2} \quad (-) \quad [2.50]$$

where β is the coefficient of volumetric thermal expansion (K^{-1}), g is the gravitational acceleration (ms^{-2}), l is a characteristic length (m), ΔT is the temperature difference between the surface and the fluid (K) and ν is the kinematic viscosity (m^2s^{-1}).

The Rayleigh number

The Rayleigh number Ra has no physical meaning, but can be useful to represent a convenient way to note the product of the Grashof and Prandtl number.

$$Ra_l = Pr Gr = \frac{\beta g l^3 \Delta T}{\nu \alpha} \quad (-) \quad [2.51]$$

2.3.4 Ventilated cavities

In ventilated cavities the Nusselt number in natural flow regimes is commonly expressed as a power law function of the Rayleigh number (Table 2.04). If the Nusselt number, averaged over the characteristic length equals 1, the heat transfer occurs by conduction. In the mixed convection regime, the Nusselt number depends on the Reynolds as well as the Rayleigh number (Table 2.04).

Table 2.04: Typical relations for the Nusselt number

Forced convection	Natural convection	Mixed convection
Nu=f(Re,Pr)	Nu=f(Ra)	Nu=f(Re,Ra)

Convection in an enclosed vertical cavity is a typical internal flow problem. As long as the edges remain intact, no external forces are applied to the in following the cavity and only natural or free convection occurs. The convection heat transfer in vertical enclosures is commonly related to the Grashof number evaluated with the cavity width (L) as characteristic length (Gr_L), the Prandtl number and the cavity aspect ratio: $A = H / L$.

The flow in naturally and mechanically ventilated cavities is different. Therefore, the development of expressions describing convective heat transfer will be split into two parts. However, it is possible that natural and forced convection coincide. For instance, in a naturally ventilated skin façade, wind pressure flow, which is by definition forced convection, may interfere with buoyancy driven natural ventilation. In this case, the co-occurrence of both convection regimes is called mixed convection.

Naturally ventilated cavities

First of all, distinction is made between narrow and wide channels. In the former, the boundary layers interfere and the developed velocity profiles of the wall merge into a single profile. In the latter, the boundary layers are considerably smaller than the cavity depth L. This is the case in short or widely spaced channels. The heat transfer in this case is similar in form to that along a single vertical plate but it is measured to be slightly higher [Rohsenow et al., 1985].

According to Bejan [1993] the wide channel limit can be identified by the following inequalities:

$$\frac{L}{H} > Ra_H^{-1/4} \quad \text{or} \quad \frac{L}{H} > Ra_L^{-1} \quad (-) \quad [2.52]$$

Bejan and Lage [1990] showed that the transition between laminar and turbulent flow along vertical plates is indicated by a critical local Grashof number (Gr_x) of order 10^9 .

Mechanically ventilated cavities

Distinction is made between the heat transfer in the entrance region and that in the fully developed regime. Bejan [1993] gives the following approximate relations to calculate the length of the flow (X) and thermal (X_T) entrance region in laminar flow:

$$\frac{X}{D_h} \cong 0.05 \text{Re}_{D_h} \quad (-) \quad [2.53]$$

$$\frac{X_T}{D_h} \cong 0.05 \text{Re}_{D_h} \text{Pr} \quad (-) \quad [2.54]$$

where D_h is the hydraulic diameter of the cross-section (Equation 2.47).

Because the velocity boundary layer thickness (X) depends on the kinematic viscosity (ν) and the thermal boundary layer thickness (X_T) depends on the thermal diffusivity (α), both entrance lengths are linked by the Prandtl number. As the Prandtl number of air is about 0.72, the thermal entrance region is somewhat shorter than the flow entrance length.

For turbulent regimes, the flow and the temperature profile become fully developed after a much shorter distance. Bejan [1993] reports the following formula:

$$\frac{X}{D_h} \cong \frac{X_T}{D_h} \cong 10 \quad (-) \quad [2.55]$$

The transition between the laminar and turbulent regime in internal flow configurations starts from $\text{Re}_{D_h} = 2000$ and turbulence starts from $\text{Re}_{D_h} = 2300$ [Rohsenow et al., 1985; and Bejan, 1993]. It should be noted that laminar flow can survive somewhat longer ($\text{Re}_{D_h} = 10^2$ to 10^4) for extremely smooth surfaces or smooth entrances. If the surface is very rough or obstructions are present in the channel, turbulence may start earlier or local eddies may appear. For flow over a vertical plate, the critical Reynolds number, based on the position along the plate (x), is $\text{Re}_x = 5 \times 10^5$ [Bejan, 1993]. The transition between laminar and turbulent flow is situated between

$$2 \times 10^4 < \text{Re}_x < 10^6 \quad (-) \quad [2.56]$$

Mixed convection

Incropera and De Witt [1981] give the following limits for natural, mixed and forced convection regimes:

$$\text{Gr}_H \gg \text{Re}_H^2 \text{ natural convection} \quad (-) \quad [2.57]$$

$$\text{Gr}_H \approx \text{Re}_H^2 \text{ mixed convection} \quad (-) \quad [2.58]$$

$$\text{Gr}_H \ll \text{Re}_H^2 \text{ forced convection} \quad (-) \quad [2.59]$$

2.3.5 Convective heat transfer coefficient equations

In this section some equations for typical convective heat transfer coefficient are given [Saelens 2002].

Enclosed cavities

For low aspect ratio enclosures with isothermal walls, the Berkovsky-Polevikov [1977] relationship recommended by Catton [1979] may be useful to determine the convective heat transfer.

$$Nu_H = 0.22 \left(\frac{Pr}{0.2 + Pr} Ra_H \right)^{0.28} \left(\frac{1}{A} \right)^{0.09} (-) \quad (2 < A < 10, Pr < 10^5, Ra_H < 10^{13}) \quad [2.60]$$

For high aspect ratios, the experimental results of ElSherbiny et al. [1982] can be applied. The characteristic length in the definitions of the Nusselt and Rayleigh number is the cavity thickness L , the temperature difference is the temperature difference between the hot and the cold pane. The results for air ($Pr \approx 0.72$) may be summarised by the following set of equations:

$$Nu_L = \max(Nu_L^{ct}, Nu_L', Nu_L^t) (-) \quad [2.61]$$

with:

$$Nu_L^{ct} = \left(1 + \left(\frac{0.104 \cdot Ra_L^{0.293}}{1 + (6310/Ra_L)^{1.36}} \right)^3 \right)^{1/3} (-) \quad [2.62]$$

$$Nu_L' = 0.242 \left(\frac{Ra_L \cdot L}{H} \right)^{0.273} (-) \quad [2.63]$$

$$Nu_L^t = 0.0605 \cdot Ra_L^{1/3} (-) \quad [2.64]$$

In this set of relations, the superscript “ct” refers to the conduction and the turbulent transition regime. The superscript “l” describes the laminar boundary-layer regime and “t” refers to the turbulent boundary-layer regime. The relations are valid for perfectly conducting walls.

Naturally ventilated cavities

Wide cavities

When the wide channel limit holds (Equation 2.52), surface heat transfer can be calculated from single wall formulas. Churchill and Chu [1975] developed empirical correlations for the wall averaged heat transfer rate from a vertical wall. The following equations are valid for air:

- For plates with Uniform Wall Temperature (UWT) the expressions yield:

$$Nu_H = 0.680 + 0.515 \cdot Ra_H^{1/4} (-) \text{ laminar regime } (Gr_H < 109) \quad [2.65]$$

$$Nu_H = (0.825 + 0.325 \cdot Ra_H^{1/6})^2 (-) \text{ laminar and turbulent regime } (10^{-1} < Ra_H < 10^{12}) \quad [2.66]$$

- For Uniform Wall heat Flux (UWF), they suggest the follow correlation:

$$Nu_H = (0.825 + 0.328 \cdot Ra_H^{1/6})^2 (-) \text{ laminar and turbulent regime } (10^{-1} < Ra_H < 10^{12}) \quad [2.67]$$

The Nusselt number in Equations 2.65 to 2.67 is based on the temperature difference between the average wall surface temperature and the constant free stream fluid temperature ($\Delta T_{w\infty}$).

Narrow cavities

If the wide channel criterion no longer holds, relations for flow between plates are used. For parallel isothermal (UWT) plates Aung [1972] has shown that in the fully developed (fd) regime (valid for very high cavities), the heat transfer from both plates to the fluid can be estimated by:

$$Nu_{L,fd} = \frac{4T^{*2} + 7T^* + 4}{90(1+T^*)^2} Ra_L \frac{L}{H} \approx \frac{1}{24} Ra_L \frac{L}{H} \quad (-) \quad \left(Ra_L \frac{L}{H} < 10 \right) \quad [2.68]$$

where:

$$T^* = \frac{T_{s,1} - T_\infty}{T_{s,2} - T_\infty} \quad (-) \quad (0 \leq T^* \leq 1) \quad [2.69]$$

The Nusselt number is based on the temperature difference between the wall surface and the inlet temperature ($\Delta T_{w\infty}$). For higher Rayleigh numbers ($Ra_L L/H > 10^3$), a laminar boundary-layer (bl) regime establishes. The observed values of the Nusselt number have the following form:

$$Nu_{L,bl} = c \left(Ra_L \frac{L}{H} \right)^{1/4} \quad (-) \quad \left(Ra_L \frac{L}{H} < 10^3 \right) \quad [2.70]$$

The analysis of Bodoia and Osterle [1962] and Aung et al. [1972] indicate a value of $c \approx 0.68$. In the case of parallel plates with uniform heat flux (UHF), the heat transfer from the plates to the fluid in the fully developed (fd) regime can be described by [Aung, 1972]:

$$Nu_{L,fd} = 0.29 \left(Ra_L^* \frac{L}{H} \right)^{1/2} \quad (-) \quad \left(Ra_L^* \frac{L}{H} < 5 \right) \quad [2.71]$$

The heat flux in the modified Rayleigh number (Ra_L^*) is defined as the average heat flux from both plates:

$$Q_s = \frac{1}{2} (Q_{s,1} + Q_{s,2}) \quad (Wm^{-2}) \quad [2.72]$$

In the laminar boundary-layer (bl) regime, the Nusselt number may be estimated by the following semi-empirical relationship [Sobel et al., 1966]:

$$Nu_{L,bl} = 0.67 \left(Ra_L^* \frac{L}{H} \right)^{1/5} \quad (-) \quad \left(10^2 \leq Ra_L^* \frac{L}{H} \leq 10^4 \right) \quad [2.73]$$

2.3.6 Convection to the surroundings

Exterior surface

The convective heat transfer at the building surface is a combination of natural convection and forced convection due to wind. Several authors, e.g. Ito et al. [1972], Sharples [1984] and Loveday and Taki [1996], give empirical correlations on the meteorological wind speed and the heat transfer coefficient.

Interior surface

The convective heat transfer from the interior surface to the ambient air may vary significantly depending to the convection regime and the presence of a heating or cooling device as described by Kalema [1992] and Beausoleil-Morrison [2000]. If no heating or cooling devices are present, the flow can be classified as natural convection along a vertical flat plate. Hence, the overall interior heat transfer coefficient ($h_{c,i}$) is mainly a function of the wall height and the temperature difference between the wall and the air. Kalema [1992] suggests to use the Alamdari and Hammond [1983] correlations for a vertical wall without heating or cooling device:

$$h_{c,i} = \left[\left(1.50 \left(\frac{\Delta T}{H} \right)^{0.25} \right)^6 + \left(1.23 (\Delta T)^{0.33} \right)^6 \right]^{\frac{1}{6}} \quad (\text{Wm}^{-2}\text{K}^{-1}) \quad [2.74]$$

where ΔT is the temperature difference between the wall and the ambient air (K) and H is the wall height (m). If heating devices are present, the flow enters a mixed convection regime. The following empirical correlations from Khalifa [1989] may be considered to estimate the heat transfer coefficient:

- vertical walls, room heated with a radiator:

$$h_{c,i} = 2.07 \Delta T^{0.23} \quad (\text{Wm}^{-2}\text{K}^{-1}) \quad [2.75]$$

- vertical walls, room heated with a fan heater (valid for surface opposite to the fan):

$$h_{c,i} = 2.92 \Delta T^{0.25} \quad (\text{Wm}^{-2}\text{K}^{-1}) \quad [2.76]$$

For the energy simulations in Chapters from 5 to 8, Equation 2.74, in order to estimate the convective heat transfer coefficient for every internal surface of the ventilated façade model is used.

2.4 Heat transfer correlation methods

The present study describes briefly two simple methods to compare the heat transfer correlations with measurement. A comparison between the measured and calculated data will be presented in Chapter 4. The first method is based on the evaluation of the Nusselt number while the second the determination of the convective coefficient inside the air cavity.

The convective heat flux from the internal wall surface to the fluid can be estimated by solving the heat balance at the surface (Equation 2.80 in Figure 2.05). The method, however, has a limited accuracy:

1. The heat flux through the surface is not measured and should be estimated by Equation 2.78 where R_{we-wi} is the surface-to-surface thermal resistance of the internal wall (as indicated in Figure 2.05). Therefore, only the layer with the highest thermal resistance (the interior wall) is considered. The thermal capacitance of layer is supposed to be negligible.
2. The radiation heat transfer is estimated by relationship 2.79, which assumes isothermal surfaces.
3. The air velocity in the channel is that measured by means of one on sensor. Consequently, the uncertainty on the convective heat flux is quite high.

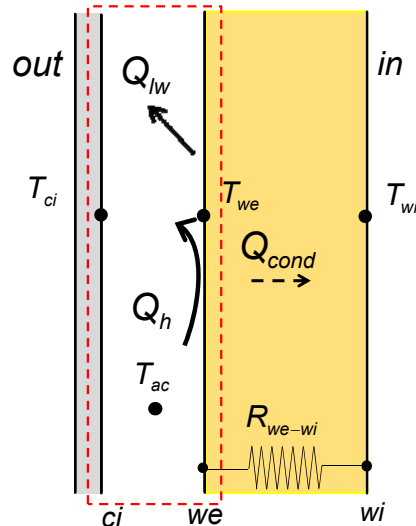


Figure 2.05: Experimental determination of the heat transfer coefficient

$$Q_h = Q_{cond} + Q_{lw} \quad (Wm^{-2}) \quad [2.77]$$

$$Q_{cond} = \frac{(T_{we} - T_{wi})}{R_{we-wi}} \quad (Wm^{-2}) \quad [2.78]$$

$$Q_{lw} = \frac{\sigma(T_{we}^4 - T_{ci}^4)}{\frac{1}{\epsilon_{we}} + \frac{1}{\epsilon_{ci}} - 1} \quad (Wm^{-2}) \quad [2.79]$$

$$Nu_H = \frac{Q_h}{(T_{we} - T_{ac}) \lambda_{air}} \frac{H}{\lambda_{air}} = \frac{h_c H}{\lambda_{air}} \quad (-) \quad [2.80]$$

An alternative approach to estimate the convective heat flux is used in Inoue et al. [1985]. Assuming the heat transfer coefficient to be equal at both sides of the cavity, the overall heat transfer coefficient can be estimated from the enthalpy change of the air flowing through the cavity (Figure 2.06).

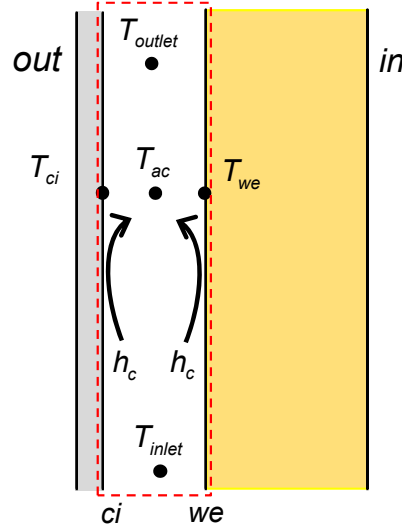


Figure 2.06: Experimental determination of the heat transfer coefficient

$$h_c = \frac{\rho_{air} c_{p,air} m_{air} (T_{inlet} - T_{outlet})}{A(T_{s,avg} - T_{ac})} \quad (Wm^{-2}K^{-1}) \quad [2.81]$$

$$T_{s,avg} = \frac{(T_{ci} - T_{we})}{2} \quad (^\circ C) \quad [2.82]$$

In Equation 2.81, ρ_{air} is the air density (kgm^{-3}), $c_{p,air}$ is the air specific heat capacity ($Jkg^{-1}K^{-1}$), m_{air} is the air flow rate (m^3s^{-1}), T_{inlet} and T_{outlet} are the inlet and outlet temperature respectively ($^\circ C$), A is the total area in contact with the fluid (m^2), $T_{s,avg}$ is the average surface temperature ($^\circ C$) and T_{ac} is the average fluid temperature ($^\circ C$).

The advantage of this method is that there is no need to estimate the exterior heat flux or the radiation heat flux but as the previous method it has a limited accuracy:

1. The convective heat flux to the fluid is small and the temperature difference between the inlet and the outlet ($T_{inlet} - T_{outlet}$) is small as well. As a consequence the accuracy is limited.
2. The considered air flow rate in the channel depending of the measured air velocity by mean only one sensor. Consequently, the uncertainty on the measured air velocity (considered uniform in the channel) is very high.
3. Two interior surfaces in the channel have very different surface characteristics (e. g. different roughness).

The next section shows a method for evaluating a parameter for the heat transfer in a wall.

2.5 Evaluation of steady-state thermal transmittance (U-value)

Winter thermal performance can be represented by means many parameters. By considering the steady state regime the U-value (steady-state thermal transmittance) is the most represent.

Traditional energy performance indicators such as the U-value are only to be seen as envelope level performance indicators, useful to determine, e.g., the rate of heat transfer in winter period in steady state regime.

However it is not suited to estimate the overall building energy performance. Under normal conditions, the U-value only depends on the material properties and thickness of the envelope layers. In fact, the U-value of ventilated façade depends on the system properties as well: airflow rate, openness of ventilation grills, et cetera.

2.5.1 U-value: classical steady state method

Normally, in order to evaluate the U-value in situ measurement it used to be the “average method” [ISO 9869 1994]. This method provides quantitative and qualitative information about the measured data and allows to estimate, for experiments long enough, some of the parameters of a building component like the U-value of a wall. The formula below gives the estimate of the U-value ($\text{Wm}^{-2}\text{K}^{-1}$) of the average method:

$$U = \frac{\sum_{j=1}^N Q_j}{\sum_{j=1}^N (T_{i,j} - T_{a,j})} \quad [2.83]$$

where j stands for the index of each observation, Q is the heat flux density through the building component, T_i is the indoor temperature and T_a is the ambient temperature. When the estimate is computed after each measurement, a convergence to an asymptotical value is observed.

If considering the exterior and interior surface temperature the Equation 2.83 becomes:

$$C = \frac{\sum_{j=1}^N Q_j}{\sum_{j=1}^N (T_{wi,j} - T_{ce,j})} \quad [2.84]$$

where Q is the heat flux density through the building component, T_{wi} is the measured internal surface temperature of the inner wall and T_{ce} is the measured external surface temperature of the skin façade. In this case the rate between heat flux Q and temperature difference ($T_{wi}-T_{ce}$) represents the thermal conductance C.

2.5.2 U-value: evaluation with European standard EN ISO 6946

The International Standard EN ISO 6946 [2007] provides the method of calculation of the thermal resistance and thermal transmittance of building components and building elements.

The calculation method is based on the appropriate design thermal conductivities or design thermal resistances of the materials and products for the application concerned. The method applies to components and elements consisting of thermally homogeneous layers (which can include air layers). In particular the Standard gives a calculation method to evaluate the thermal resistance both for unventilated and ventilated air layer. The mode of ventilation is difficult to determine because other methods in literature are indicate. For example the Italian Standard UNI

11018 [2003] indicates another ventilation classification (slightly or well ventilated) depending by the rate between the air cavity thickness and the height of façade.

However, for the unventilated air layer usually can be used specific thermal resistance [EN ISO 6946, 2007] as function of the thickness of the air layer and the heat direction. Instead for the (slightly) ventilated air layer the thermal resistance value depends from the ventilation grills area. If the ventilation grills are $> 500 \text{ mm}^2$ but $< 1500 \text{ mm}^2$ per metre of length (in the horizontal direction) the thermal resistance R_T is given from:

$$R_T = \frac{1500 - A_V}{1000} R_{T,u} + \frac{A_V - 5000}{1000} R_{T,v} \quad [2.85]$$

where A_V is the area (mm^2) of ventilation grills, $R_{T,u}$ is the total thermal resistance (m^2KW^{-1}) with an unventilated air layer and $R_{T,v}$ is the total thermal resistance (m^2KW^{-1}) with a well-ventilated air layer.

The thermal resistance of a well-ventilated air layer is given when the ventilation grills are $>1500 \text{ mm}^2$ per metre of length (in the horizontal direction). Such as reported in the Standard, the total thermal resistance of a building component containing a well-ventilated air layer shall be obtained by disregarding the thermal resistance of the air layer and all other layers between the air layer and external environment, and including an external surface resistance corresponding to still air. Alternatively, the corresponding value of internal surface resistance ($R_{si}=0.13 \text{ m}^2\text{K W}^{-1}$ if the heat direction is horizontal) may be used.

A comparison between the measured and calculated data will be presented in Chapter 4.

2.6 Conclusion

In this Chapter an overview of basic theoretical analysis for naturally ventilated façades is given.

In the section 2.1.2 if is to assume that the average values of the convection coefficients and the cross-section average cavity air velocity are known, an expression for the cavity air temperature (at specific height) was explained.

Further a limited evaluation of two correlation methods for the convective heat transfer coefficient and for the steady-state thermal transmittance respectively was presented.

CHAPTER 3

RAINSCREEN VENTILATED SKIN FAÇADE - ENERGY SIMULATION MODEL

3.1 Introduction

As stated before, the objective of the present work is to investigate the thermal behaviour of such complex system, as ventilated skin façades by means of building performance evaluation tools. One of the techniques which may be employed to achieve this is modelling and simulation.

Modelling is the art of developing a model which faithfully represents a complex system. Simulation is the process of using the model to analyze and predict the behaviour of the real system. Simulation may be based on a physical model (to scale or real size), some (e.g. electric) analogue, or a numerical model. The present work uses the current most wish spread technique: digital computer modelling and simulation.

Modelling and simulation, like experimentation, have become indispensable engineering techniques in the fields of design (e.g. of buildings, plant configurations, and on the component level) and operation (system control, understanding, and interaction).

It should be noted though that simulation and experimentation are complementary: experimentation to discover new unknown phenomena or for validation purposes, and simulation to understand interactions of the known components of a system.

A model of the test building of the rainscreen ventilated skin façade of this work was created by using the simulation program ESP-r (Environmental Systems Performance, Research version), which is a transient simulation program based on the finite volume technique [Clarke 2001]. By using ESP-r, it is possible to model all the energy fluxes and the fluid flows within combined building and plant systems subject to dynamically varying boundary conditions.

The decision to work with the ESP-r has many reasons. For example ESP-r is clearly a research orientated environment, with the objective to simulate the real world as rigorously as possible to a level which is dictated by international research efforts/results on this matter. Other aspects are connected to sets out to take fully into account all building & plant energy flows and their interconnections and also because ESP-r's source code is thoroughly available and well accessible. Furthermore the system has been - and still is - the subject of various international validation programmes.

First, a brief history of building energy simulation and the used building energy simulation program are presented. The Section 3.3 describes ESP-r's thermal simulation methodology, and then the chapter will continues with the modelling setup of rainscreen ventilated skin façades with ESP-r.

3.2 History about building simulation tools (Saelens, 2002)

Until the mid 1960's, easy hand-calculation methods were used to predict the energy consumption in buildings. Heating was frequently estimated by the degree day method [ASHRAE,1997], while, especially in North America, a common approach to estimate the cooling needs was the equivalent full load hour method [Ayres and Stamper, 1995]. Although useful in a time where computational resources were limited and expensive, the methods simplified and neglected some important

factors such as solar and internal gains, ventilation and infiltration, transient effects, occupant behaviour, equipment efficiency, et cetera. However, some of these drawbacks were accounted for by choosing appropriate limit temperatures. The first simulation methods appeared in the mid 1960's. A typical modelling strategy was to divide the simulation in three sequential steps. Firstly, the building load was calculated using approximate techniques, then the loads were used as an input for the air-conditioning equipment (cooling and heating coils, fans, etc.) and finally, the outcome of the second stage was used to design the energy conversion machines (chillers, furnaces, cooling towers, etc.). Because of this sequential nature, the interaction between the building and the system was ignored. The first simplified building load models used time averaging techniques to estimate transient effects and internal gains. The response factor method of Stephanson and Mitalas [1967] significantly improved the capability of the models to predict transient effects. This room-air weighting method disconnected solar radiation from heat transfer through the envelope by using algebraic summation and weighting factors. In the 1970's, heat balance methods [e.g. Kusuda, 1976] replaced the room-air weighting factors and were able to include most heat exchange phenomena in a physical correct manner. Although z-transfer functions were still common to calculate wall heat transfer [Stephanson and Mitalas, 1971; and Mitalas, 1978], the heat balance method allowed new, more accurate numerical techniques, such as finite difference methods [Clarke, 2001], to be implemented. Simultaneously with the research efforts on improving the thermal models, extended research on airflow modelling was conducted. The first models date from the early 1970's. Multi-zone network methods were used to estimate infiltration and inter-zone airflow. A review is available from Feustel and Dieris [1992]. In addition to inter-zone modelling, computational fluid dynamics (CFD) gained popularity. They were used to calculate in-ambient airflow [Nielsen, 1974]. In the mid and late 1980's, thermal and airflow simulation models were combined. Maver and Clarke [1984] integrated multi-zone network models into the thermal model ESP.

More recently, CFD has been implemented in building simulation tools to more accurately predict in-ambient airflow [Negrão, 1995; and Loomans, 1998]. Increasing efforts are made to use CFD to improve the calculation of convective heat transfer at internal surfaces [Loomans 1998; and Beausoleil-Morrison 2000].

A more elaborate evolution of building simulation tools is given by Clarke and Maver [1991], Beausoleil-Morrison [2000], Al-Homoud [2001] and Clarke [2001].

3.3 Thermal model

This section presents an overview of the ESP-r thermal simulation methodology. More detailed information is given by Clarke [2001]. A brief description of the control-volume heat-balance approach of the method reported thoroughly by Ian Beausoleil-Morrison [2000] is described.

3.3.1 *Finite-difference control-volume heat-balance approach*

ESP-r is based on the numerical discretization and simultaneous solution of heat-balance methods. In particular, ESP-r simulates the thermal state of buildings by means of a finite-difference formulation based on a control-volume heat-balance to represent all relevant energy flows.

The building can be discretized by representing air volumes (such as rooms), opaque and transparent fabric components (walls, windows, roofs, floors), solid-fluid interfaces (such as the internal and external surfaces of walls and windows), and plant components (such as boilers and heat exchangers) with finite-difference *nodes*. Numerous nodes are fixed through each fabric component to represent these multi-layered constructions. Figure 3.01 presents a few nodes as an example to represent any building component.

A heat balance considering the relevant energy flow paths is written for each node. These balances are given in algebraic and discrete form, and thus approximate the partial differential

equations which govern the heat transfer. As each heat balance expresses the thermal interaction between a node and its neighbours, the resulting equation set links all inter-node heat flows over time and space. A simultaneous solution is solved on the equation set to predict—for a given point in time—the thermal state of each node and the heat flows between nodes.

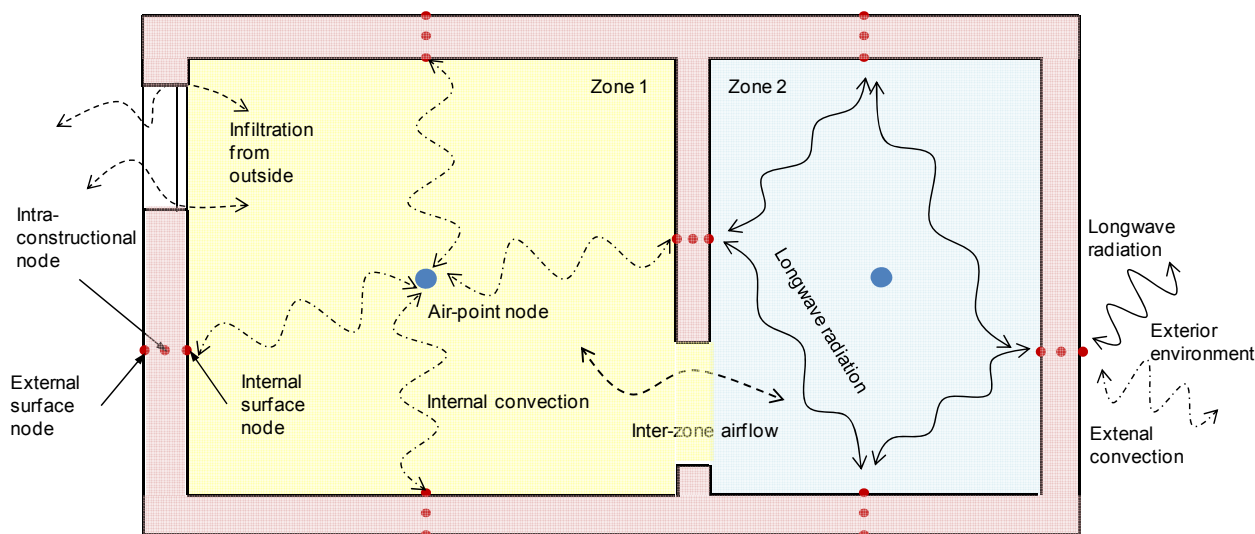


Figure 3.01: Finite-difference discretization and inter-nodal heat flows

3.3.2 Heat balance for intra-constructional nodes

Heat exchange within opaque fabric components is so much complex, usually involving numerous modes of heat transfer: solid conduction, gaseous conduction, convection within porous materials, and radiation. In ESP-r usually each homogeneous layer is represented by three nodes: one at each layer boundary and one within the layer. Figure 3.02 shows this nodal distribution for a typical wall section.

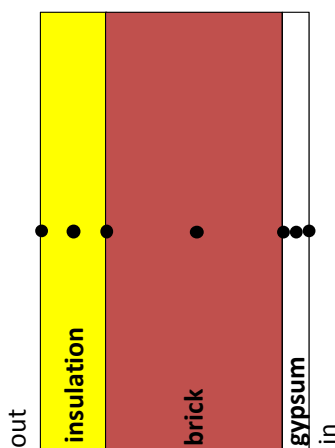


Figure 3.02: Nodal discretization for a typical opaque fabric component

Figure 3.03 represents intra-constructional nodes located within a homogeneous material layer. The node labelled with “*l*” represents that one under consideration while those “*l+1*” and “*l-1*” represent the immediate neighbours in the direction of heat flow (*x*-direction).

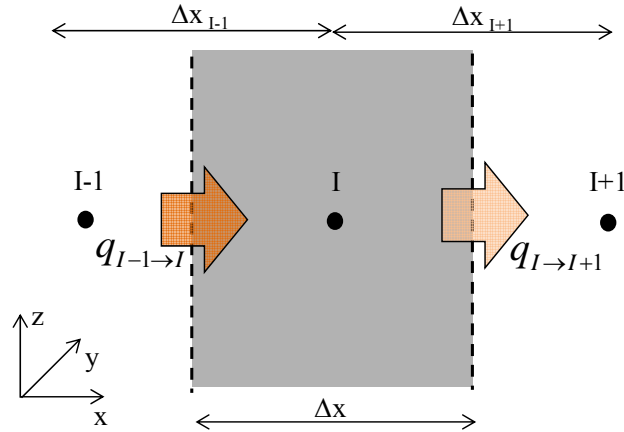


Figure 3.03: Heat balance on node within homogeneous layer of multi-layer construction

The heat balance of control volume (CV) associated with node *I*'s may be described with three terms as depicted in Figure 3.04.

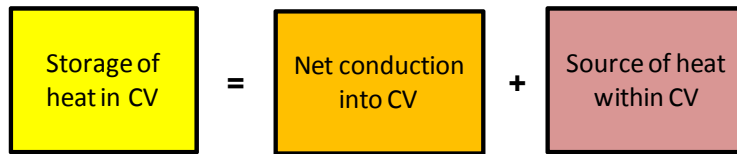


Figure 3.04: Heat balance for node's control volume

This relation simply means that the material will store or release energy in proportion to the amount of heat transferred in by conduction and in proportion to the amount of heat generation. The rate of change of the control volume's temperature characterizes the storage term. The source term represents interaction with a plant component. The balance equation sketched Figure 3.04 is expressed in mathematical terms by,

$$\rho c_p \frac{\partial T}{\partial t} = -\frac{\partial Q_x}{\partial x} + q_{plant}''' \tag{3.01}$$

where c_p is the specific heat ($J\ kg^{-1}\ K^{-1}$) and ρ the density ($kg\ m^{-3}$) of the material; T is temperature ($^{\circ}C$ or K); t is time (s); q''_x is the conductive heat flux in the x -direction ($W\ m^{-2}$); and q'''_{plant} is the heat generated from the plant component ($W\ m^{-3}$).

Equation 3.01 can be approximated by integrating over the control volume,

$$\int_{\Delta V} \rho c_p \frac{\partial T}{\partial t} dV = -\int_{\Delta V} \frac{\partial Q_x}{\partial x} dV + \int_{\Delta V} q_{plant}''' dV \tag{3.02}$$

and by representing the first derivative of temperature in time term with a backwards difference scheme over the finite time-step Δt ,

$$(\rho c_p \Delta x \Delta y \Delta z)_I \frac{T_I^{t+\Delta t} - T_I^t}{\Delta t} = q_{I-1 \rightarrow I} - q_{I \rightarrow I+1} + q_{plant} \tag{3.03}$$

T_I^t is the temperature of node *I* at the beginning of the time-step. This is a known quantity, a result of the simulation of the previous time-step. $T_I^{t+\Delta t}$ is the temperature of node *I* at the end of the

time-step, a quantity yet to be solved. Time t is known as the current time and time $t+\Delta t$ is known as the future time.

$q_{l-1 \rightarrow l}$ and $q_{l \rightarrow l+1}$ are the conductive heat transfers across the surfaces of the control volume (W), as shown in Figure 3.03. These terms may be approximated in discrete form using the nodal temperatures. The explicit form of the approximations results when current time temperatures are used,

$$q_{l-1 \rightarrow l} \approx \frac{\lambda_{l-1} \Delta y \Delta z}{\Delta x_{l-1}} (T_{l-1}^t - T_l^t) \quad [3.04]$$

$$q_{l \rightarrow l+1} \approx \frac{\lambda_{l+1} \Delta y \Delta z}{\Delta x_{l+1}} (T_l^t - T_{l+1}^t) \quad [3.05]$$

where λ_{l-1} is the thermal conductivity ($W m^{-1} K^{-1}$) of the material between nodes l and $l-1$, and λ_{l+1} is the thermal conductivity of the material between nodes l and $l+1$. Substituting Equations 3.04 and 3.05 into Equation 3.03 and expressing the plant injection at the current time gives to the fully explicit form of the discretized approximation of the heat balance,

$$\frac{(\rho c_p \Delta x \Delta y \Delta z)_l}{\Delta t} (T_l^{t+\Delta t} - T_l^t) = \frac{\lambda_{l-1} \Delta y \Delta z}{\Delta x_{l-1}} (T_{l-1}^t - T_l^t) - \frac{\lambda_{l+1} \Delta y \Delta z}{\Delta x_{l+1}} (T_l^t - T_{l+1}^t) + q_{plant}^t \quad [3.06]$$

If the conductive heat flows and the plant term are approximated using future-rather than present-values, the fully implicit form of the heat balance results,

$$\frac{(\rho c_p \Delta x \Delta y \Delta z)_l}{\Delta t} (T_l^{t+\Delta t} - T_l^t) = \frac{\lambda_{l-1} \Delta y \Delta z}{\Delta x_{l-1}} (T_{l-1}^{t+\Delta t} - T_l^{t+\Delta t}) - \frac{\lambda_{l+1} \Delta y \Delta z}{\Delta x_{l+1}} (T_l^{t+\Delta t} - T_{l+1}^{t+\Delta t}) + q_{plant}^{t+\Delta t} \quad [3.07]$$

ESP-r approximates the heat balance with an equally weighted average of the explicit and implicit relations. This is known as the Crank-Nicolson difference formulation, and is preferred over the fully explicit and fully implicit schemes for its numerical stability. Thus, adding equations 3.06 and 3.07, dividing through by volume ($\Delta x \Delta y \Delta z$), and grouping the future time terms on the left and the current time terms on the right gives,

$$\begin{aligned} & \left[\frac{2(\rho c_p)_l}{\Delta t} + \frac{\lambda_{l-1}}{\Delta x \Delta x_{l-1}} + \frac{\lambda_{l+1}}{\Delta x \Delta x_{l+1}} \right] T_l^{t+\Delta t} - \left[\frac{\lambda_{l-1}}{\Delta x \Delta x_{l-1}} \right] T_{l-1}^{t+\Delta t} - \left[\frac{\lambda_{l+1}}{\Delta x \Delta x_{l+1}} \right] T_{l+1}^{t+\Delta t} - \frac{q_{plant}^{t+\Delta t}}{\Delta x \Delta y \Delta z} \\ & = \left[\frac{2(\rho c_p)_l}{\Delta t} - \frac{\lambda_{l-1}}{\Delta x \Delta x_{l-1}} - \frac{\lambda_{l+1}}{\Delta x \Delta x_{l+1}} \right] T_l^t - \left[\frac{\lambda_{l-1}}{\Delta x \Delta x_{l-1}} \right] T_{l-1}^t - \left[\frac{\lambda_{l+1}}{\Delta x \Delta x_{l+1}} \right] T_{l+1}^t - \frac{q_{plant}^t}{\Delta x \Delta y \Delta z} \end{aligned} \quad [3.08]$$

This is the basic equation ESP-r employs to characterize the heat balance for nodes located within homogeneous material layers of opaque multi-layered constructions. It considers heat storage, conduction to adjacent nodes, and plant interaction. All unknown solution variables (nodal temperatures and plant injections) are collected on the left, and known quantities are on the right.

3.3.3 Heat balance for internal surface nodes

In this section the focus is on nodes located at internal surfaces. Figure 3.05 shows a node (l) located on the internal surface of a construction. As before, the left face of the control volume (in

grey) is located between nodes I and $I-1$. The right face, however, is located at the interface between the wall and the ambient air.

The neighbouring node to the right ($I+1$) represents the room's air-point. The heat balance for node I 's control volume has a similar structure to that for the intra-constructional node, but includes two additional modes of heat transfer,

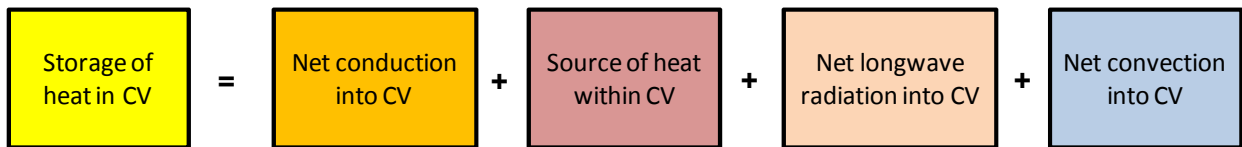
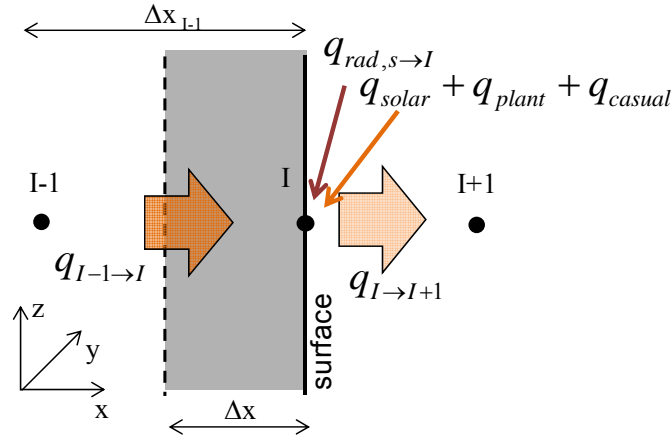


Figure 3.05: Heat balance on node at internal-surface

Since conduction into the control volume occurs only at the boundary with the next-to-surface node ($I-1$), the discretized explicit form of the conduction term is,

$$\text{Net conduction into CV} = \frac{\lambda_{I-1} \Delta y \Delta z}{\Delta x_{I-1}} (T_{I-1}^t - T_I^t) \quad [3.09]$$

In addition to plant injection, the source term includes solar gains and longwave radiation from sources of heat within the room. The explicit form is given by,

$$\text{Source of heat within CV} = q_{solar,I}^t + q_{cas-rad,I}^t + q_{plant,I}^t \quad [3.10]$$

where $q_{solar,I}^t$ is the solar radiation absorbed at node I at the current time, $q_{cas-rad,I}^t$ represents the radiant energy absorbed from casual sources (such as occupants, lights, etc.), $q_{plant,I}^t$ represents a radiant plant input to node I .

The longwave radiation term represents the net heat exchange with surrounding surfaces that are in longwave contact (i.e. other internal surfaces of the room). The discretized explicit form is given by,

Net longwave radiation into CV	$= \sum_{s=1}^N h_{r,s \rightarrow l}^t \Delta y \Delta z (T_s^t - T_l^t)$	[3.11]
--------------------------------	--	--------

N is the number of surrounding surfaces in longwave contact, $h_{r,s \rightarrow l}^t$ is a linearized radiation heat transfer coefficient ($\text{W m}^{-2} \text{K}^{-1}$). These coefficients are recalculated at each time-step on a surface-by-surface basis. A grey-body exchange that considers diffuse surface reflections and employs geometric view factors is used to calculate the radiation coefficients. These geometric view factors are either determined from geometric relations or with ray-tracing procedures. The convection term represents heat exchange between the ambient air and the solid surface. The ambient air is treated as uniform. Consequently, the temperature at node $l+1$ represents conditions throughout the room.

The convection term is given in discretized explicit form by,

Net convection into CV	$= h_{c,l}^t \Delta y \Delta z (T_{l+1}^t - T_l^t)$	[3.12]
------------------------	---	--------

where $h_{c,l}^t$ is the convective heat transfer coefficient ($\text{W m}^{-2} \text{K}^{-1}$) between the surface at node l and the ambient air-point, evaluated at current time. The convective coefficients are recalculated at each time-step on a surface-by-surface. This contrasts with the treatment of some other simulation programs which employ time-invariant convection coefficients. By default, the Alamdari and Hammond [1983] correlations for buoyancy-driven flow are used (see section 2.2.6). These equations represent the convection coefficient as a function of the surface height and the surface-air temperature difference. Separate correlations are used for: vertical surfaces; stably-stratified horizontal surfaces and buoyant flow from horizontal surfaces.

Therefore, although ESP-r recalculates convection coefficients as the simulation evolves, it cannot adapt the calculation approach in response to changes in air flow regimes.

Substituting equations 3.09 through 3.12 into Equation of the Figure 3.05 and representing the storage term with a backwards difference scheme, to the explicit form of the heat balance is obtained. The implicit form of the heat balance results when convective and radiation coefficients, and the conduction, convection, radiation, and source the terms are evaluated with future values. Concatenating these, dividing through by volume, and grouping future time terms on the left and current time terms on the right results in the generalized form of the internal-surface heat balance,

$$\begin{aligned}
 & \left[\frac{2(\rho c_p)_I}{\Delta t} + \frac{\lambda_{I-1}}{\Delta x \Delta x_{I-1}} + \frac{h_{c,I}^{t+\Delta t}}{\Delta x} + \frac{\sum_{s=1}^N h_{r,s \rightarrow I}^{t+\Delta t}}{\Delta x} \right] T_I^{t+\Delta t} - \left[\frac{\lambda_{I-1}}{\Delta x \Delta x_{I-1}} \right] T_{I-1}^{t+\Delta t} \\
 & - \left[\frac{h_{c,I}^{t+\Delta t}}{\Delta x} \right] T_{I+1}^{t+\Delta t} - \frac{\sum_{s=1}^N h_{r,s \rightarrow I}^{t+\Delta t} T_s^{t+\Delta t}}{\Delta x} - \frac{q_{solar,I}^{t+\Delta t}}{\Delta x \Delta y \Delta z} - \frac{q_{cas-rad,I}^{t+\Delta t}}{\Delta x \Delta y \Delta z} - \frac{q_{plant,I}^{t+\Delta t}}{\Delta x \Delta y \Delta z} = \\
 & \left[\frac{2(\rho c_p)_I}{\Delta t} - \frac{\lambda_{I-1}}{\Delta x \Delta x_{I-1}} - \frac{h_{c,I}^t}{\Delta x} + \frac{\sum_{s=1}^N h_{r,s \rightarrow I}^t}{\Delta x} \right] T_I^t - \left[\frac{\lambda_{I-1}}{\Delta x \Delta x_{I-1}} \right] T_{I-1}^t \\
 & - \left[\frac{h_{c,I}^t}{\Delta x} \right] T_{I+1}^t - \frac{\sum_{s=1}^N h_{r,s \rightarrow I}^t T_s^t}{\Delta x} - \frac{q_{solar,I}^t}{\Delta x \Delta y \Delta z} - \frac{q_{cas-rad,I}^t}{\Delta x \Delta y \Delta z} - \frac{q_{plant,I}^t}{\Delta x \Delta y \Delta z}
 \end{aligned} \tag{3.13}$$

This is the basic equation ESP-r employs to characterize the heat balance for internal-surface nodes. This equation considers heat storage, conduction within the innermost layer of the fabric, convection with ambient air, longwave radiation exchange with surrounding surfaces, and absorption of solar radiation, radiant casual gains, and radiant plant injections. Although the coefficients are more complex, this equation has the same form as that for intra-constructural nodes (Equation 3.07).

3.3.4 Heat balance for air-point nodes

The exchange mode for heat transfer between the zone air and internal surfaces is convection. Consequently, convective coefficients also appear in the heat balance for the zone air. Figure 3.06 shows a node representing the air-point of a zone and also the heat balance for the air-point. In this case, node I represents the air-point and the nodes labelled S represent the surface nodes of the bounding constructions.

Node J represents the air-point of another zone while Node O represents the outdoor air. In this case the ambient air is treated as uniform as well and the absorption of radiation in the air is neglected. Consequently, node I represents conditions throughout the control volume.

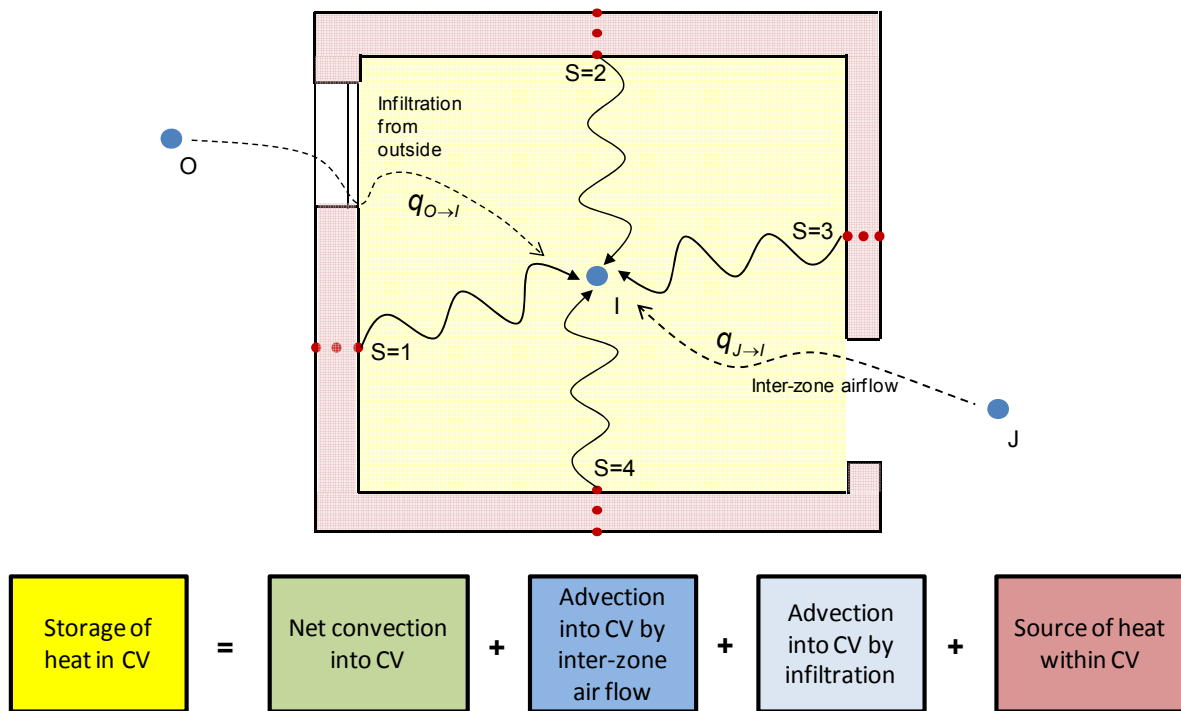


Figure 3.06: Heat balance on air-point node

The convection term represents the total heat transfer from all bounding surfaces (walls, roof, floor, windows) to the ambient air, and is given in discretized explicit form by,

$$\text{Net convection into CV} = \sum_{S=1}^N h_{c,S}^t A_s (T_S^t - T_I^t) \quad [3.14]$$

where N is the number of bounding surfaces. A_s is the area (m^2), and $h_{c,S}^t$ the current time convective heat transfer coefficient, for surface S . The convective coefficients are evaluated in the same manner as for the internal surface nodes.

The advection terms represent the thermal energy carried by air flowing into the control volume from other zones or from the outdoors. These terms are given in discretized explicit form by,

$$\text{Advection into CV by inter-zone air flow} = \sum_{J=1}^M m_{J \rightarrow I}^t c_p (T_J^t - T_I^t) \quad [3.15]$$

$$\text{Advection into CV by infiltration} = m_{0 \rightarrow I}^t c_p (T_0^t - T_I^t) \quad [3.16]$$

M is the number of zones supplying air to the control volume, $m_{J \rightarrow I}^t$ is the air flow from zone J to zone I ($kg s^{-1}$) at the current time and $m_{0 \rightarrow I}^t$ is the infiltration rate ($kg s^{-1}$) from the outdoors for the

current time. T_j^t and T_0^t are the current time temperatures of the air-point in zone J and the outdoor air, respectively.

There are various techniques for establishing $m_{J \rightarrow J}^t$ and $m_{0 \rightarrow J}^t$. The most general approach is to employ a network air flow model to calculate the infiltration and inter-zone air flows in response to prevailing weather conditions and thermal states within the building. This was used to model channels of the rainscreen ventilated walls of this work.

The source term can be given in discretized explicit form by,

$$\begin{array}{|c|} \hline \text{Source of heat} \\ \text{within CV} \\ \hline \end{array} = q_{cas-conv,l}^t + q_{plant,l}^t \quad [3.17]$$

where $q_{cas-conv,l}^t$ is the heat transferred convectively from casual sources (such as occupants, lights, office equipment) at the current time and $q_{plant,l}^t$ represents a convective plant input to node l at the current time.

When the explicit and implicit forms of the heat balance (Figure 3.06) are added, the equation divided by the volume (VOL_{room}), and the future time terms collected on the left and the current time terms on the right, the following relation results,

$$\begin{aligned} & \left[\frac{2(\rho c_p)_l}{\Delta t} + \frac{\sum_{s=1}^N h_{c,s}^{t+\Delta t} A_s}{VOL_{room}} + \frac{\sum_{J=1}^M m_{J \rightarrow J}^{t+\Delta t} c_p}{VOL_{room}} + \frac{m_{0 \rightarrow J}^{t+\Delta t} c_p}{VOL_{room}} \right] T_l^{t+\Delta t} - \left[\frac{\sum_{s=1}^N h_{c,s}^{t+\Delta t} A_s T_s^{t+\Delta t}}{VOL_{room}} \right] \\ & - \left[\frac{\sum_{J=1}^M m_{J \rightarrow J}^{t+\Delta t} c_p T_J^{t+\Delta t}}{VOL_{room}} \right] - \left[\frac{m_{0 \rightarrow J}^{t+\Delta t} c_p T_0^{t+\Delta t}}{VOL_{room}} \right] - \frac{q_{cas-conv,l}^{t+\Delta t}}{VOL_{room}} - \frac{q_{plant,l}^{t+\Delta t}}{VOL_{room}} = \\ & \left[\frac{2(\rho c_p)_l}{\Delta t} + \frac{\sum_{s=1}^N h_{c,s}^t A_s}{VOL_{room}} + \frac{\sum_{J=1}^M m_{J \rightarrow J}^t c_p}{VOL_{room}} + \frac{m_{0 \rightarrow J}^t c_p}{VOL_{room}} \right] T_l^t - \left[\frac{\sum_{s=1}^N h_{c,s}^t A_s T_s^t}{VOL_{room}} \right] \\ & - \left[\frac{\sum_{J=1}^M m_{J \rightarrow J}^t c_p T_J^t}{VOL_{room}} \right] - \left[\frac{m_{0 \rightarrow J}^t c_p T_0^t}{VOL_{room}} \right] - \frac{q_{cas-conv,l}^t}{VOL_{room}} - \frac{q_{plant,l}^t}{VOL_{room}} \end{aligned} \quad [3.18]$$

This is the basic simulation equation ESP-r employs to characterize the heat balance for ambient air-point nodes. It considers heat storage by the ambient air, convection to the bounding constructions, inter-zone and infiltration air flows, convective casual gains, and convective plant injections.

More detailed information about the solution methods and the procedure for solving the above reported equations may be found in [Clarke, 2001].

3.4 Modelling setup of rainscreen ventilated skin façades with ESP-r

More models of the test building were created by using the above mentioned simulation program ESP-r (see Chapters 5 and 6) and were discretized by using a finite number of nodes representing air volumes as stated in the section 3.2.1. Figure 3.0.7 shows a screenshot of the ESP-r model used to modeling the studied test cell.

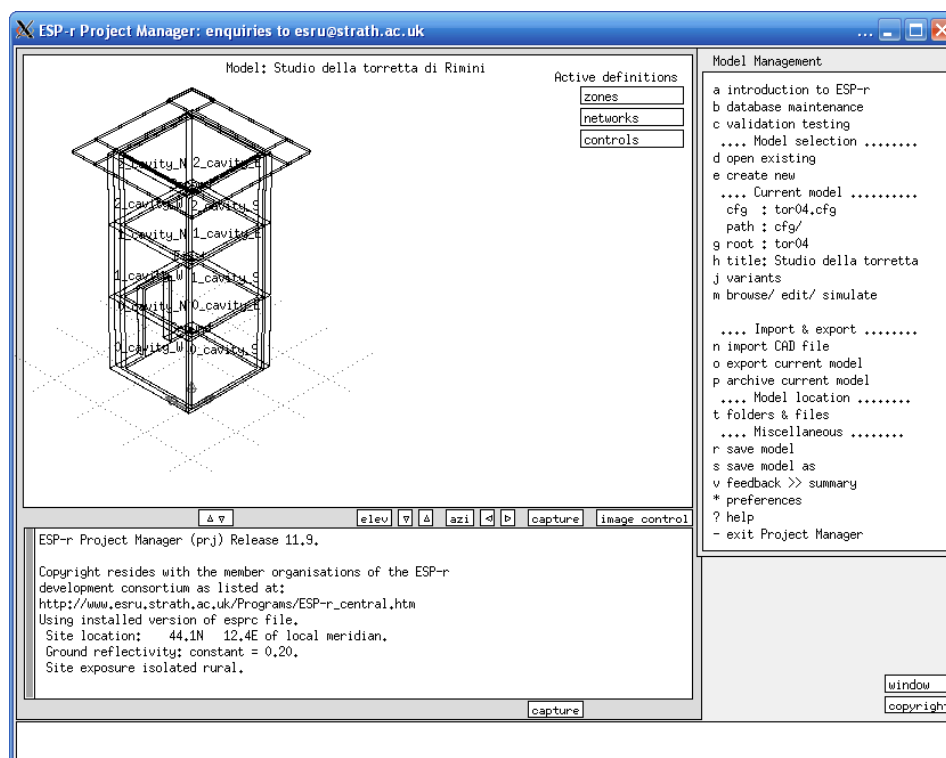


Figure 3.07: Screenshot of the test cell in ESP-r

In this work, rainscreen ventilated skin façades of the test building were studied numerically using specific nodal networks model; airflow networks were integrated with the corresponding thermal network model so that the calculated airflows are based on nodal temperatures from the thermal model, and the resulting predicted airflows are used in the energy balances of the thermal simulation with an iterative procedure of solution. In Figure 3.08 all the nodes used to model the rainscreen ventilated structure are shown.

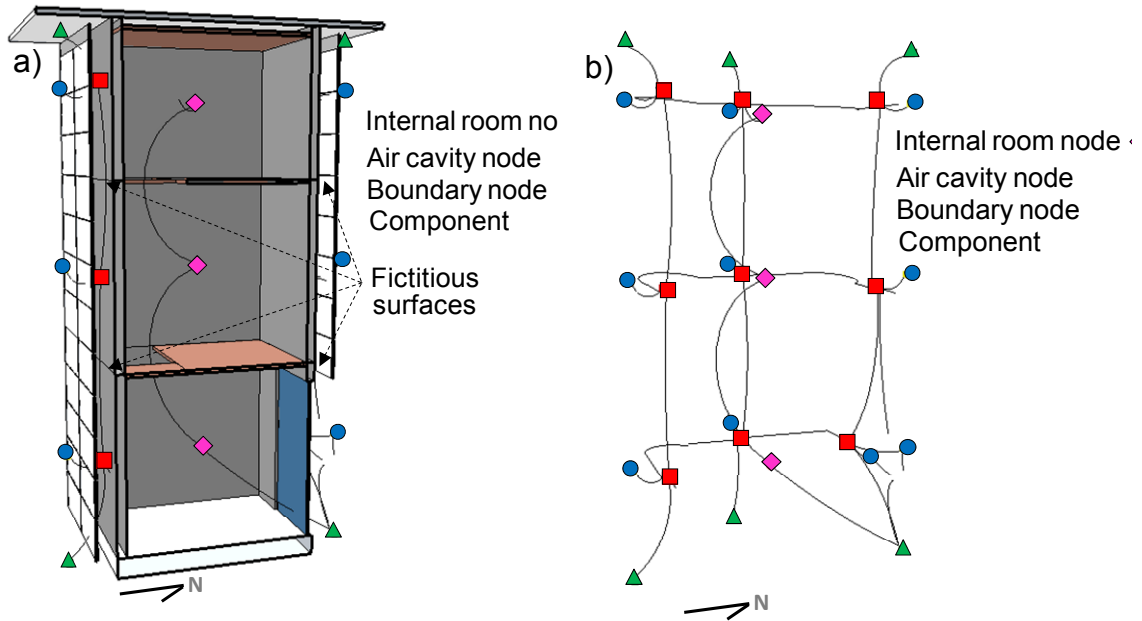


Figure 3.08: Airflow and thermal network model: (a) isometric view; (b) skeleton: nodes and links.

In order to model the whole test building, the rainscreen wall is divided into a stack of three zones adjacent to each of the floor levels (Figure 3.08a). Three zones are divided by fictitious transparent surfaces (Figure 3.09) with high conductivity, negligible thermal mass and high emissivity, and coupled by an airflow network which also includes the inlet opening at the bottom and the top outlet of the façade.

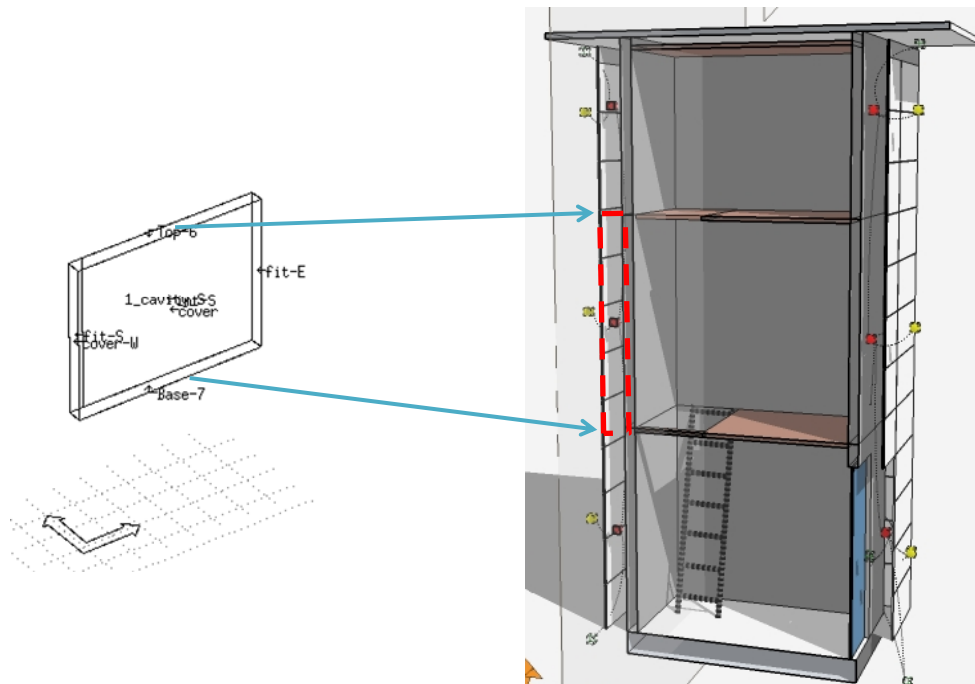


Figure 3.09: One of three air cavity zones of the ventilated southern façade.

As reported by Leal et al. [2003] the number of nodes (zones) linked by an air flow network to the thermal network is of fundamental importance in order to take into account in the model the natural convection effects in a building. However, no rules have been developed up to now in order to know the number of nodes needed for an optimal simulation of such cases.

In this specific case, the airflow and the number of thermal zones have been chosen according to the position of temperature sensors used in the experimental analysis of the test building (in according to Figure 3.09).

Since the air cavity is being treated as a set of thermal zones, the heat transfer coefficients used by ESP-r for the inner surface of the air channel are the same as for room inner surfaces. These coefficients have been computed by using the Alamdari-Hammond [1983] correlations as a function of the temperature difference between the surface and the ambient air (ΔT) and the surface height (H):

$$h_{c,i} = \left[\left(1.50 \left(\frac{\Delta T}{H} \right)^{0.25} \right)^6 + \left(1.23 (\Delta T)^{0.33} \right)^6 \right]^{\frac{1}{6}} \quad (Wm^{-2}K^{-1}) \quad [3.19]$$

According to Poizaris [2006] and confirmed by Costola et al. [2009] the air flow in the cavity is dependent on the wind pressure conditions on the building's skin, on the stack effect and on the discharge coefficient (C_d) of the openings. Unfortunately there are no experimental measurements of discharge coefficients for the open joints and the ventilation grilles of this analyzed test cell.

In this analysis, the grilles at the bottom and the top of the ventilated façade were modelled as a standard orifice airflow component with a discharge coefficient equal to 0.65 and an opening area (A) equal to 50% of the geometric area. Also the open joints in the façade were modelled as standard orifice airflow components with a discharge coefficient equal to 0.65 and opening area equal to the geometric area. Fazio and Kontopidis [1988] and Kimura [1977] have proposed alternative models in order to take into account the air exchange through the open joints but during the set-up of the model of the rainscreen it was shown that the final results were weakly influenced by the model adopted for the open joints.

In the model two air flow networks were used: one model represents the thermal and flow paths inside the air cavity and another model represents those inside the rooms. The air flow network inside the air cavity simply consists in of three air nodes for each side of the test cell. Each node is linked to the other by means of vertical links and by horizontal links. In Figure 3.08b all the nodes used to model the rainscreen ventilated structure are shown.

The mass flowrate of air (indicate with " $m_{J \rightarrow I}^t$ " in Equation 3.15) between two nodes (for example J and I in Figure 3.06) may be calculated by using the pressure difference existing between the nodes according to the following equation:

$$m_{J \rightarrow I}^t = C_d A \sqrt{2 \rho_{air} \Delta P_{J,I}} \quad [3.20]$$

in which C_d is the discharge coefficient of the opening, A is the total opening area, ρ_{air} is the air density (kgm^{-3}) and $\Delta P_{J,I}$ is the pressure difference between two nodes.

Figure 3.10 presents a scheme of heat fluxes for various kinds of nodes used for the rainscreen ventilated façade by ESP-r. By using Equations 3.04, 3.05, 3.11, 3.12, 3.15 and 3.16 it is possible to define the heat and mass balance equations for nodes located within homogeneous material layers (yellow circles in Figure 3.10) and/or for internal surface nodes (black circles in Figure 3.10) and/or for the ambient air-point nodes (red, blue and magenta circles in Figure 3.10): this procedure enables a nodal network model for a whole building or for some specific components of the envelope to be built.

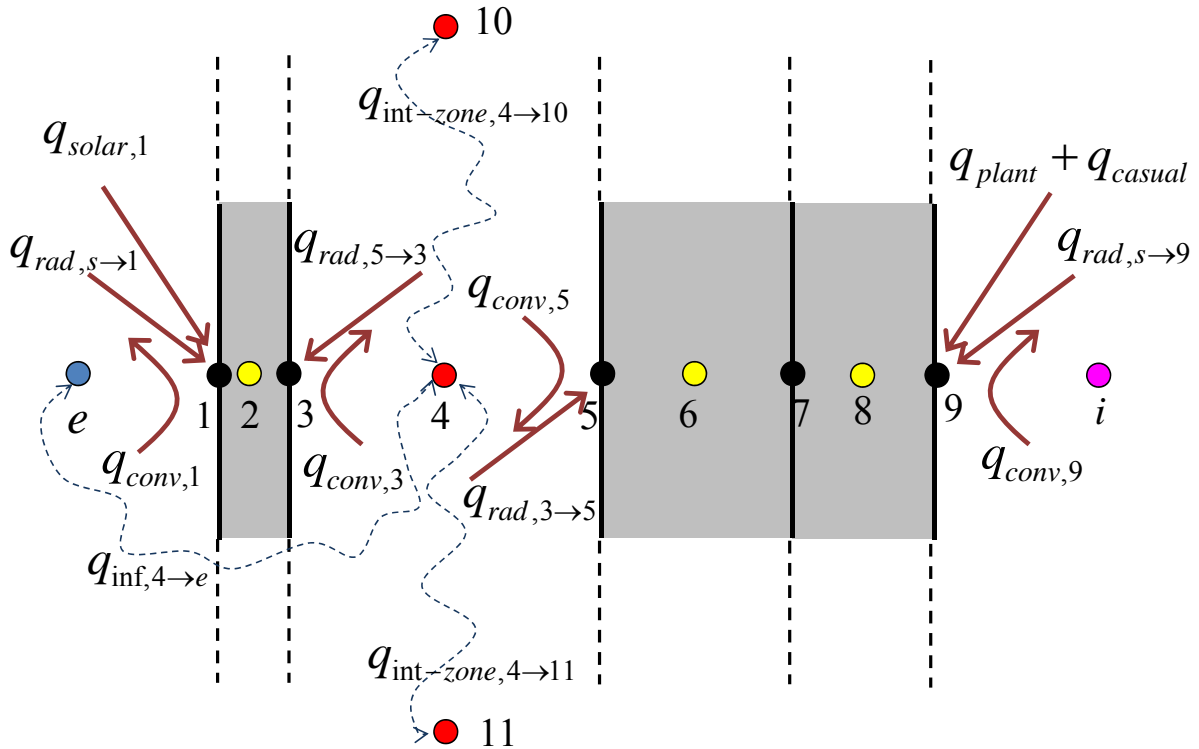


Figure 3.10: Heat fluxes for various kinds of nodes: nodes in homogeneous material layers (yellow circles), nodes at internal surfaces (black circles) and nodes for air points (red, blue and magenta circles).

Although this procedure may be useful in many cases, it is sometimes necessary to couple BS solvers with a CFD analysis, for example when flows in the airspace are complex as reported by Manz and Frank [2005].

In the thermal model of the test building a value of 0.2 for ground reflectivity was adopted. Thermal bridges of the test building were not included in the model as they were considered negligible. The cooling/heating system was introduced into the model by imposing a constant value of the room temperature.

3.5 Conclusion

This chapter has provided an overview of ESP-r’s simulation methodology. Its approaches for modelling the thermal domain, inter-zone air flow, and intra-zone air flow and heat transfer were described. Further, the heat balance for intra-constructional nodes, internal surface nodes and air-point nodes were given. The default convection heat transfer used for internal surface nodes is given by the Alamdari-Hammond [1983] correlations and it is also used for the analyzed rainscreen ventilated skin façades.

In Section 3.3 details on the modelling setup of rainscreen ventilated skin façades were described. Most of ventilation component (ventilation grills and joints) were modelled as a common standard orifice airflow component with a discharge coefficient equal to 0.65 (there are no experimental measurements on the real discharge coefficient). The air mass flux between nodes was calculated by using the difference of pressure existing between nodes. Finally a scheme of most heat fluxes for various kinds of nodes used for the rainscreen ventilated façade by ESP-r was shown.

CHAPTER 4

RAINSCREEN VENTILATED SKIN FAÇADE - EXPERIMENTAL SETUP

4.1 Introduction

This chapter describes on the measurements carried out on a rainscreen ventilated skin façade. Field measurements were performed during the 2009/10 winter and summer season in a test building located in San Mauro Pascoli (Italy).

Firstly, the measurement set-up is used to extend the knowledge of the thermal behaviour of the rainscreen ventilated façades. The set-up allows a more accurate control, measurement and change of the different patterns compared to in situ measurements. Secondly, the data are used to correlate parameter as cavity air temperature and velocity with climate data as solar radiation and ambient temperature.

Climate measurements of the local zone both for winter and summer are described, as well as an accurate description of the horizontal and vertical gradient temperature inside ventilated walls. The thermal analysis of this envelope component evidenced that the ventilated façade is able to reverse the direction of the heat flux through the envelope in regions characterized by large solar irradiation during the winter and the summer with moderate wind velocity, when the indoor-outdoor air temperature difference is small, thereby reducing the energy consumption required for indoor heating and cooling. In order to investigate the summer thermal performance of the rainscreen wall component a series of tests were performed through 12 different patterns of ventilated façade. The summer study evidenced a stronger correlation between both the cavity air temperature and velocity mainly with solar radiation and ambient temperature.

4.2 The test building

The test building is located in Italy, San Mauro Pascoli - Forlì Cesena (latitude 44.11°N, longitude 12.43°E). It was completed in November 2009 with the purpose of detailed investigations of the rainscreen wall energy performance. The building has a squared base of 2.89 m on the inner side and height of 2.67 m. There are three floors for a total internal height of 7.75 m. The door is on the north side and there are no windows (Figure 4.01a). The structure is realized mainly with steel profiles and wood (floor). All external walls are three-layered with a middle layer composed of a ventilated 24 cm air cavity and an external layer composed of stone cladding (Figure 4.01b).

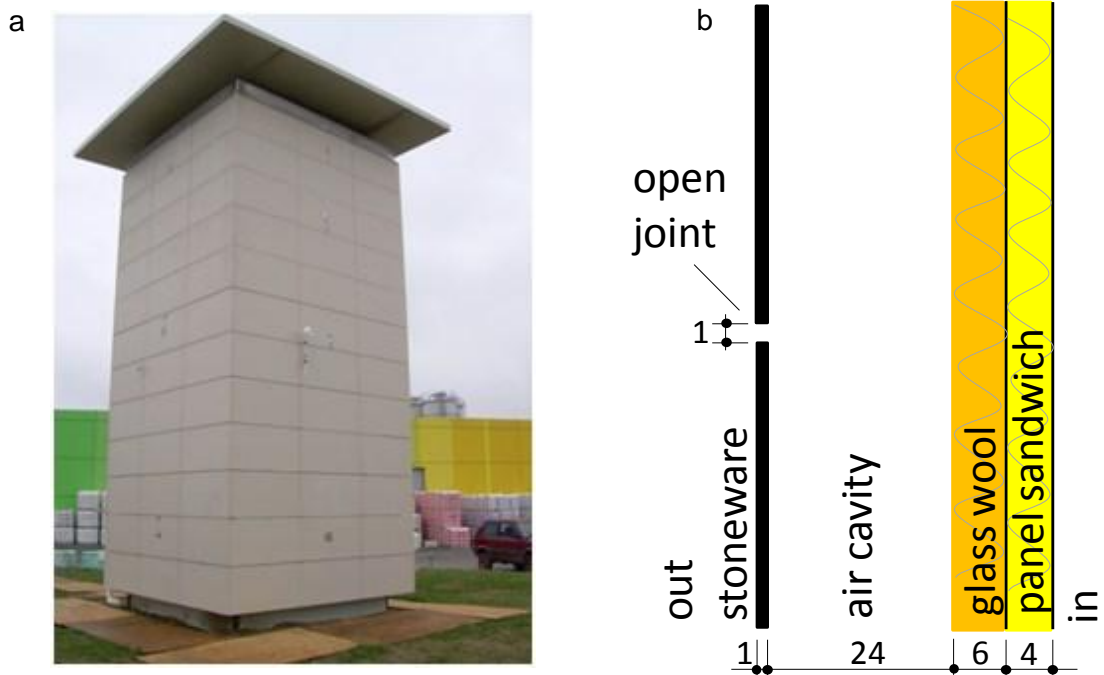
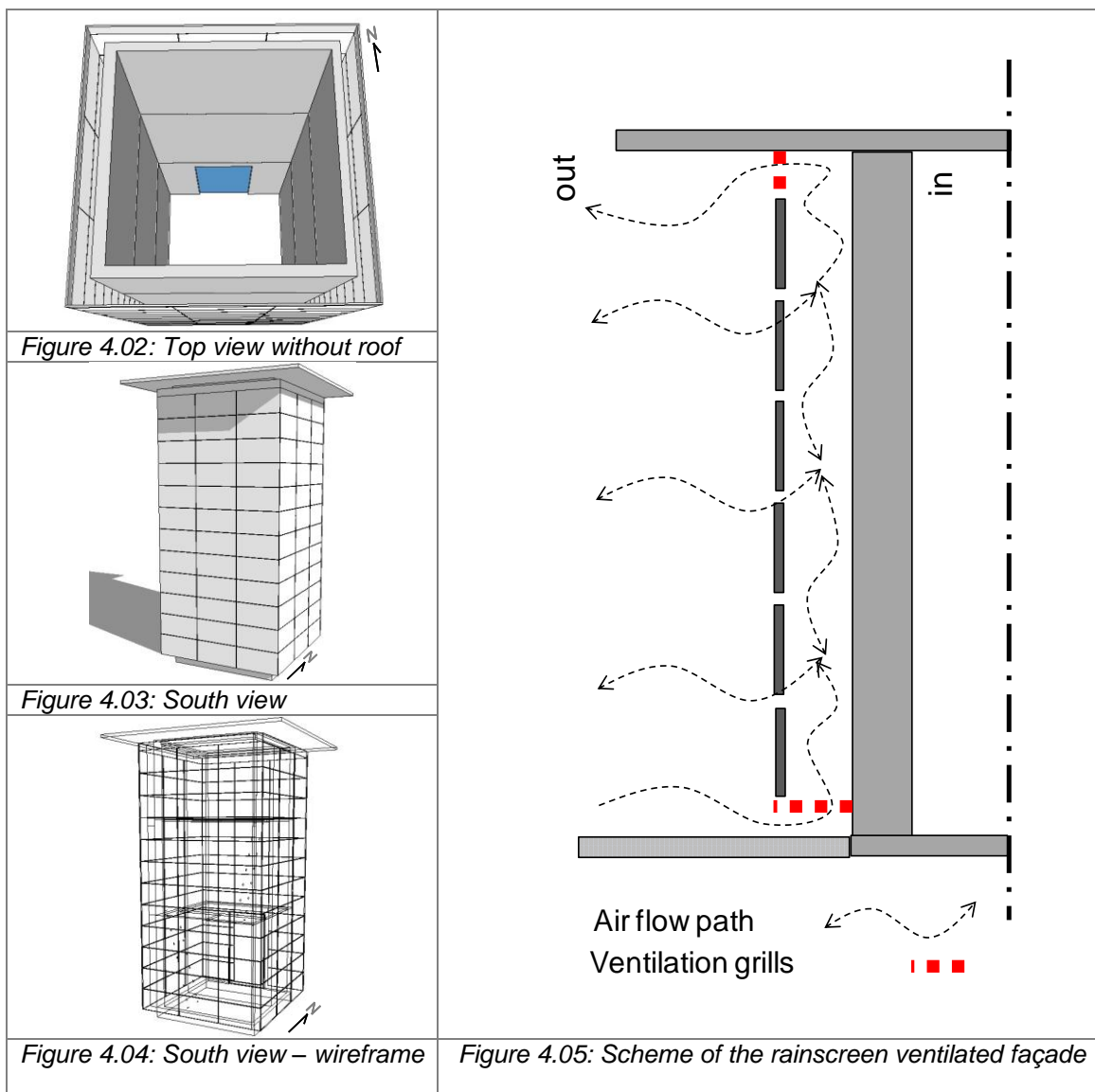


Figure 4.01: (a) Test building and (b) lay-out of the rain-screen walls (dimensions in cm)

The stone cladding consists of porcelain stoneware tile systems with open joints (Figures 4.01b and 4.05) that are separated from the inside wall by the ventilated air cavity (Figure 4.02). At the top and at the bottom of this tower ventilation grills are located (Figure 4.05). The roof consists of a sandwich panel and is not ventilated. The ground floor is made of an upper layer of wood, a second layer comprising an unventilated cavity and a third layer of cement mortar in contact with soil. All the properties of the materials of the external wall of the test building are given in Table 4.01.



A horizontal solar obstruction (Figures 4.01a and 4.03), setting of about 70 cm protects the top grill from rainy weather.

Table 4.01: Thermal properties of the layers of the external walls.

Layer	Thickness (cm)	Thermal conductivity ($\text{W m}^{-1} \text{K}^{-1}$)	Density (kg m^{-3})	Specific Heat ($\text{J kg}^{-1} \text{K}^{-1}$)
Stoneware	1	1.30	2300	840
Air cavity	24	-	-	-
Glass wool	6	0.04	30	1200
Aluminium	0.2	160	2800	880
EPS	4	0.04	70	1200
Aluminium	0.2	160	2800	880

In order to investigate winter and summer thermal performance of the rainscreen wall component, a series of tests were carried out, during two periods: the first period goes from January 1st to March 31st 2010 and the second one goes from July 2nd to September 17th 2010. In July 2010, additional settings on the external configuration were tested.

4.3 Measurement sensors

Façades are exposed to real weather conditions, but only the South and West sides have been equipped with a series of sensors. The sensors include 72 thermocouples, 2 hotwire anemometers and one pyranometer.

T-type thermocouples were used with a declared accuracy of ± 0.5 C (class 1 according to EN 60584-2, range: $-270\div 400$ °C) using standard calibration. The accuracy of hotwire air speed transmitters was of ± 0.04 m/s +2% of reading if the measurement ranged $0.05\div 1$ ms^{-1} . The pyranometer was a Second Class LP (PYRA 03) with a range of $0\div 2000$ Wm^{-2} and an accuracy $<|\pm 2|$ %. In Table 2 the basic characteristic of sensors are summarised.

Table 4.02: Characteristics of the measurement sensors.

Sensor	Type	Range	Accuracy
Thermocouple	T	$-270\div 400$ °C	± 0.5 °C
Hotwire Air Speed Transmitters	HD2903TC	$0.05\div 1$ ms^{-1} ($0.05\div 20$ ms^{-1})	± 0.04 m/s +2% of reading (± 0.2 m/s +3% of reading)
Pyranometer	Second Class LP PYRA 03	$0\div 2000$ Wm^{-2}	below ± 2 %

Each wall is divided along the vertical direction of the cavity into 3 sections as shown in Figure 4.06a; sensors were placed in each section along the cavity (Figure 4.06b) and outside.

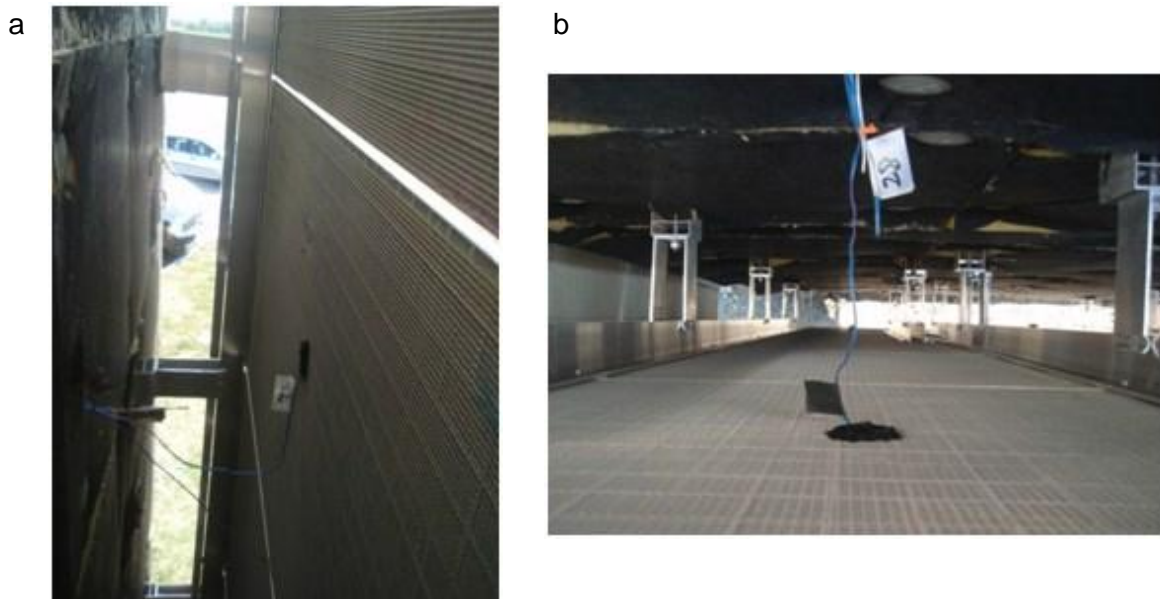


Figure 4.06: (a) Three sections of the vertical ventilated duct (b) Thermocouples in air cavity: top view.

The following measurement instruments were used during the experimental tests:

- 7 temperature sensors fixed on the external side of the rainscreen. All the sensors were shielded with an aluminium foil from the direct solar radiation (point “a” in Figures 4.07 and 4.08);
- 17 temperature sensors to monitor the temperature distribution along the walls of the ventilated cavity. Thermocouples were fixed to the surface of the duct with silicone adhesive (point “b” in Figures 4.07 and 4.08);
- 17 temperature sensors used in order to determine the vertical distribution of the air temperature along the cavity. Sensors were positioned in the middle of the air duct (point “c” in Figures 4.07 and 4.08);

- 11 temperature sensors for the determination of the temperature on the external side of the thermal insulation (point “d” in Figures 4.07 and 4.08);
- 17 temperature sensors on the inner surface of test building (point “e” in Figures 4.07 and 4.08);
- 3 temperature sensors for the determination of the indoor air temperature at the centre of each room;
- 2 hotwire anemometers located at a height of 7 m on the southern and western façade (in the middle of the ventilated air ducts, labelled “f1” and “f2” respectively in Figures 4.07 and 4.08);
- 1 pyranometer (Second Class pyranometer according to ISO 9060) for the determination of the global solar radiation on the South wall (“g” in Figure 4.07).

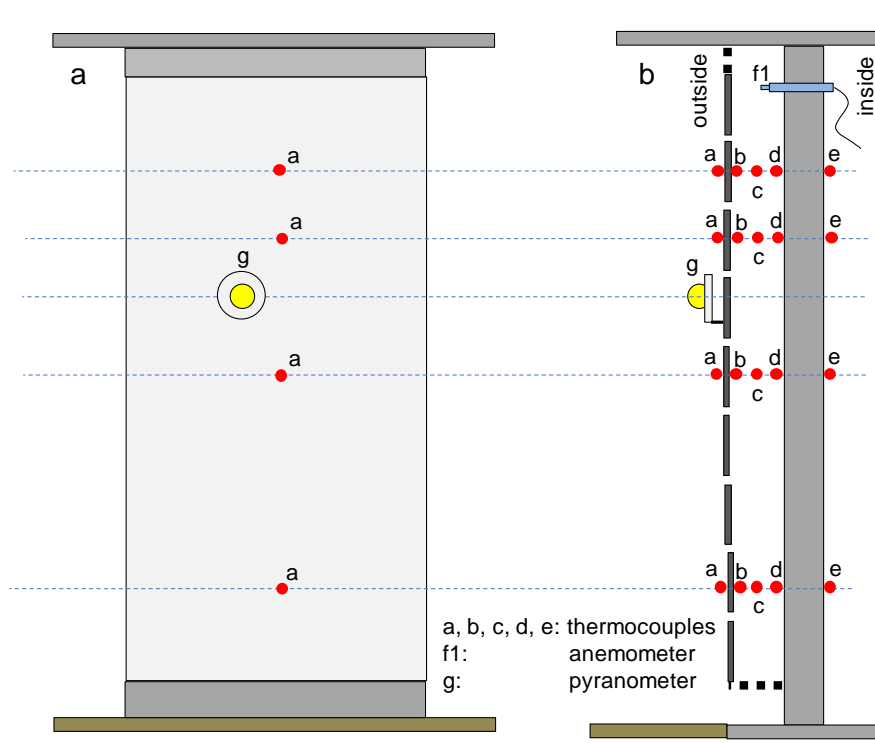


Figure 4.07: Layout of measurement sensors: (a) front view, (b) section view (South façade)

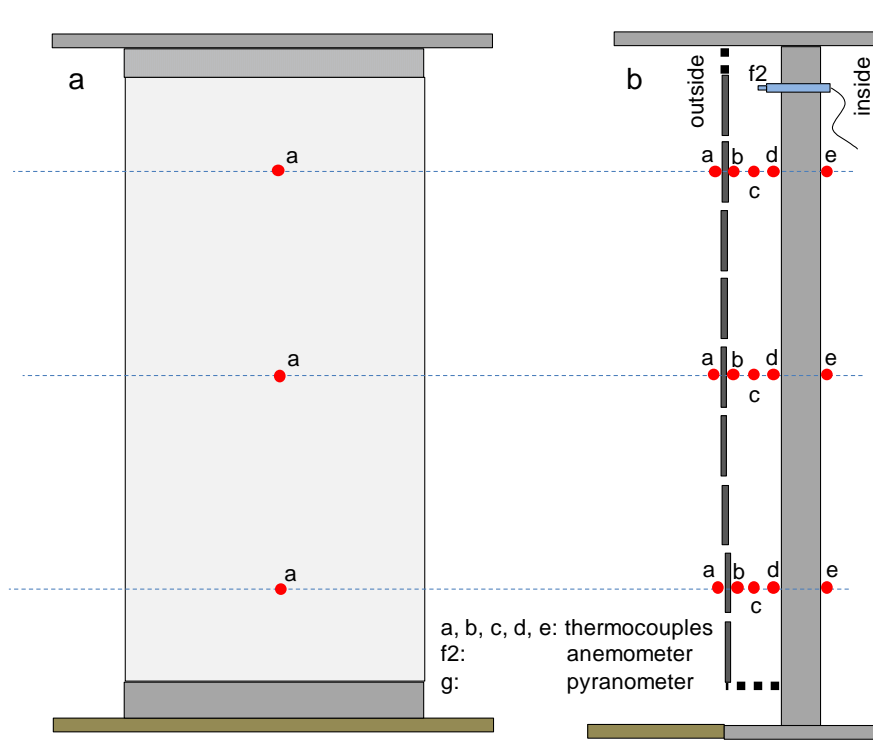


Figure 4.08: Layout of measurement sensors: (a) front view, (b) section view (West façade)

All sensors were connected to a dedicated Data Acquisition System (National Instruments). Acquisition and recording of the data were done by a computer station using Labview software. Data were recorded at intervals of 5 min and could be monitored remotely by using an Internet connection. Wind direction, wind speed, ambient temperature and ambient relative humidity were monitored every 5 min by a weather station installed close to the test rig. The test building was heated continuously to a room temperature of 20 °C in the winter period and 25° C in the summer period by means of a heat pump system.

4.4 Analysis of the local weather data (winter period)

For the purpose of the model validation (described in Chapter 4 and 5), measured local weather data for three months (January 1st– March 31st 2010) were used. The measured local weather data include ambient temperature (AT) and ambient relative humidity (ARH), wind speed (WS) and direction (WD) and total vertical (South side) global solar radiation (HGSR). In Figures 4.09-4.11 trends of the local climate data during the tested winter period are shown. The ambient temperature varied between -6 and 20°C with a high relative humidity (typically higher than 70%).

The wind speed during the whole period was less than 5 ms^{-1} with a predominant direction between South and South-West (Jan-Feb) and South-East and South (Feb-Mar).

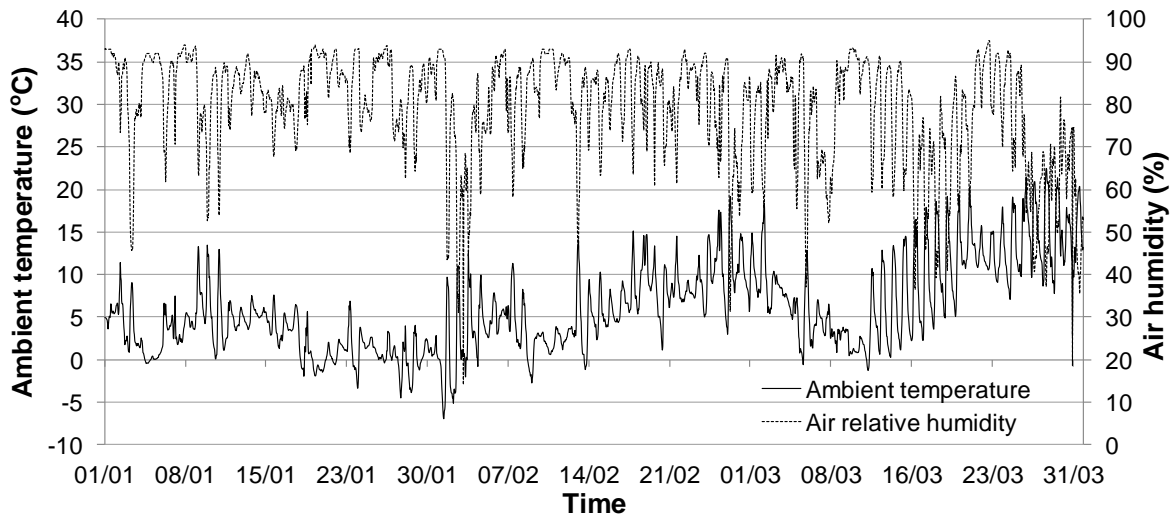


Figure 4.09: Ambient temperature and air humidity.

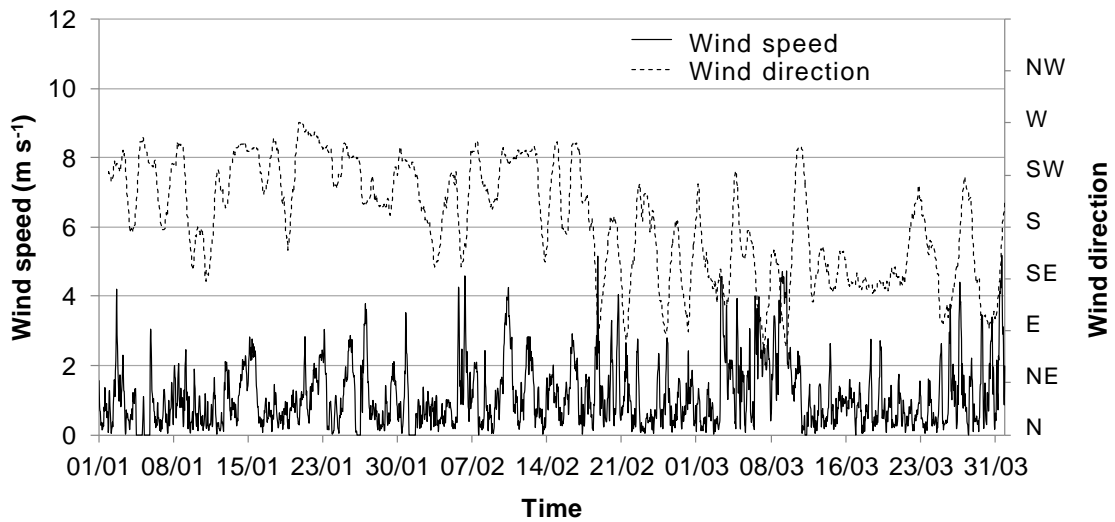


Figure 4.10: Wind speed and wind direction.

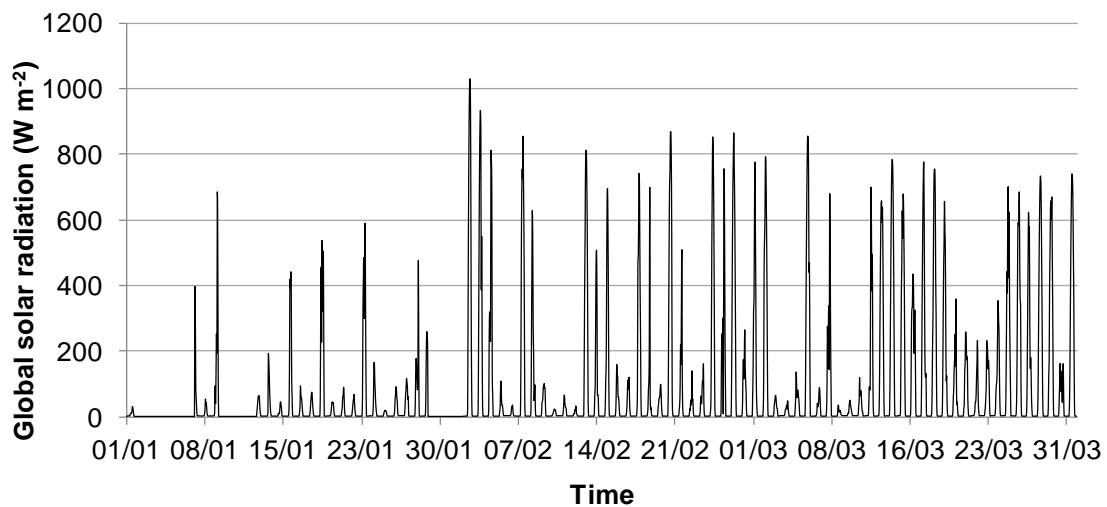


Figure 4.11: Vertical global solar radiation on the South side.

In Table 4.03 the ambient temperature (AT), ambient relative humidity (ARH), vertical global solar radiation on the South side (VGSR), wind speed (WS) and wind direction (WD) of the analyzed period (two weeks per month) are given.

It possible to notice that the minimum ambient temperature was reached in the first week of February, while the maximum one at the end of March. The average ambient relative humidity was around 80% and the maximum vertical global solar radiation reached on the South façade was about 1029 Wm⁻² in February. The average wind speed was about 1.1 ms⁻¹ with peak value of about 5 ms⁻¹. The wind direction is quite variable but with the prevailing direction around SSW in January and February and SSE in March. In Table 4.4 monthly statistical climate data are reported.

Table 4.03: Overview of the climate measurements of local zone, maximum, minimum and average of the periods (two weeks per month)

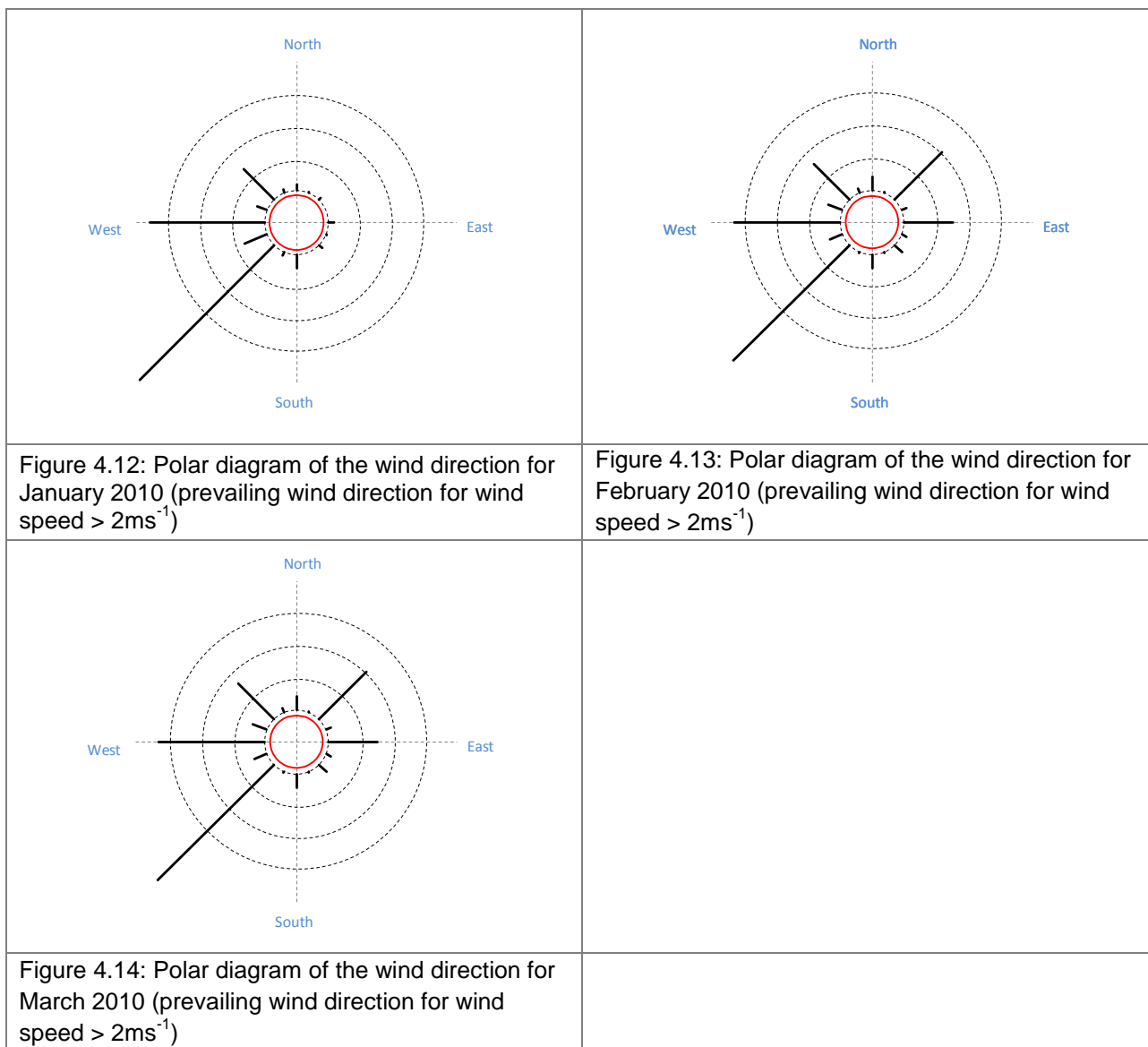
period		AT (°C)	ARH (%)	VGSR (Wm ⁻²)	WS (ms ⁻¹)	WD (-)
01/01–14/01	max	11.9	94	685	4.2	-
	min	-0.6	46	0	0.0	-
	avg	3.7	84	104	0.8	SSW
15/01–29/01	max	6.0	94	589	3.8	-
	min	-4.9	63	0	0.0	-
	avg	1.1	84	125	1.1	SSW
01/02–14/02	max	9.8	93	1029	4.6	-
	min	-5.7	14	0	0.0	-
	avg	2.8	79	282	1.2	SSW
15/02–28/02	max	17.3	93	867	5.2	-
	min	0.5	31	0	0.0	-
	avg	8.0	81	246	1.1	SE
1/03–14/03	max	15.3	93	854	4.7	-
	min	-1.7	37	0	0.0	-
	avg	4.9	79	240	1.5	-
15/03–31/03	max	19.8	95	776	5.2	-
	min	0.9	19	0	0.0	-
	avg	11.8	69	282	1.0	SSE

Table 4.04: Overview of the climate measurements of local zone, maximum, minimum and average of the periods (month)

period		AT (°C)	ARH (%)	VGSR (Wm ⁻²)	WS (ms ⁻¹)	WD (-)
01/01–29/01	max	11.9	94	685	4.2	-
	min	-4.9	46	0	0.0	-
	avg	2.4	84	119	1.0	SSW
01/02–28/02	max	17.3	93	1029	5.2	-
	min	-5.7	14	0	0.0	-
	avg	5.5	80	262	1.1	SSW
01/03–31/03	max	19.8	95	854	5.2	-
	min	-1.7	19	0	0.0	-
	avg	8.7	74	265	1.3	SSE

In order to evaluate the predominant wind direction polar diagrams [Davis and Ekern, 1977] are used. In Figures 4.12-4.14 graphs of above mentioned polar diagrams for analyzed periods are shown.

Only the prevailing wind direction for the wind speed over to 2 ms⁻¹ are indicated in the following figures. For the analyzed period it is possible to notice that the prevailing wind direction with high wind speed was South-West and West direction in January, quite variable, South-West prevailing, in February and March.



4.5 Monitoring measurements: winter period

In this section typical results that were extracted from the set of measurements made on the test building are shown. The large number of temperature sensors enables a detailed study of the temperature distribution in the main regions of the building and its envelope, which can be used in order to calculate all the heat fluxes involved in the thermal balance of the building.

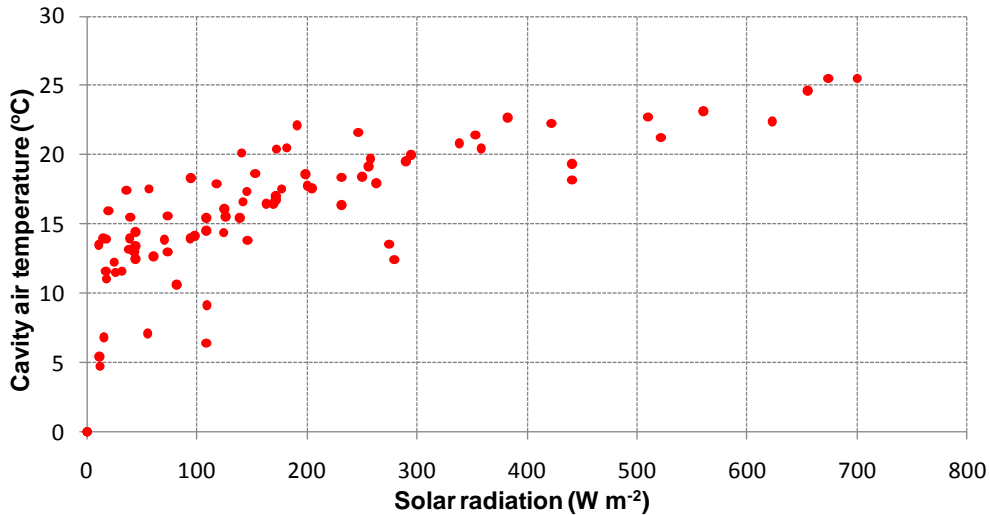


Figure 4.15: Typical trend of the average value of the cavity air temperature as a function of the global solar vertical radiation on South side (period: March 19-25, 2010).

In Figure 4.15 the correlation between the vertical global solar radiation on the South side and the hourly average value of the cavity air temperature is shown. It can be noticed how the scatter in the data decreases for large values of the solar radiation, as also observed by Ong [2003]. Conversely, for low values of solar radiation ($<200 \text{ W m}^{-2}$) the spread of the cavity air temperature is very large.

In Figure 4.16 the correlation between the wind speed and the hourly average value of the both cavity air velocity of west and south sides is shown. Only measured values corresponding to absence of solar radiation (night-time and overcast sky) were considered. It can be noticed how the level of correlation between these parameters tends to improve for large values of wind speed. The prevailing direction wind for this period (from February 10th to February 16th) was about South-West. A similar trend can also be noticed both for the western and the southern side.

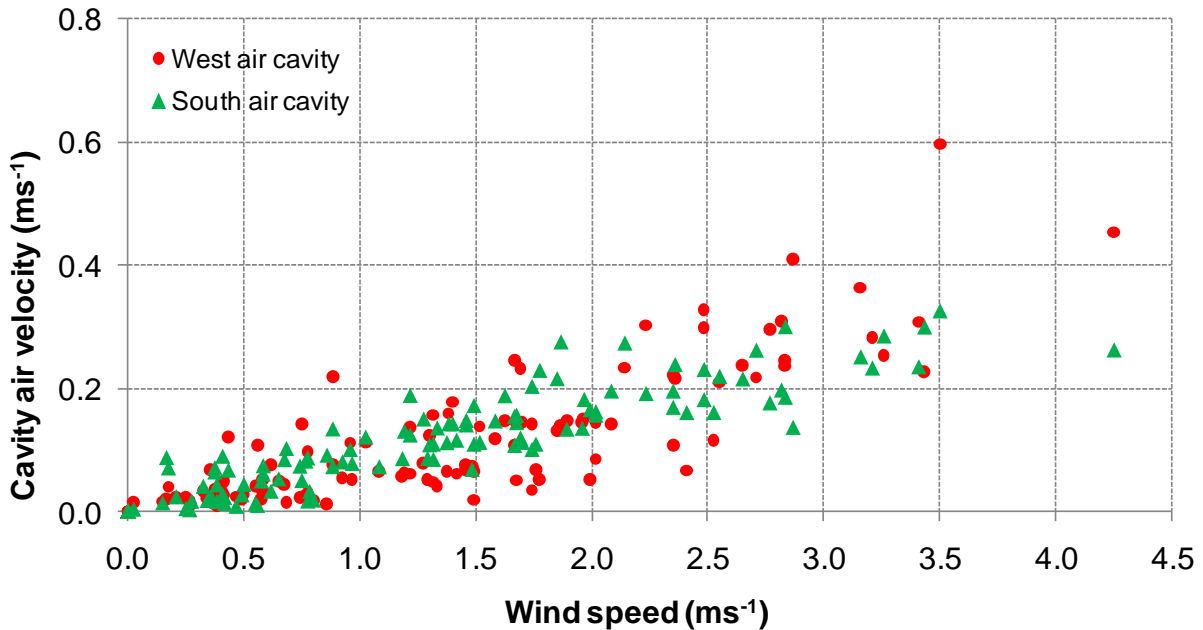


Figure 4.16: Trend of the average value of the cavity air velocity as a function of the wind speed on West and South sides (period: from 10 to 16 February 2010).

In Figure 4.17 the vertical temperature gradient along the air cavity of the South wall on a typical spring day (March 28th 2010) as a function of the incident global solar radiation is depicted. It can be noticed that the typical vertical temperature distribution presents a maximum along the air cavity near the top of the channel. This trend is shifted in towards increasing temperatures for larger values of the instantaneous global solar radiation. It is possible to see that when the vertical global solar radiation reaches its daily maximum values (733 W m^{-2}) the air temperature is greater than 30° C when the ambient temperature is equal to 19° C . The maximum value of the air temperature tends to decrease when the solar radiation decreases. The decrease of the temperature near the exit of the vertical cavity is due to the presence of the horizontal solar obstruction which shades the external layer close to the ventilation grill.

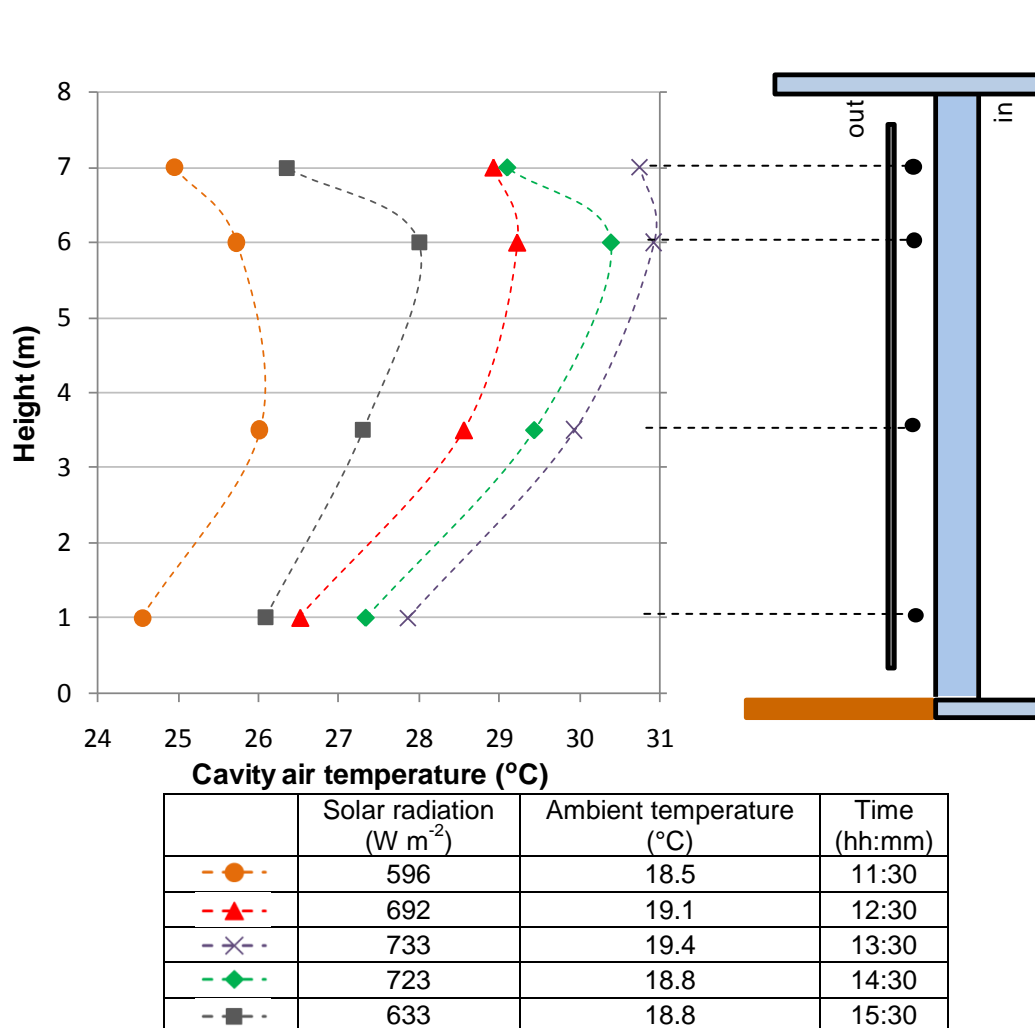


Figure 4.17: Vertical temperature gradients along the air cavity (March 28th 2010) – South side

In Figures 4.18 and 4.19 the trend of the hourly values of the temperature measured in the wall is depicted. These data show the variation of the outside wall temperature, of the cavity air temperature and of the inside wall temperatures during the central daily hours of two different days in the winter period characterized by a large and a low outdoor-indoor air temperature difference (18K in Figure 4.18 and 2K in Figure 4.19). By analyzing the data shown in Figure 4.18 and 4.19 it is evident that during the winter the role of the outside layer is to absorb the solar radiation in order to increase the wall temperature of the cavity: this value influences the mean cavity air velocity due to the buoyancy effect. Of course, the cavity air velocity is related also to the wind velocity so the final value of the air flow rate through the cavity is obtained as the combined effect of the wind and the solar radiation which changes the wall temperature of the cavity. For this reason, in Figure 4.18

and 4.19 the measured value of the average cavity air velocity is given together with the global solar radiation incident on the external surface of the rainscreen.

It is evident in Figure 4.18 that, even for low ambient temperature, ($T_{ext}=5^{\circ}\text{C}$), the outside wall of the cavity can reach a temperature near 20°C for solar radiation values larger than 450Wm^{-2} . Higher temperature on the outside wall means greater temperature values on the cavity walls which implies a reduction of the heat flux from the room to the external environment. Moreover the temperature gradient inside the wall of the ventilated façade is progressively reduced when the incident solar radiation on the external surface of the rainscreen increases which results in a significant reduction of the heat losses through this component. For the same reason, during the winter season high values of the cavity air flow rate are not desirable, because the convective heat transfer between the air and the inside wall reduces the temperature on the inside wall of the cavity and increases the heat flux through the inside wall.

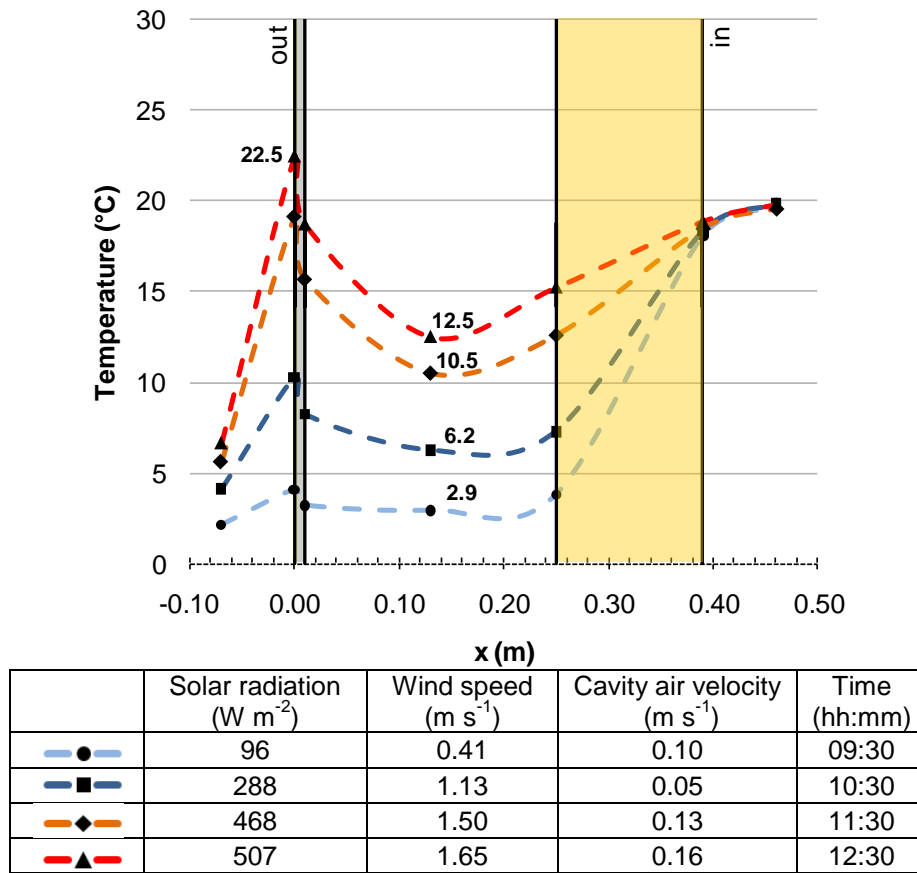


Figure 4.18: Trend of the average values of the measured temperature and cavity air velocity of the South ventilated wall for different hours (February 14th 2010). Global solar radiation and wind speed both are reported (prevailing wind direction W).

It is interesting to compare the temperature profiles shown in Figure 4.18 for a typical winter day with a low ambient temperature with the profiles depicted in Figure 4.19 obtained for a day characterized by a reduced temperature difference between outside and inside and high solar radiation (a typical situation which can occur at the beginning and at end of the winter season). The most important difference between these two situations is related to the direction of the heat flux through the inner wall of the ventilated façade. In fact, Figure 4.19 represents a typical situation in which the ventilated façade is able to reverse the direction of the heat flux through the wall and in which the façade become an active component for the heating of the indoor environment. For this reason, especially in regions characterized by large solar irradiation during the winter and

moderate wind velocity, this kind of component can give a contribution to the reduction of the energy consumption related to indoor heating during winter.

The data of Figure 4.18 and 4.19 show that, since the direction and magnitude of the heat fluxes through the walls is an unsteady phenomena linked to the instantaneous values of the ambient temperature, of the wind velocity and of the incident global solar radiation, a dynamic simulation of these components is necessary in order to obtain an “a-priori” evaluation of the energy saving due to the use of the ventilated façade.

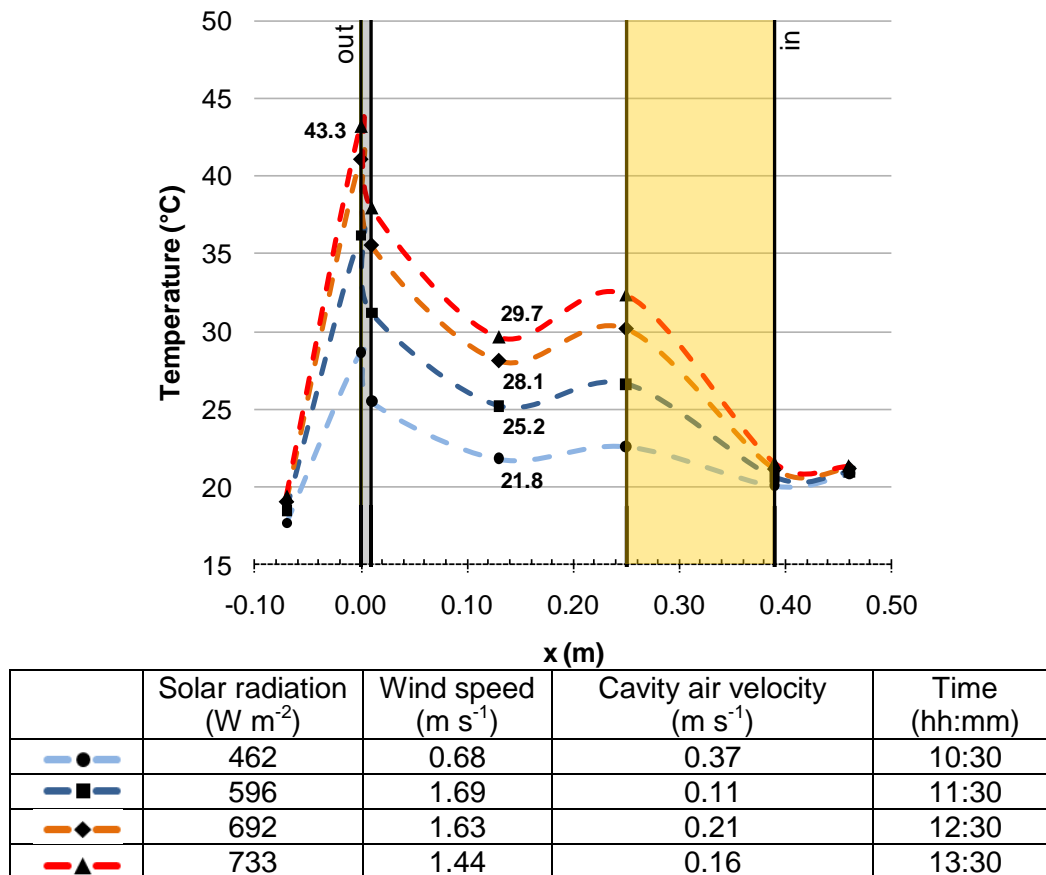


Figure 4.19: Trend of the average values of the measured temperature and of the cavity air velocity of the South ventilated wall for different hours (March 28th 2010). Global solar radiation and wind speed both are reported (prevailing wind direction SW).

In Figure 4.20 the vertical gradient temperature along the air cavity of the South wall at two different times (2:30 on February 02nd and 13:30 on March 28th 2010) is depicted. There were four sensors in the air cavity fixed to a different height (1 m, 3.5 m, 6 m and 7 m from the ground). In Figure 4.20 the temperature difference between that measured by each sensor and the first one, placed at 1m-height is indicated.

It can be noticed that both vertical temperature distributions present a maximum along the air cavity near the top of the channel. For the temperature gradient of the day-time on March 28th it is possible to see that when the vertical global solar radiation reached its daily maximum values (733 Wm⁻²) the air temperature difference was about 3 K (3K is the difference between 30.9° C and 27.9° C when the ambient temperature is 19.4° C). The decrease of temperature near the exit of the vertical cavity is due to the presence of the horizontal solar obstruction which shades the external layer close to the ventilation grill. The temperature gradient of the night-time on February 2nd it was rather smaller than before because there was no influence of solar radiation. In this case the maximum temperature difference was less than 1 K and there was no decrease near the exit.

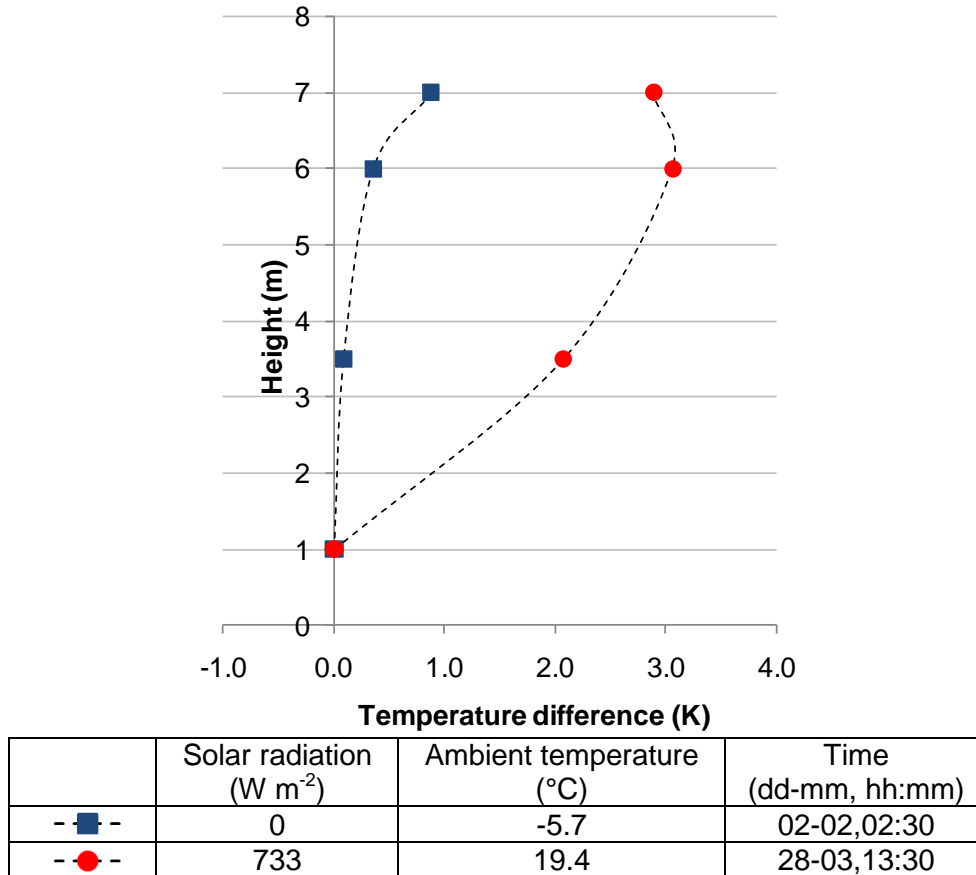


Figure 4.20: Vertical temperature gradients along the air cavity – South side

In Figure 4.21 values of the measured temperature inside the wall are reported. These data show the variation of the outside wall temperature of the cavity air temperature and of the inside wall temperatures at two different times of the winter period characterized by the largest and the lowest outdoor-indoor air temperature difference between (24.2 K at 2:30 on February 2nd and 2 K at 13:30 on March 28th). The outdoor temperature on February 2nd was the lowest of the whole winter period and the vertical global solar radiation at the time on March 28th was the highest of the winter period. These trends of the temperature represent the two most extreme conditions for the analyzed winter period analyzed.

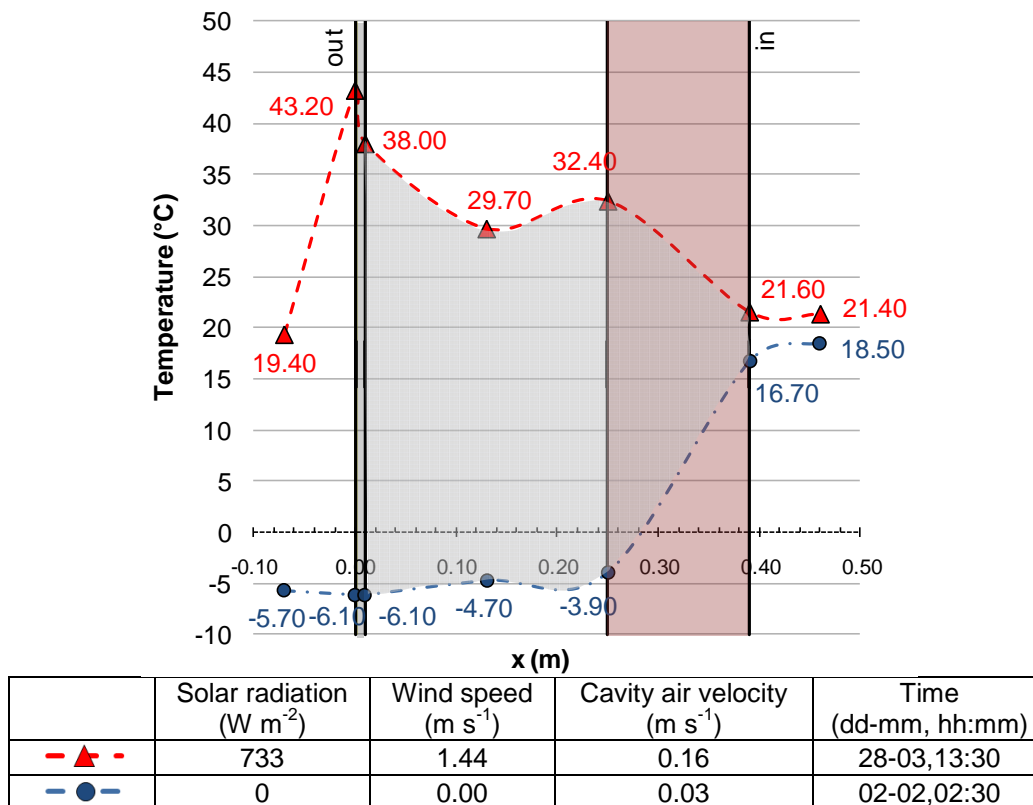


Figure 4.21: Trend of the average values of the measured temperature of the South ventilated wall for two different time (February 2nd and March 28th 2010). Vertical global solar radiation, wind speed and cavity air velocity are also reported (prevailing wind direction SW).

It is interesting to compare the temperature profile shown in Figure 4.21 for an extreme winter night-time (02:30 on February 02nd) characterized by a low ambient temperature with the profile obtained for a day-time (13:30 on March 28th) characterized by a reduced temperature difference between in and out and high solar radiation (a typical situation which can occur at the beginning and at end of the winter season). The most important difference between these two conditions is related to the direction of the heat flux through the inside wall of the ventilated façade. As stated before, this trend represents a typical situation in which the ventilated façade is able to reverse the direction of the heat flux through the wall and in which the façade become an active component for the heating of the indoor environment. For this reason, especially in regions characterized by large solar irradiation during the winter and moderate wind velocity, this kind of component can give a contribution to the reduction of the energy consumption related to the indoor heating during the winter.

In that case, it is possible to evaluate the amount of hours of the reversal the direction of the heat flux through the wall. By considering:

$$\Delta T = T_{we} - T_{wi} \quad (4.01)$$

where T_{we} is the average of measured temperatures on the external side of the thermal insulation (toward to the air cavity) and T_{wi} is the average of measured temperatures on the inner surface of test building, if the $\Delta T > 0$ it is possible to obtain a reversal of the direction of the heat flow. In that specific case the amount of hours for $\Delta T > 0$ represents 5.5% (122 h, about 5 days) of the total hours (2038) in the analyzed period (from January 1st to March 31st 2010). The reversal of the

direction of the flux depends mainly both of the solar radiation and the outdoor temperature. By considering the dimensionless factor [Marinosci et al., 2010a]

$$\eta_h = \frac{I_{vg,h} \cdot T_{e,h}}{I_{vg,ave} \cdot T_{e,ave}} \quad (4.02)$$

where $I_{vg,h}$ is the vertical global solar radiation at the time h , $T_{e,h}$ is the outdoor temperature at the time h , $I_{vg,ave}$ is the average of vertical global solar radiation in the analyzed period and finally $T_{e,ave}$ is the average of outdoor temperature in the analyzed period, and by considering also the temperature slope of the internal wall $\frac{\Delta T}{\Delta x}$ where Δx is the thickness of the internal wall (0.1 m), it is possible to obtain a correlation between the temperature slope of the internal wall and the above mentioned dimensionless factor η_h .

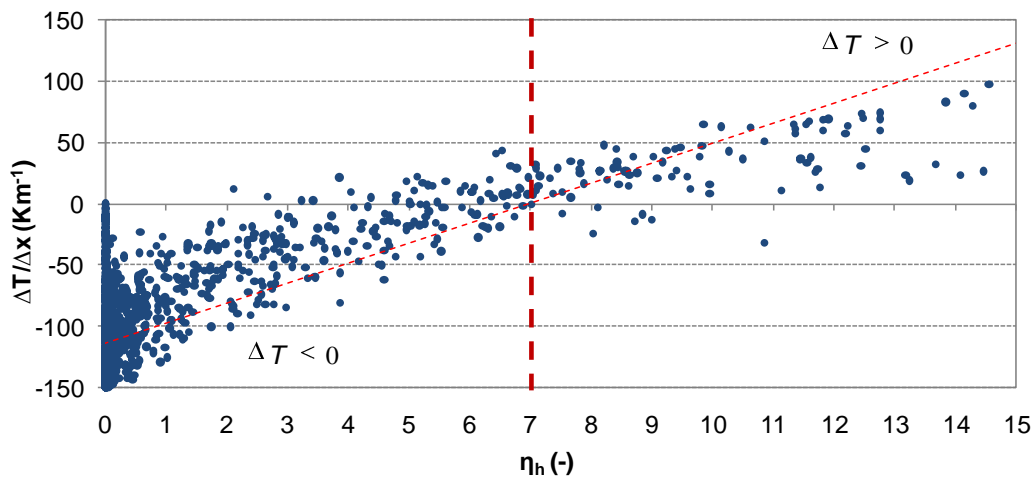


Figure 4.22: Temperature slope of the internal wall (southern side) as a function of the dimensionless factor η_h for the whole period (from January 1st to March 31st 2010).

The data of Figure 4.22 show that, since the ΔT between each surface temperature of the internal wall (South side) is less than 0 value then there is not a reversal of direction of the flux through the wall. The behavior of this wall is typical for the winter period. On the other hand, if the ΔT is positive then it is possible to obtain a reversal of the flux. In this latter case heating for the test building may be no necessary because the internal temperature is higher than 20 °C. However it is important to highlight that this behavior is influenced by the low thermal inertia of the wall under test.

The dimensionless factor η_h of the Equation 4.02 may be used like an energy performance index of this specific ventilated wall for other different climate zone as suggest by Marinosci et al. [2010a]. In fact, if the η_h parameter is below than 7 then it is possible to obtain a reverse flow for this studied VF. However, these results are valid only for local weather conditions. In order to validate the above mentioned consideration, several empirical validations for different weather climates are necessary.

4.6 Analysis of measurements of rainscreen ventilated skin façades in the winter period

This section presents an analysis on the distribution of cavity air temperature in specific times followed by an accurate analysis of the temperature at the inner wall.

4.6.1 Air cavity temperature

In this section the temperature distribution in the air cavity is analyzed in detail. In Figures from 4.23 to 4.26 the vertical temperature difference for four hours both on the southern and western façade on March 28th 2010 are depicted. The vertical global solar radiation, the ambient (AT) and internal (Ti) air room temperatures are reported also.

In the Figure 4.23 the vertical temperature difference at 9:30 was depicted and it possible to notice that it was about 2 K for both façade, but with different values. If the South, the cavity air temperature ranged from about 17° C to 19° C while in the West from 14° C to 16° C. It can also be notice that the air temperature stratification was higher on the top of façades than at the bottom. During this time the solar radiation was quite low while the ambient temperature was about 15° C.

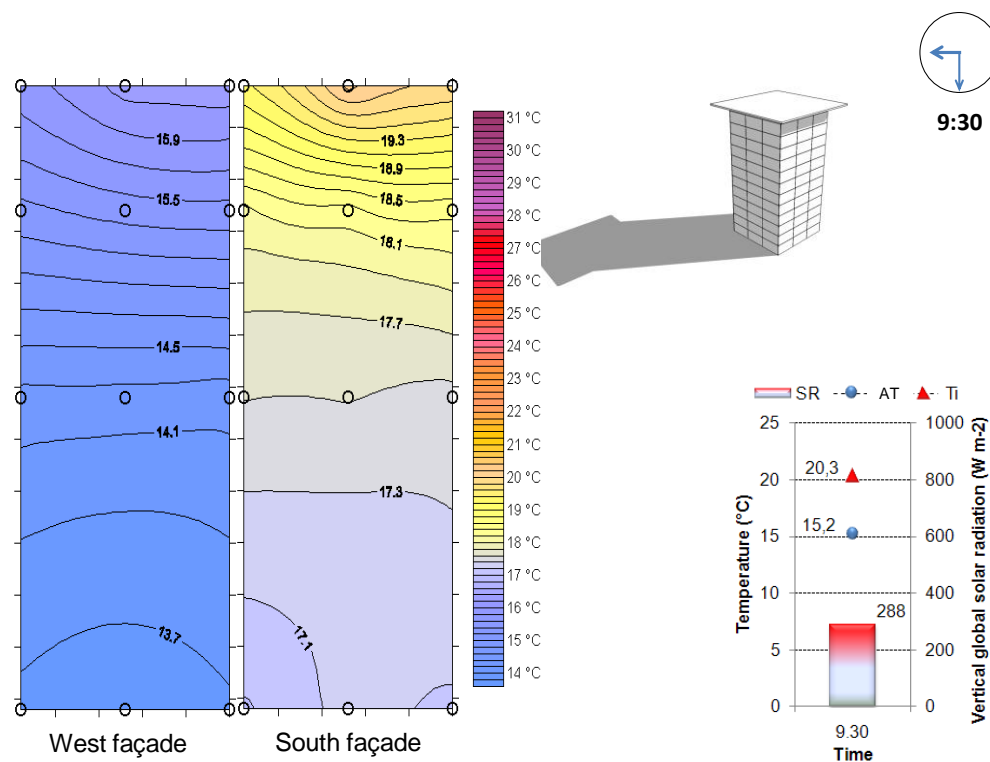


Figure 4.23: Distribution of cavity air temperature for the South and West façade (9:30, March 28th 2010).

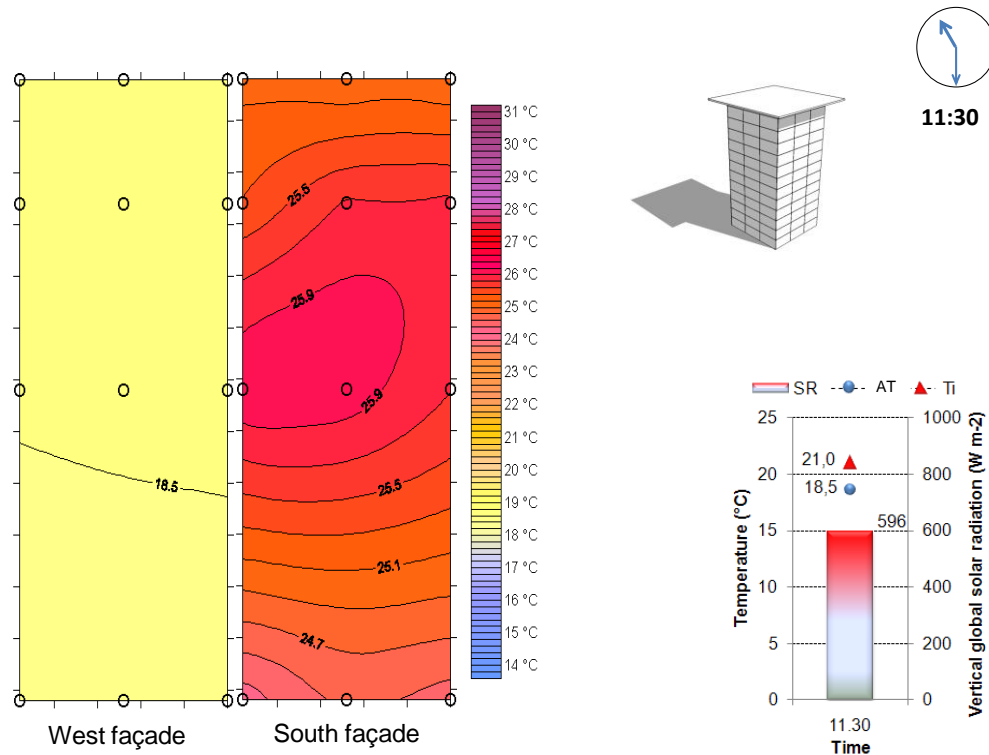


Figure 4.24: Distribution of cavity air temperature for the South and West façade (11:30, March 28th 2010).

In Figure 4.24 the vertical temperature difference at 11:30 on March 28th 2010 is depicted. In this case both solar radiation (596 Wm^{-2}) and ambient temperature (18.5° C) were higher than at previous time (Figure 4.23). It is interesting to observe the different behavior of the West façade by comparing with the South façade. If the cavity air temperature of the South façade was around 25° C while those one of the West façade was around 18° C (quite lower than before and near to ambient temperature). Further, the cavity air temperature of the South façade was more stratified than the West one.

Figure 4.25 shows the vertical temperature difference at 13:30 when the solar radiation on the South façade was very high. In fact the cavity air temperature of the South façade reached its daily maximum, about 31° C on the top part of façade with a vertical global solar radiation of about 733 Wm^{-2} (maximum daily value) and ambient temperature of about 19° C . Both the vertical air and stratification temperature difference of the South side were much higher than the one at the West side: the cavity air temperature ranged between $28^\circ\text{--}31^\circ \text{ C}$ while the one on the West side was quite uniform, around 21° C .

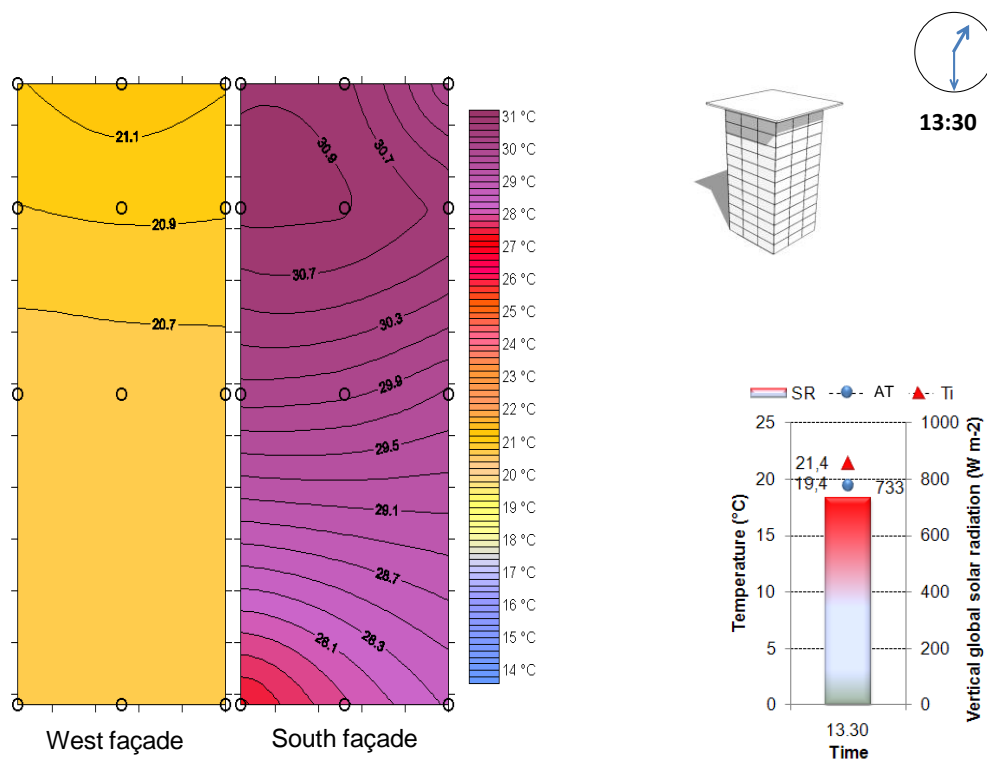


Figure 4.25: Distribution of cavity air temperature for the South and West façade (13:30, March 28th 2010).

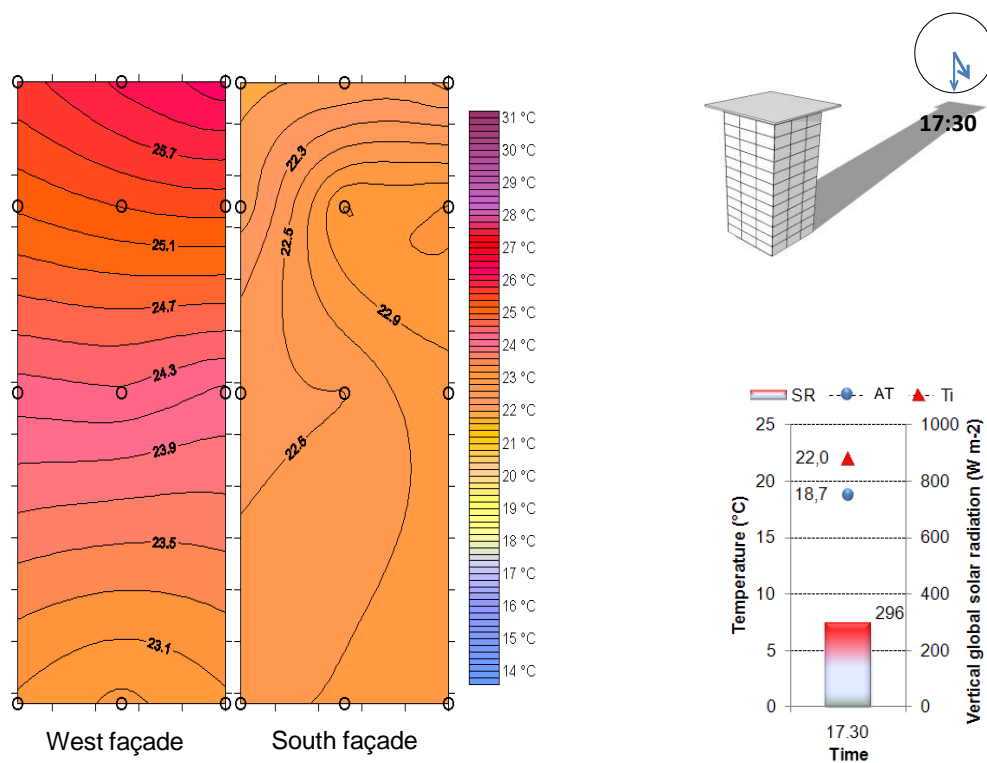


Figure 4.26: Distribution of cavity air temperature for the South and West façade (17:30 March 28th 2010).

Finally in Figure 4.26 the vertical temperature difference at 17:30 when the solar position on the West façade was very high is shown. In this case the cavity air temperature of the West façade reached its maximum daily value, about 26°C on the top part of façade with a vertical global solar radiation of about 296 Wm⁻² and ambient temperature of about 19° C. Both the vertical air and stratification temperature difference of the West side were much higher than the ones on the South side: the cavity air temperature ranged from 23° C to 26° C while that one on the West side was quite uniform around 22° C.

4.6.2 Temperatures in the wall

In this section will be to give detailed analysis of inside temperatures of ventilated façades. In Table 4.05 and 4.06 the average measurements of all sensors for the winter period (two weeks per month) both for the South and West façade are summarized. Starting from right to left: the ambient temperature (AT), the exterior surface temperature of the external skin (T_{ce}), the interior surface temperature of external skin (T_{ci}), the cavity air temperature (T_{ac}), the exterior surface temperature of internal wall (T_{we}), the interior surface temperature of internal wall (T_{wi}), the indoor temperature (T_i) and finally the cavity air velocity (CAV).

Table 4.05: Summary of the (hourly) average measurements for the analyzed winter period for the South façade (st. dev.)

period	AT (°C)	T _{ce} (°C)	T _{ci} (°C)	T _{ac} (°C)	T _{we} (°C)	T _{wi} (°C)	T _i (°C)	CAV (ms ⁻¹)
01/01–14/01	3.7 (2.5)	5.7 (6.4)	5.1 (5.3)	4.7 (3.5)	5.2 (4.1)	10.4 (6.1)	11.0 (6.6)	0.1 (0.1)
15/01–29/01	1.1 (2.4)	2.5 (4.2)	2.2 (3.6)	2.3 (2.6)	3.3 (2.8)	17.9 (0.6)	19.5 (0.6)	0.1 (0.1)
01/02–14/02	2.8 (2.8)	5.9 (5.9)	5.1 (3.6)	4.4 (2.6)	5.6 (5.2)	18.3 (0.7)	19.8 (0.6)	0.1 (0.2)
15/02–28/02	8.0 (3.1)	10.4 (7.2)	9.8 (6.1)	9.3 (4.1)	10.1 (4.6)	18.9 (0.6)	20.1 (0.3)	0.2 (0.2)
01/03–14/03	4.9 (3.5)	7.7 (8.6)	7.0 (7.3)	6.5 (5.1)	7.4 (5.6)	18.6 (0.6)	19.9 (0.4)	0.3 (0.3)
15/03–31/03	11.8 (4.3)	15.0 (9.1)	14.0 (8.0)	13.4 (5.8)	13.9 (6.3)	19.7 (0.9)	20.6 (0.5)	0.2 (0.3)

Table 4.06: Summary of the (hourly) average measurements for the analyzed winter period for the West façade (st. dev.)

period	AT (°C)	T _{ce} (°C)	T _{ci} (°C)	T _{ac} (°C)	T _{we} (°C)	T _{wi} (°C)	T _i (°C)	CAV (ms ⁻¹)
01/01–14/01	3.7 (2.5)	3.9 (3.3)	3.9 (3.1)	3.9 (2.7)	4.4 (2.8)	10.6 (6.1)	11.0 (6.6)	0.0 (0.1)
15/01–29/01	1.1 (2.4)	1.6 (3.1)	1.6 (2.8)	1.7 (2.3)	2.8 (2.2)	18.2 (0.6)	19.5 (0.6)	0.1 (0.1)
01/02–14/02	2.8 (2.8)	3.5 (5.0)	3.4 (4.3)	3.4 (3.2)	4.5 (3.3)	18.5 (0.7)	19.8 (0.6)	0.1 (0.1)
15/02–28/02	8.0 (3.1)	9.1 (5.2)	8.9 (4.6)	8.6 (3.5)	9.6 (3.6)	19.2 (0.5)	20.1 (0.3)	0.1 (0.1)
01/03–14/03	4.9 (3.5)	6.2 (6.5)	5.9 (5.6)	5.7 (4.1)	6.9 (4.3)	18.9 (0.6)	19.9 (0.4)	0.1 (0.1)
15/03–31/03	11.8 (4.3)	13.5 (7.5)	13.0 (6.6)	12.5 (4.9)	13.4 (5.1)	20.1 (0.8)	20.6 (0.5)	0.1 (0.1)

It is interesting to observe that the average cavity air temperature was always higher than ambient temperature for each period. This occurs for both western and southern façades, but while the difference between cavity and ambient was 1 to 2 degrees in the case of the former, it always stayed below 1° C for the latter. Cavity Air velocity values were not much high, higher in February and March than in January for the South façade, while about 0.1 ms⁻¹ for the entire period for the

West façade. The indoor temperature was around 20° C for each period but in January the heat system was turned off for a few days. In the Figure 4.27 it possible to see the ambient temperature, the cavity air temperature, the indoor temperature and the vertical global solar radiation on the South side. The cavity air temperature is always higher than ambient temperature in sunny day times. In Figure 4.28 the same temperature are shown also for the West façade.

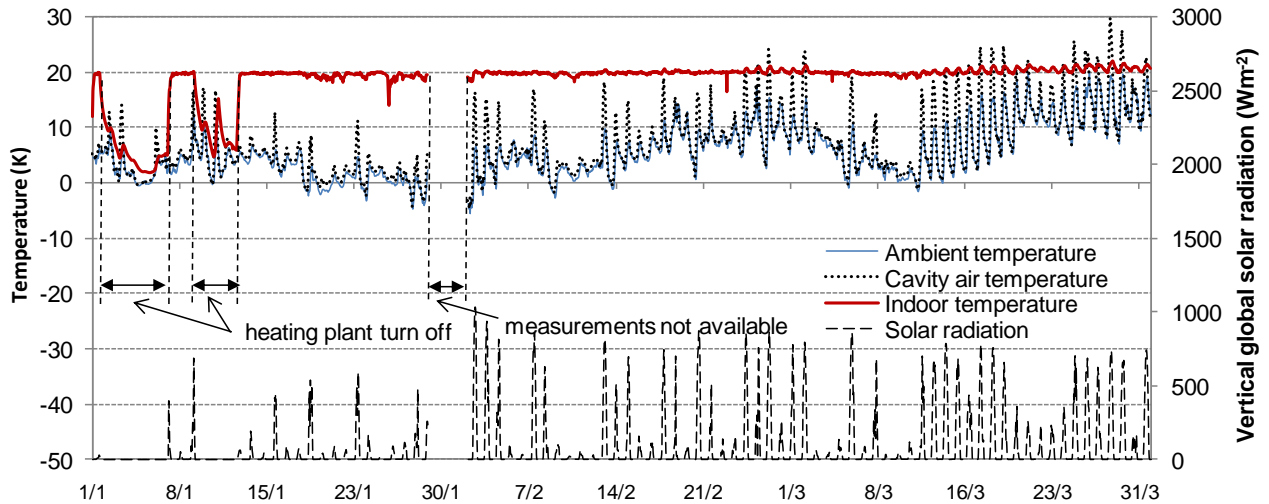


Figure 4.27: Overview of the average measurements for the winter period for the South façade

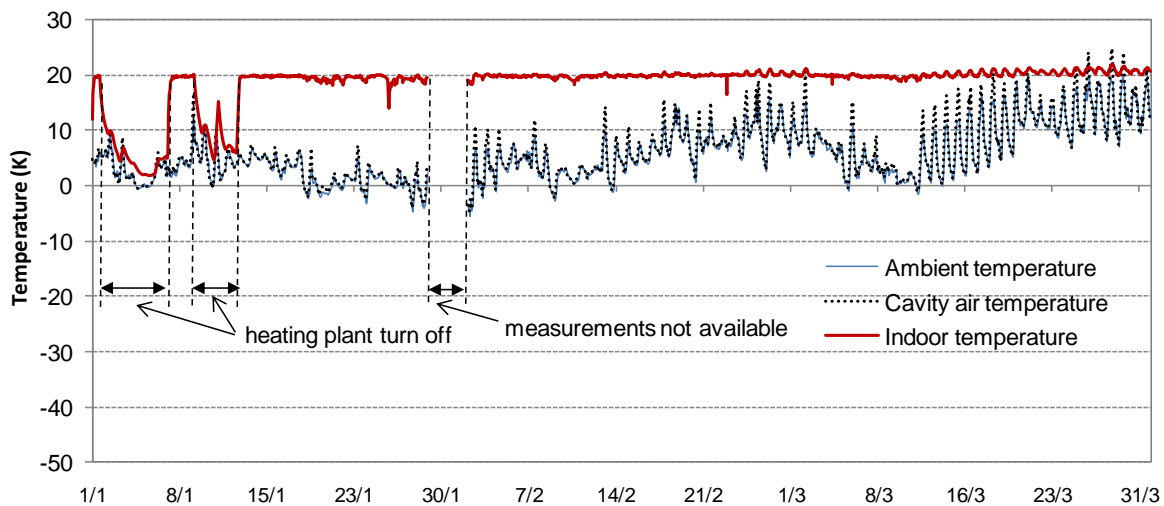


Figure 4.28: Overview of the average measurements for the winter period for the West façade

4.6.3 Cavity air velocity

There is a stronger correlation between the cavity air velocity and weather conditions such as the solar radiation and the ambient temperature. In Figure 4.29 the cavity air velocity correlated with both the temperature difference (difference between the cavity air temperature and the ambient temperature) and the vertical global solar radiation on the South side are depicted. Firstly one can notice similar trend of solar radiation and temperature difference and further for high values of solar radiation (or difference temperature) matching high values of cavity air velocity. This correlation is more evident for cavity air velocities less than 0.5 ms^{-1} while for the rest of velocities, the spread is bigger.

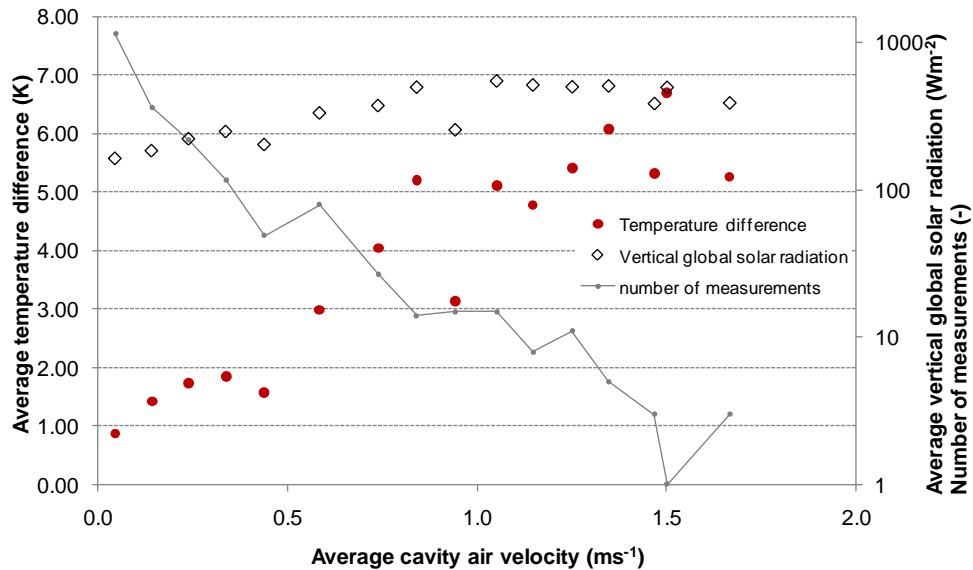


Figure 4.29: Correlation between both the cavity air velocity and the temperature difference (cavity air temperature-ambient temperature) and vertical global solar radiation for the South façade (period from January 01st to March 31st 2010).

Figures 4.30-4.32 present the temporal distribution of the ambient temperature (AT), the exterior surface temperature of external skin (T_{ce}), the cavity air temperature (T_{ac}), the interior surface temperature of internal wall (T_{wi}), the indoor temperature (T_i) correlated with cavity air velocity (CAV) and vertical global solar radiation (VGSR) for the South façade during three different weeks of the winter period analyzed.

In Figure 4.30 it possible to notice that there was one day with high solar radiation compared with other days. In particular, in the 23 January day as soon as the solar radiation exceeds 300 Wm^{-2} , the exterior surface temperature of skin façade exceeds the cavity air temperature of about 4° C . The difference between the cavity air temperature and the ambient temperature reached 11° C when the solar radiation was about 600 Wm^{-2} and the ambient temperature about 5° C . As consequence the cavity air velocity increased over 0.5 ms^{-1} but it was not influenced only by solar radiation as one may see on January 25th and 26th. In fact the cavity air velocity of those days reached values higher than 0.5 ms^{-1} also without solar radiation.

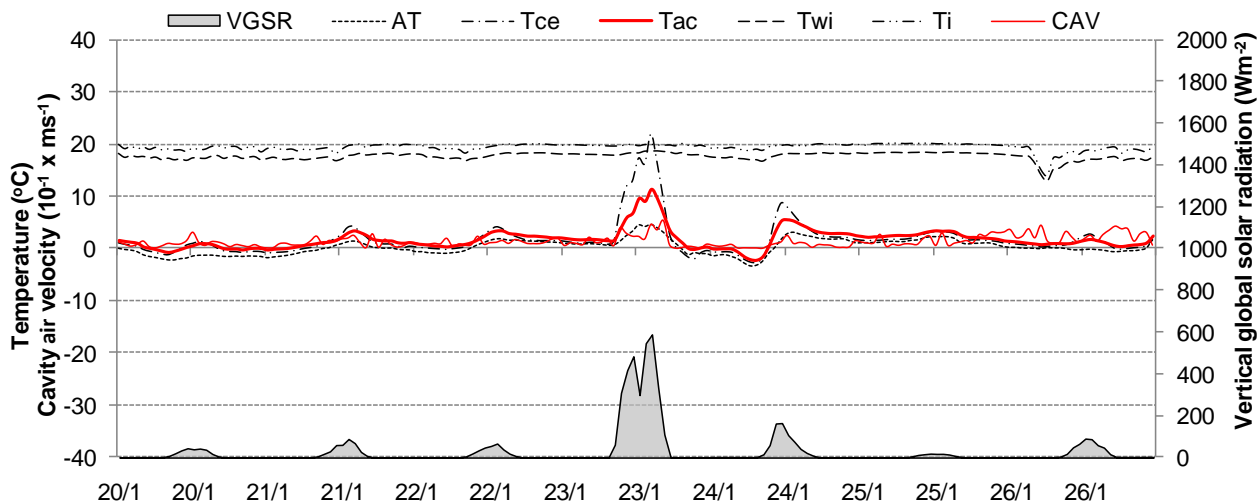


Figure 4.30: Temporal distribution of the ambient temperature (AT), the exterior surface temperature of the skin (T_{ce}), the cavity air temperature (T_{ac}), the interior surface temperature of inner wall (T_{wi}), the indoor temperature (T_i) correlated with cavity air velocity (CAV) and vertical global solar radiation ($VGSR$) for the South façade (from January 20th to January 26th 2010).

In Figure 4.31 a typical example of the influence of the wind on cavity air velocity is shown. In this figure measurements from February 03rd to February 09th 2010 are shown. There were days with high solar radiation and other days without any. The wind speed was quite low ($< 1 \text{ ms}^{-1}$) except on February 05th and 06th when it reached values above 4 ms^{-1} (the prevailing wind direction was South-West). The cavity air velocity reached values of about 1 ms^{-1} (February 07th) while vertical global solar radiation exceeded 800 Wm^{-2} . In days with high solar radiation the external surface temperature of the skin façade reached values above 35° C (February 03rd) with a difference temperature between cavity air and ambient temperature of about 10° C .

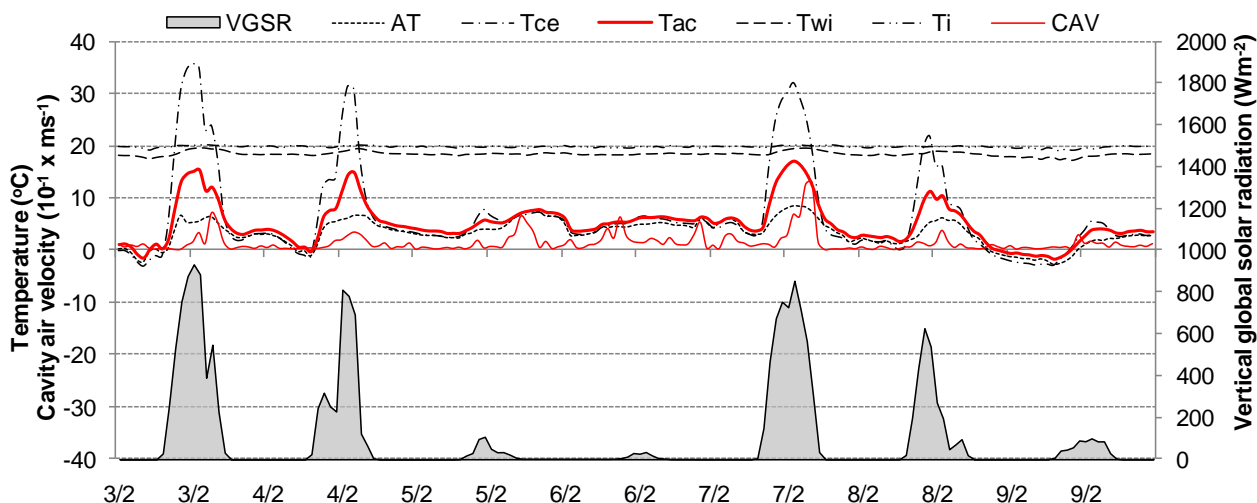


Figure 4.31: Temporal distribution of the ambient temperature (AT), the exterior surface temperature of the skin (T_{ce}), the cavity air temperature (T_{ac}), the interior surface temperature of inner wall (T_{wi}), the indoor temperature (T_i) correlated with cavity air velocity (CAV) and vertical global solar radiation ($VGSR$) for the South façade (from February 03rd to February 09th 2010).

Figure 4.32 shows the measurements from March 17th to March 23th 2010. This week was very interesting because the wind speed was mostly quite low (less than 1 ms^{-1}) from March 20th to

March 23rd. In those four days the cavity air velocity was influenced from solar radiation even if the measured vertical solar radiation was only about 200 Wm⁻².

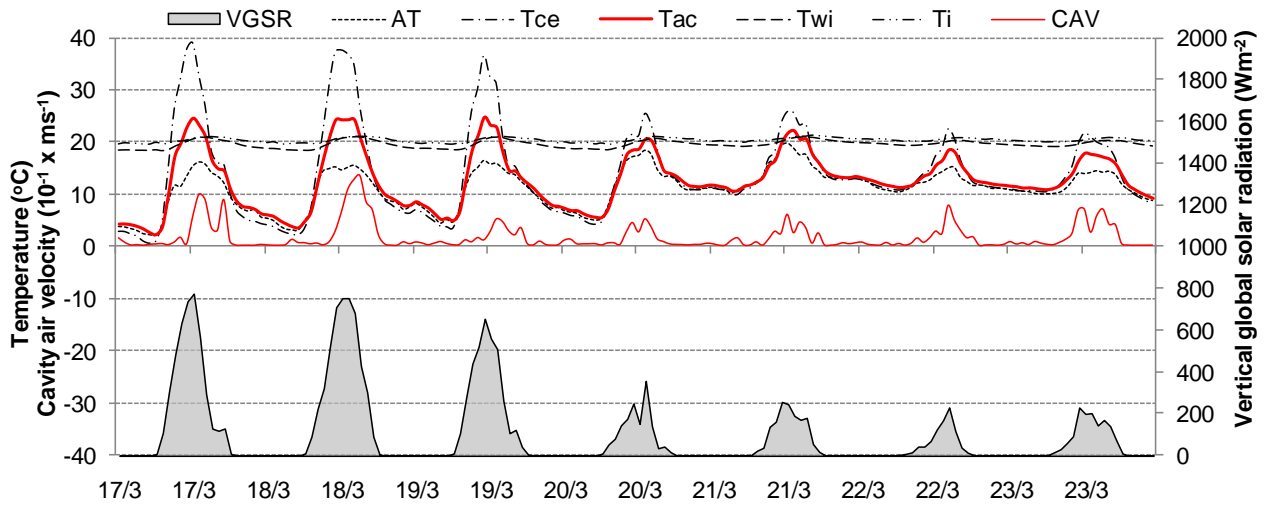


Figure 4.32: Temporal distribution of the ambient temperature (AT), the exterior surface temperature of the skin (T_{ce}), the cavity air temperature (T_{ac}), the interior surface temperature of inner wall (T_{wi}), the indoor temperature (T_i) correlated with cavity air velocity (CAV) and vertical global solar radiation (VGSR) for the South façade (from March 17th to March 23rd 2010).

4.6.4 Comparison of the heat transfer correlations with measurements

In Section 2.3 of the Chapter 2 two analytical methods for the evaluation of the convection coefficient were presented. Now we see the comparison with the measured data starting with the first method.

For this particular analysis only the western ventilated façade is considered. This consists of porcelain stoneware tile systems with bright surface finish with joints closed, air cavity of 24 cm and ventilation grills partially opened (Figure 4.33).

In this case, comparison of the Grashof (Gr_H) number and the squared Reynolds number (Re_H^2) show that the average ratio (Gr_H/Re_H^2) is of the order of 10^4 . Thus, natural convection is the dominant regime and the wide channel criterion (Equation 2.52) holds, indicating that Equations 2.65 to 2.67 can be used.

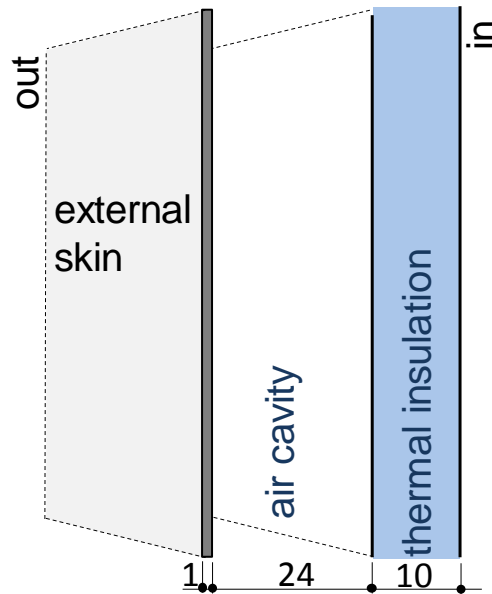


Figure 4.33: Isometric view of the considered ventilated façade (dimensions in cm)

The trend of values are presented in Figure 4.34 shows that the present measurement setup is not well suited to derive or even check relations for the convection coefficients with the proposed method (Equation 2.66 and 2.67). In spite of the considerable spread, some tendencies can be observed. The average Nusselt numbers tends to increase with increasing Reynolds number but with a considerable spread as observed from Saelens [2002]. The calculated Rayleigh numbers (Ra_H) are smaller than 10^{10} , indicating that the main flow is laminar and turbulent. The error bars represent the intervals in which 60% of almost all data are contained.

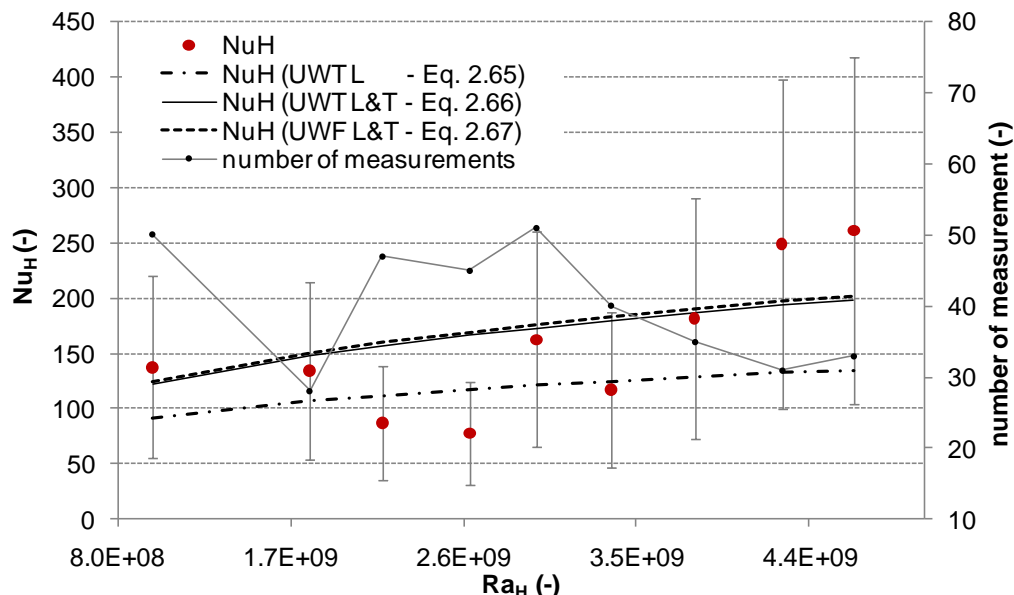


Figure 4.34: Experimentally determined interior panel Nusselt number as a function of the Rayleigh number for the naturally ventilated façade. The error bars represent the intervals in which 60% of data are contained.

The second method regards the evaluation of convective coefficient which depends from the enthalpy change of the air flowing through the cavity (Eq. 2.81 in Chapter 2).

Figure 4.35 shows the results for as a function of the average cavity air velocity. Two heat transfer coefficient correlation are depicted: the first one obtained by means experimental data and the second obtained by means Alamdari and Hammond correlation. In Figure 4.35 similar trends for both heat transfer coefficient are depicted. It is possible to notice that the former (experimental data) of two mentioned trends is always higher than the latter values (Alamdari and Hammond correlation).

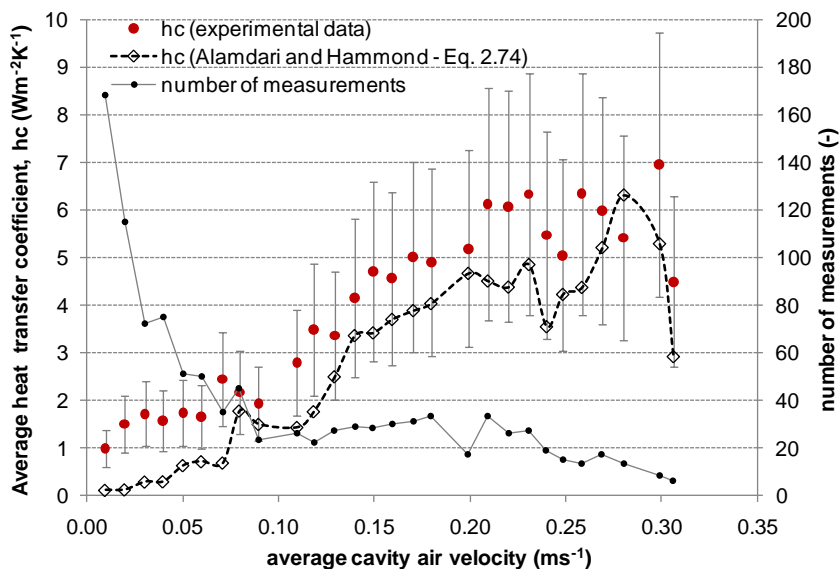


Figure 4.35: Experimentally determined heat transfer coefficient as a function of the average air cavity velocity for the naturally ventilated façade and comparison Alamdari and Hammond correlation. The error bars represent the intervals in which 40% of data are contained.

In spite of the considerable spread, some tendencies can be observed. Both average heat transfer coefficient parameters tend to increase with increasing average cavity air velocity except at some values of velocity (over of about 0.25 m s^{-1}). However a considerable spread was observed and for this test it possible to conclude that is very difficult to estimate the heat transfer coefficient for this kind of walls. The error bars represent the intervals in which 40% (except for cavity air velocity below of 0.08 ms^{-1}) of Alamdari and Hammond correlation data are contained.

For this reason in order to simulate energy balance in the air cavity the simple correlation given by Equation 2.74 will be used to estimate the convective heat transfer coefficient in the air cavity of the ventilated façade model.

4.6.5 Evaluation of U-value of the ventilated façade in the winter period

In Section 2.4 of the Chapter 2 the “average method” [ISO 9869 1994] for the evaluation of the thermal transmittance (U-value) were presented.

The mentioned above method if used in the present rainscreen ventilated skin façades, however, has a limited accuracy because the heat flux through the component is not measured. In fact it is estimated by Equation 3.04 indicated in Chapter 3, while temperature values are obtained by winter field measurements.

The rainscreen ventilated façades consists of stone cladding slab systems with bright surface finish with open joints, ventilation grills partially open and air cavity 24 cm both for the southern and the western façade.

For this specific analysis the period was considered from January 13^{trd} to February 13th 2010. In Figure 4.36 and 4.37 it possible to see a convergence to an asymptotical value of thermal

conductance evaluated through Equation 2.84 (Chapter 2) respectively for the southern and the western façade. It is interesting to observe that only after few days the C-value converges to the same value for the both façades.

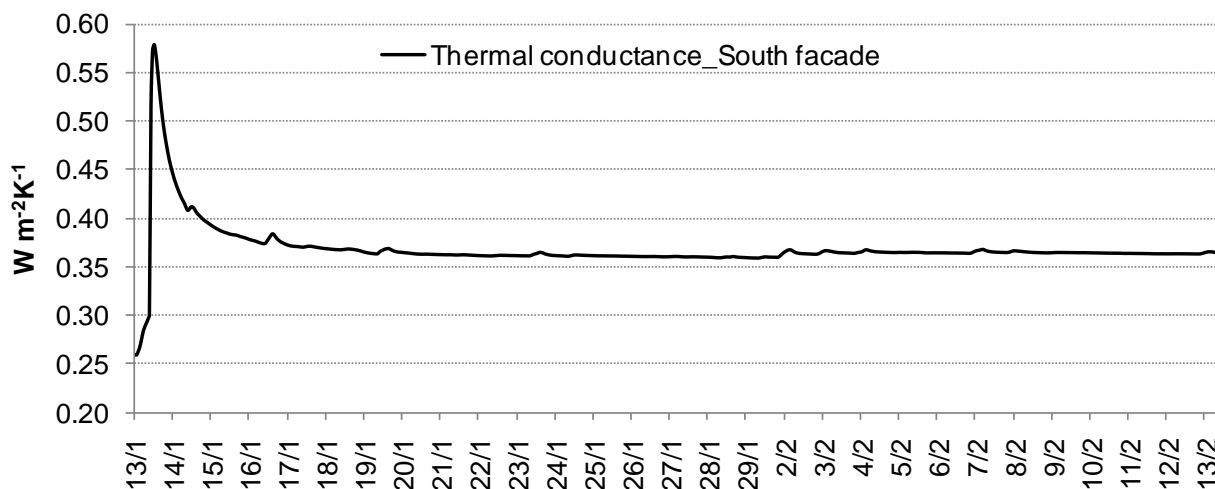


Figure 4.36: Estimation of the U-value by the average method (South façade)

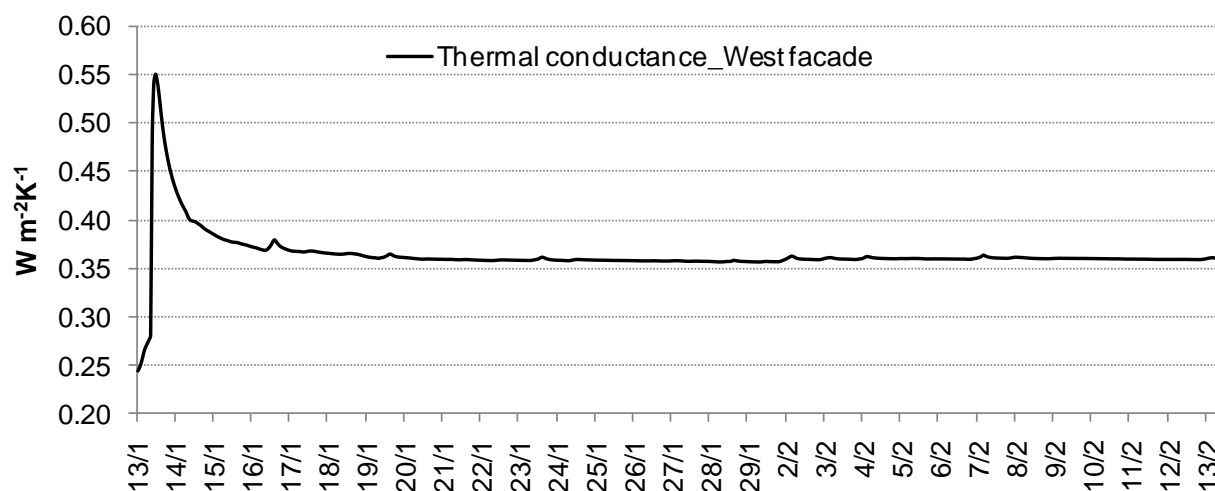


Figure 4.37: Estimation of the U-value by the average method (West façade)

It can be observed that it in the sets of data with less than 50 points the C-value presents a statistical oscillation. In particular the statistical oscillations of the southern façade C-value (Figure 4.36) are higher than the ones of the western façade (Figure 4.37).

For the regime between 100 and 400 points the estimation of the C-value of the southern façade (western façade) is ranged between 0.371 (0.368) $\text{Wm}^{-2}\text{K}^{-1}$ and 0.358 (0.357) $\text{Wm}^{-2}\text{K}^{-1}$. The difference between the two values is less than 5% as required by standard ISO 9869 [1994] and the estimation procedure converge to the estimated C-value 0.358 (0.357) $\text{Wm}^{-2}\text{K}^{-1}$.

By considering also both internal ($R_{si} = 0.13 \text{ m}^2\text{K W}^{-1}$) and external surface resistance ($R_{se} = 0.04 \text{ m}^2\text{K W}^{-1}$) the U-value for both façade is equal to the same value of $0.337 \text{ Wm}^{-2}\text{K}^{-1}$.

The air layer of the rainscreen ventilated façade in the winter period corresponds in a well-ventilated air layer in accordance to the Standard EN ISO 6946 [2007].

In Table 4.07 thermal resistances of layers of the rainscreen ventilated façade in accordance to the EN ISO 6946 [2007] are listed.

Table 4.07: Thermal resistance of layers of the rainscreen ventilated skin façade in accordance to EN ISO 6946:2007

Layers	s	λ	R
From inside to outside	(cm)	(Wm ⁻¹ K ⁻¹)	[m ² K W ⁻¹]
Internal surface resistance	-	-	0.13
Alluminium	0.2	160	1.25 x 10⁻⁵
Insulation	4,0	0,035	1.14
Alluminium	0.2	160	1.25 x 10⁻⁵
Thermal insulation	0.06	0.04	1.50
Air layer (5.3.4 - Well-ventilated air layer)	-	-	0.13

The sum of thermal resistances of layers amounts to 2.90 m²K W⁻¹ and the corresponding U-value is given by:

$$U = \frac{1}{R_T} = \frac{1}{2,90} = 0,344 \quad (\text{Wm}^{-2}\text{K}^{-1})$$

It is interesting to observe that the difference between the U-value evaluated in accordance to the Standard and that evaluated with the “average method” is only 2%. In Table 4.08 the results evaluated for two methods are indicated.

Table 4.08: Comparison between two methods to evaluate U-value

Method	U-value (Wm ⁻² K ⁻¹)
Average method (Section 2.4.1)	0.337
EN ISO 6946:2007 (Section 2.4.2)	0.334

4.7 Analysis of the local weather data (summer period)

In order to investigate the summer thermal performance of the rainscreen wall component, a series of tests were performed, during the period from July 2nd to September 17st 2010. Tests were carried out with different setup of walls (twelve patterns in Figure 4.38) concerning a different rainscreen material, a different color of the external material and a different thickness of the air gap. In addition, the influence of ventilation inside the air cavity through a series of setup concerning opened/closed joints and opened/partially opened/closed grills was evaluated. In Figure 4.38 and in Table 4.09 twelve patterns (six for each analyzed side) are shown graphically and descriptively.

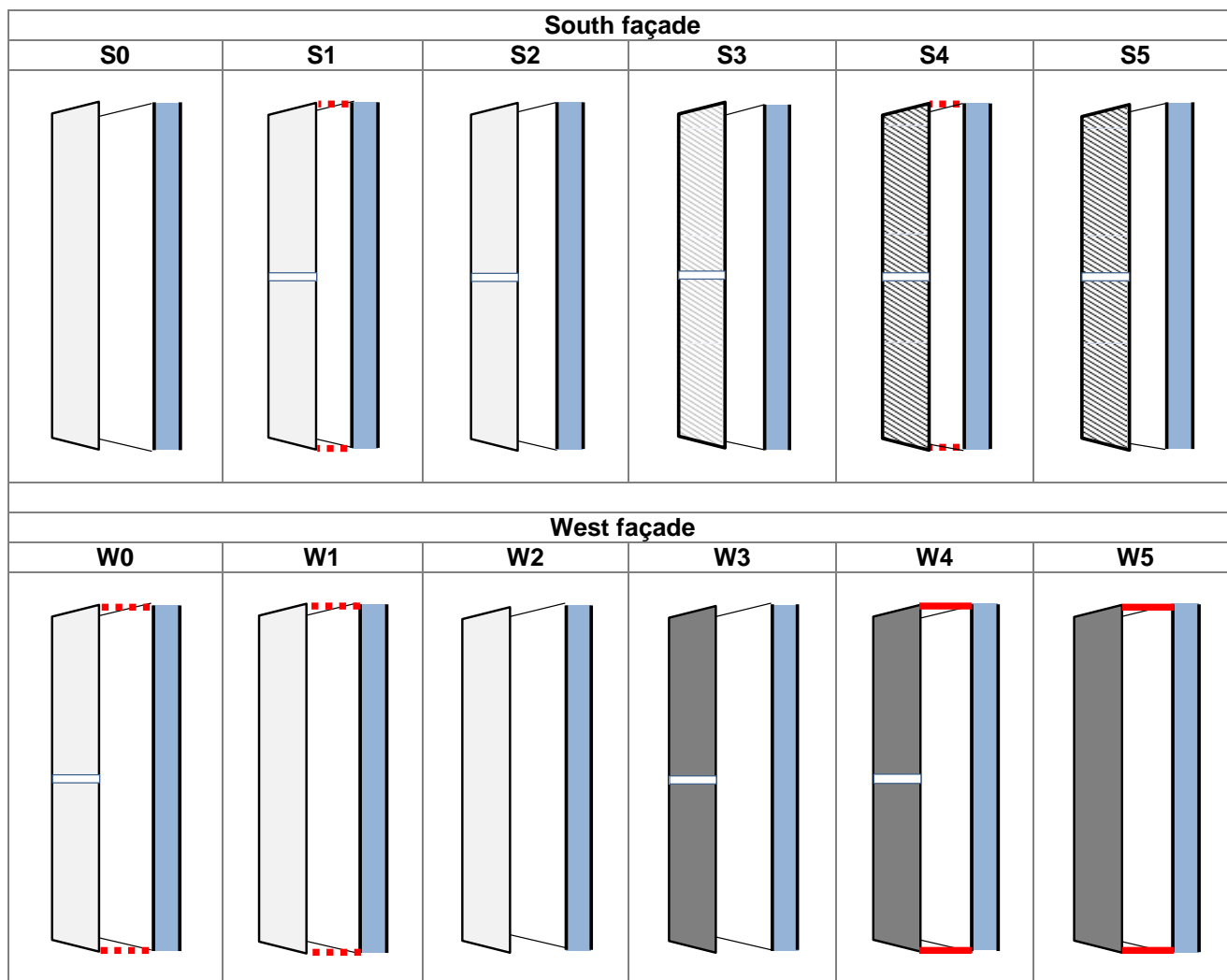


Figure 4.38: Isometric views of all patterns of the rain-screen walls

Table 4.09: Patterns for rainscreen ventilated façade on the West and South side

Pattern	Air cavity (cm)	Ventilation grills	Joints	Skin finish	Skin material	Start monitoring	End monitoring
(South façade)							
S0	24	Completely Open	close	Bright	Stone cladding	02/07/2010	04/07/2010
S1	10	Partially open	open	Bright	Stone cladding	09/07/2010	15/07/2010
S2	10	Completely open	open	Bright	Stone cladding	17/07/2010	31/07/2010
S3	10	Completely open	open	Bright	aluminium	03/08/2010	23/08/2010
S4	10	Partially open	open	dark	aluminium	26/08/2010	06/09/2010
S5	10	Completely open	open	dark	aluminium	11/09/2010	17/09/2010
(West façade)							
W0	24	Partially open	open	Bright	Stone cladding	02/07/2010	04/07/2010
W1	24	Partially open	close	Bright	Stone cladding	09/07/2010	15/07/2010
W2	24	Completely open	close	Bright	Stone cladding	17/07/2010	31/07/2010
W3	24	Completely open	open	dark	Stone cladding	03/08/2010	23/08/2010
W4	24	close	open	dark	Stone cladding	26/08/2010	06/09/2010
W5	24	close	close	dark	Stone cladding	11/09/2010	17/09/2010

As in the winter period, the measured local weather data include ambient temperature (AT) and ambient relative humidity (ARH), wind speed (WS) and direction (WD) and horizontal global solar radiation (HGSR) in the summer period. In this case the pyranometer sensor was fixed on the roof of the test cell in horizontal position.

The analysed summer period was divided into six sub-periods. The test cell has two different patterns for each sub-period: one pattern for southern façade and one for the western façade respectively. In Table 4.09 it possible to see the start and end monitoring time for each sub-period analysed.

In Figures 4.39-4.41 the overview of trends of the local climate data during the summer period tested is shown. The whole summer period goes from July 02nd to September 17th 2010 and was subdivided in six sub-periods (indicated by numbers from 0 to 5) and labelled as well in the follow figures.

The external air temperature varied between 12 and 36° C with an average ambient relative humidity of about 60% (Figure 4.39) and the horizontal global solar radiation reached values greater than 900 Wm⁻² (Figure 4.41). The wind speed was mostly low except for a few hours when it reached speeds above 14 ms⁻¹. The wind direction is quite variable, but South-East is the prevailing one (Figure 4.40).

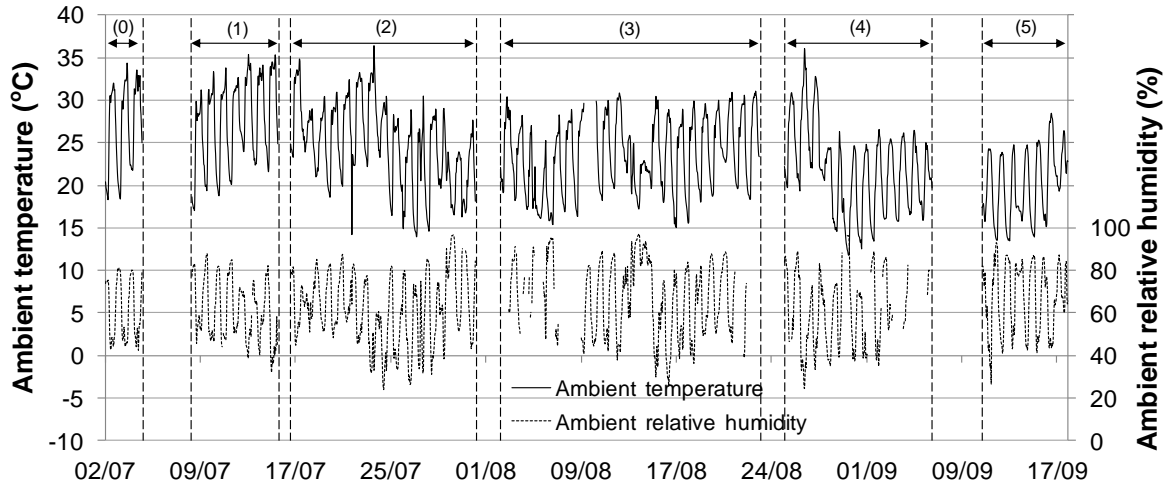


Figure 4.39: Overview of ambient temperature and ambient relative humidity for each summer sub-period (0-5) from July 2nd to September 17st 2010.

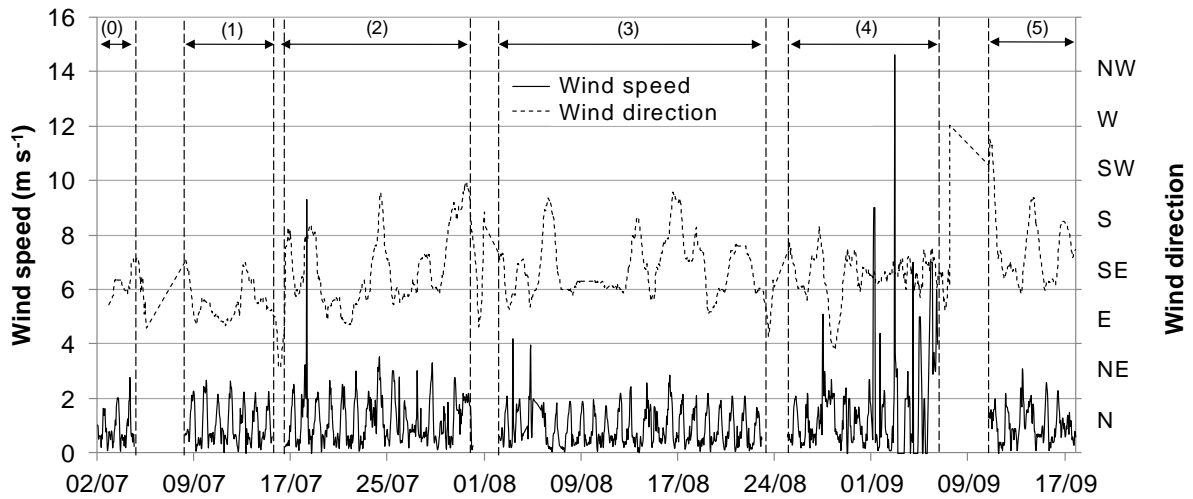


Figure 4.40: Overview of wind speed and wind direction for each summer sub-period (0-5) from July 2nd to September 17st 2010.

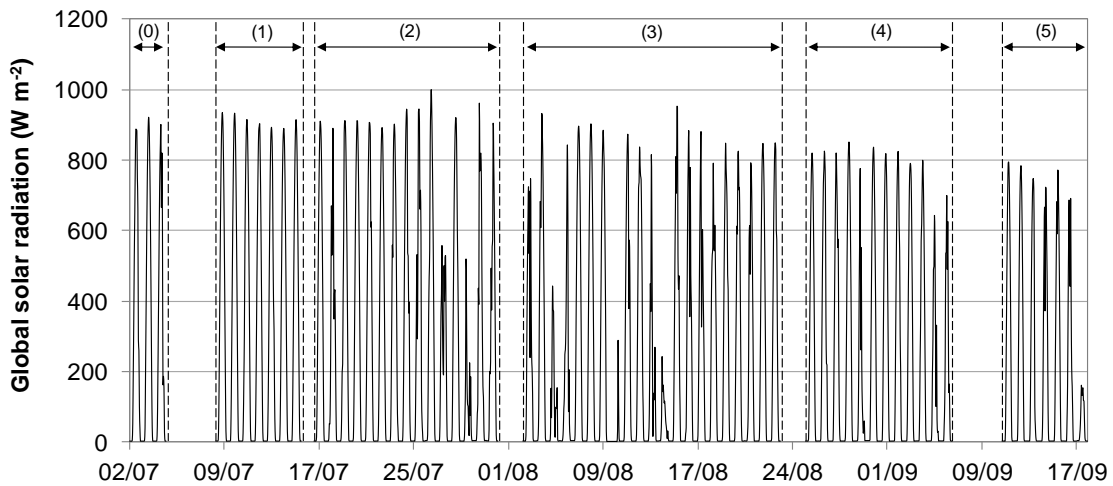


Figure 4.41: Overview of horizontal global solar radiation for each summer sub-period (0-5) from July 2nd to September 17st 2010.

In Table 4.10 the ambient temperature (AT), ambient relative humidity (ARH), horizontal global solar radiation (HGSR) and wind speed (WS) of the analyzed sub-periods are listed.

It is interesting to notice that the minimum ambient temperature of whole summer period analysed (11.7°C) was reached in the sub-period indicated with the number 4 (from August 26th to September 06th 2010) and that maximum one (36.4°C) in the sub-period indicate with number 2 (from July 17th to July 31st 2010). The average ambient relative humidity was around 60% and the maximum horizontal global solar radiation reached was about 999 Wm^{-2} in July. The average wind speed was about 1.1 ms^{-1} (value similar to average wind speed occurring in the winter period) but with unusual peak values of 9 and 14 ms^{-1} . The wind direction is quite variable but with the prevailing direction due South-East.

Table 4.10: Overview of the climate measurements of zone, maximum, minimum and average of the summer sub-period (0-5)

Sub-period		AT ($^{\circ}\text{C}$)	ARH (%)	HGSR (Wm^{-2})	WS (ms^{-1})
(sub-period 0) 02/07–04/07	max	34.3	81	921	2.8
	min	18.2	43	0	0.1
	avg	27.1	61	307	0.9
(sub-period 1) 09/07–15/07	max	35.4	88	934	2.7
	min	17.0	32	0	0.0
	avg	27.6	61	329	1.0
(sub-period 2) 17/07–31/07	max	36.4	96	999	9.3
	min	13.9	24	0	0.0
	avg	24.7	62	279	1.2
(sub-period 3) 03/08–23/08	max	31.0	97	974	4.2
	min	15.0	26	0	0.0
	avg	23.4	67	288	1.0
(sub-period 4) 26/08–06/09	max	36.1	99	850	14.6
	min	11.7	35	0	0.0
	avg	21.7	66	235	1.5
(sub-period 5) 11/09–17/09	max	28.4	93	962	3.1
	min	13.4	41	0	0.0
	avg	20.1	68	164	1.1

In Figures 4.42-4.47 polar diagrams [Davis and Ekern, 1977] for the sub-periods are shown. It is to be demonstrated that only the prevailing wind direction for the wind speed above 2 ms^{-1} are indicate in following graphs. It possible to notice that the prevailing wind direction (for wind speed above 2ms^{-1}) was very variable for each sub-period considered even if in sub-periods number 0 and number 1 the prevailing wind direction was North-East.

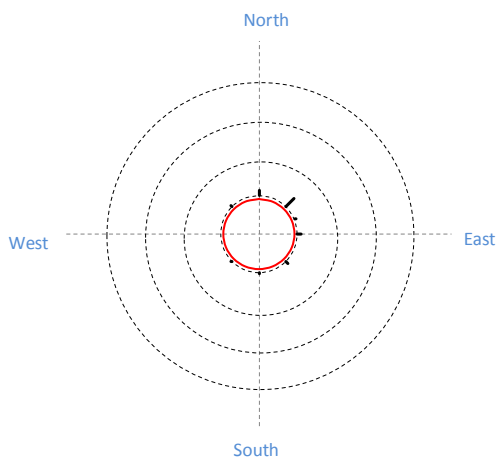


Figure 4.42: Polar diagram of the wind direction for the sub-period number 0 (from July 02nd to July 04th). Prevailing wind direction for wind speed above 2ms⁻¹.

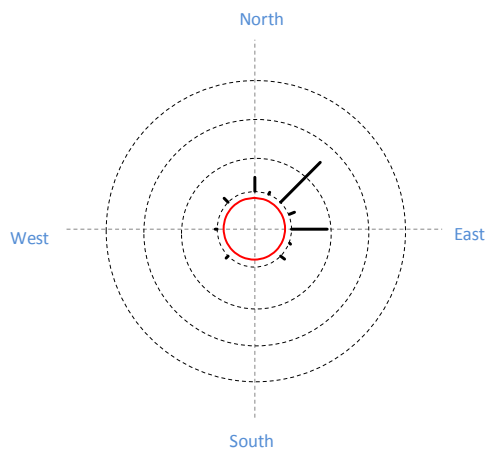


Figure 4.43: Polar diagram of the wind direction for the sub-period number 1 (from July 09th to July 15th). Prevailing wind direction for wind speed above 2ms⁻¹.

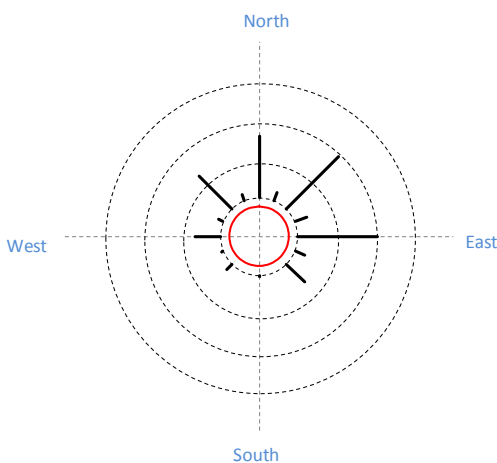


Figure 4.44: Polar diagram of the wind direction for the sub-period number 2 (from July 17th to July 31st). Prevailing wind direction for wind speed above 2ms⁻¹.

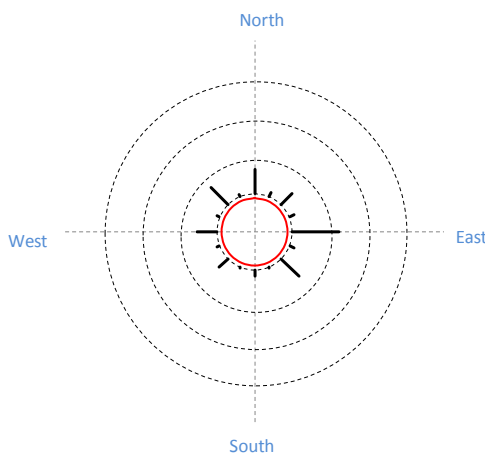


Figure 4.45: Polar diagram of the wind direction for the sub-period number 3 (from August 03rd to August 23th). Prevailing wind direction for wind speed above 2ms⁻¹.

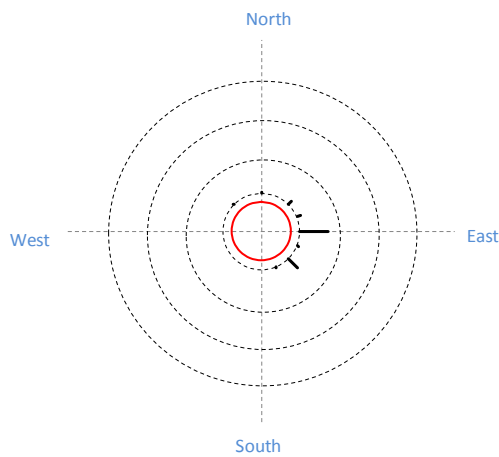


Figure 4.46: Polar diagram of the wind direction for the sub-period number 4 (from August 26th to September 06th). Prevailing wind direction for wind speed above 2ms^{-1} .

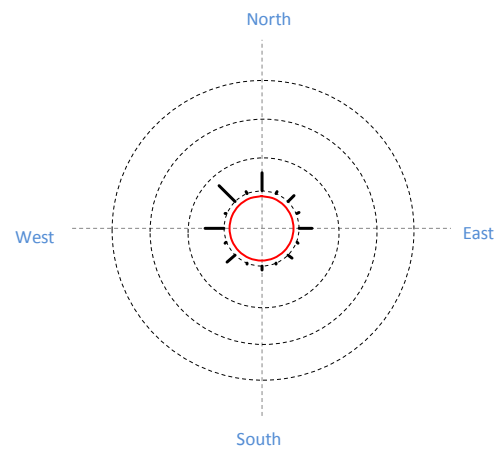
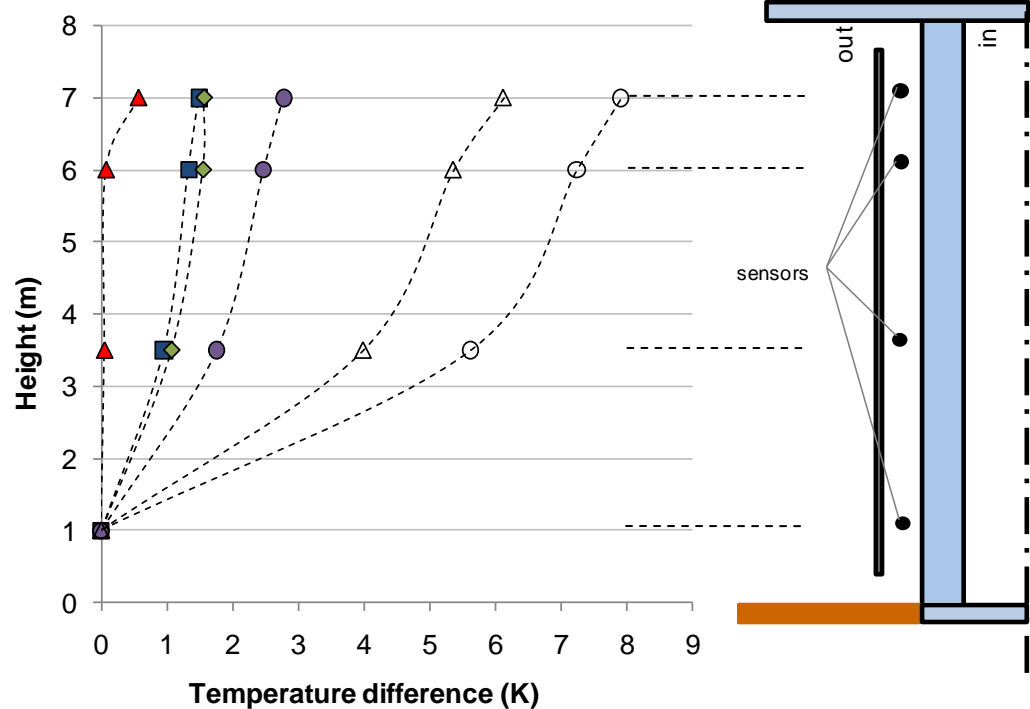


Figure 4.47: Polar diagram of the wind direction for the sub-period number 5 (from September 11th to September 17th). Prevailing wind direction for wind speed above 2ms^{-1} .

4.8 Monitoring measurements: summer period

In this section typical summer results that were extracted from the set of measurements obtained from the test building are shown. The large number of temperature sensors enables a detailed study of the temperature distribution in the main regions of the building and its envelope, which can be used in order to calculate all the heat fluxes involved in the thermal balance of the building.

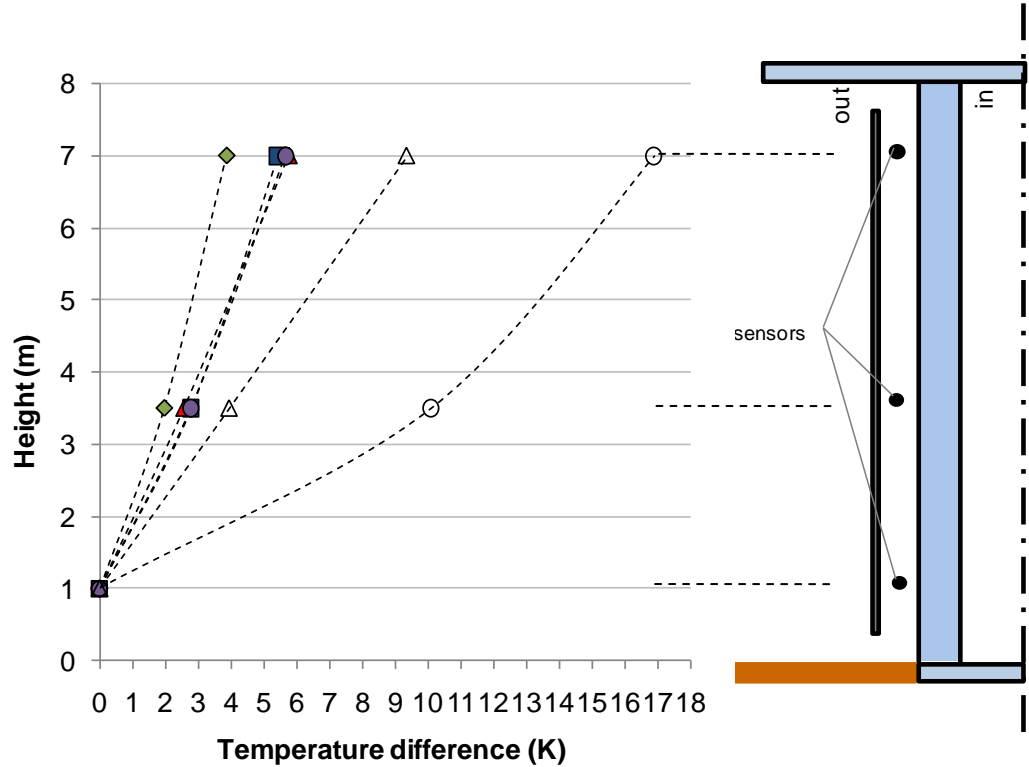
In Figures 4.48 and 4.49 the maximum vertical temperature gradient at each period monitored along the air cavity respectively of the South and of the West walls for different patterns of ventilated façades are shown. In Figures 4.48 and 4.49 the temperature difference between each sensor and the sensor placed at the lowest height are shown. For each wall configuration only the maximum temperature difference reached inside the air cavity has been indicated. In Figure 4.48 one may see that patterns S0, S1, S2 and S3 have a temperature difference ranging 3 K, while patterns S4 and S5 it is respectively reached 6 and 8 K (skin in aluminum material with a dark finish). The highest value of air velocity in the south channel (1.80ms^{-1}) was reached through the pattern S5 with a temperature difference between the sensor at the top and bottom of about 8 K.



pattern		HGSR (W m^{-2})	AT ($^{\circ}\text{C}$)	CAV (m s^{-1})	Time (dd-mm, hh:mm)
S0	--■--	845	32.9	0.7	(04-07 – 12:30)
S1	--▲--	838	28.4	0.5	(09-07 – 11:30)
S2	--◆--	909	33.6	1.1	(17-07 – 12:30)
S3	--●--	475	28.9	1.2	(21-08 – 12:30)
S4	--△--	794	23.4	1.1	(31-08 – 14:30)
S5	--○--	783	23.4	1.8	(12-09 – 13:30)

Figure 4.48: Vertical cavity air temperature of patterns (from S0 to S5) on the South façade

In the Figure 4.49 temperature differences for measurements cavity air in the western façade carried out sensors placed at difference heights are depicted. Comparing Figures 4.48 and 4.49 one can notice two different points in time when the maximum air temperature difference occurs. Despite the presence of different patterns, the measured maximum cavity air temperature difference occurs in at noon for the southern façade and in the afternoons for the western façade. The measured maximum cavity air temperature difference of patterns W4 and W5 reached 9°C and 17°C respectively. In this case the air velocity is lower than the other configurations because both the bottom ventilation grills and the top ones are completely closed. The measured highest air velocity for the western façade was about 1.4 m s^{-1} with a cavity air temperature difference of about 4°C in the configuration W2.



patternn		HGSR ($W m^{-2}$)	AT ($^{\circ}C$)	CAV ($m s^{-1}$)	Time (dd-mm, hh:mm)
W0	--■--	362	34.3	0.1	(03-07 – 18:30)
W1	--▲--	345	35.3	0.4	(15-07 – 18:30)
W2	--◆--	329	27.6	1.4	(31-07 – 18:30)
W3	--●--	132	27.7	0.8	(08-08 – 19:30)
W4	--△--	381	24.0	0.1	(01-09 – 17:30)
W5	--○--	299	24.0	0.1	(14-09 – 17:30)

Figure 4.49: Vertical cavity air temperature of patterns (from W0 to W5) on the West façade

In Figures 4.50 and 4.51 the trend of the hourly values of the measured wall temperatures are shown. These data present the variation of the outside wall temperature, of the cavity air temperature and of the inside wall temperatures during the central daily hours of a typical summer day (July 13rd 2010) of the monitored period for two different patterns S2 and W2. The pattern S2 (southern side) consists of porcelain stoneware tile systems with bright surface finish with joints opened and the ventilation grills partially opened (50% of the total area) and the width of air cavity was 10 cm. Besides, pattern W2 (western side) consists of a porcelain stoneware tile systems with bright surface finish with joints closed and the ventilation grills partially opened, the width of air cavity was 24 cm. By analyzing the data shown in Figures 4.50 and 4.51 it is evident that during the summer the role of the outside layer is to absorb the solar radiation in order to increase the wall temperature of the cavity: this value influences the mean cavity air velocity due to buoyancy effects. The cavity air velocity is related also to the wind velocity so the final value of the air flow rate through the cavity is obtained as the combined effect of the wind and the solar radiation which changes the wall temperature of the cavity.

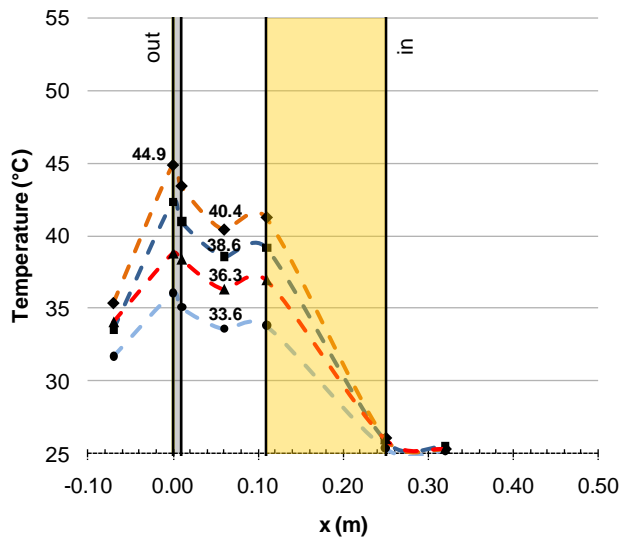


Figure 4.50: Temperature trend in the S2 patterns for a sunny hot day (13/07/2010 - South façade)

	HGSR ($W m^{-2}$)	WS ($m s^{-1}$)	CAV ($m s^{-1}$)	Time (hh:mm)
●	692	1.6	0.4	10:30
■	876	1.4	0.6	12:30
◆	864	1.1	0.6	14:30
▲	551	2.1	0.2	16:30

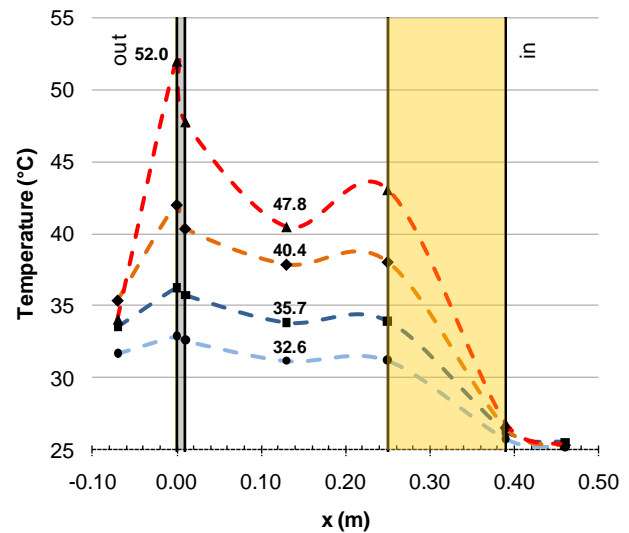


Figure 4.51: Temperature trend in the W2 patterns for a sunny hot day (13/07/2010 - West façade)

	HGSR ($W m^{-2}$)	WS ($m s^{-1}$)	CAV ($m s^{-1}$)	Time (hh:mm)
●	692	1.6	0.1	10:30
■	876	1.4	0.1	12:30
◆	864	1.1	0.2	14:30
▲	551	2.1	0.2	16:30

Comparing Figures 4.50 and 4.51 it can be noticed that the maximum temperatures inside the two walls were reached at two different moments in time. The air cavity and exterior surface rainscreen temperature of the western façade reached 48° C and 52° C respectively (16:30) while these of the southern façade reached 40° C and 45° C respectively (14:30). It is interesting to see that the above mentioned maximum temperatures are reached at different times and with different ambient temperature and solar radiation (35.4° C and 864 Wm^{-2} for the South façade and 34.1° C and 551 Wm^{-2} for the West façade respectively). The measured air velocities in channels (CAV) are significantly different because of the different cavity widths. One may see also that the western wall was more thermally stressed than the southern one and the temperature gradients in the walls were markedly different. In addition, the temperature difference between two measurements was larger for the western orientation. In other words, the thermal flux from the outer wall facing south is lower than the one for the western. In spite of the warm day selected, the maximum air velocity in the cavity on the southern façade reached 0.6 ms^{-1} while in the West façade was only 0.2 ms^{-1} probably due to the partially opened ventilation grills. The trend of inside wall temperatures was very similar at 14:30. In fact, the cavity air temperatures were similar, while the exterior surface temperatures of skins were different for 3° C (42° C for the West façade and 45° C for South façade respectively). Conversely at 16:30 there was a difference of about 10 K for the air cavity and about 8 K for the exterior surface (34° C on the south and 52° C on the West respectively).

In Figures 4.52 and 4.53 respectively patterns W5 on the West façade and S0 on the South façade are depicted. The pattern W5 consists in porcelain stoneware tile systems with dark in color with joints closed and grills ventilation were completely closed and the thickness of air cavity was 24 cm. Besides, the pattern S0 consists in porcelain stoneware tile systems with light in color with joints closed and grills ventilation were completely opened and the thickness of air cavity was 24 cm.

In both models it is possible to notice a vertical temperature gradient inside the wall with different values of temperature, especially for cavity air temperature: if the maximum value was recorded at 17:30 on the West façade, while that on the South side was recorded at 12:30. The indoor

temperature of the test cell was different for the two patterns: if W5 was maintained below 25° C, while in the other pattern S0 was free to float because in this small period the thermal plant was turned off. As the pattern W5 every opening was closed, the cavity air temperature reached higher values than the S0 pattern, despite the difference for the ambient temperature. In addition, the exterior skin temperature was very high due to its dark colour. The surface temperature of rainscreen W5 pattern of external dark pane has reached about 57° C while that of the inner pane appears to be higher. It is assumed that this fact is due to the quite inertia of cover plate and delayed thermal effects of solar radiation. Another interesting aspect is the increase in cavity air temperature than ambient one. If cavity air temperature of pattern W5 there was an increase of about 20° C while in the pattern S0, the increase was only 3° C. It may also notice that every temperature magnitude of the cavity air temperature were very different for the two patterns: temperature magnitudes of pattern W-5 were between 5° and 9° C, while those ones of the pattern S0 were between 1° and 2° C.

Air cavity velocities of the pattern W5 were quite low compared to those ones of pattern S0. There being no openings in the pattern W5 is assumed that the measured velocity of the sensor relates to the only buoyancy effects.

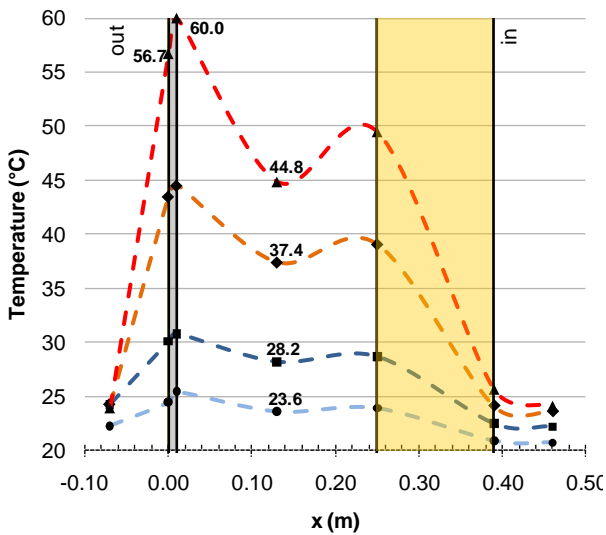


Figure 4.52: Temperature trend in the W5 patterns for a sunny hot day (11/09/2010 - West façade)

	HGSR (W m ⁻²)	WS (m s ⁻¹)	CAV (m s ⁻¹)	Time (hh:mm)
●	706	1.6	0.0	11:30
■	793	2.0	0.1	13:30
◆	642	1.3	0.2	15:30
▲	321	0.8	0.2	17:30

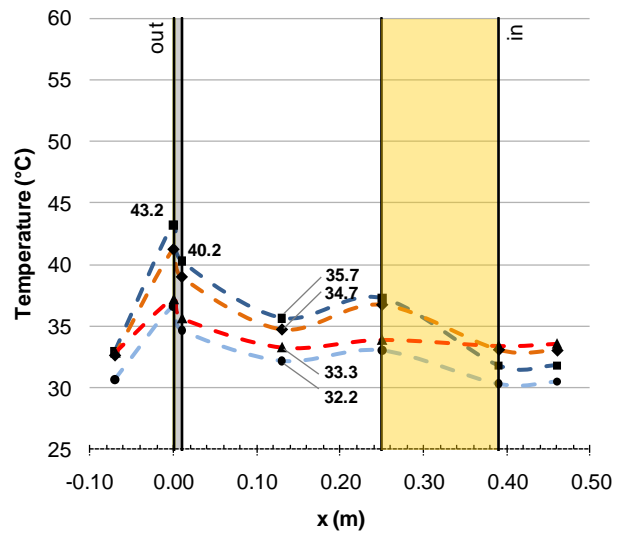


Figure 4.53: Temperature trend in the S0 patterns for a sunny hot day (04/07/2010 - South façade)

	HGSR (W m ⁻²)	WS (m s ⁻¹)	CAV (m s ⁻¹)	Time (hh:mm)
●	650	1.2	0.6	10:30
■	845	1.0	0.7	12:30
◆	664	2.0	0.6	14:30
▲	609	1.6	0.7	16:30

In Figures 4.54 and 4.60 respectively patterns W3 on the West façade and S4 on the South façade are depicted. The pattern W3 consists in porcelain stoneware tile systems with dark in color with joints opened and grills ventilation were completely opened and the thickness of air cavity was 24 cm. Besides, the pattern S4 consists in aluminum slab systems with dark in color with joints opened and grills ventilation were partially opened and the thickness of air cavity was 10 cm. In this case, as previous analyzed patterns, it is possible to notice a vertical temperature gradient inside the wall with different values temperature, especially for cavity air temperature. As both exterior skin patterns was dark in colour, surface temperature of them respectively reached about 52° C for the W3 pattern and 57° C for the S4 pattern as the previous pattern W5.

Also in the W3 pattern the inner temperature of external pane was lower than that outer one. In the S4 pattern the thickness of exterior aluminium skin was very low (about 0.5 mm) and as consequence also its thermal inertia was low also.

Unlike the previous, it's very interesting the increasing of the cavity air temperature comparing with the ambient temperature. If cavity air temperature of pattern W3 there was an increase of about 6° C while in the pattern S4, the increase was about 10° C.

The measured air velocities in channels are quite different; probably due at the different thickness of the relative cavities and to different internal cavity temperatures.

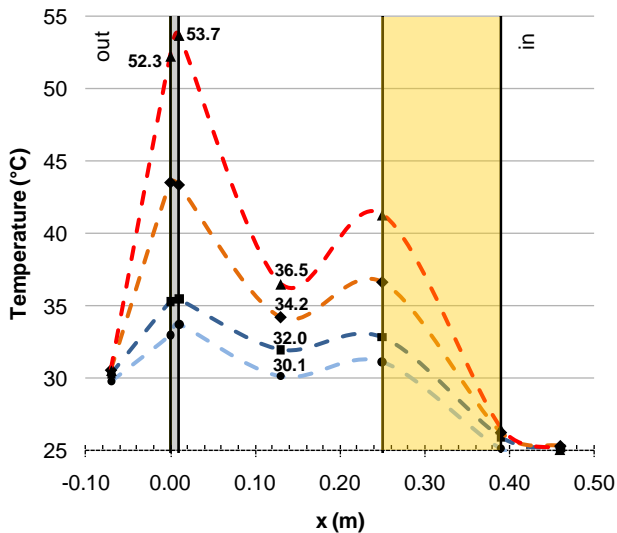


Figure 4.54: Temperature trend in the W3 patterns for a sunny hot day (23/08/2010 - West façade)

	HGSR (W m ⁻²)	WS (m s ⁻¹)	CAV (m s ⁻¹)	Time (hh:mm)
●	751	1.03	0.16	11:30
■	848	1.68	0.62	13:30
◆	599	1.3	0.68	15:30
▲	346	1.48	0.91	17:30

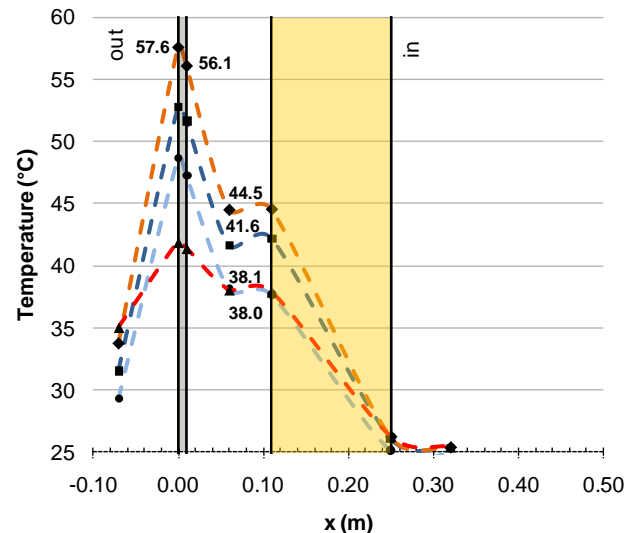


Figure 4.60: Temperature trend in the S4 patterns for a sunny hot day (27/08/2010 - South façade)

	HGSR (W m ⁻²)	WS (m s ⁻¹)	CAV (m s ⁻¹)	Time (hh:mm)
●	607	0.7	0.79	10:30
■	772	1.8	1.23	12:30
◆	793	2.2	0.95	14:30
▲	354	0.8	0.38	16:30

4.9 Analysis of measurements of rainscreen ventilated skin façades in summer period

In this section will be analyzed in details distribution of the measured temperatures and cavity air velocity into walls for every pattern.

In Table 4.11 and 4.12 the average hour measurements (obtained through mean arithmetic) of all sensors for the summer analyzed sub-period (from 0 to 5) both for the South and West façade are quoted. Starting from right to left it possible to see: the ambient temperature (AT), the exterior surface temperature of external skin (T_{ce}), the interior surface temperature of exterior skin (T_{ci}), the cavity air temperature (T_{ac}), the exterior surface temperature of internal wall (T_{we}), the interior surface temperature of internal wall (T_{wi}), the indoor temperature (T_i) and finally the cavity air velocity (CAV).

It is interesting to see that the average cavity air temperature was always higher than ambient temperature for each pattern, especially for patterns with external skin with a dark in color (respectively S4 and S5 for the South façade and W3, W4 and W5 for the West façade).

The average summer cavity air velocity values were higher than winter cavity air velocity except for patterns W4 and W5 (basically because grills ventilation were completely closed). The highest average cavity air velocity was reached for patterns respectively S1 and S5 for the South façade and W1 for the West façade. The average indoor temperature was been around 24° C for each period except in the sub-period indicate with number 0 (see Table 4.10) because the thermal plant system was turned off.

Table 4.11: Overview of the average measurements for the analyzed patterns for the South façade (st.dev.)

Pattern	AT (°C)	T _{ce} (°C)	T _{ci} (°C)	T _{ac} (°C)	T _{we} (°C)	T _{wi} (°C)	T _i (°C)	CAV (ms ⁻¹)
S0 (02/07–04/07)	27.1 (5.0)	29.2 (8.0)	28.3 (7.1)	27.3 (5.4)	27.9 (6.0)	30.5 (2.3)	30.8 (2.2)	0.4 (0.2)
S1 (09/07–15/07)	27.6 (5.0)	29.2 (7.6)	28.7 (7.3)	28.2 (6.1)	28.2 (6.1)	24.9 (1.0)	24.8 (0.7)	0.7 (0.2)
S2 (17/07–31/07)	24.7 (4.9)	26.2 (6.9)	25.7 (6.7)	25.3 (5.6)	25.5 (6.1)	24.2 (1.6)	24.2 (1.4)	0.5 (0.3)
S3 (03/08–23/08)	23.4 (4.3)	26.1 (7.4)	25.7 (6.9)	24.6 (5.3)	24.6 (5.3)	23.8 (1.5)	23.9 (1.4)	0.5 (0.4)
S4 (26/08–06/09)	21.7 (5.1)	27.7 (13)	27.2 (12.4)	24.7 (7.9)	24.7 (8.1)	23.2 (2.0)	23.2 (1.9)	0.4 (0.4)
S5 (11/09–17/09)	20.1 (4)	26.4 (13.2)	25.8 (12.4)	22.8 (6.9)	22.9 (7.1)	22.3 (2.0)	22.3 (1.9)	0.7 (0.6)

Table 4.12: Overview of the average measurements for the analyzed patterns for the West façade (st.dev.)

Sub-periods	AT (°C)	T _{ce} (°C)	T _{ci} (°C)	T _{ac} (°C)	T _{we} (°C)	T _{wi} (°C)	T _i (°C)	CAV (ms ⁻¹)
W0 (02/07–04/07)	27.1 (5.0)	30.0 (9.4)	29.3 (8.3)	27.6 (5.9)	28.5 (6.4)	31.0 (2.3)	30.8 (2.2)	0.2 (0.2)
W1 (09/07–15/07)	27.6 (5.0)	31.6 (11.1)	30.8 (9.8)	28.6 (6.8)	29.4 (7.6)	25.3 (1.1)	24.8 (0.7)	0.6 (0.1)
W2 (17/07–31/07)	24.7 (4.9)	27.8 (9.7)	27.0 (8.4)	24.9 (5.4)	25.6 (6.0)	24.6 (1.7)	24.2 (1.4)	0.3 (0.3)
W3 (03/08–23/08)	23.4 (4.3)	27.3 (10.5)	27.5 (10.5)	24.1 (5.4)	25.2 (6.6)	24.2 (1.6)	23.9 (1.4)	0.3 (0.3)
W4 (26/08–06/09)	21.7 (5.1)	25.9 (11.4)	26.6 (12.3)	24.3 (8.4)	25.1 (9.1)	23.6 (2.2)	23.2 (1.9)	0.0 (0.0)
W5 (11/09–17/09)	20.1 (4.0)	24.1 (10.9)	24.6 (11.7)	22.9 (8.3)	23.6 (9.0)	22.6 (2.1)	22.3 (1.9)	0.0 (0.0)

In Figures 4.56 and 4.57 the ambient temperature, the cavity air temperature, the indoor temperature and the horizontal global solar radiation for the South and West façade are depicted. It is interesting to notice that the trend of cavity air temperature was always above the ambient temperature in sunny day times especially in sub-periods labeled 4 and 5. In fact in those periods patterns consists in external skin with a dark in color and as consequence temperatures through walls were highest than rest of other patterns.

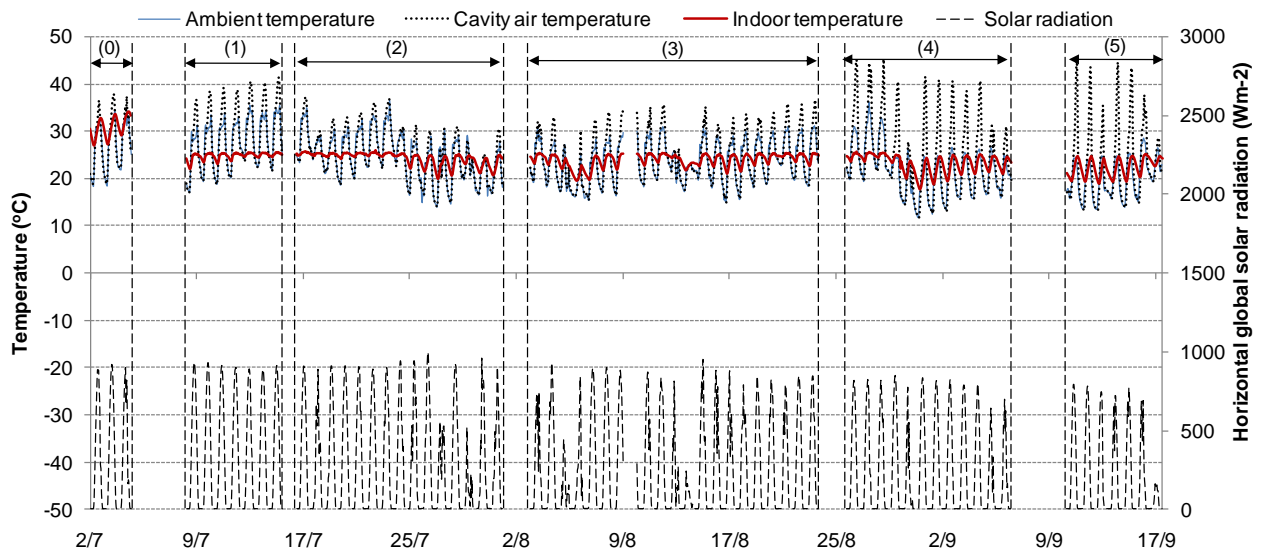


Figure 4.56: Overview of the average measurements for the summer sub-periods (0-5) for the South façade

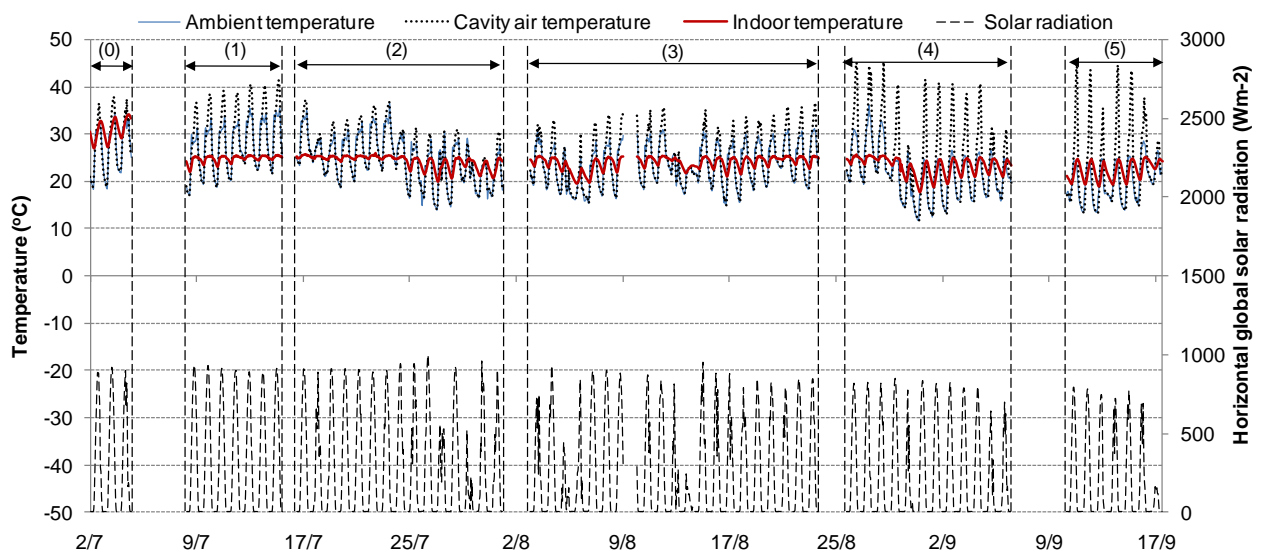


Figure 4.57: Overview of the average measurements for the summer sub-periods (0-5) for the West façade

4.9.1 Influence of the local weather data on the cavity air velocity

As the winter period, there was a stronger correlation between the cavity air velocity and climate forces for example as the solar radiation and the ambient temperature also in this analyzed summer period. In order to study the influence of climate forces on the cavity air velocity a series of comparison between different patterns were been considered.

First of all it will see the influence of the grills ventilation through the comparison between patterns with grills ventilation partially opened and other pattern with grills ventilation completely opened. For example patterns S1 and S2, consisting in an external skin in stone cladding and also S4 and S5 consisting in an external skin in aluminum, both for the South façade. The comparison of patterns respectively between W1 and W2 and between W3 and W5 (orientated on the West side) were considered as well.

In the Figure 4.58 the comparison between the average air cavity velocities of patterns S1 and S2 (both for the South façade) correlated with the average temperature differences (obtained from difference between the cavity air temperature and the ambient temperature) are shown. The

pattern S1 consists in stone cladding slab systems with light in color with joints opened and grills ventilation were partially opened and the thickness of air cavity was 10 cm, while the pattern S2 is the same setup of pattern S1 but presents grills ventilation completely opened. The absence of grills ventilation in the pattern S2 increases the cavity air velocity than the pattern S1. In Figure 4.58 it possible to notice differences was correlated with temperature difference. For high values of the ambient temperature there were high values of the air cavity velocities. The values of cavity air velocity of pattern S2 (with grills ventilation) were higher than the relative values of pattern S1 (without grills ventilation). The same aspects may be seeing also in Figure 4.59 concerning a comparison between patterns S4 and S5. Those mentioned patterns consist in the same configuration setup respectively of patterns S1 and S2 but with different external skin. The external skin of patterns S4 and S5 consists in aluminum slab systems with dark in color. The cavity air velocity of the configuration without grills ventilation (S5) was higher than the configuration with grills ventilation (S4).

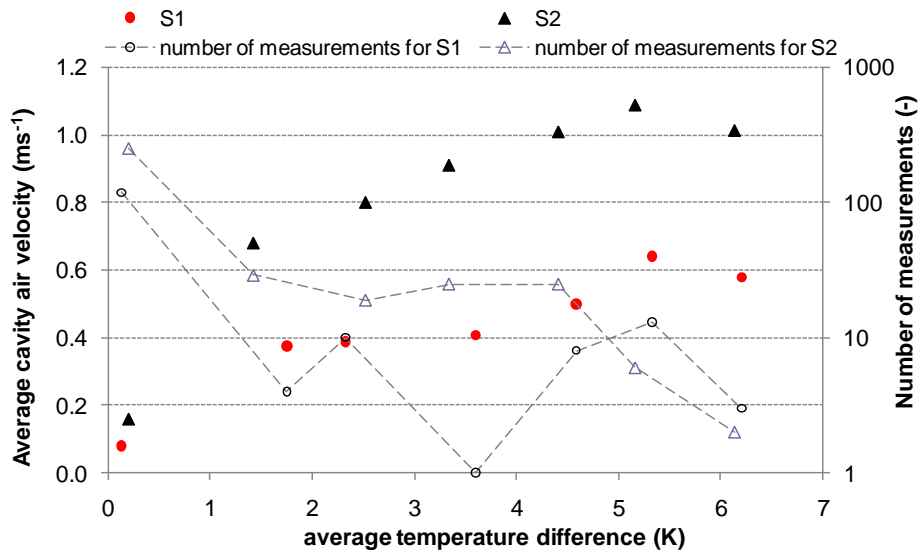


Figure 4.58: Comparison between the cavity air velocity of patterns S1 and S2 correlated with temperature difference (cavity air temperature-ambient temperature)

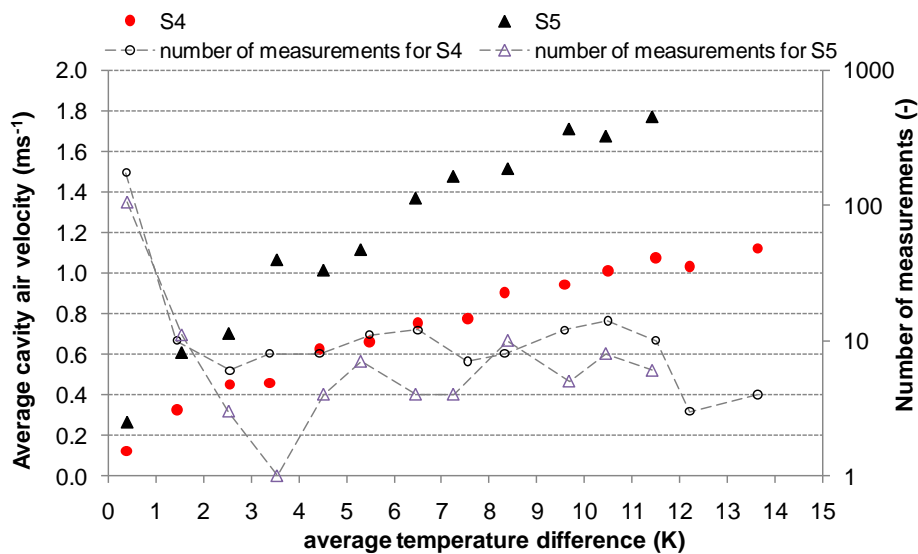


Figure 4.59: Comparison between the cavity air velocity of patterns S4 and S5 correlated with temperature difference (cavity air temperature-ambient temperature)

In order to define the influence of grills on the West façade the comparison between patterns W1 and W2 was studied. The pattern W1 consists in stone cladding slab systems with light in color with joints closed and grills ventilation were partially opened and the thickness of air cavity was 24 cm, while the pattern W2 was the same setup of pattern W1 but presents grills ventilation completely opened. In Figure 4.60 it possible to notice the different trend of air cavity velocities of two patterns. As previous patterns on the South façade also in this case the cavity air velocity of the pattern without grills (W2) was quite higher than the pattern with grills (W1). The presence of the grills ventilation both on the South façade and West façade decreases the cavity air velocity about of 50%.

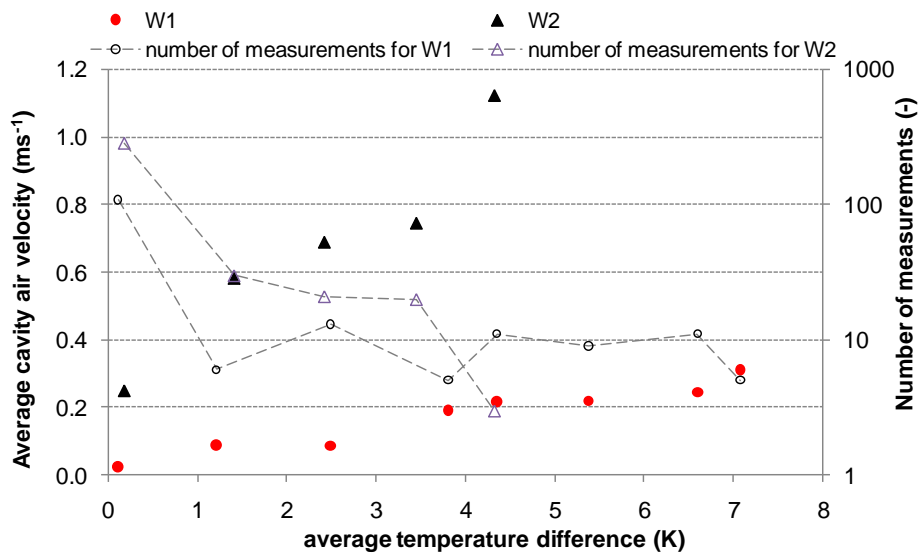


Figure 4.60: Comparison between the cavity air velocity of patterns W1 and W2 correlated with temperature difference (cavity air temperature-ambient temperature)

Another interesting comparison is that between patterns W3 and W5 (both orientated on the West side). The pattern W3 consists in stone cladding slab systems with dark in color with joints opened and grills ventilation were completely opened and the thickness of air cavity was 24 cm, while the pattern W4 was the same setup of pattern W1 but presents grills ventilation completely closed.

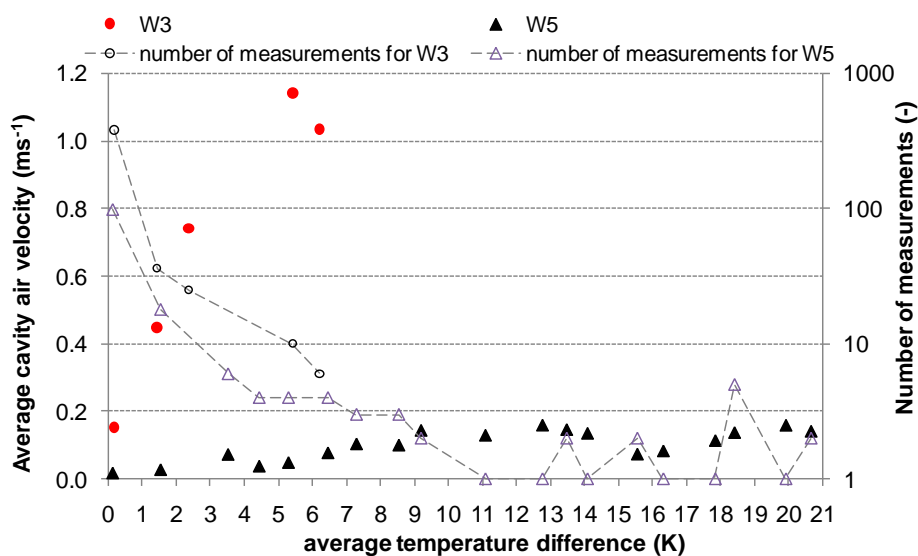


Figure 4.61: Comparison between the cavity air velocity of patterns W3 and W5 correlated with temperature difference (cavity air temperature-ambient temperature)

In this case the absence of the external ventilation through the wind was very interesting because it possible to see the buoyancy forces effects. The air cavity velocities (Figure 4.61) were lower than 0.2 ms^{-1} for the pattern with grills ventilation completely closed while the pattern with grills ventilation completely opened presented values much high.

4.9.2 Influence of the thickness of the air cavity

In addition to the influence of local weather data, the cavity air velocity of the ventilated façade is strongly correlated also with the thickness of the channel. Figure 4.62 presents a comparison between air cavity velocities of patterns S1 and W1. Patterns S1 and W1 basically were consisted in similar configuration setup but with different air cavity thickness. If the pattern on the South side (S1) presents a thickness of 10 cm while the pattern on the West side (W1) presents a thickness of 24 cm. In Figure 4.62 it possible to notice the different magnitude of two cavity air velocity trend. Two trends were shifted cause the different orientation.

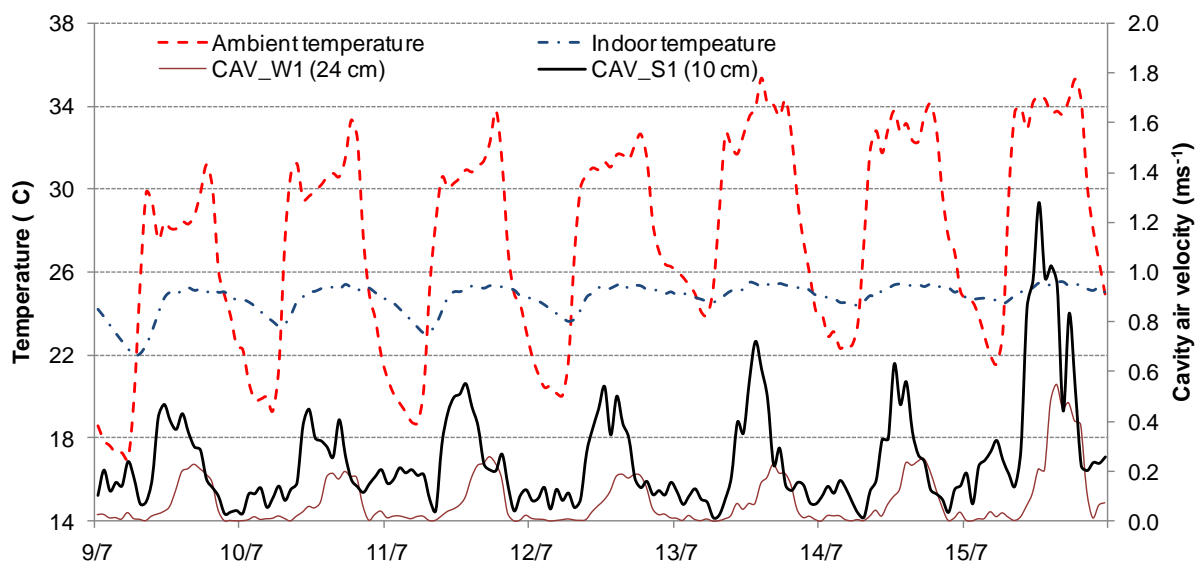


Figure 4.62: Comparison between the cavity air velocity of the pattern S1 (South façade) and cavity air velocity of the pattern W1 (West façade). Period from July 09th to July 15th 2010.

4.9.3 Influence of patterns setup on measured parameters

Figures 4.63-4.75 present temporal distributions of ambient temperature (AT), exterior surface temperature of the skin (T_{ce}), cavity air temperature (T_{ac}), interior surface temperature of inner wall (T_{wi}), indoor temperature (T_i) correlated with cavity air velocity (CAV) and horizontal global solar radiation (HGSR) for each pattern of ventilated façades during six sub-periods for the summer period. The indoor temperature was kept below 25°C for the whole summer period except the first sub-period (from July 02nd to July 04th 2010) as consequence the thermal plant was turned off.

The first sub-period (from July 02nd to July 04th 2010) was characterized by only three monitored days and it was smaller than the other sub-periods. The average ambient temperature was 27°C with the maximum and minimum values of 34 and 18°C respectively and the average wind speed was 0.9 ms^{-1} , while the maximum horizontal solar radiation reached 921 Wm^{-2} . Patterns in this sub-period were S0 for the South façade and W0 for the West façade respectively. Configuration setups of the above mentioned patterns are described in Table 4.09. Pattern S0 consists of stone cladding slab systems with bright finish with close joints, ventilation grills completely open, air cavity of 24 cm of width, while pattern W0 had the same setup of pattern S0 but with open joints and ventilation grills partially open.

In Figures 4.63 and 4.64 it possible to notice the two trends of temperatures concerning the two mentioned above patterns. The indoor temperature was floating freely in this period because the thermal plant was turned off: it was reached a value of 34° C when the ambient temperature was 30° C. The maximum cavity air velocity of the South façade (pattern S0) was 0.8 ms⁻¹ (average value 0.4 ms⁻¹) while the value on the West façade was 0.6 ms⁻¹ (average value 0.2 ms⁻¹). The exterior surface temperature of the West façade skin reached 50° C in the afternoons and was higher than temperature of the South façade skin (40° C). Conversely the cavity air temperature for both patterns was similar for this summer sub-period.

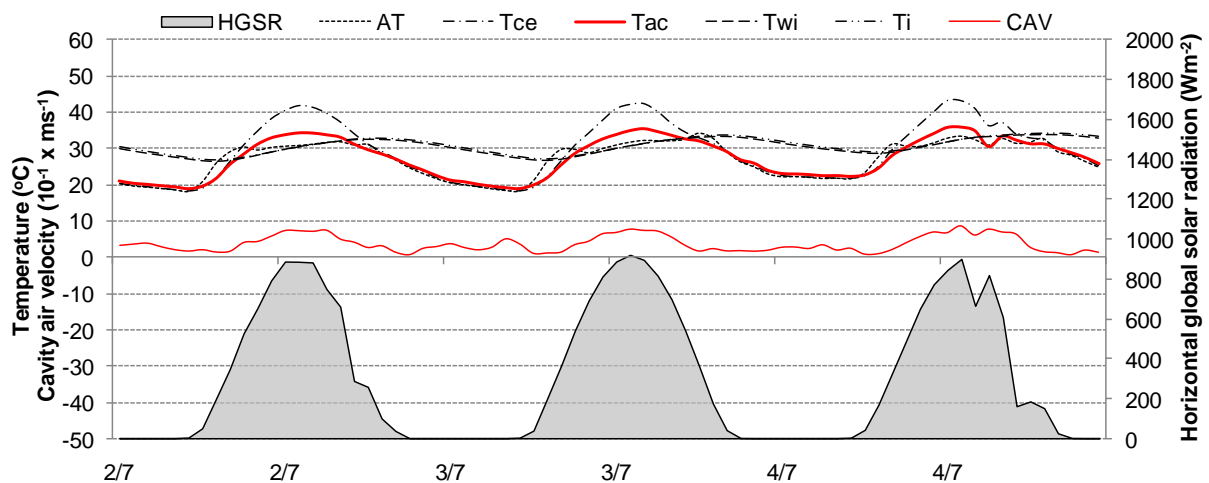


Figure 4.63: Temporal distribution of the ambient temperature (AT), the exterior surface temperature of the skin (T_{ce}), the cavity air temperature (T_{ac}), the interior surface temperature of inner wall (T_{wi}), the indoor temperature (T_i) correlated with cavity air velocity (CAV) and horizontal global solar radiation (HGSR) for the pattern S0 (South façade, period from July 02nd to July 04th 2010).

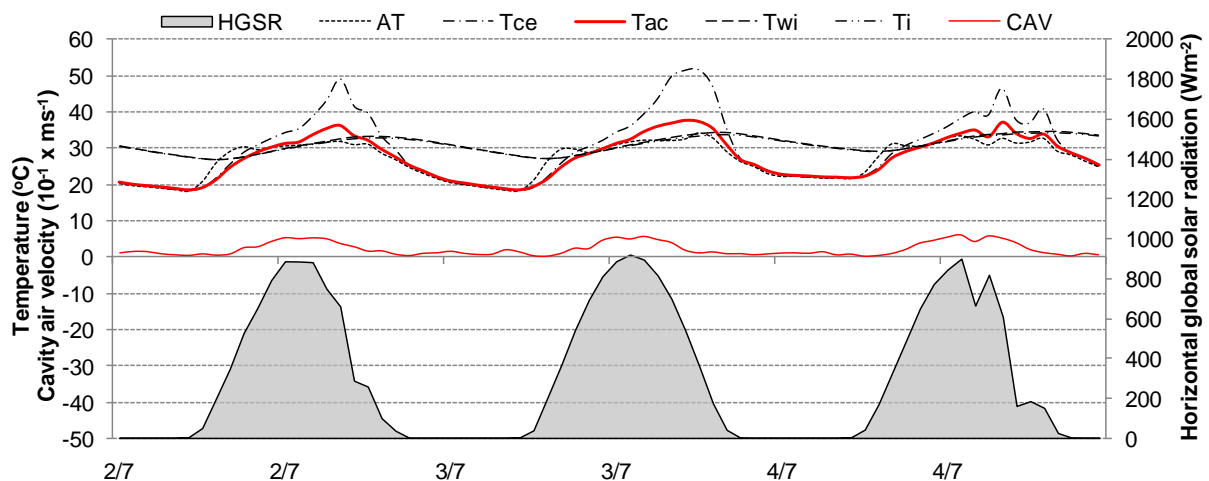


Figure 4.64: Temporal distribution of the ambient temperature (AT), the exterior surface temperature of external skin (T_{ce}), the cavity air temperature (T_{ac}), the interior surface temperature of internal wall (T_{wi}), the indoor temperature (T_i) correlated with cavity air velocity (CAV) and horizontal global solar radiation (HGSR) for the pattern W0 (West façade, period July 02nd to July 04th 2010).

The second sub-period (from July 09th to July 15th 2010) was characterized by only one week. The average ambient temperature was 28° C with the maximum and the minimum value of 35° and 17° C respectively and the average wind speed was 1 ms⁻¹, while the maximum horizontal solar radiation reached 934 Wm⁻². Patterns in this sub-period were S1 for the South façade and W1 for the West façade respectively. Configuration setups of the above mentioned patterns are described in Table 4.09. Pattern S1 consists of stone cladding slab systems with bright finish with open joints, ventilation grills were partially open and the air cavity of 10 cm, while pattern W1 had the same setup of the pattern S0 but with close joints and a air cavity of 10 cm. In this case the main difference between the two patterns was the thickness of the air cavity. Figures 4.65 and 4.66 show the temperature trends of the two patterns. As the air cavity thickness of the South façade was higher than at those the West façade, the measured cavity air velocity on the South was higher than those on the West. Unlikely the exterior surface temperature of the West façade skin reached value above 55° C in the afternoons and was higher than that of the South façade (about 45° C). Beside the cavity air temperature for both patterns was similar also for this summer sub-period.

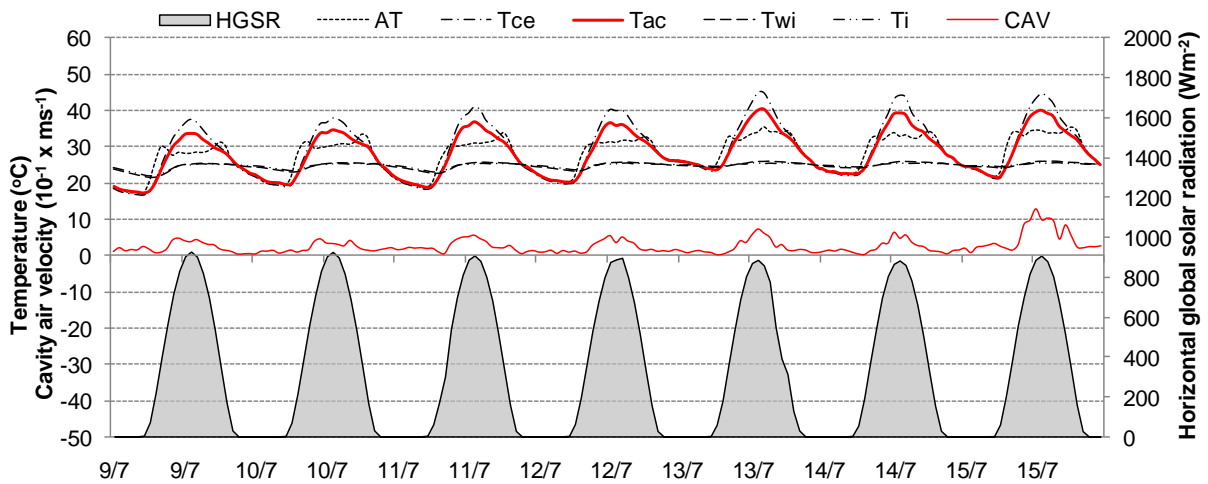


Figure 4.65: Temporal distribution of the ambient temperature (AT), the exterior surface temperature of the skin (T_{ce}), the cavity air temperature (T_{ac}), the interior surface temperature of inner wall (T_{wi}), the indoor temperature (T_i) correlated with cavity air velocity (CAV) and horizontal global solar radiation (HGSR) for the pattern S1 (South façade, period from July 09th to July 15th 2010).

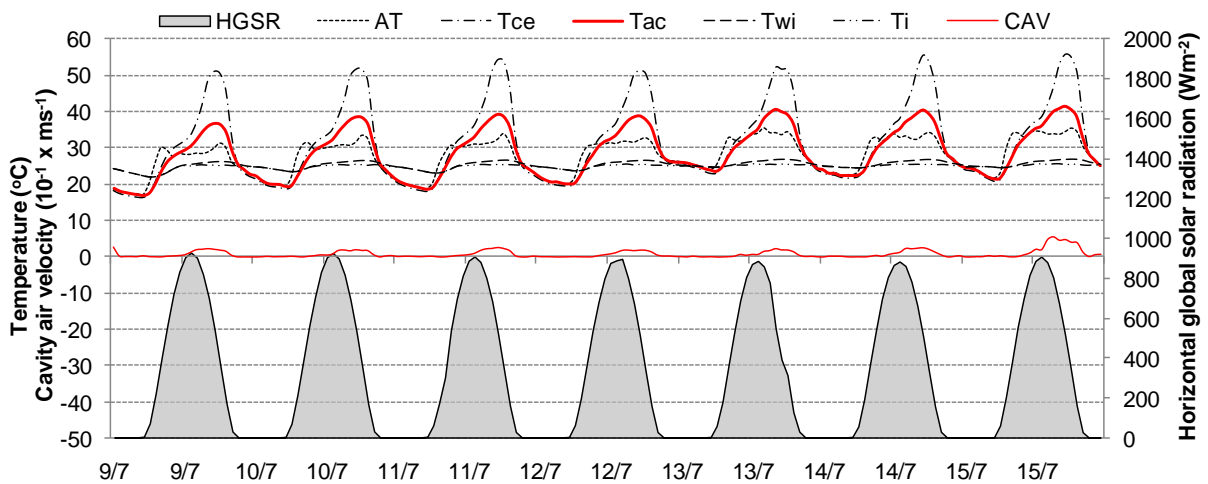


Figure 4.66: Temporal distribution of the ambient temperature (AT), the exterior surface temperature of the skin (T_{ce}), the cavity air temperature (T_{ac}), the interior surface temperature of inner wall (T_{wi}), the indoor temperature (T_i) correlated with cavity air velocity (CAV) and horizontal global solar radiation (HGSR) for the pattern W1 (West façade, period from July 09th to July 15th 2010).

The third sub-period (from July 17th to July 31st 2010) was characterized by two weeks. The average ambient temperature was 25° C with the maximum and the minimum value 36° and 14° C respectively. The average wind speed was 1.2 ms⁻¹, while the maximum horizontal solar radiation reached 999 Wm⁻² (the highest value of all analyzed sub-periods). Patterns in this sub-period were S2 for the South façade and W2 for the West façade respectively. Configuration setups of above mentioned patterns are described in Table 4.09. Both patterns S2 and W2 were the same configuration of the previous patterns S1 and W1 but without ventilation grills. In this case openings at the top and at the bottom were completely opened respectively. In Figures 4.67 and 4.68 it possible to see the temperature trends of the two patterns. The measured cavity air velocity on the South was higher than those of the West façade. The exterior surface temperature of the West façade skin reached peak values about 50° C during several days in the afternoons and was higher than these of the South façade (about 40° C).

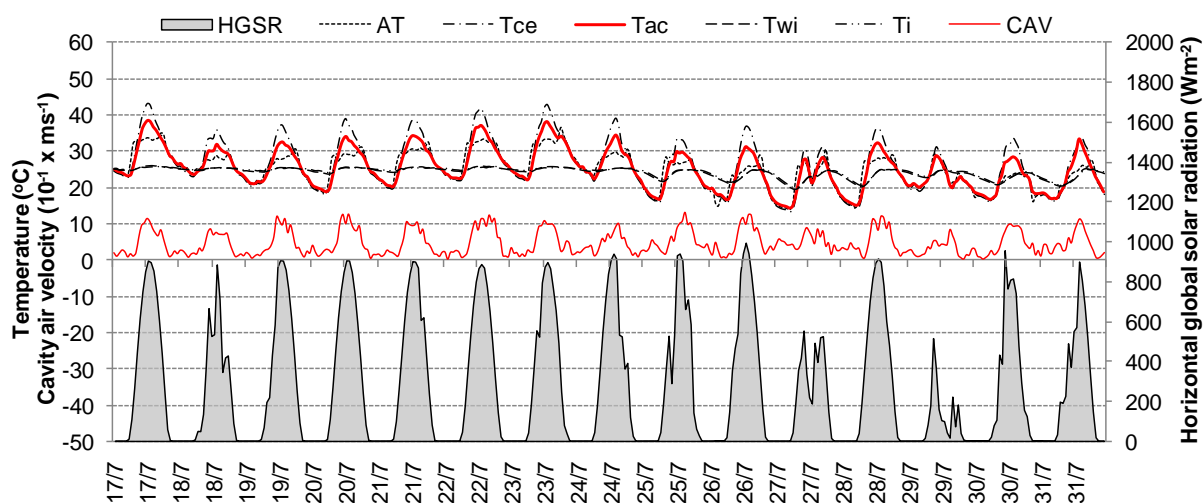


Figure 4.67: Temporal distribution of the ambient temperature (AT), the exterior surface temperature of the skin (T_{ce}), the cavity air temperature (T_{ac}), the interior surface temperature of inner wall (T_{wi}), the indoor temperature (T_i) correlated with cavity air velocity (CAV) and horizontal global solar radiation (HGSR) for the pattern S2 (South façade, period from July 17th to July 31st 2010).

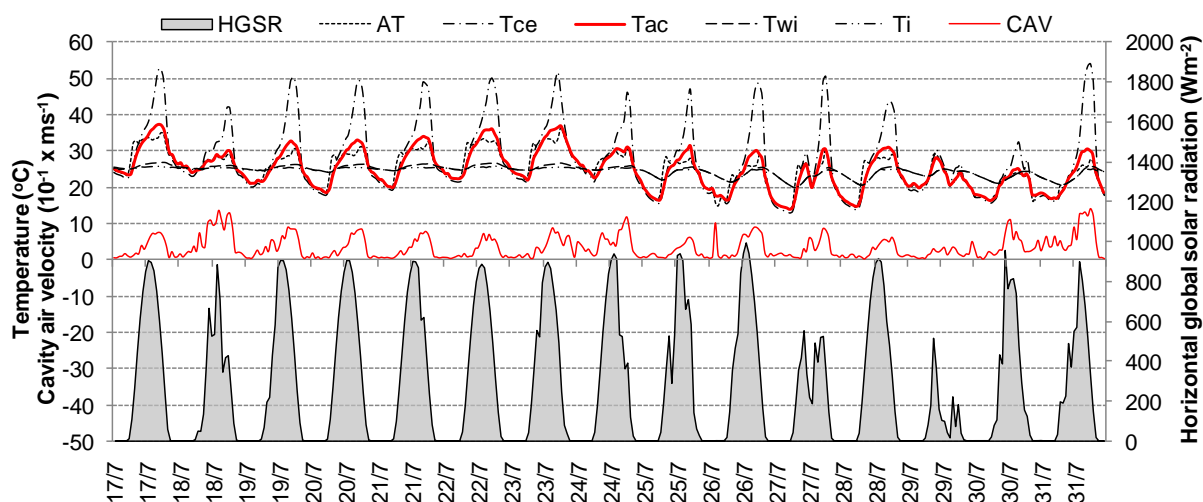


Figure 4.68: Temporal distribution of the ambient temperature (AT), the exterior surface temperature of the skin (T_{ce}), the cavity air temperature (T_{ac}), the interior surface temperature of inner wall (T_{wi}), the indoor temperature (T_i) correlated with cavity air velocity (CAV) and horizontal global solar radiation (HGSR) for the pattern W2 (West façade, period from July 17th to July 31st 2010).

The fourth sub-period (from August 03rd to 23rd 2010) was longest than the other sub-periods, in fact it was characterized from three weeks. The average ambient temperature was 23° C with the maximum and the minimum value 31° and 15° C respectively. The average wind speed was 1.0 ms⁻¹, while the maximum horizontal solar radiation reached 974 Wm⁻². Patterns in this sub-period were S3 for the South façade and W3 for the West façade respectively. Configuration setups of above mentioned patterns are quoted in Table 4.09. Pattern S3 consists of aluminum slab systems with bright finish with open joints, ventilation grills completely open and air cavity of 10 cm, while pattern W3 was completely different. In particular, pattern W3 consists of stone cladding slab systems with dark finish with open joints, ventilation grills completely open and air cavity of 24 cm. In this case the influence of skin material and skin color was studied. In Figures 4.69 and 4.70 it possible to see the main difference of the two temperature trends of the two patterns. As the color of the exterior skin of the West façade was darker than those of the South façade, the measured exterior surface temperature (55° C) on the West was much higher than those on the South (about 40° C). The cavity air velocity for both patterns was similar for this summer sub-period even if the values of the South façade were a little higher than those of the West façade.

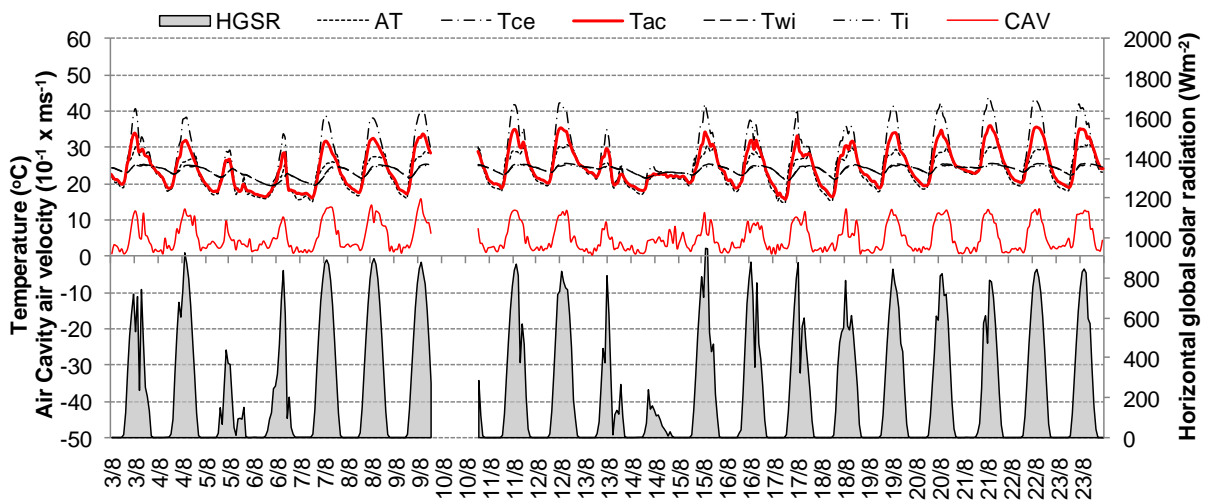


Figure 4.69: Temporal distribution of the ambient temperature (AT), the exterior surface temperature of the skin (T_{ce}), the cavity air temperature (T_{ac}), the interior surface temperature of inner wall (T_{wi}), the indoor temperature (T_i) correlated with cavity air velocity (CAV) and horizontal global solar radiation (HGSR) for the pattern S3 (South façade, period from August 03rd to August 23rd 2010 - measurements data to August 10th was not available).

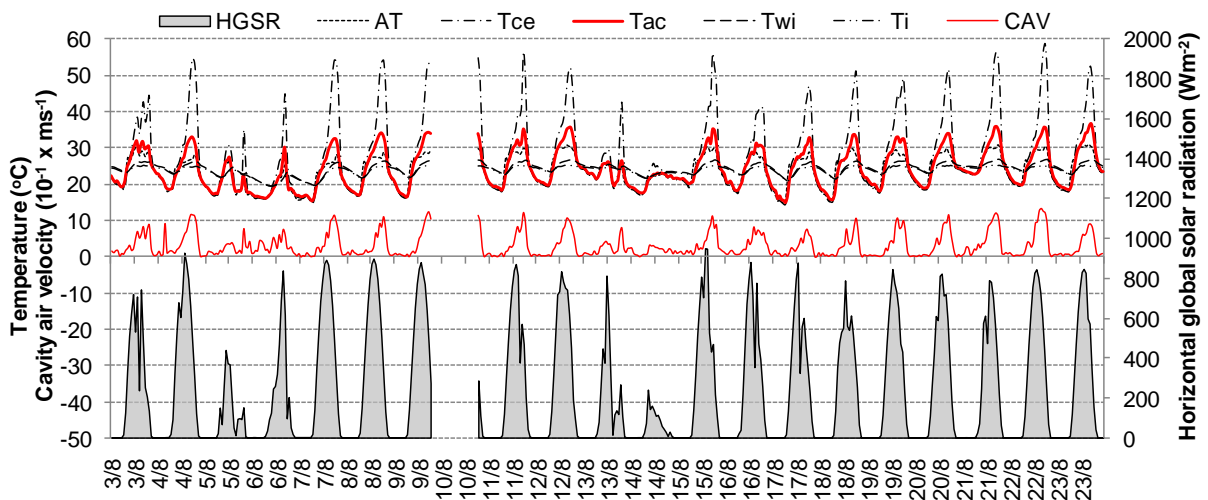


Figure 4.70: Temporal distribution of the ambient temperature (AT), the exterior surface temperature of the skin (T_{ce}), the cavity air temperature (T_{ac}), the interior surface temperature of inner wall (T_{wi}), the indoor temperature (T_i) correlated with cavity air velocity (CAV) and horizontal global solar radiation ($HGSR$) for the pattern W3 (West façade, period from August 03rd to August 23rd 2010 - measurements data to August 10th was not available).

The fifth sub-period (from August 26th to September 06th 2010) was characterized by one week period such as the last sub-period. The average ambient temperature was 22° C with the maximum and the minimum value 36° and 12° C respectively. The average wind speed was 1.5 ms⁻¹, while the maximum horizontal solar radiation reached 850 Wm⁻². Patterns in this sub-period were S4 for the South façade and W4 for the West façade respectively. Configuration setups of above mentioned patterns are quoted in Table 4.09. Pattern S4 consists of aluminum slab systems with dark finish with open joints, ventilation grills partially open and the air cavity of 10 cm, while pattern W4 is the same setup of the previous pattern W3 but with ventilation grills completely close. In Figures 4.71 and 4.72 it possible to see the temperature trends of patterns. The exterior surface temperature of the both skin façade reached values of 55° C while the cavity air temperature on the West façade is higher than that of the South façade. Probably this aspect was due at the absence of ventilation in the channel of the West façade such as also confirmed by cavity air velocity depicted in Figure 4.72.

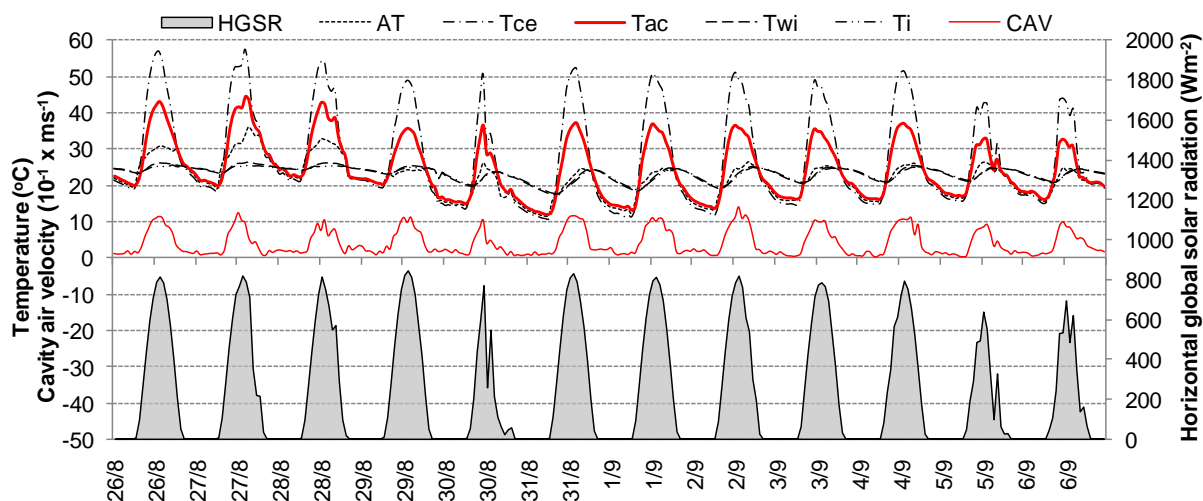


Figure 4.71: Temporal distribution of the ambient temperature (AT), the exterior surface temperature of the skin (T_{ce}), the cavity air temperature (T_{ac}), the interior surface temperature of inner wall (T_{wi}), the indoor temperature (T_i) correlated with cavity air velocity (CAV) and horizontal global solar radiation ($HGSR$) for the pattern S4 (South façade, period from August 26th to September 06th 2010).

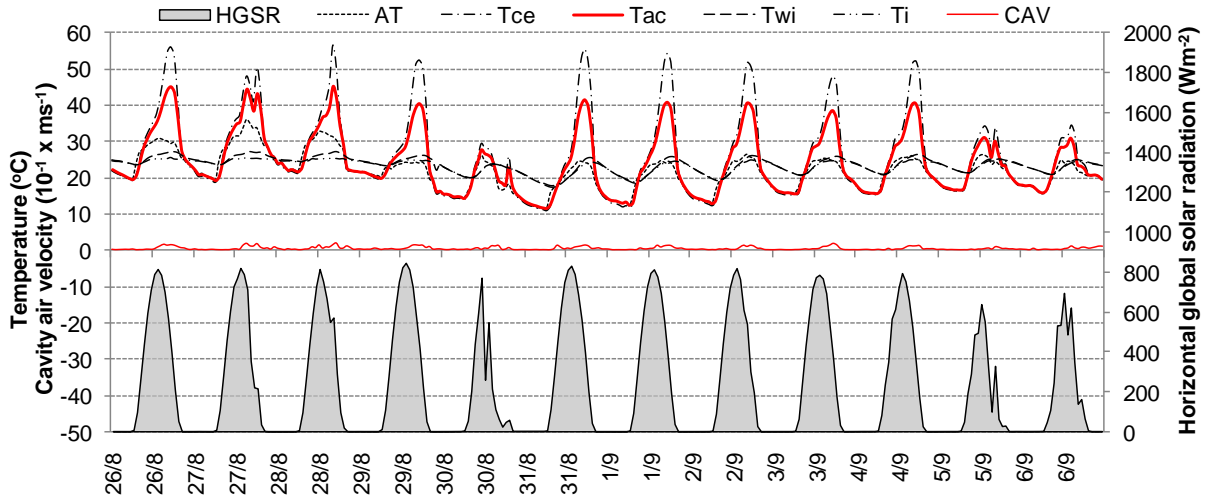


Figure 4.72: Temporal distribution of the ambient temperature (AT), the exterior surface temperature of the skin (T_{ce}), the cavity air temperature (T_{ac}), the interior surface temperature of inner wall (T_{wi}), the indoor temperature (T_i) correlated with cavity air velocity (CAV) and horizontal global solar radiation (HGSR) for the pattern W4 (West façade, period from August 26th to September 06th 2010).

Patterns in the last sub-period (from September 11th to September 17th 2010) were S5 for the South façade and W5 for the West façade respectively. The average ambient temperature was 20° C with the maximum and the minimum value 28° and 13° C respectively. The average wind speed was 1.0 ms⁻¹, while the maximum horizontal solar radiation reached 960 Wm⁻². Configuration setups of above mentioned patterns are quoted in Table 4.09. The pattern S5 had the same configuration of the previous pattern S4 but without ventilation grills while the pattern W5 had the same setup of the previous pattern W5 but with close joints. The exterior surface temperature of the West skin façade reached values of about 60° C while its cavity air temperature 45° C in spite the low ambient temperature (average ambient temperature 20° C). The absence of ventilation in the channel causes very high temperature in the wall such as also confirmed by graphs in Figure 4.74. Conversely the cavity air velocity in the South side (ventilation grills completely opened) reached values of about 2.0 ms⁻¹ with a decrease of the cavity air temperature (35° C).

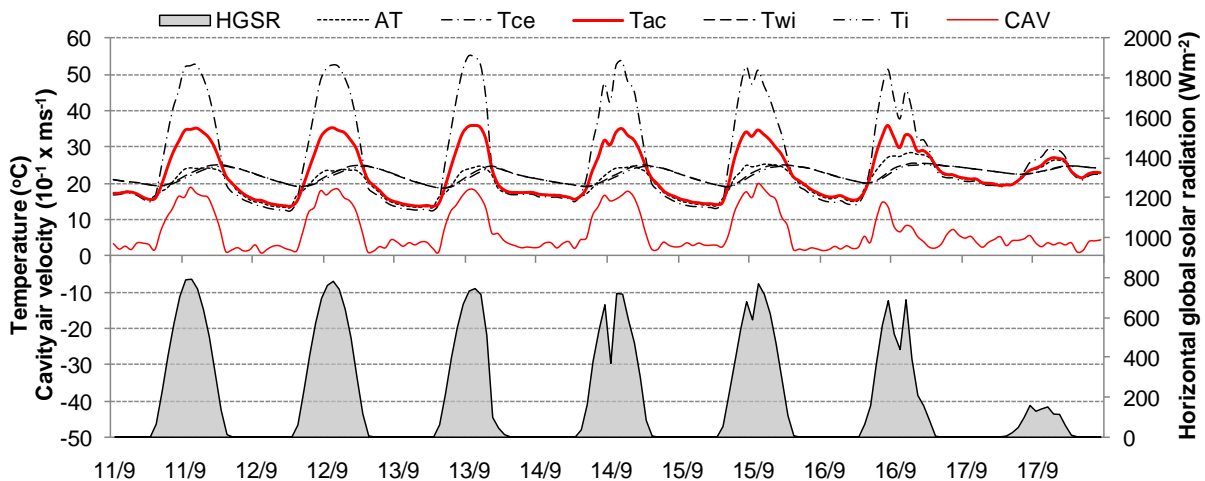


Figure 4.73: Temporal distribution of the ambient temperature (AT), the exterior surface temperature of the skin (T_{ce}), the cavity air temperature (T_{ac}), the interior surface temperature of inner wall (T_{wi}), the indoor temperature (T_i) correlated with cavity air velocity (CAV) and horizontal global solar radiation (HGSR) for the pattern S5 (South façade, period from September 11th to September 17th 2010).

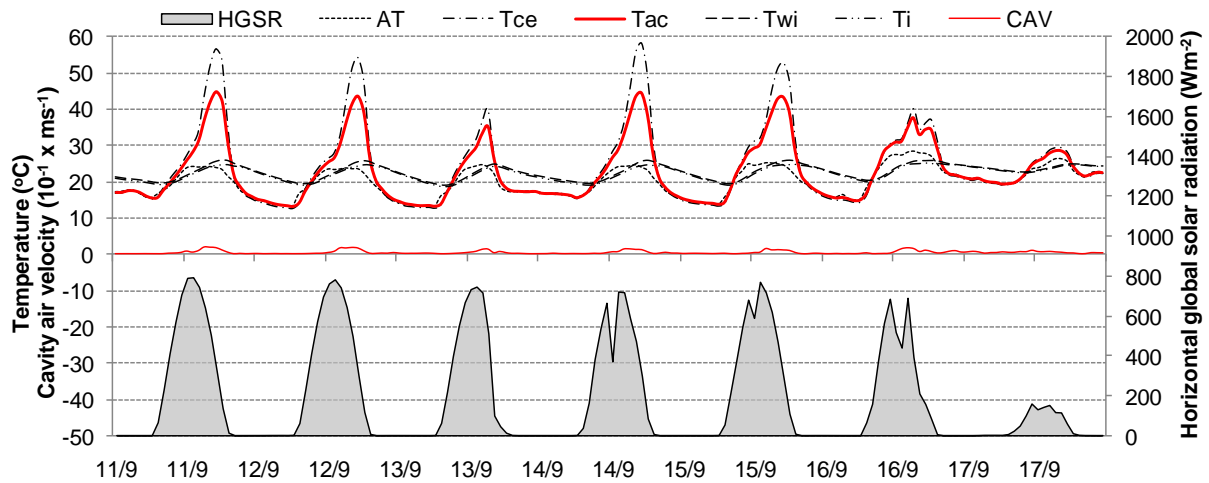


Figure 4.74: Temporal distribution of the ambient temperature (AT), the exterior surface temperature of the skin (T_{ce}), the cavity air temperature (T_{ac}), the interior surface temperature of inner wall (T_{wi}), the indoor temperature (T_i) correlated with cavity air velocity (CAV) and horizontal global solar radiation ($HGSR$) for the pattern W5 (West façade, period from September 11th to September 17th 2010).

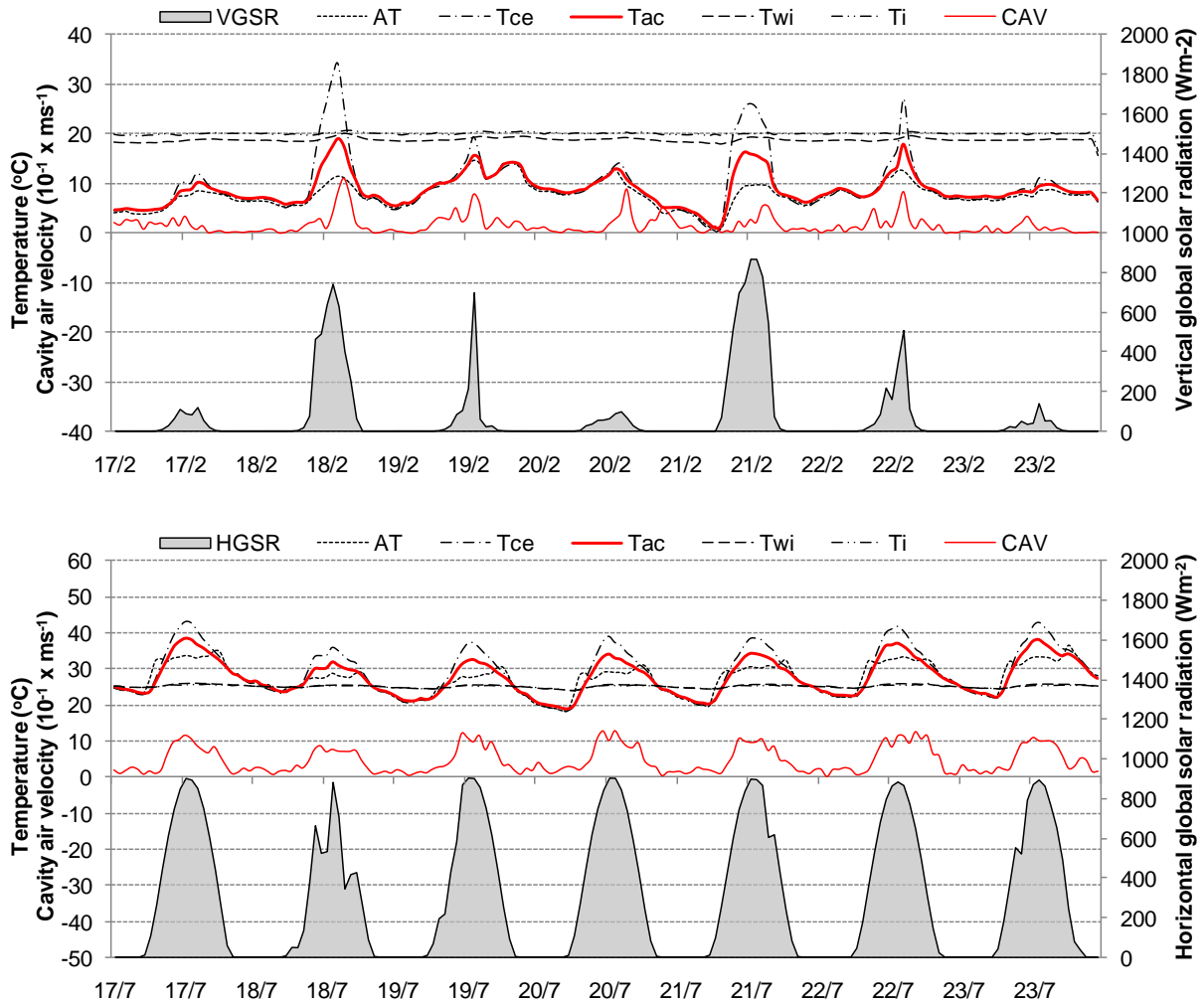


Figure 4.75 Temporal distribution of the ambient temperature (AT), the exterior surface temperature of external skin (T_{ce}), the cavity air temperature (T_{ac}), the interior surface temperature of internal wall (T_{wi}), the indoor temperature (T_i) correlated with cavity air velocity (CAV), the horizontal global solar radiation (HGSR) and the vertical global solar radiation (VGSR) for two different pattern of ventilated façade in a typical winter period at the top and in a typical summer period at the bottom.

4.10 Conclusion

This chapter reports on an experimental set-up of a naturally ventilated skin façade or simply called rainscreen ventilated façade. The temperature profiles as well as the cavity air velocity were continuously measured during the winter and the summer periods. The measurements are used to better understand the complexity of ventilated skin façades, to relate them to energy objectives, to evaluate energy modelling assumptions and to derive some parameters and relationships. Analysis of the temperature profiles shows that the surface and cavity temperature are mainly determined not only by the setup of openings as well as of ventilation grills and open joints, but also by the air cavity thickness and the finish of the external skin of ventilated façades.

In the winter, the ventilated façade cavity is quite warmer than the exterior temperature in the typical sunny day. In the summer, the cavity temperature becomes rather hot and very hot with dark finish of the skin and in absence of the ventilation in the channel (see section 4.8.3). In Figure

4.75 it possible to notice a comparison between the thermal behaviour of the ventilated façade in the winter and the summer periods.

Usually the airflow in the ventilated *skin façade* is governed by the pressure difference between the lower and upper ventilation grills. Thermal buoyancy was shown to be the dominating force for low wind speeds. As the average wind speed in summer was low, the flow conditions in summer could be relatively well described by the combination of thermal buoyancy and wind pressure differences.

The experimental campaign has shown that the measurement system of the air velocity within the cavity must be improved by using a larger number of sensors distributed along the cavity and more accurate sensors for low values of velocity. However in the winter period probably the low velocity was due to the large thickness of the air cavity adopted in this ventilated façade (24 cm). In the summer period and with a smaller thickness (10 cm) the air cavity velocities were a little much higher (1-2 ms⁻¹).

Further a limited experimental evaluation of the correlations for the convective heat transfer coefficient is presented. The spread on the results, however, shows that obtaining a reliable expression for the heat transfer coefficient is very difficult. As consequence a simple correlation (Equation 2.74) is useful to estimate the convective heat transfer coefficient for energetic purposes.

Finally another experimental evaluation of the steady-state thermal transmittance of rainscreen ventilated façade was given. In winter period the measured steady-state thermal transmittance of rainscreen ventilated façade was agrees with the value estimated by Standard EN ISO 6946 [2007].

CHAPTER 5

EMPIRICAL VALIDATION MODELLING VENTILATED RAINSCREEN IN WINTER PERIOD

5.1 Introduction

In this chapter the thermal behaviour of a rainscreen ventilated façade has been investigated numerically. As stated in the previous Chapter 4, field measurements were performed during the 2009/10 winter season in a test building located in San Mauro Pascoli (Italy) having a square base with an inner side of 2.89 m and a total internal height of 7.75 m. The external walls of this tower are rainscreen ventilated façades with a 24 cm air cavity and an external side composed of stoneware with open joints. Ventilation grills are located at the top and at the bottom of the tower. In this work the modelling of the test building using a dynamic thermal simulation program (ESP-r) is presented and the main results discussed. In order to study the rainscreen ventilated façade three different multi-zone models were defined (see chapter 3) and comparison with the experimental results has been made in order to select the best ESP-r air flow network for the modelling of this kind of envelope component.

Section 5.2 describes a numerical study in order to select the best ESP-r air flow network for the simulation. Comparisons between measured and predicted values are shown in the section 5.3. The Chapter ends with remarks on comparisons and conclusions about the validation of the rainscreen ventilated façade winter model.

5.2 Model validation (winter period)

In this section a study is observed which defines the best airflow network model to adopt for the simulation of a rainscreen ventilated façade using ESP-r. In the definition of the appropriate airflow network model for the tested façade, it is necessary to determine if the joints and grills (in Chapter 1 more detailed are given) of the ventilated façade are important for the airflow model or if the role of these components can be considered negligible in the estimation of the thermal performance of the façade.

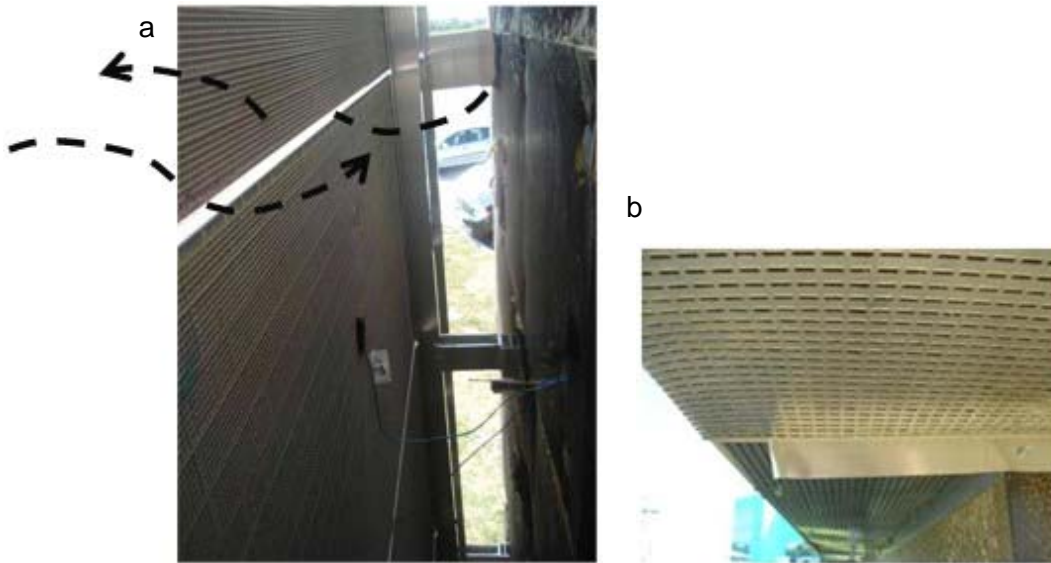


Figure 5.01: (a) Open joints (left) and (b) ventilation grills at the bottom (right) for one rainscreen ventilated façade.

In order to answer this open question the tested façade was modelled in ESP-r by means of three different airflow network models (Figure 5.02):

- The flow network considers joints and grills at the bottom and the top as closed (in the cavity there is only thermal buoyancy between the cavity and internal room and wind effects are not included in the analysis). This model is called model A.
- The flow network considers all the joints closed; the grills at the bottom and the top are considered partially open (see Sections 1.2 and 3.3). This model is called model B.
- The flow network takes into account the real conditions of the ventilated façade: joints are completely opened and grills are partially opened. This model is called model C

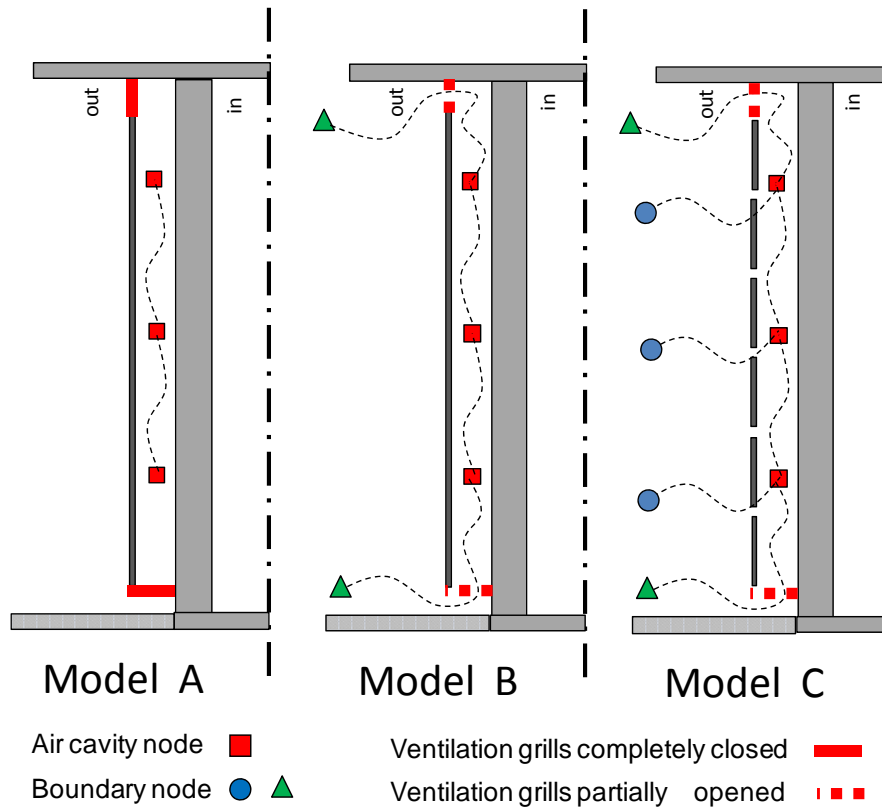


Figure 5.02: Three different airflow network models of rainscreen ventilated façades modelled in ESP-r.

The comparison between results obtained by using models A and C can also be useful in order to highlight the significance of wind and buoyancy-driven flow effects on the thermal performance of the ventilated façade during the winter season. In fact, it is well known that forced circulation of the air in the cavity during winter can reduce the thermal insulation of the façade significantly, with negative effects on the building energy demand. To establish what is the best airflow network model for this kind of ventilated façade the measured values (M) and the ESP-r predictions ones (X) are compared by using as input for ESP-r the climate data recorded during the test period. For the purpose of model validation, measured local weather data for three months (January 1st–March 31st 2010) were used. The measured local weather data include external air temperature and air humidity, wind speed and direction and total vertical (South side) global solar radiation. More details about the external weather data used in the simulation can be found in the Section 4.4 of Chapter 4.

By using these climate data as input data in the ESP-r software and solving the balance equations (3.03, 3.04, 3.10, 3.11, 3.14 and 3.15 reported in the Chapter 3) of the airflow network model adopted, the hourly average values of the temperature of the nodes of the network can be calculated.

Assuming X_t is the predicted value at hour t from ESP-r and M_t the corresponding measured value at the same instant of time, it is possible to analyse the capability of the adopted model to predict the measured values by using the following statistical parameters:

$$DMIN = \min(X_t - M_t) \quad [5.01]$$

$$DMAX = \max(X_t - M_t) \quad [5.02]$$

$$MEANDT = \sum_{t=1}^n \frac{(X_t - M_t)}{n} \quad [5.03]$$

$$RSQMEANDT = \sqrt{\sum_{t=1}^n \frac{(X_t - M_t)^2}{n}} \quad [5.04]$$

where n is the number of total hours in the period selected for the comparison.

Tables 5.01 and 5.02 show the results for the cavity air temperature of the West and South façades by using different airflow network models for the ventilated façade (models A, B and C). It is interesting to observe that the difference between the predicted and the measured values of the air cavity along the West and the South façades change significantly with the model adopted. In particular, model A in which the effects of the wind through the grills and joints are completely ignored tends to overestimate the temperature in the cavity with respect the measured values. The difference is very large especially in the South façade; this fact confirms the role of the forced air circulation due to the wind during the winter on the thermal conditions of the façade. On the contrary, that differences between the results obtained by using models B and C are quite small. This fact indicates that the role of the open joints can be considered negligible in the tested conditions.

In order to quantify the different performances of the models the Pearson coefficient (R-squared) can be calculated by using its classical definition:

$$R^2 = \left(\frac{\sum_{t=1,n} (X_t - \bar{X})(M_t - \bar{M})}{\sqrt{\sum_{t=1,n} (X_t - \bar{X})^2 \sum_{t=1,n} (M_t - \bar{M})^2}} \right)^2 \quad [5.05]$$

in which \bar{X} and \bar{M} are the mean values of the predicted (X_t) and the measured (M_t) values.

If model A is adopted for the ventilated wall the numerical results exhibit a large disagreement with the experimental results; the R^2 coefficient of correlation quoted in Table 5.01 and 4.02 between the measured values and the predicted ones of the cavity air temperature is less than 0.84 for the West-facing wall and 0.91 for the South façade. These values demonstrate that, when model A is adopted, the agreement with the experimental data is strongly influenced by the orientation of the considered ventilated wall and increases for walls exposed to large values of the solar radiation. In fact, in this case the air circulation within the cavity is due to the temperature difference between the cavity walls and the air only and this difference increases with the incident solar radiation. It is interesting to observe that R^2 increases by 16% between model A and the model C which reveals the better accuracy of the latter. On the contrary, the variation of R^2 between model B and model C is modest. One can conclude that during the simulation of the rainscreen ventilated façade the presence of the open joints can be ignored in the modelling without a significant decrease in the accuracy of the numerical results [Marinosci et al. 2010b]. Also, by ignoring the open joints, the airflow network model becomes simpler and the numerical solution of the balance equations faster.

Table 5.01: Results for cavity air temperature of the West façade

Airflow network model	DMAX (K)	DMIN (K)	MEANDT (K)	RSQMEANDT (K)	R ²
Model A	18.09	-8.37	-0.25	2.50	0.8345
Model B	5.94	-5.66	0.02	1.06	0.9680
Model C	5.13	-5.87	0.04	1.03	0.9711

Table 5.02: Results for cavity air temperature of the South façade

Airflow network model	DMAX (K)	DMIN (K)	MEANDT (K)	RSQMEANDT (K)	R ²
Model A	24.51	-11.88	-0.46	2.79	0.9103
Model B	5.25	-8.53	-0.42	1.58	0.9762
Model C	4.99	-7.85	-0.53	1.47	0.9795

Results of Tables 5.01 and 5.02 confirm that the selection of the airflow network model is very important in order to predict the thermal performances of a ventilated façade, as it has been noted by Strachan [2008], Strachan and Vandaele [2008], Pedrini et al. [2002] and Bronson et al. [1992] in the past. On the basis of these results model C has been selected as the best method to model the tested rainscreen ventilated façade.

For the West-facing façades, the cavity temperature monitored from January 1st to March 31st was compared with the values generated by ESP-r using models A, B and C. The difference in the predictive capability of models A, B and C can be observed by comparing the data of Figure 5.03 (model A), 4.04 (model B) and 4.05 (model C). For model A the deviation from the bisector (perfect solution) is larger than 33% while for the model B it is near to 22% and for the model C it is smaller than 18%. These data confirm the values of the R² parameter given in Table 5.01. The good prediction capability of model C is confirmed also by the comparison between the experimental and the numerical data obtained by ESP-r for the South-facing façade: in fact the R-squared coefficients go from a value of 0.9711 for the West-facing façade to the value of 0.9795 for the South-facing façade.

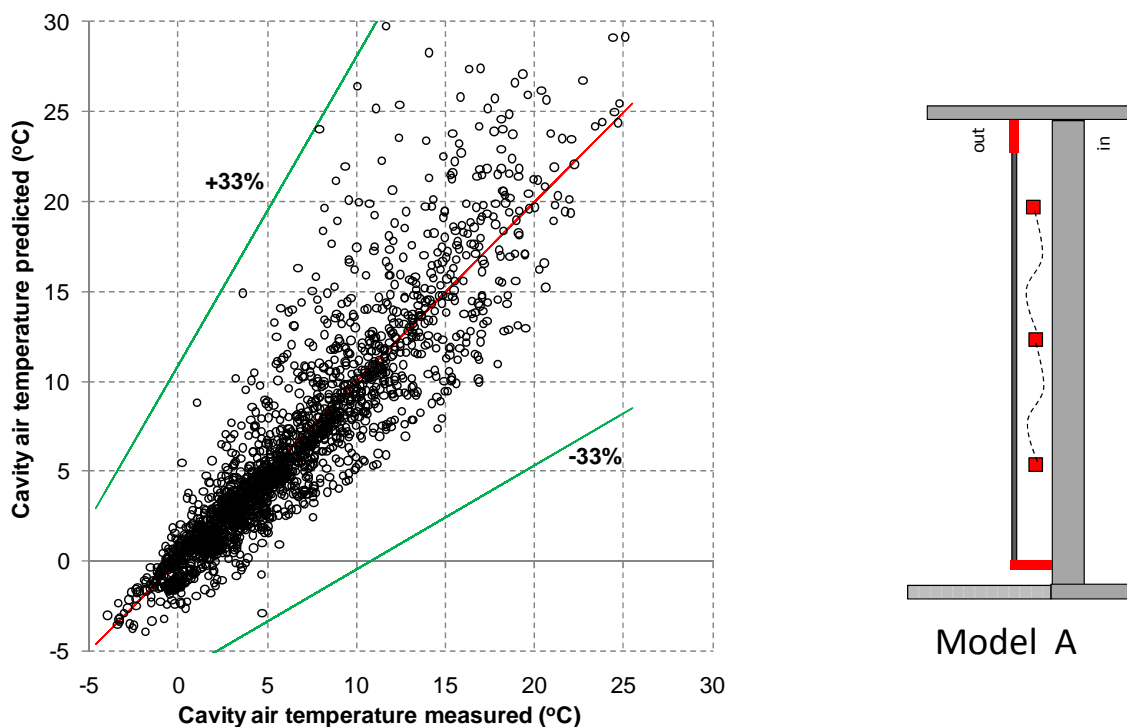


Figure 5.03: Correlation between measured and predicted cavity air temperatures on the West side for three months for model A.

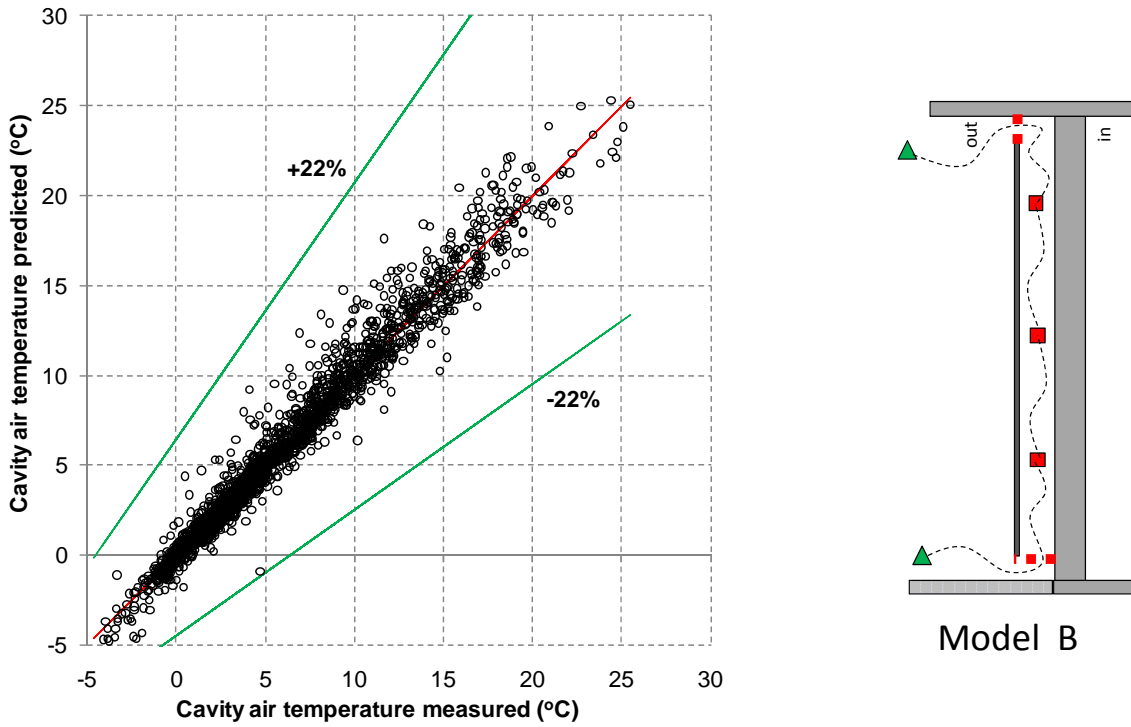


Figure 5.04: Correlation between measured and predicted cavity temperatures on the West side for three months for model B.

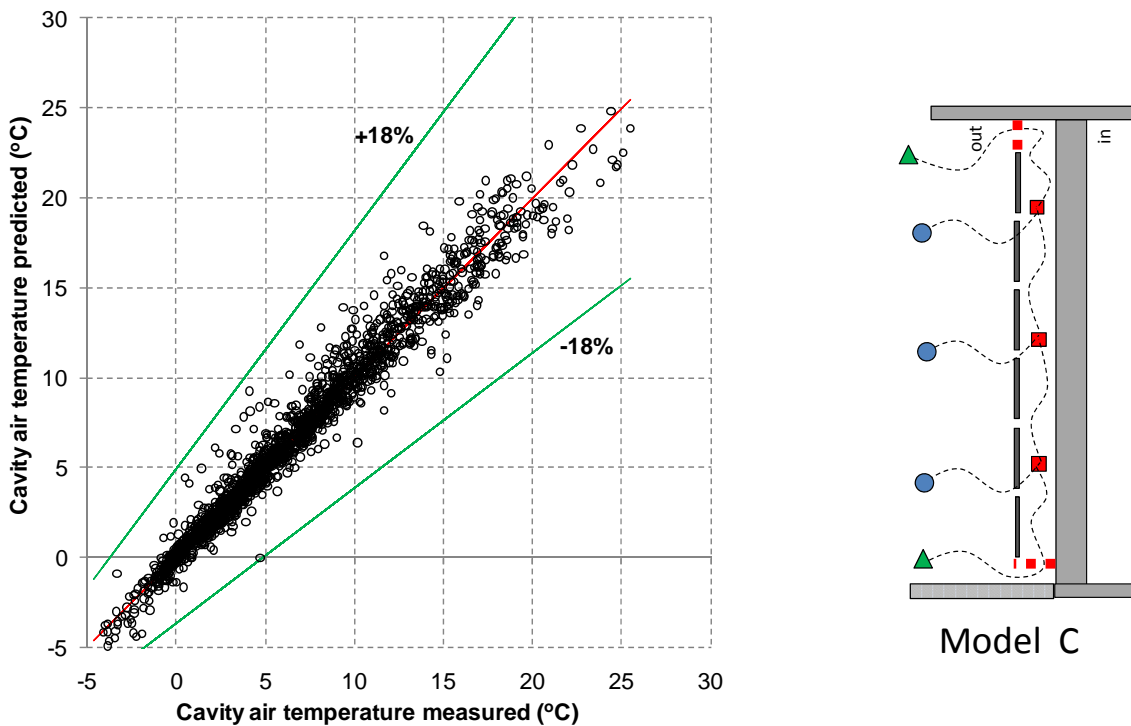


Figure 5.05: Correlation between measured and predicted cavity air temperatures on the West side for three months for model C.

As underlined before, an interesting result of this comparison is that model B and model C have similar predictive capabilities for the cavity air temperature; in fact, if the value of the R^2 parameter

linked to the West and the South-facing façade obtained by adopting the models C and B are compared, this parameter increases only by 0.32-0.33% going from model B to model C. This result highlights that the adoption of a simpler air flow network in which all the joints of the rainscreen cover are considered closed can guarantee accurate results with reduced CPU time and therefore, especially for long dynamic simulations, model B is preferable to model C.

5.3 Comparison with monitored data (winter period)

The previous analysis showed that Model B gave the best compromise between accuracy and model complexity for general modelling purposes. However, for the detailed comparisons between measured and predicted results presented in this section, model C has been used. Thus the adopted air flow network takes into account the real conditions of the ventilated façade with joints opened and grills partially opened. The numerical results obtained by means of the ESP-r model of the rainscreen ventilated façade in terms of external surface temperature and cavity air velocity have been compared with the measured corresponding quantities during the whole test period. As stated before, three parameters are primarily responsible for the thermal performance of the ventilated façade: (i) the solar radiation on the external surface (ii) the external air temperature (iii) the wind velocity and direction. The comparisons that are presented in this section aim at demonstrating that the model of the ventilated façade is able to take into account the combined effects of these quantities.

Figure 5.06a shows the comparison between the measured and predicted values of the external rainscreen surface temperature during the week from February 19th to February 25th 2010 on the South side of the façade. In Figure 5.06b the measured values of vertical global solar radiation on the South side and external air temperature for the same period are shown. As evidenced by Figure 5.06b, the selected period was characterized by a large variation of the measured values of solar radiation ranging from 27 to 868 Wm⁻². It was selected in order to test the capability of the model to predict the thermal behavior of the ventilated façade exposed to highly variable incident solar radiation. The simulated rainscreen surface temperature agrees very well with measured data and this fact confirms that the model is able to correctly take into account the role played by the solar radiation and by the external air temperature. During this period the wind velocity was variable with high value about 5 ms⁻¹ (19/02) and less than 3-4 ms⁻¹ on other days, with a predominant South-West direction. However, the data of Figure 5.06a show that the model underestimates the external rainscreen surface temperature when solar radiation is absent.

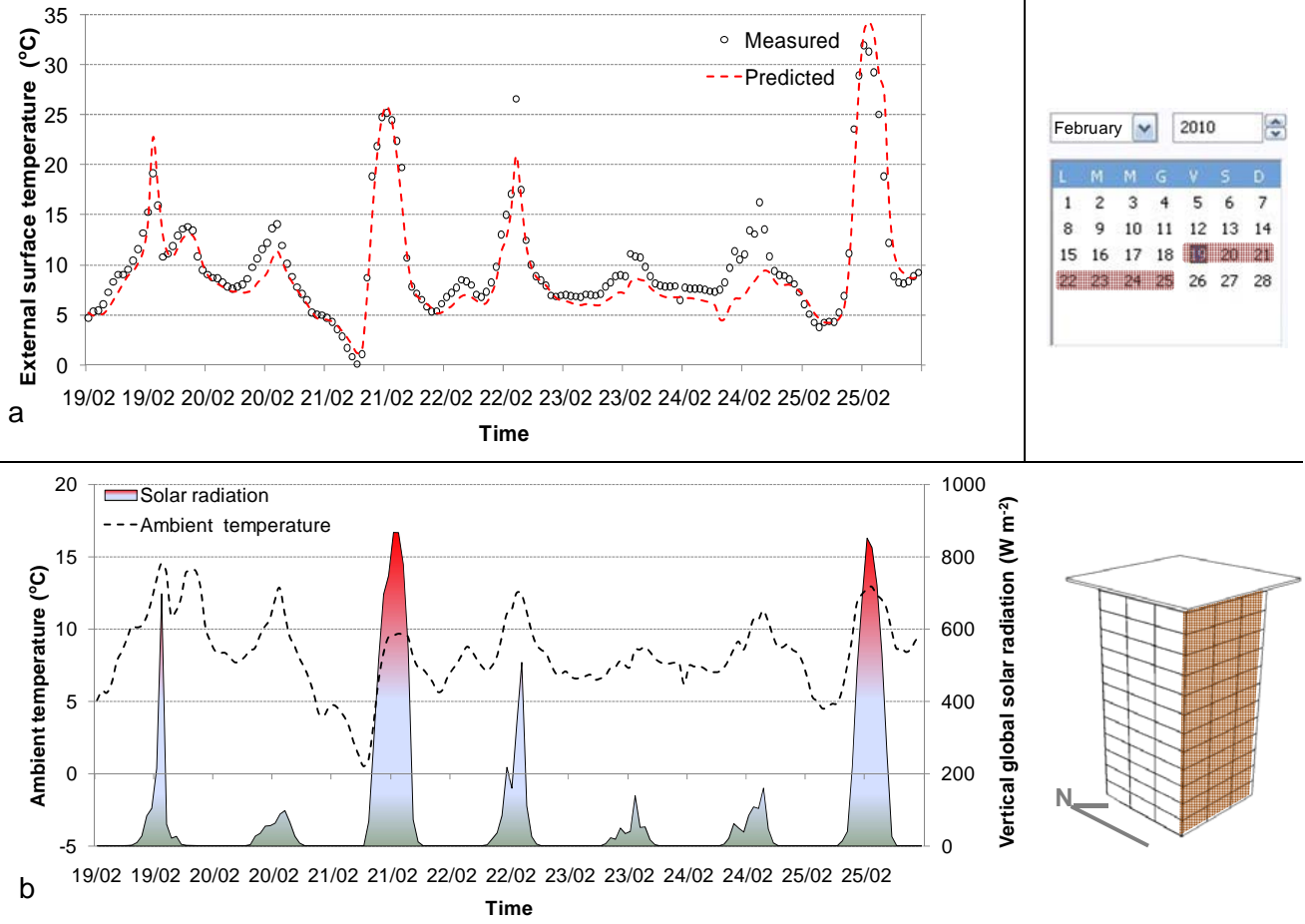


Figure 5.06: (a) Comparison of measured and predicted results of the external surface temperature on South side. (b) Vertical global solar radiation during the tests.

The above mentioned aspects can be seen also in Figure 5.07, which depends comparison between the measured and predicted values of the external rainscreen surface temperature during another week (from February 12nd to February 18th 2010) on the West side of the façade. A possible reason for this is the uncertainty associated with estimating long-wave radiation transfer to the sky at night.

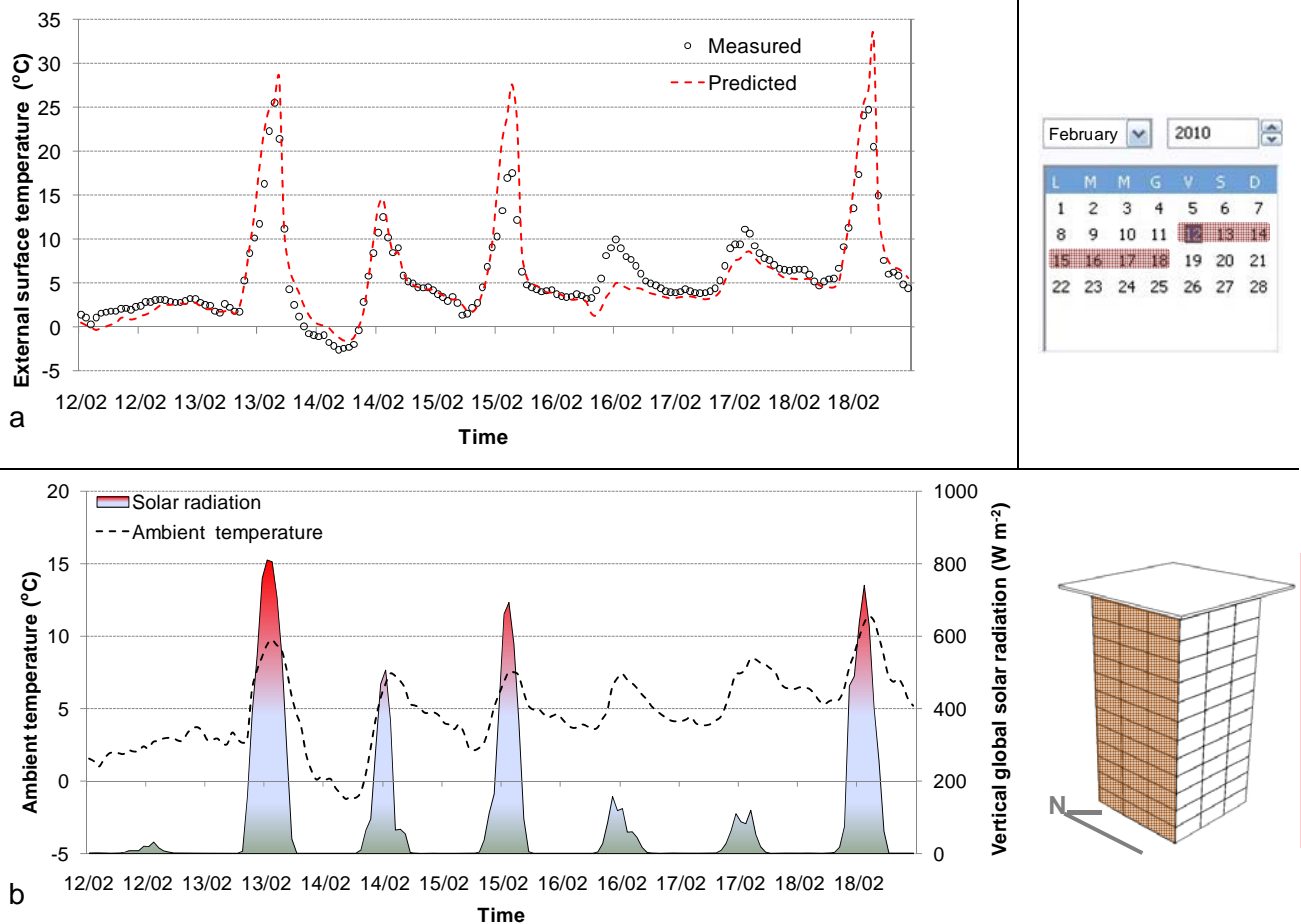


Figure 5.07: (a) Comparison of measured and predicted results of the external surface temperature on West side. (b) Vertical global solar radiation during the tests.

Comparison between the numerical and the experimental data for the whole test period (January-March) showed that the role played by the wind velocity on the was generally the most difficult effect to predict. Figure 5.08a shows the comparison between the experimental and the numerical hourly average data of the cavity air velocity during three days characterised by low external air temperatures (-0.6°C), low solar radiation (40 Wm^{-2}) and wind velocities between 0 and 1.5 ms^{-1} for the West façade with a variable direction between West and East (Figure 5.08b). It is interesting to observe that typical cavity air velocities have a low value during this period (less than 0.12 ms^{-1}) and this fact is beneficial in order to reduce the heat losses through the façade during the winter. The low values of the velocity, confirmed also by the data in Figures 4.19 and 4.20 (see Section 4.5 in the Chapter 4), are generally due to the large thickness of the air cavity adopted in this ventilated façade (24 cm). The data of Fig. 4.08a show that during a night without wind the measured velocity tended to be strongly variable, due to the thermal buoyancy, although measured and predicted results are in agreement within one order of magnitude. During the day, the model and the experimental data showed some small discrepancies. It is important to note that comparisons are difficult at low air velocities, particularly in view of the large uncertainties of the hot wire anemometer measurements. However, the level of agreement was considered acceptable.

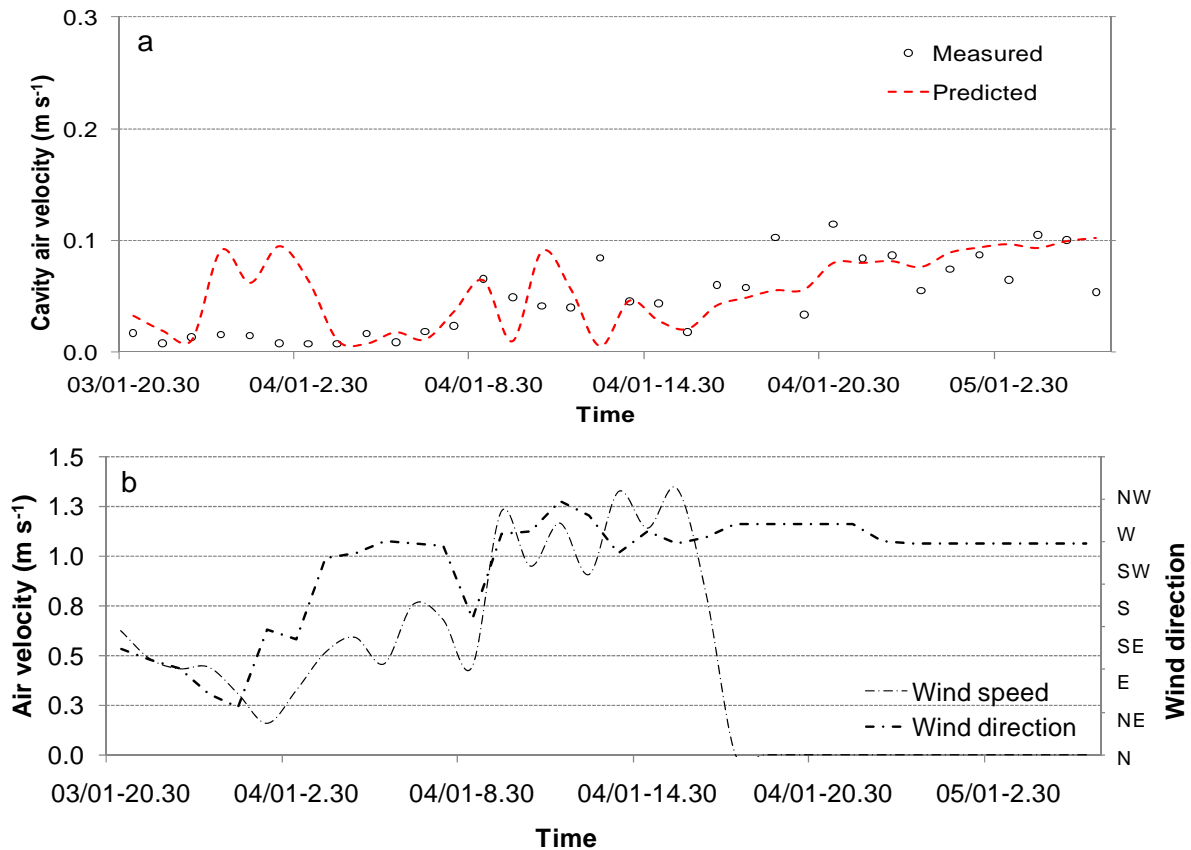


Figure 5.08: (a) Comparison of measured and predicted results of the cavity air velocity – West façade. (b) Wind speed and direction during the tests.

Finally, a test was carried out on the capability of the model of the whole building to predict the trend of the indoor air temperature during a period in January (two weeks) in which the heating plant of the tower was turned off. Figure 5.09 shows the trend of the experimental values of the indoor air temperature of the test building compared to the numerical data obtained by using ESP-r. Some discrepancies between the measured and the numerical data can be seen: in particular the ESP-r simulation (in this specific case) seems to overestimate the thermal insulation and the thermal inertia of the building; in fact the predicted indoor air temperature is generally larger than the measured values both in steady-state and unsteady periods. Such small discrepancies can be due to some inaccurate information on thermophysical properties of the materials involved in the structural elements of the building such as thermal conductivity, specific heat and also the surface properties such as emissivity. A similar trend has been evidenced by Leal et al. [2003] who used ESP-r for the analysis of the thermal behaviour of ventilated building components. It is important to remember when processing these results that the tested envelope was built with light materials and for this reason it is characterized by a lower thermal capacity with respect to the typical envelope components used in real buildings. As a consequence, the time constant of this test building is low and the indoor air temperature is much more sensitive to the changes in the boundary conditions than in a building with more massive construction. However, the data shown in this work demonstrate that the reliability of the numerical model of the rainscreen ventilated façade built with ESP-r can be considered satisfactory for design studies of such building components.

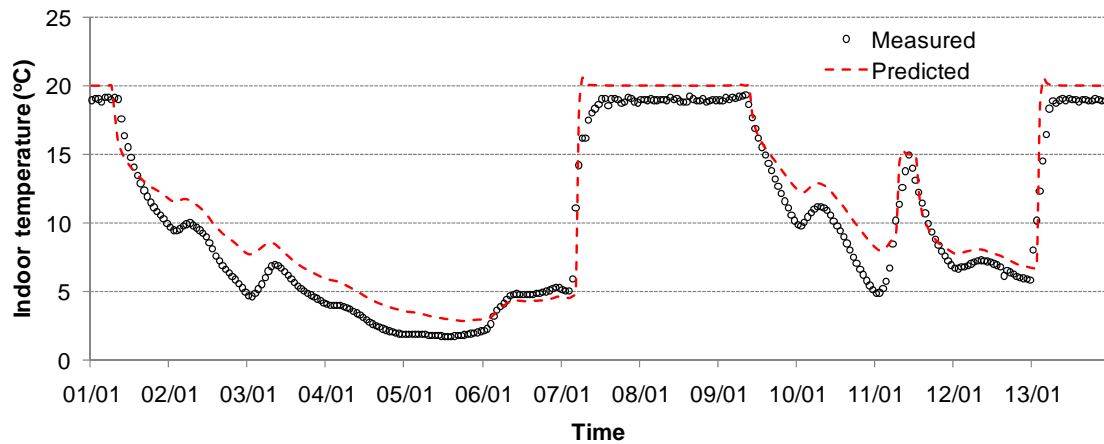


Figure 5.09: Comparison between the measured and predicted results of the internal air room temperature.

5.4 Remarks

Results presented in this chapter about the thermal behaviour of the rainscreen skin envelope were limited to the winter period. An extended thermal analysis for typical summer conditions in the next chapter (Chapter 5) will be described. In addition, effects of the indoor air re-circulated through the cavity on the energy consumption of a building will be studied in the future by using ESP-r and other dynamic software. Additional simulations with a CFD code for the analysis of the air flow patterns through the ventilated cavity, particularly if coupled with the BS models, would be useful in providing results comparable with this study.

Although the comparisons have evidenced a good capability of the model to predict the thermal behaviour of the ventilated façade, the experimental campaign has shown that the measurement system of the air velocity within the cavity must be improved by using a larger number of sensors distributed along the cavity and more accurate sensors for low values of velocity.

5.5 Conclusion

The behaviour of this envelope component has been investigated both experimentally and numerically. Field measurements were performed during the 2009/10 winter season in a test building located in San Mauro Pascoli (Italy). The modelling of the test building was made using ESP-r. Three different multi-zone models were defined and the comparison with the experimental results was used in order to select the best ESP-r air flow network for the modelling of this kind of envelope component.

The main results obtained can be summarized as follows:

- If the thermal model of the ventilated wall does not include the open grills at the bottom and at the top of the wall and the presence of the open joints on the external rainscreen surface, the numerical results exhibit, as expected, a large disagreement with the experimental results. In this case, the agreement with the experimental data is strongly influenced by the orientation of the considered ventilated wall and the temperature increases for walls exposed to large values of the solar radiation. The air circulation within the cavity is due to the temperature difference between the cavity walls and the air only and this difference increases with the incident solar radiation.
- In the modelling of the rainscreen ventilated façades the presence of the external open joints can be ignored without decreasing the accuracy of the numerical results significantly.

Conversely, by ignoring the open joints, the airflow network model becomes simpler and the numerical solution of the balance equations is faster. For this reason, this kind of model can be suggested as more appropriate for long-term dynamic simulations in which CPU time saving can be important.

- The ESP-r model of this component underestimates the external rainscreen surface temperature during the night when the solar radiation is absent; on the contrary, in the presence of high levels of solar radiation, when the effect of this parameter becomes predominant with respect to the effects due to the ambient temperature and to the wind, the agreement with the experimental data is very good.
- The typical air cavity velocities predicted by the ESP-r model are very low (less than 0.12 ms^{-1}) and these values are confirmed the experimental data. The low velocity is due to the large thickness of the air cavity adopted in this ventilated façade (24 cm).
- It was shown that the model of the whole building could predict the trend of the indoor air temperature during the period in which the heating plant of the tower was turned off, although the ESP-r simulation overpredicts the degree of thermal insulation and the thermal inertia of the building, probably due to uncertainties in thermophysical properties of the materials involved in the structural elements of the building.

CHAPTER 6

EMPIRICAL VALIDATION MODELLING VENTILATED RAINSCREEN IN SUMMER PERIOD

6.1 Introduction

In this chapter the thermal behaviour of a rainscreen ventilated façade during the summer period has been investigated numerically. As in the previous chapter one section describes a numerical study to select the best ESP-r air flow network for simulations (Section 6.2). The model setup in the ESP-r software is explained and finally the results are validated. Comparisons between measured and predicted values are shown in section 6.4. The Chapter ends with remarks and conclusions on the validation of the rainscreen ventilated façade summer model.

6.2 Upgrade for the test cell in the summer period

In order to investigate the summer thermal performance of the rainscreen wall component, a series of tests were performed, during the period from July 2nd to September 17st 2010. Tests were carried out with different wall setups (seven patterns) concerning a different external rainscreen material, a different color of the external skin and a different thickness of the air cavity. In addition, the influence of ventilation inside the air cavity through a series of conditions concerning opened/closed joints and opened/partially/closed grills was analyzed.

All data on geometric features, thermal properties of building components, location, description of the test cell, can be found in Chapter 4. However a brief description of ventilated walls will be given. As stated in the Section 4.2 (Chapter 4), all external walls are three-layered with a middle layer composed of a ventilated air cavity and an external layer. The external layer consists of an opaque cover (in the summer period either stone cladding or aluminum materials was used) with open joints that are separated from the inner wall by the ventilated air cavity. At the top and at the bottom of this tower the ventilation grills are located. A horizontal solar obstruction, about 70 cm over the external side, provides protect the top grids from weather. The façade is subjected to real weather conditions, but only the South and West sides have been equipped with a series of sensors.

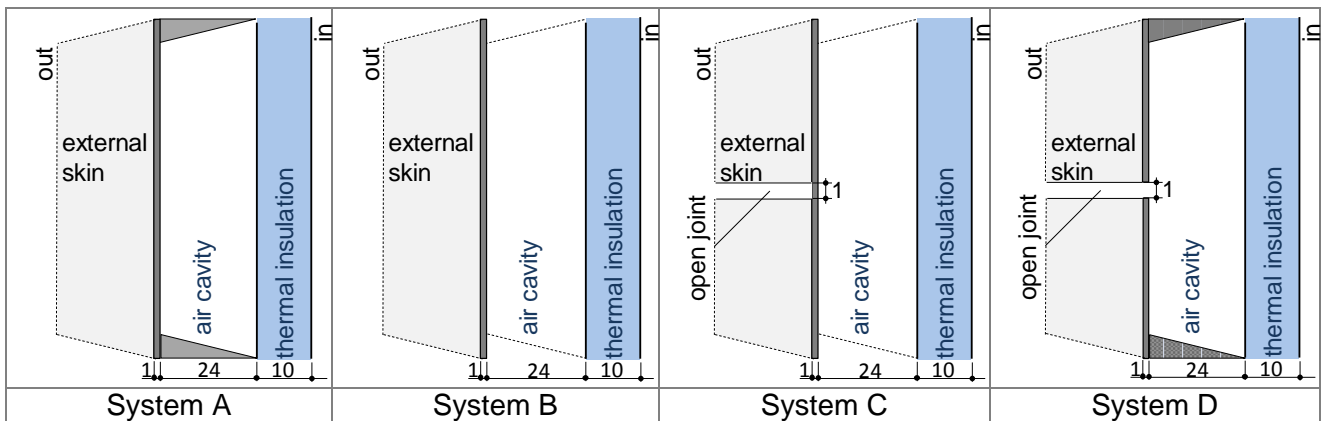


Figure 6.01: Isometric view of the rain-screen walls (dimensions in cm)

Every sensor used in experimental measurements is described in the Section 4.3 (Chapter 4). As for the winter setup each wall of the test cell was divided along the vertical direction of the cavity into 3 sections; sensors were located in each section along the cavity and outside. Of course, all sensors were connected to a dedicated Data Acquisition System. Data were recorded at intervals of 5 min and can be monitored remotely by using an Internet connection. The test cell was cooling continuously at room temperature of 25 °C by means of a heat pump system.

The analyzed patterns according to the configurations shown in Figure 6.01 were collected. In details, the studied configurations for the summer are:

- N° 1 pattern with ventilation grills at the top and at the bottom completely closed and joints closed. This configuration is called System A;
N° 2 patterns with ventilation grills at the top and at the bottom completely opened and joints closed. This configuration is called System B;
- N° 2 patterns with ventilation grills at the top and at the bottom completely opened and joints opened. This configuration is called System C;
- N° 2 patterns with ventilation grills at the top and at the bottom partially closed and joints opened. This configuration is called System D.

Table 6.01 shows the characteristics of each configuration tested More details on the type of patterns may be found in Chapter 4.

Table 6.01. Patterns for rainscreen ventilated façade on the West and South side

System	Patterns	Orientation	Air cavity (cm)	Ventilation grills	Joints	Skin finish	Skin material	Start monitoring	End monitoring
A	W5	West	24	Completely close	Close	Dark	Stone cladding	11/09/2010	17/09/2010
B	S0	South	24	Completely open	Close	Bright	Stone cladding	02/07/2010	04/07/2010
	W2	West	24	Completely open	Close	Bright	Stone cladding	17/07/2010	31/07/2010
C	S5	South	10	Completely open	Open	Dark	Alluminium	11/09/2010	17/09/2010
	W3	West	24	Completely open	Open	Dark	Stone cladding	03/08/2010	23/08/2010
D	S4	South	10	Partially close	Open	Dark	Alluminium	26/08/2010	06/09/2010
	W0	West	24	Partially close	Open	Bright	Stone cladding	02/07/2010	04/07/2010

6.3 Modelling setup for the summer period

More models of the test cell were created by using the simulation program ESP-r, which is a transient simulation program based on the finite volume technique (Chapter 3). As stated before, by using ESP-r, it is possible to model all the energy fluxes and the fluid flows within combined building and plant systems subject to dynamically varying boundary conditions.

In this work, rainscreen ventilated skin façades of the test cell was studied numerically using some nodal flow network model; an airflow network was integrated with the corresponding thermal network model so that the calculated airflows are based on nodal temperatures from the thermal model, and the resulting predicted airflows are used in the energy balances of the thermal simulation with an iterative solution procedure. More details on the model used can be found in Chapters 3 and 4. The thermal properties of rainscreen materials are the same used for the winter model as for Table 4.01 (Chapter 4) except for the patterns on the South side S0 and S4 (aluminium with dark finish) and that one on the West side the W5 (dark finish). The most important properties of the external skin of the ventilated façade are given in Table 6.02. The emissivity value of the aluminium was measured in the lab for a test sample by means an infra-red camera technique as indicate in ASTM E1933-99a [2010]. The solar absorption coefficients for bright and dark surface finishes of any materials were found to be 0.3 and 0.9 respectively, they are used in the dynamical simulation.

Table 6.02: Thermal properties of the externals skin

Layer	Thickness (cm)	Thermal conductivity ($\text{W m}^{-1} \text{K}^{-1}$)	Density (kg m^{-3})	Specific Heat ($\text{J kg}^{-1} \text{K}^{-1}$)	Emissivity (-)
Stoneware	1.0	1.30	2300	840	0.90
Alluminum	0.05	160	2800	840	0.22

In order to model the whole test building, the rainscreen wall is divided into a stack of three zones adjacent to each of the floor levels. More modeling details are reported in Chapter 4. It is known [Poizaris 2006, Costola 2009] that the air flow in the cavity is dependent on the wind pressure conditions on the building's skin, on the stack effect and the discharge coefficient (C_d) of the openings, but unfortunately there are no experimental measurements on the discharge coefficient for the open joints and the ventilation grills of this test cell.

In this analysis, the grilles at the bottom and the top of the ventilated façade were modelled as a standard orifice airflow component with a discharge coefficient equal to 0.65 and an opening area equal to 50% of the geometric area for the model with ventilation grills partially close and an opening area equal to 100% of the geometric area for models of the ventilation grills completely opened. Also the open joints in the façade were modelled as standard orifice airflow components with a discharge coefficient equal to 0.65 and opening area equal to the geometric area. There are two type of air flow network: one representing thermal and flow path inside the air cavity and another inside rooms of the test cell. The air flow network inside the air cavity simply consists of three air nodes for each side of the test cell. Each node is linked together by means vertical links and also horizontal links. More information about the air-flow scheme can be found in Section 3.3.

In order to define the seven patterns of the four systems in ESP-r, four different models were modeled as shown in Figure 6.02.

Model A consists only of twelve internal air cavity nodes representing the buoyancy effects and there are no links with surrounding because both ventilation grills and joints are modelled as closed. The air flow network of model B is the same as that of model A but air cavity internal nodes for each side are linked with two connections representing the ventilation grills modelled as completely opened. Model C is the same setup of B but with joint connections with the surrounding because joints are modelled opened. In this case the geometric area of the ventilation grills was coincident with geometric area of the grills. Finally, model D is the same as C but the geometric area of the ventilation grills was considered to be 50% of the total projected area. Thermal bridges of the test building were not included in the model as they were considered negligible. The cooling system was introduced into the model by imposing a constant value of the room temperature.

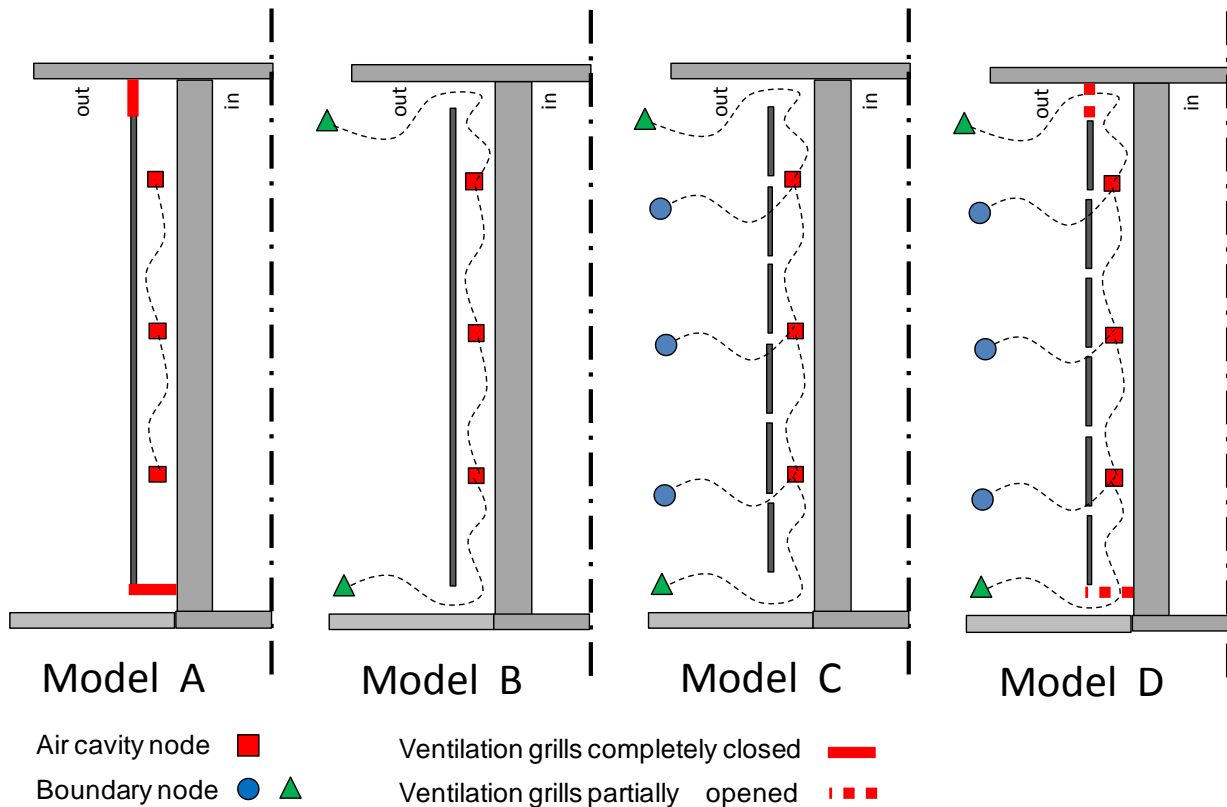


Figure 6.02: Model setups in ESP-r (A - D)

6.4 Model validation (summer period)

The aim of this study is to analyse the accuracy for four models by using Esp-r as dynamic simulation software. Each pattern was modelled in ESP-r by means four different airflow network models as depicted in Figure 6.02:

- The flow network considers joints and grills at the bottom and the top as closed (in the cavity there is only thermal buoyancy between the cavity and internal room and wind effects are not included in the analysis). This model was used for the pattern W5 and is called model A.
- The flow network considers all joints closed; the ventilation grills at the bottom and the top are considered completely open. This model was used for both patterns S0 and W2 and is called model B.
- The flow network considers all joints opened; the ventilation grills at the bottom and the top are considered completely open: This model was used for both patterns S5 and W3 and is called model C.
- The flow network considers all joints opened; the ventilation grills at the bottom and the top are considered partially opened: This model was used for both patterns S4 and W0 and is called model D.

For the purpose of model validation, measured local weather data for about three months (July 2nd– September 17st 2010) were used. The measured local weather data include external air temperature and air humidity, wind speed and direction and horizontal global solar radiation.

In Table 6.03, the maximum, the minimum and the average ambient temperature (AT), ambient relative humidity (ARH), horizontal global solar radiation (HGSR), wind speed (WS) and prevailing wind direction (WD) of the local climate data during the tested summer period are quoted.

Table 6.03: Summary of sub-period weather conditions

Sub-period		AT (°C)	ARH (%)	HGSR (Wm ⁻²)	WS (ms ⁻¹)
(sub-period 0) 02/07–04/07	max	34.3	81	921	2.8
	min	18.2	43	0	0.1
	avg	27.1	61	307	0.9
(sub-period 2) 17/07–31/07	max	36.4	96	999	9.3
	min	13.9	24	0	0.0
	avg	24.7	62	279	1.2
(sub-period 3) 03/08–23/08	max	31.0	97	974	4.2
	min	15.0	26	0	0.0
	avg	23.4	67	288	1.0
(sub-period 4) 26/08–06/09	max	36.1	99	850	14.6
	min	11.7	35	0	0.0
	avg	21.7	66	235	1.5
(sub-period 5) 11/09–17/09	max	28.4	93	962	3.1
	min	13.4	41	0	0.0
	avg	20.1	68	164	1.1

It possible to notice that during the tested period the external air temperature varied between 12 and 36° C with an average air humidity of about 60% and the horizontal global solar radiation reached values greater than 900 Wm⁻². The wind speed was mostly low except in a few time that reached peak values of about 9 and 14 ms⁻¹. The wind direction is quite variable, but South-East is prevailing.

In order to quantify the different performances of the models the Pearson coefficient (R-squared) and other statistical parameters (more details are given in Section 5.2) were calculated. In Table 6.04 results for the cavity air temperature of all analyzed patterns (Table 6.01) for four models (Figure 6.02) of the West and South façades by using different airflow network models for the ventilated façade patterns (Figure 6.01) are listed. It is interesting to observe that the difference between the predicted and the measured values of the air cavity along the West and the South façades for each pattern change significantly with the model adopted. Statistical data as the maximum (D_{MAX}) and the minimum (D_{MIN}) difference between the measured and predicted cavity air temperature, the average difference (MEANDT), the root mean square difference (RSQMEANDT) and finally the Pearson coefficient (R-SQUARED) are listed.

Table 6.04: Results for cavity air temperature of the simulated patterns

MODEL	Grills ventilation	joints	pattern	D _{MAX} (K)	D _{MIN} (K)	MEANDT (K)	RSQMEANDT (K)	R-SQUARED (-)
A	close	close	W-5	8.28	-9.22	-0.33	2.66	0.9014
B	open	close	S-0	3.49	-2.31	0.13	1.20	0.9511
			W-2	4.72	-2.09	0.56	0.96	0.9693
C	open	open	S-5	1.62	-5.77	-0.92	1.90	0.9519
			W-3	8.01	-5.35	0.91	1.80	0.9055
D	Partially open	open	S-4	3.81	-7.07	-0.29	1.74	0.9600
			W-0	2.44	-3.42	0.27	0.90	0.9766

It is interesting to observe that the R² parameter values of cavity air temperature are quiet high (good accuracy) for all patterns, especially for models B and D (R² higher than 0.95).

If models B, C and D are adopted for the ventilated wall the numerical results exhibit a good agreement with the experimental data; the R² coefficient in Table 6.04 between the measured and

the predicted values of the cavity air temperature is higher than 0.95 for the West and South-facing walls.

It is interesting to notice that the R^2 parameter of models B, C and D is quite high if different patterns are adopted.

In Figures 6.03-6.06 cavity air temperature correlations between measured and predicted values respectively for the pattern W5 (model A), W2 (model B), S5 (model C) and S4 (model D) are plotted. It possible to see that the discharge from the bisector line (corresponding to the perfect solution) of the model A is not very larger (14%) than those other models (8-11%). These data confirm the values of the R^2 parameter given in Table 6.04.

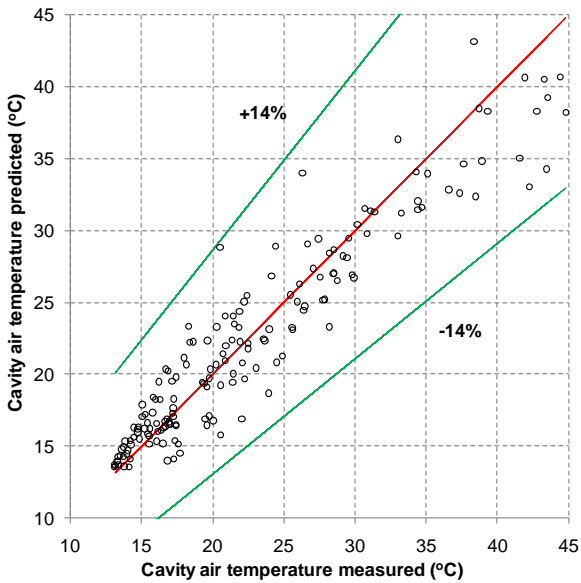


Figure 6.03: Correlation between measured and predicted cavity air temperatures of the W5 patterns for model A.

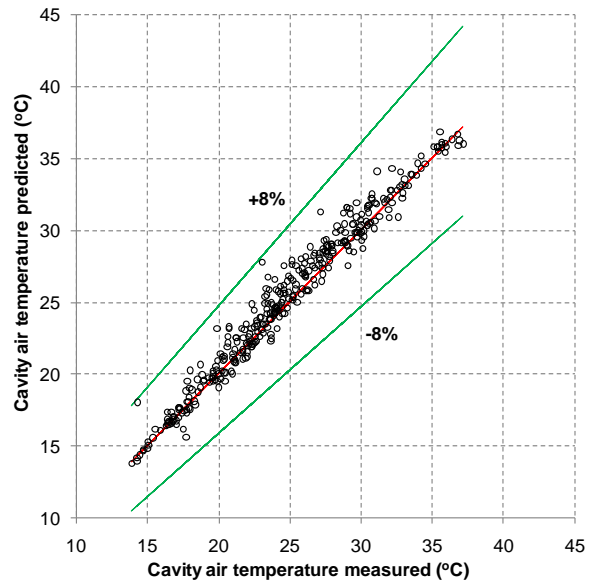


Figure 6.04: Correlation between measured and predicted cavity air temperatures of the W2 patterns for model B.

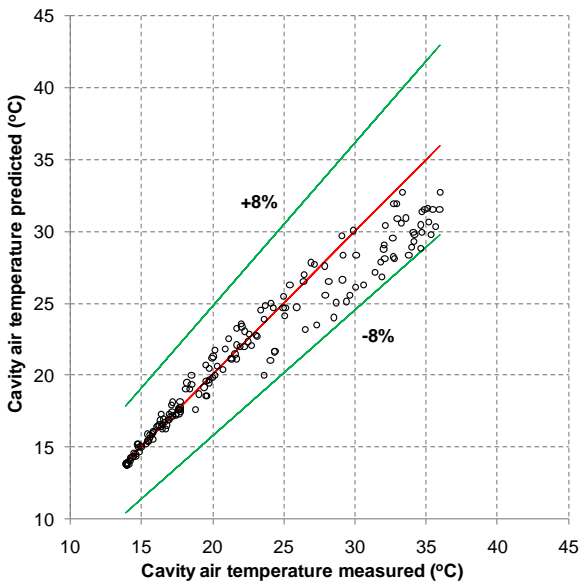


Figure 6.05: Correlation between measured and predicted cavity air temperatures of the S5 patterns for model C.

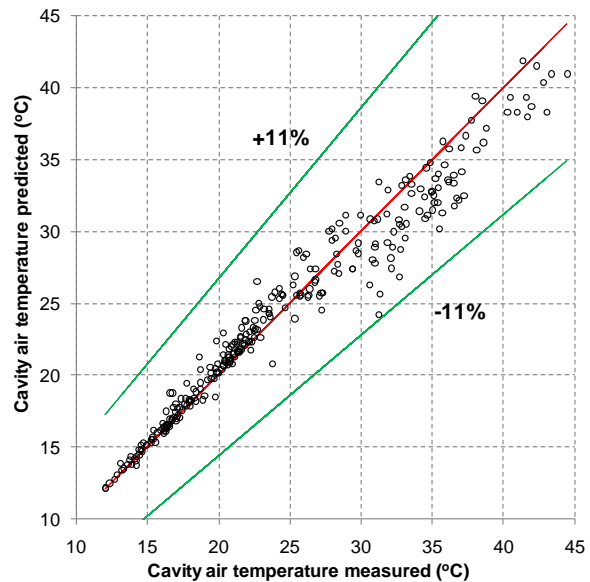


Figure 6.06: Correlation between measured and predicted cavity air temperatures of the S4 patterns for model D.

An interesting result of this comparison is that models B and D have similar predictive capability for the cavity air temperature; in fact, if the value of the R^2 parameter linked to South (S0 and S4 patterns) and West (W0 and W2 patterns) facing façade obtained by adopting the models B and D are compared, it can be shown that this parameter changes only by 1.0-1.6% going from one model to the other D.

6.5 Comparison with monitored data (summer period)

The previous analysis showed that models A, B, C and D represent the best compromise between accuracy and model complexity for general modelling purposes.

The numerical results obtained by means of the ESP-r model of the rainscreen ventilated skin façade in terms of temperature predicted of the wall have been compared with the corresponding measured quantities during the whole test period. The following figures from 6.07 to 6.10 show the measured and predicted temperatures:

- Ambient temperature;
- Exterior surface temperature of external skin;
- Interior surface temperature of external skin ;
- Cavity air temperature;
- Exterior surface temperature of internal wall;
- Interior surface temperature of internal wall (or Internal surface room temperature);
- Indoor temperature.

The measured (M) and predicted (P) temperatures were obtained through arithmetic averaging both for sensors (measured data) and nodes (predicted data). The Figures show two temperature trend over time: one time represents the maximum cavity air temperature reached (trend temperatures at the top) and the second time represents the minimum cavity air temperature reached (trend temperatures at the bottom). In addition, the horizontal global solar radiation (HGSR), the wind and direction (WD) speed (WS) and cavity air velocity (CAV) are indicated.

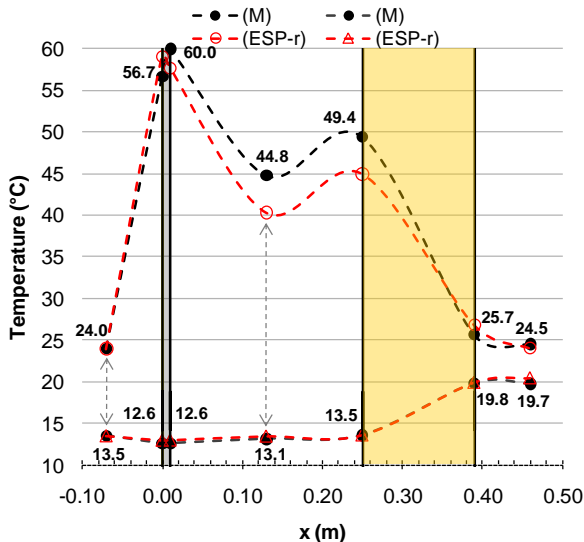
In Figures 6.07 and 6.08 two monitored patterns W5 (model A) and W2 (model B) are depicted. In Table 6.02 the setup configurations of both patterns are listed.

As seen in the graph, ambient temperature varied between 13.5° C and 24.0° C and horizontal global solar radiation reached 962 Wm^{-2} . The cavity air temperature ranged between 13.1 ° C and 44.8° C and the surface temperature of the external skin was lower than that inner side. The surface skin temperature of the W5 pattern reaches 56.7° C while the inner reached 60° C. This temperature rise was not predicted by the dynamic simulation software, possibility because of the lack of reliable information on the thermal inertia of the skin. The cavity air temperature appears to be higher than the ambient temperature by comparing all configurations, despite the ambient temperature is quite low in the analyzed period. The cavity air temperature of the pattern W5 is the highest of the all analyzed configurations. Probable this is likely due to the absence of external ventilation in the channel and to the dark finish of the external skin.

Unlike the case of maximum temperature, the measured and predicted temperatures and also the cavity air velocities agree quite well for the case of the minimum temperature. The air cavity and the exterior surface of the internal wall measured and predicted temperature do not agree. In this case the model needs further calibration with more the thermal properties of the material. However trends at the top of the follow figures regarding the weather critical for the ventilated façade in this period, especially if it will to observe the influence of solar radiation.

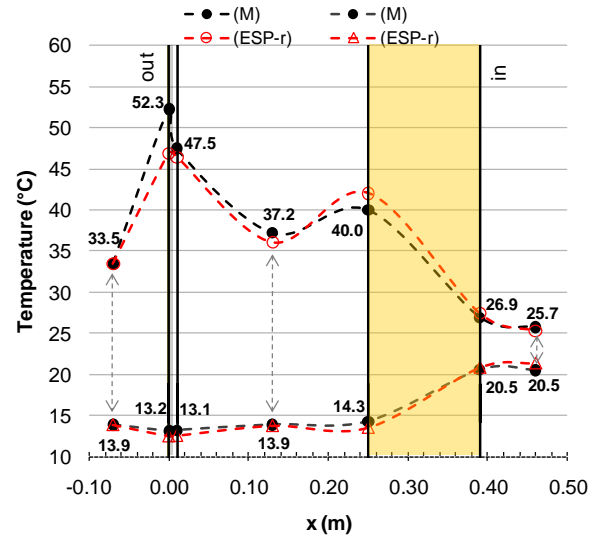
The cavity air temperature W2 pattern was agreed quite well also for the critical trends depicted in Figure 6.08. In this case the ambient temperature varied between 13.9° and 33.5° C and the horizontal solar radiation reached 999 Wm^{-2} (the highest value of the whole summer period). Despite the bright finish of the external rainscreen skin its exterior surface temperate high

temperature above 52° C. It possible to see a discrepancy between predicted and measured temperature for the exterior surface of the rainscreen, but the other temperatures agree. It possible to notice two different temperature slopes inside the wall, if one compare two patterns W5 and W2. Despite the low ambient temperature for the W5 pattern the wall was more thermal stressed than the W2 pattern. The temperature difference between the exterior and internal surfaces of inner wall is about 25 K for the W5 pattern, while that difference was about 15 K for the inner wall of W2 pattern.



	Time (gg/mm hh.mm)	SR (W m ⁻²)	WS (m s ⁻¹)	WD (-)	CAV (m s ⁻¹)
—●—	11/09 17.30 (M)	321	0.80	NNE	0.17
-○-	11/09 17.30 (P)	321	0.80	NNE	0.34
-▲-	12/09 6.30 (M)	2	0.30	SSW	0.00
-△-	12/09 6.30 (P)	2	0.30	SSW	0.01

Figure 6.07: Temperature trend in the W-5 patterns (Model A)

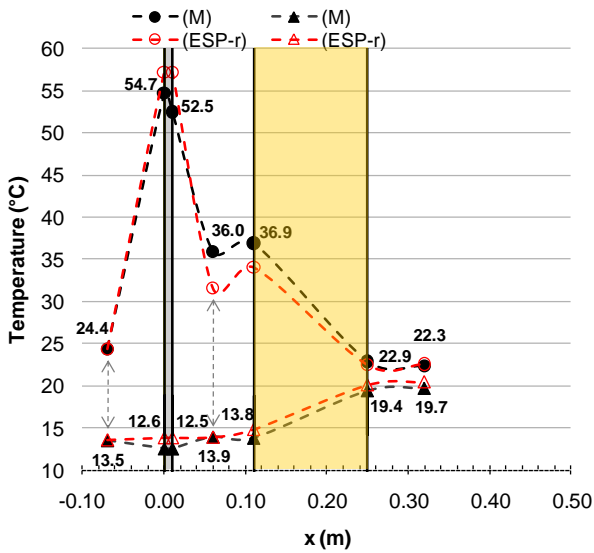


	Time (gg/mm hh.mm)	SR (W m ⁻²)	WS (m s ⁻¹)	WD (-)	CAV (m s ⁻¹)
—●—	17/07 16.30 (M)	610	2.53	E	0.75
-○-	17/07 16.30 (P)	610	2.53	E	0.38
-▲-	27/07 5.30 (M)	1	0.88	SSE	0.13
-△-	27/07 5.30 (P)	1	0.88	SSE	0.11

Figure 6.08: Temperature trend in the S-0 patterns (Model B)

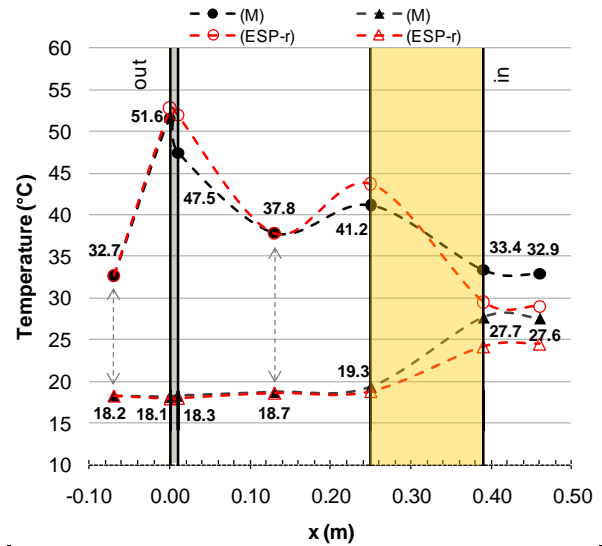
In Figures 6.09 and 6.10 two others monitored patterns (S5 and W0) are plotted. The S5 pattern consists of an aluminum slab system with dark finish with joints opened, air cavity of 10 cm and ventilation grills completely opened. The S5 pattern concerns the South façade and this monitored period was the same for the W5 pattern. Both exterior surface temperatures of the external skin southern and western façade were about 55° C. There were many difference between the pattern W5 (West façade) and pattern S5 (South façade). Most of them regard the external skin material and its color, the air cavity thickness and also the ventilation openness. As a consequence it is possible to see a different value of the cavity air temperature S5 pattern compared with that for the W5 pattern. In Figure 6.09 it possible to observe that measured and predicted values of temperature agree quite well except the one of the air cavity one plotted at the top.

Finally the trend of temperature of the W0 pattern is shown in Figure 6.10. This pattern consists of a porcelain stoneware tile systems with bright finish with joints opened, air cavity of 24 cm and ventilation grills partially opened. In the monitored period the ambient temperature varied between 18.2° C and 32.7° C and the horizontal global solar radiation reached 921 Wm⁻². The cavity air temperature ranged from 18.7° to 37.8° C and the exterior surface temperature of the external skin reached 52° C. The measured and predicted temperatures and cavity air velocities agree quite well expect indoor temperature. Calculated indoor temperatures appear to under predict the ones measured. In this period the thermal system was turned off and the air room temperature was floating freely. Cavity air velocity was quite low but both measured and predicted values agreed.



	Time (gg/mm hh.mm)	SR (W m ⁻²)	WS (m s ⁻¹)	WD (-)	CAV (m s ⁻¹)
—●—	13/09 13.30 (M)	746	1.80	NE	1.81
-○-	13/09 13.30 (P)	746	1.80	NE	0.39
—▲—	12/09 6.30 (M)	2	0.30	SSW	0.15
-△-	12/09 6.30 (P)	2	0.30	SSW	0.08

Figure 6.09: Temperature trend in the S5 pattern (Model C)



	Time (gg/mm hh.mm)	SR (W m ⁻²)	WS (m s ⁻¹)	WD (-)	CAV (m s ⁻¹)
—●—	03/07 17.30 (M)	540	2.03	NEE	0.19
-○-	03/07 17.30 (P)	540	2.03	NEE	0.29
—▲—	02/07 5.30 (M)	3	0.65	SE	0.05
-△-	02/07 5.30 (P)	3	0.65	SE	0.05

Figure 6.10: Temperature trend in the W0 pattern (Model D)

6.6 Remarks and conclusions

Results presented in this Chapter about the thermal behaviour of the rainscreen skin envelope were limited to the summer period. Of course, as stated in Chapter 4, additional simulations with a CFD (Computational Fluid Dynamic) code for the analysis of the air flow patterns through the ventilated cavity, particularly if coupled with BS (Building energy Simulation) models, would be useful in providing further results.

The dynamic thermal behaviour of the ventilated façade is strongly influenced by weather conditions (i.e. solar radiation on the external surface, ambient temperature and wind speed and direction), thermal and geometrical properties (i. e. different materials, different thickness of the air cavity, different openness of ventilation grills and joints and also different colour of the exterior surface of the external skin). Comparisons described in this section aim to demonstrate that the model of the ventilated façade is able to take into account the combined effects of these quantities.

CHAPTER 7

DYNAMIC THERMAL PERFORMANCE OF THE VENTILATED RAINSCREEN FAÇADE

7.1 Introduction

Many works focus on the thermal performance of this complex system. For example Kairys and Karbauskaite [2003] analyzed the transient heat flux through a vertical lightweight wall with and without a naturally ventilated cavity for a selected extreme day. They showed a 30% decrease in the maximum heat flux on the inner surface of a wall with a naturally ventilated cavity compared to a wall with no cavity. Balocco [2002 and 2004] used a steady state calculation model to simulate and to study the energy performances of a ventilated façade and also to compare different façade systems. Results show that it is possible to obtain a relevant solar cooling effect when the air cavity width of the chimney is longer than 7 cm. Biwole et al. [2008] stated that the optimal width for the ventilation channel for roofs must lie between 6 and 10 cm. Ciampi et al. [2003] illustrated an analytical method suitable for design applications, in order to evaluate the energy performance of ventilated façades. Faggembauu et al. [2003a, 2003b] used a specific numerical code to simulate the behaviour of a typical ventilated façade over the course of one year in Mediterranean climatic conditions. They defined two parameters to summarize the performance of a double ventilated façade. These parameters were also evaluated to the present work, but the results obtained are not suitable at the rainscreen ventilated façade typology.

In this Chapter the summer thermal performance of analyzed rainscreen ventilated façade is illustrated. Thermal performances in summer period are characterized by the dynamic thermal transmittance [EN ISO 13786 2007] for every analyzed summertime pattern. Two equations for dynamic parameter are used. The main aim of this chapter is to investigate on the best summer thermal performance of all monitored patterns in summer period (see Chapter 4).

A study on the summer dynamic thermal performance for different configuration setups of rainscreen walls was carried. In particular, influences of ventilation grills, air cavity thickness, skin's colour, skin's material, orientation of façade were investigated.

7.2 Summer thermal performance

In the summer period it is quite difficult to evaluate the thermal performance by only one indicator parameter. In the dynamic regime the steady state thermal transmittance is not suited to estimate the overall building energy performance: many dynamic indicator parameters can represent the summer thermal performance such as for example, the time lag (or phase lag) [R.J. Duffin 1984, Asan and Sancaktar 1997], the decrement factor [Asan 2006], the thermal heat capacity [M.G. Davies 2004] et cetera. The time lag describes the time it takes for an external heat wave to propagate from the outer surface to the inner surface of walls. The decrement factor is the ratio of the amplitudes of the external heat flux and the internal propagated wave. Time lag and decrement factor are very important characteristics to determine the heat storage capabilities of any material but recently another summer thermal indicator called periodic thermal transmittance (or dynamic thermal transmittance) Up-value (see Section 7.31) is also used. Those dynamic thermal characteristics of a building construction can be calculated using the analytical method in according to the EN ISO 13786 [2007]. The method is based on the work of Carslaw and Jaeger

[1959], who showed that temperatures and heat fluxes on both sides of one building component can be calculated with linear equations when the temperatures vary sinusoidally.

The one-dimensional analytical model for a transient flux calculation from the EN ISO 13786 standard can only be used for a building construction with no cavity or with a closed cavity. For a transient heat flux calculation through a long lightweight building construction with a ventilated cavity a control volume method must be used. In this section ESP-r software will be used to solve the differential equations of mass, momentum and energy conservation for the rainscreen ventilated skin façade in order to evaluate the parameter requested by the Standard [EN ISO 13786 2007].

7.2.1 Periodic thermal transmittance

The periodic thermal transmittance (or dynamic thermal transmittance) Y_{ie} is a complex quantity defined as the complex amplitude of the density of the heat flow rate through the surface of the component adjacent to the internal zone (\hat{q}_{si}), divided by the complex amplitude of the temperature (usually ambient temperature) in external zone (\hat{t}_a) when the temperature in the internal zone is held constant.

In practical terms, periodic thermal transmittance represents the heat flow rate through the internal surface of the component when the ambient temperature varies as a sinusoidal function. It is evident that a low value of the periodic thermal transmittance corresponds to the better summer thermal performance of the building component.

It can be expressed (in complex terms) by the follow formula [EN ISO 13786 2007]:

$$Y_{ie} = -\frac{\hat{q}_{si}}{\hat{t}_a} = -\frac{1}{Z_{12}} \quad [7.01]$$

where Y_{ie} is the periodic thermal transmittance (complex number) and Z_{12} (complex number) is the element for the heat transfer matrix (complex number) which depends only on the thermo-physical characteristics of the building component. More information details can be found in the Standard EN ISO 13786 [2007].

The absolute value of Up-value can also be express by:

$$U_p = \frac{|q''_{si,max} - q''_{si,min}|}{|t_{a,max} - t_{a,min}|} \quad (\text{Wm}^{-2}\text{K}^{-1}) \quad [7.02]$$

where U_p is the absolute value of the periodic thermal transmittance, $q''_{si,max}$ and $q''_{si,min}$ are the maximum and minimum of the density of heat flux through the internal surface of the component respectively, $t_{a,max}$ and $t_{a,min}$ are the maximum and minimum ambient temperatures.

Corrado and Paduos [2010] suggest to use the equivalent temperature (known also such sol-air temperature) in Equation 7.02 instead of ambient temperature in order to take in account the solar radiation and also the thermal interaction between the external skins of the façade with the external environment.

Sol-air temperature [R.J. Duffin 1984, ASHRAE 2005] is the ambient temperature that, in the absence of all radiation changes gives the same rate of heat inflow into the surface as would the combination of incident solar radiation I , radiant energy exchange with the sky q_{sky} and other outdoor surroundings q_{grd} , and convective heat exchange with outdoor air.

It can be expressed as:

$$t_{sol-air} = t_a + \frac{\alpha \cdot I + q''_{sky} + q''_{sur}}{h_e} \quad (^\circ\text{C}) \quad [7.03]$$

where $t_{sol-air}$ is the sol-air temperature ($^\circ\text{C}$), t_a is the ambient temperature ($^\circ\text{C}$), α is the absorptance of surface for solar radiation (-), I is the total solar radiation incident on the surface (Wm^{-2}), h_e is coefficient of heat transfer by long-wave radiation and convection at the outer surface ($\text{Wm}^{-2}\text{K}^{-1}$), q''_{sky} and q''_{sur} are respectively the long-wave radiation incident on the surface from sky and surroundings (Wm^{-2}).

Taking the sol-air temperature instead of t_a , Equation 7.01 can be expressed as:

$$U'_p = \frac{|q''_{si,max} - q''_{si,min}|}{|t_{sol-air,max} - t_{sol-air,min}|} \quad (\text{Wm}^{-2}\text{K}^{-1}) \quad [7.04]$$

where U'_p is the absolute value of the periodic thermal transmittance, $q''_{si,max}$ and $q''_{si,min}$ are respectively the maximum and minimum of the heat flux through the internal surface of the component, $t_{sol-air,max}$ and $t_{sol-air,min}$ are respectively the maximum and minimum of the sol-air temperature expressed by the Equation 7.03 [Corrado and Paduos 2010].

7.2.2 Comparison of periodic thermal transmittance of analyzed summertime patterns

In this section a comparison of the thermal performance of the summertime patterns described in Chapter 6 using both U_p -value (Equation 6.02) and U'_p -value (Equation 6.04).

More detailed information on the analyzed summertime patterns of rainscreen ventilated skin façade can be found in Chapter 6, but a brief summary of their characterization following.

Regarding the South façade, patterns S0, S1 and S2 consist of stone cladding with bright finish while S3, S4 and S5 consist of an aluminium slab system. Ventilation grills of pattern S1 were partially open (50% of the geometric area) while the remaining were completely open. Patterns S3 and S5 consists of aluminium slab system, ventilation grills completely open but the colour of the former was light while that one of the latter was darker. Pattern S4 consists of an aluminium slab system with dark finish and ventilation grills partially open. Only S0 had closed joints.

Regarding the West façade, every analyzed pattern consists of a stone cladding system.

Skins of patterns W0, W1 and W2 were light in colour while W3, W4 and W5 were dark finish. Ventilation grills of patterns W0 and W1 were partially open (50% of the geometric area) while rest being totally open. Unlike previous patterns, ventilation grills of W4 and W5 configuration were completely closed. Patterns with joints opened were W0, W3 and W4 while those ones with joints closed were W1, W2 and W5.

The standard EN ISO 13786 [2007] needs a sinusoidal function to describe ambient temperature. In this case one typical day of the monitored summer period (from July 2nd to September 17th) was selected (see Chapter 4). The transient ambient temperature was built using a sine function with amplitude ($t_{a,max} - t_{a,min}$) 10.0 K around an average daily value of 24.4 $^\circ\text{C}$ with a maximum value at 14:30 (30.0 $^\circ\text{C}$) and a minimum at 4:30 (20.0 $^\circ\text{C}$). The indoor air temperature was a constant value of 26.0 $^\circ\text{C}$.

The horizontal global solar radiation was above 900 Wm^{-2} and the wind speed was considered constant and equal to 1 ms^{-1} (due North). In Figure 7.01 sinusoidal trend of the ambient temperature and solar radiation are depicted.

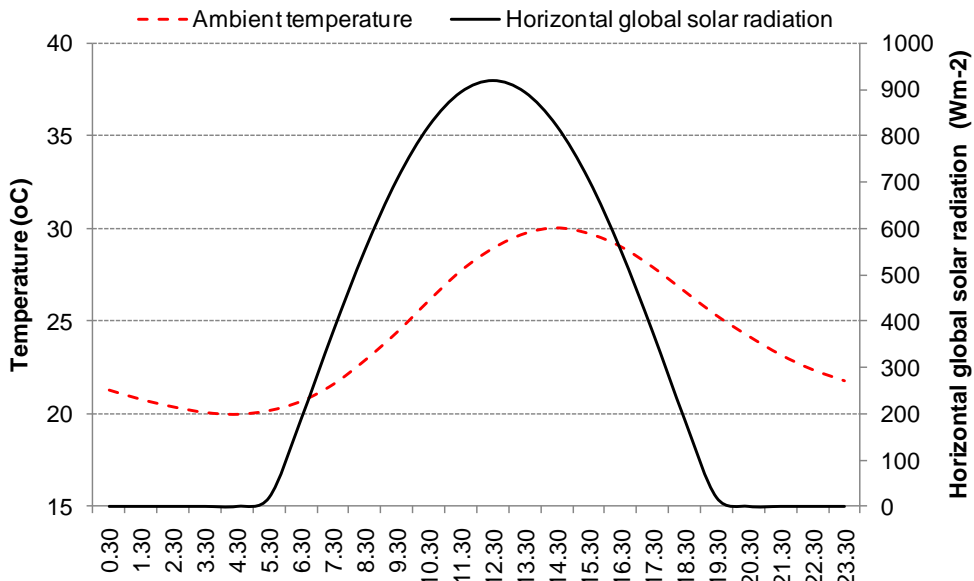


Figure 7.01: Trend of ambient temperature and horizontal global solar radiation for typical summer day

The Standard EN ISO 13786 [2007] takes into account only some thermal properties of building components such thickness (m), thermal conductivity ($\text{Wm}^{-2}\text{K}^{-1}$), density (kgm^{-3}) and specific heat ($\text{Jkg}^{-1}\text{K}^{-1}$) and for this reason it s not suited for such complex envelopes. Other parameters such hemispherical emissivity of the surface and absorbance of the surface for solar radiation, the different rate of air flow (or ventilation grills area) and different orientation are not taken in account for the Up-value estimation. For this reason the Up-value estimated with the Standard procedure is the same value for each different pattern both for the South and West façades.

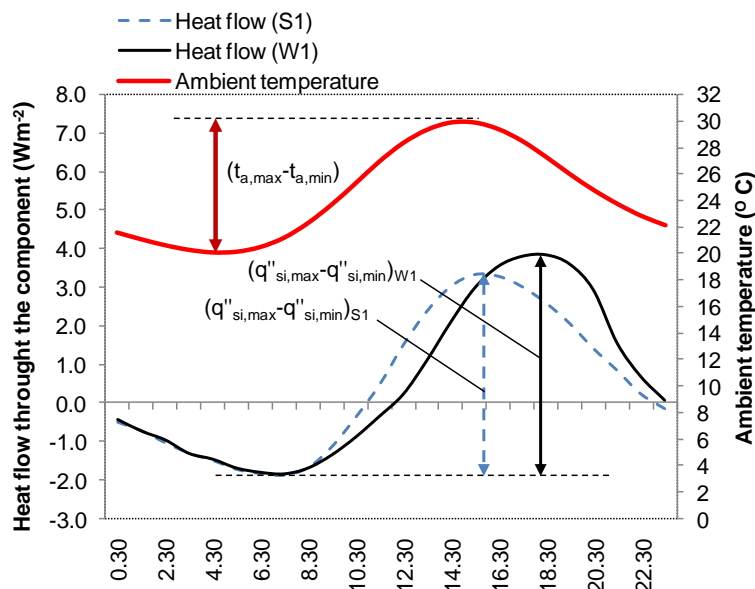
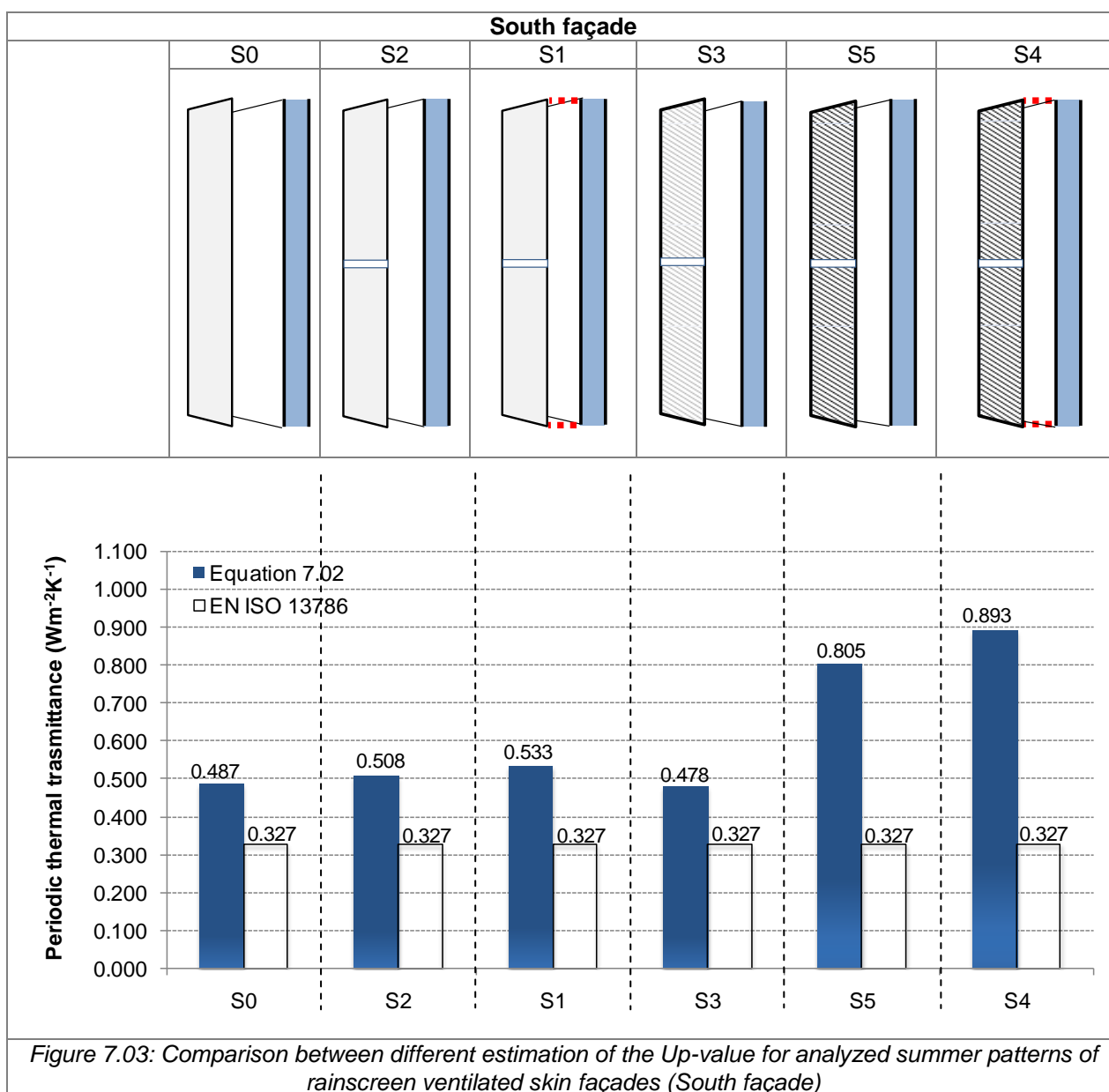


Figure 7.02: Trend of ambient temperature and heat flow through the S1 and W1 patterns respectively

In order to evaluate the Up-value considering also every other parameter mentioned above, the Equation 7.02 can be used to express the summer thermal performance of rainscreen ventilated

skin façade. Both temperature amplitude ($t_{a,max} - t_{a,min}$) and density of heat flow rate amplitude ($q''_{si,max} - q''_{si,min}$) were obtained by means of the ESP-r software (see Chapter 3, Section 3.3). In Figure 7.02 density of heat flow trends of the S1 and W1 patterns respectively and ambient temperature are depicted. For example, the value $0.533 \text{ Wm}^{-2}\text{K}^{-1}$ for S1 pattern (southern façade) in Figure 7.02 is obtain from the rate between 5.22 Wm^{-2} (density of heat flow rate amplitude) and 9.80 K (temperature amplitude). Beside, the value $0.583 \text{ Wm}^{-2}\text{K}^{-1}$ for W1 pattern (western façade) is obtain from the rate between 5.71 Wm^{-2} and the same temperature amplitude (9.80 K). It is interesting to observe that the density of heat flow trend for W1 patterns (western façade) is shifted on the right and higher in comparison with the southern pattern (S1).

In Figures 7.04 and 7.05 comparison between different estimation of Up-values for analyzed summer patterns (from S0 to S5) of rainscreen ventilated skin façades on the South and on West side respectively are depicted.



Firstly, by comparison Up-values obtained respectively by means Equation 7.02 and Standard procedure EN ISO 13786 [2007] for both orientations it can be seen that the former Up-value is

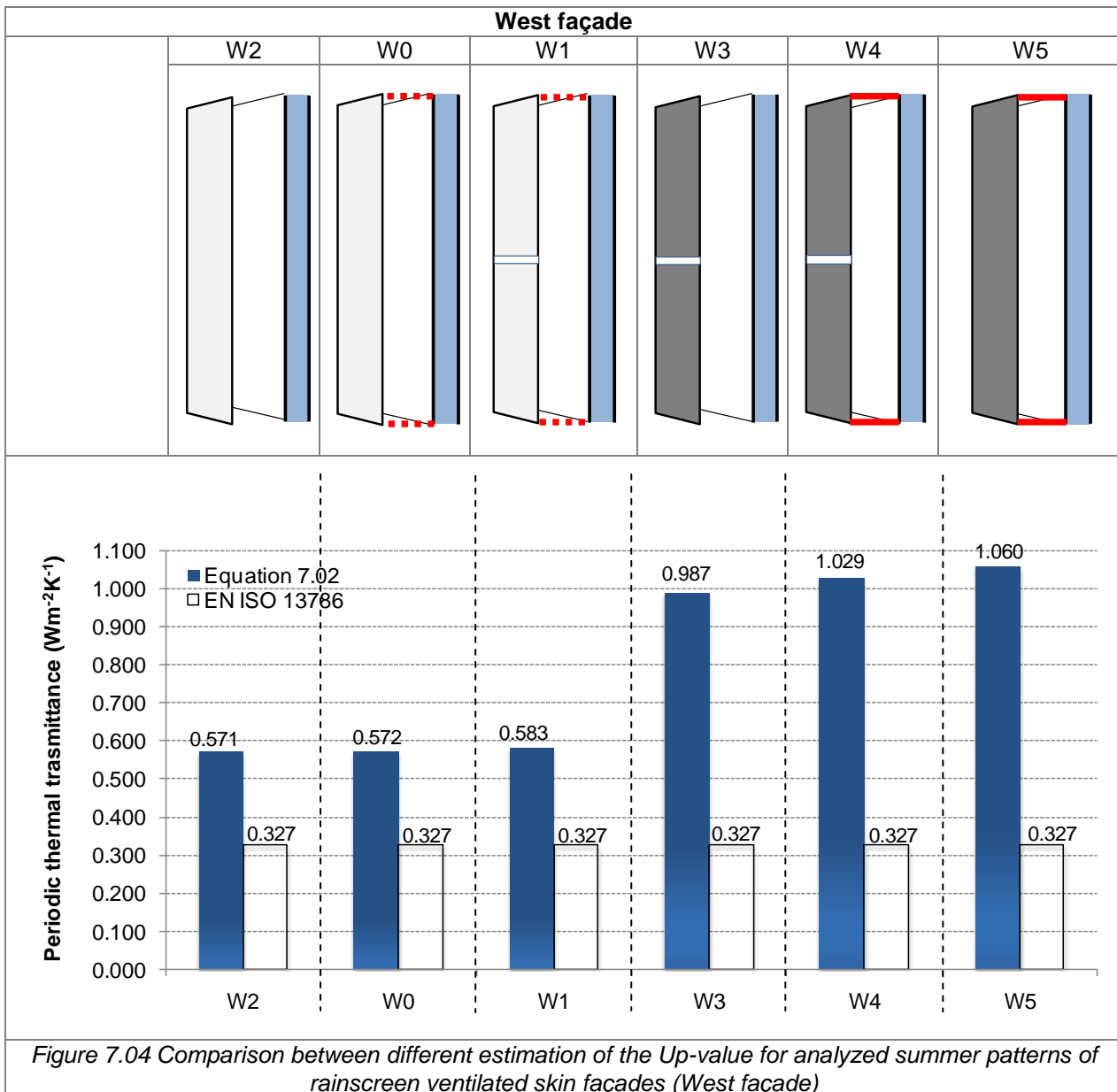
always higher than the latter for every pattern. This suggests that the estimated U_p -value with the Standard procedure over-predicts the summer thermal performance of rainscreen ventilated skin façade. Secondly, U_p -values are different for each analyzed pattern. As consequence of this it possible to state that U_p -values depend from the thickness of the air cavity, ventilation grills, opening joints between slabs, skin colour, skin material and also orientation of the façade (U_p -values of S0 and W2 are respectively 0.487 and $0.571 \text{ Wm}^{-2}\text{K}^{-1}$).

By comparison between S0 and S2 patterns (Figure 7.03) it possible to see the influence of the air cavity thickness on the U-value. In fact, in spite of opened joints the U-value of the S2 pattern ($0.508 \text{ Wm}^{-2}\text{K}^{-1}$) is higher than U-value of the S0 pattern ($0.487 \text{ Wm}^{-2}\text{K}^{-1}$). Probably this increase of the U-value (lower summer thermal performance) is due to the lower air flow enthalpy in the S2 pattern (air cavity of 10 cm) by comparison with the S0 pattern (air cavity of 24 cm).

A reverse phenomenon can be observed by comparison of patterns S1 with S2 and W1 with W2 patterns respectively. In this case the U_p -values of patterns without ventilation grills (S2 and W2, U_p -values of 0.508 and $0.571 \text{ Wm}^{-2}\text{K}^{-1}$) were smaller than patterns with ventilation grills (S1 and W1, U_p -values of 0.533 and $0.583 \text{ Wm}^{-2}\text{K}^{-1}$).

In Figure 7.03 it possible to notice also that U-values of patterns with aluminium slab are smaller than U-values of patterns with stone cladding. For example the U-value of S2 pattern (stone cladding) is $0.508 \text{ (Wm}^{-2}\text{K}^{-1})$ while that of the S3 pattern (aluminium slab) is $0.478 \text{ (Wm}^{-2}\text{K}^{-1})$. The pattern with aluminium slab appears more performance than that one with stone cladding (about 6%). The thermal performance of S3 pattern ($0.478 \text{ Wm}^{-2}\text{K}^{-1}$) decreases if its external skin colour becomes dark (S5 pattern, $U_p = 0.805 \text{ Wm}^{-2}\text{K}^{-1}$) and more so with ventilation grills partially opened (S4 pattern, $U_p = 0.893 \text{ Wm}^{-2}\text{K}^{-1}$).

Similar considerations may be obtained by comparison of the West patterns depicted in Figure 7.04. It is interesting to notice that U_p -values for the W2 and W0 pattern are very similar despite the different setup configurations. Another interesting aspect is the high U_p -value for W3, W4 and W5 in comparison to the rest of patterns. A dark colour for the external skin and a badly well ventilated channel correspond to a lower performance for this kind of envelope.



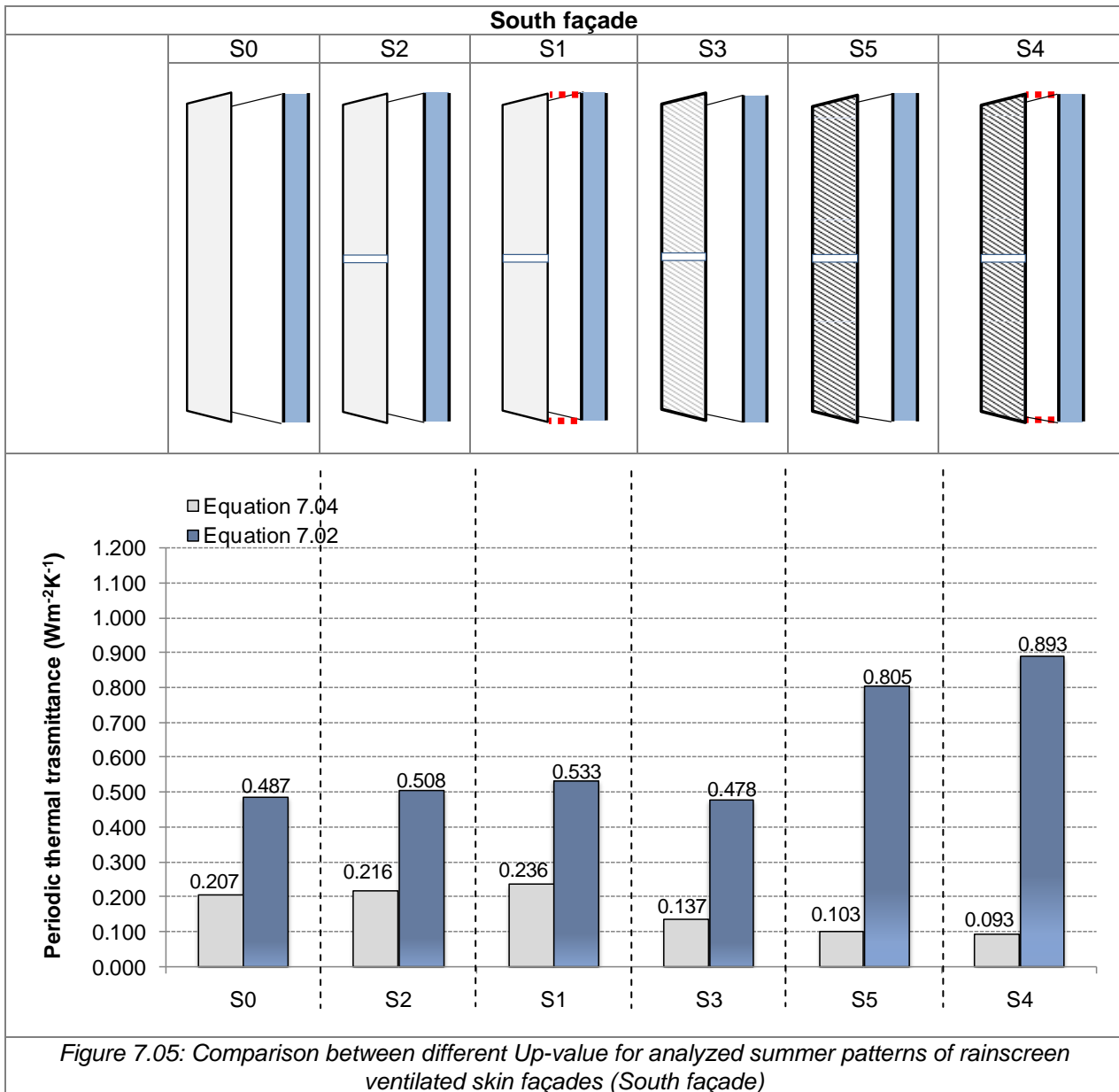
This analysis shows that the best configuration of the rainscreen ventilated skin façade with stone cladding for the summer period is the S0 pattern for the South façade ($U_p = 0.487 \text{ Wm}^{-2}\text{K}^{-1}$) and W2 and W0 patterns for the West façade (0.571 and $0.572 \text{ Wm}^{-2}\text{K}^{-1}$ respectively). The performance of the aluminium skin appears higher ($U_p = 0.478 \text{ Wm}^{-2}\text{K}^{-1}$) than those ones of stone cladding skin ($U_p = 0.508 \text{ Wm}^{-2}\text{K}^{-1}$). The U_p -value of the stone cladding with dark finish is higher than those in aluminium with dark finish.

The periodic thermal transmittance was then evaluated with sol-air temperature instead of the ambient temperature the results are illustrated in the following.

Another way to estimate the summer thermal performance of this complex envelope is to comparison the U_p -values indicated with the Equation 7.04 suggests by Corrado and Paduos [2010].

In this case sol-air temperature was used instead of ambient temperature. Sol-air temperature depends on the absorptance and emissivity of surface for solar radiation and also on the total solar radiation incident on the surface. For this reason, one sol-air temperature for each pattern is calculated.

In Figure 7.05 and 7.06 comparisons of U'p-values (Eq. 7.04) and Up-value (Eq. 7.02) respectively for the South and West façades are depicted.

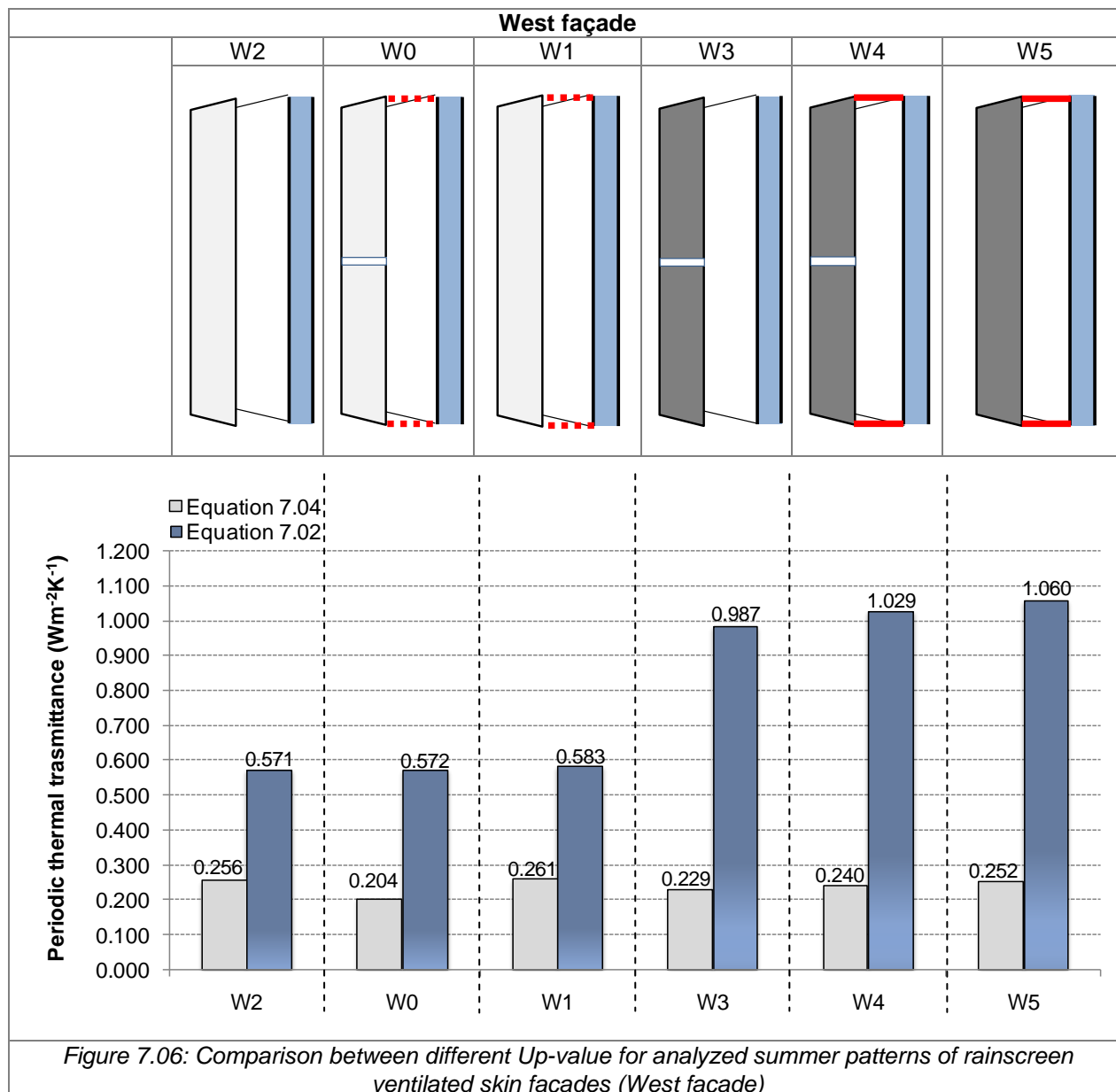


Firstly, by comparison of the U'p-values obtained respectively by means Equation 7.04 and Standard procedure EN ISO 13786 [2007] for both orientations it shows that the former on always smaller than the latter for all patterns. Contrary to the previous comparison, this suggests that the estimated U'p-value with Equation 7.04 overpredicts the summer thermal performance in comparison with the Standard procedure [EN ISO 13786 2007] and the Eq. 7.02 (evaluation of the Up-value with ambient temperature) respectively.

The largest differences between Up-values and U'p-values can be observed in patterns with dark skin.

Unlike the previous parameter, this U'p-value is very different for each pattern especially for those with dark skins. In fact in this case U'p-values for S4, S5, W3, W4 and W5 patterns are smaller than the correspond to Up-values. The explanation lies in the values of sol-air temperature, skin patterns with dark colour present high peak value of sol-air temperature then a high difference temperature ($t_{sol-air, max} - t_{sol-air, min}$) and consequent by a small value of U'p-value. This analysis was

highlighted that patterns with dark skin and absence of channel ventilation present high summer thermal performance. It is evident that if periodic thermal transmittance to be estimated with sol-air temperature instead of ambient temperature, in Equation 7.02 Up-value would overpredicts the summer thermal performance for ventilated façades and it is no suited for to evaluate the thermal performance of this kind of wall.

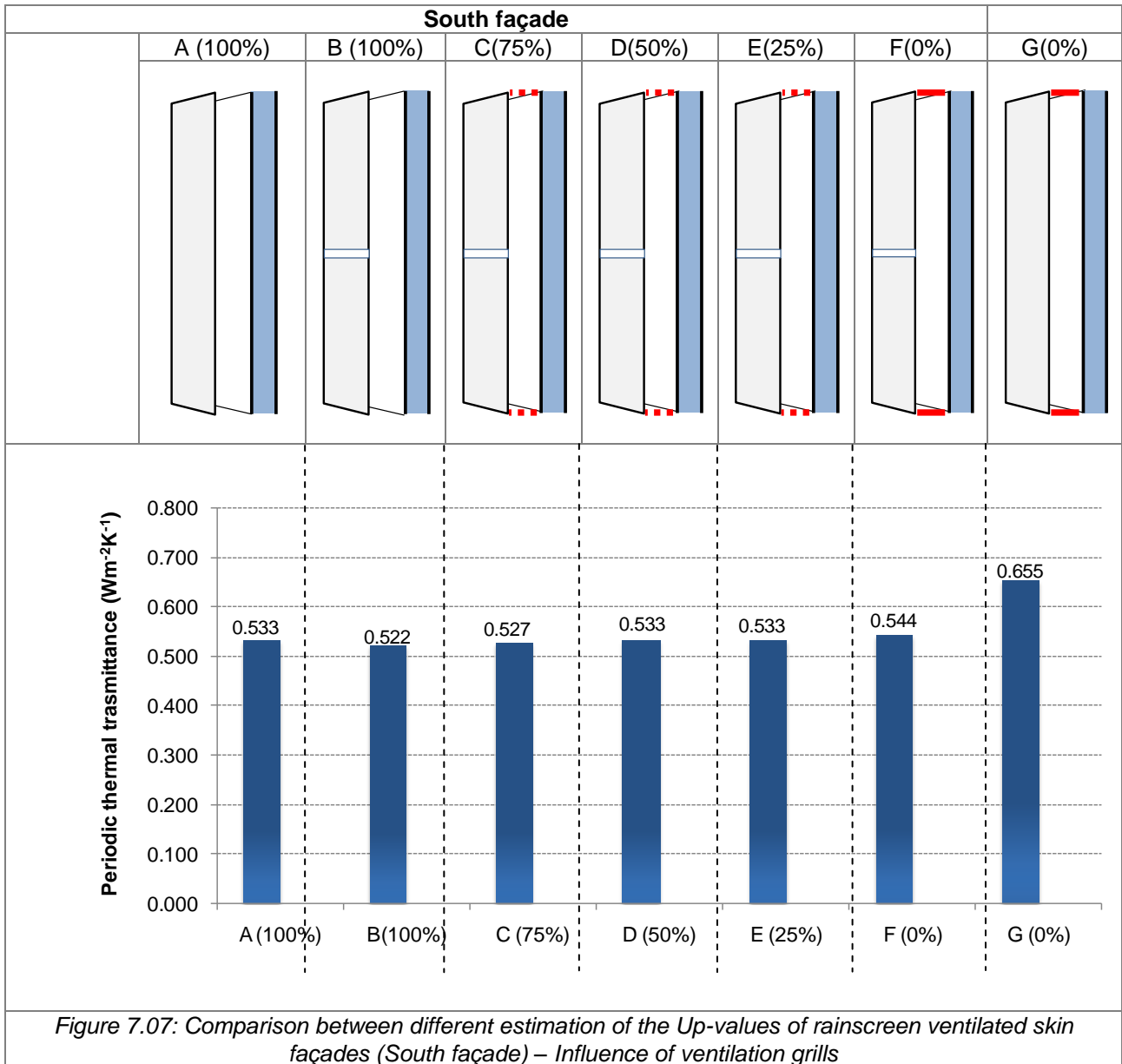


7.3 Analysis of dynamic thermal performance

In order to investigate the best summer thermal performance of rainscreen ventilated skin façade a study of the dynamic thermal performance for different configuration setups of rainscreen walls was made. Many different element influence the summer thermal performance. There are many open questions regarding the thermal performance of this complex envelope; some of them are the influence of ventilation grills, air cavity thickness, skin's colour, skin's material, orientation of façade.

7.3.1 Influence of ventilation grills

In this section the summer thermal performance of different ventilation grills will be studied by comparing the periodic thermal performance described in the previous section (Section 7.2.1). Thermo-physical properties of the ventilated wall studied can be found in Chapter 4 and the boundary conditions used are reported in Section 7.2. In particular, for this analysis a South façade with a stone cladding was selected. The air cavity thickness was 10 cm for all patterns.



In Figure 7.07 seven patterns were chosen with different opening of the ventilation grills. The first from left labelled with A has in ventilation grills completely open and joints closed while the last one labelled G no openings were present. Patterns with percentages in brackets (100%, 75%, 50%, 25% and 0%) represent different opening rate, of the upper and lower ventilation grills. A percentage of 100% represents ventilation grills completely opened while 0% is for completely closed grills.

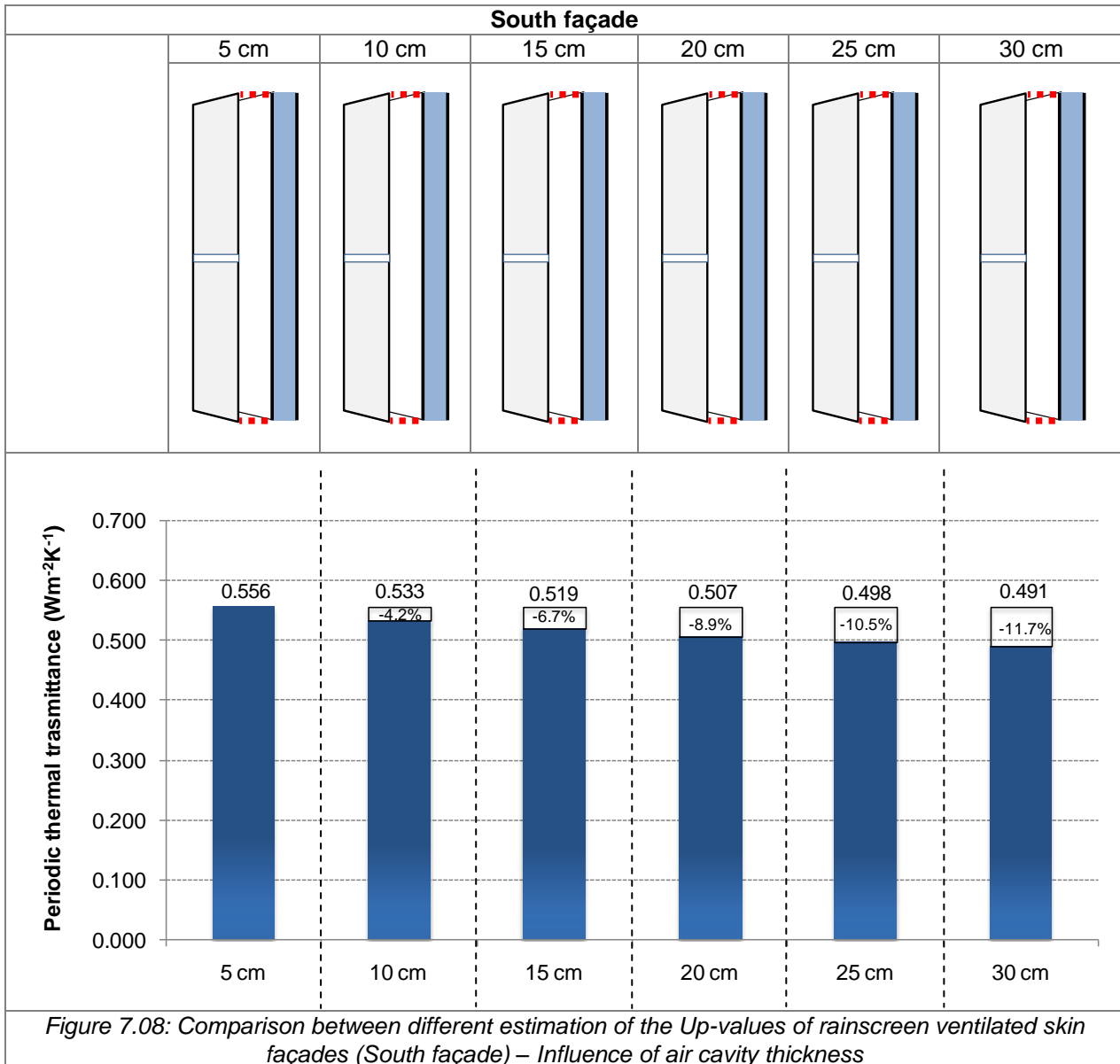
In Figure 7.07 it is interesting to observe that the smallest Up-value correspond to pattern B, with ventilation grills and joints opened. If the area of ventilation grills decreases then the Up-value

increases (lower summer thermal performance). Further, the U_p -value of pattern A is 2% higher than that of B (open joints). Patterns D, E and A have the same value of periodic thermal performance and in this case ventilation grills with geometric area $< 50\%$ do not influence the U_p -value. Moreover the U_p -value of pattern G ($0.655 \text{ Wm}^{-2}\text{K}^{-1}$, no opening) is higher about 22% than pattern A ($0.533 \text{ Wm}^{-2}\text{K}^{-1}$) and about 20% than F ($0.544 \text{ Wm}^{-2}\text{K}^{-1}$). The good ventilation in the channel improves the U_p -value of about 20% for this particular configuration of rainscreen ventilated skin façade. The pattern D in Figure 7.07 corresponds to the pattern S1 in the previous figures.

7.3.2 Influence of air cavity thickness

In this section the influence of air cavity thickness will be discussed for different patterns of rainscreen ventilated skin façade. The analyzed pattern (South façade) consists of a stone cladding tile system light in colour, ventilation grills partially open (50% of geometric area) and joints opened. The investigated air cavity thicknesses vary from 5 to 30 cm. The aim of this analysis is to find the best summer thermal performance of this particular pattern by means of the periodic thermal transmittance.

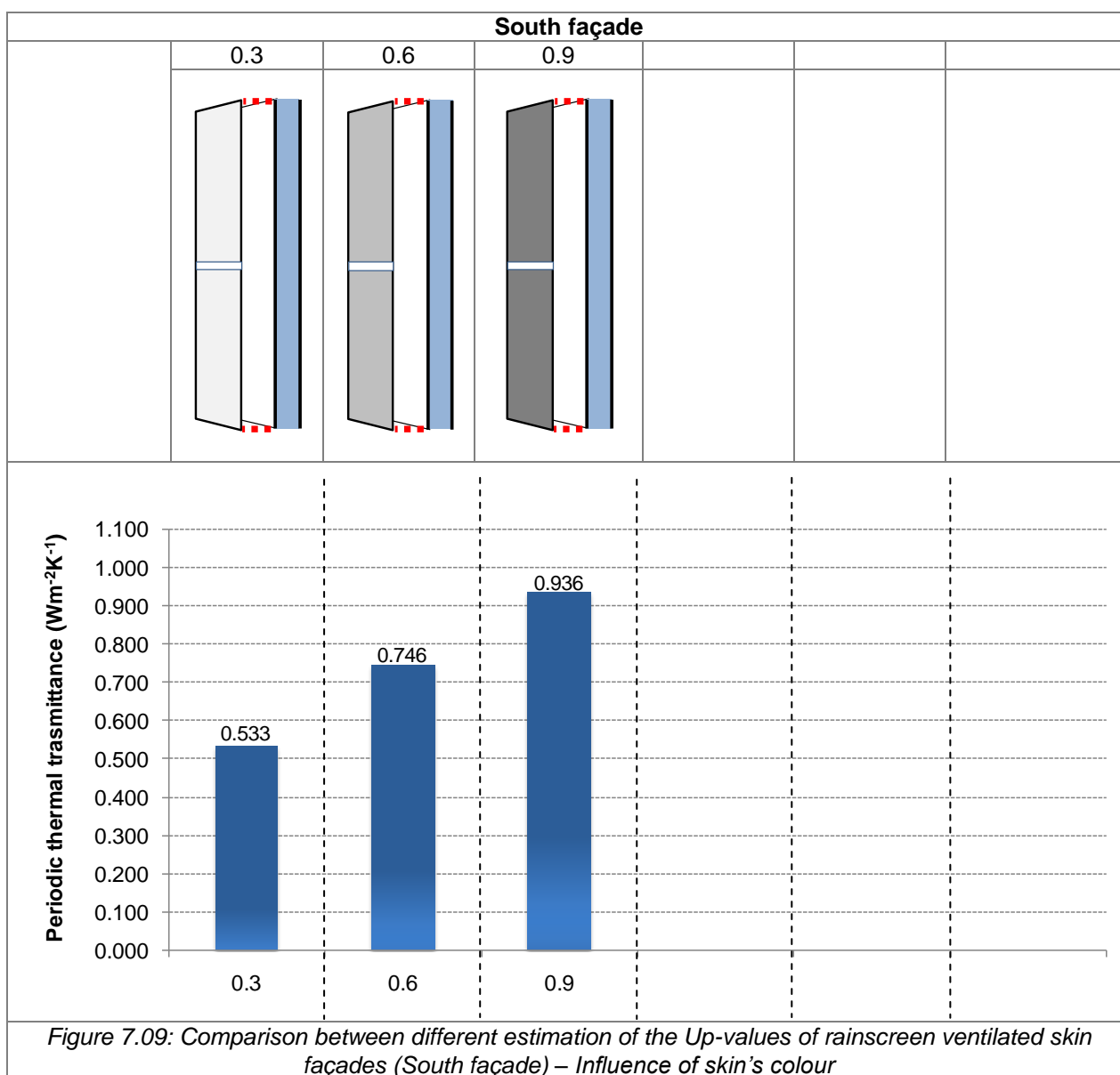
In Figure 7.08 six patterns for different air cavity thickness are depicted. It is interesting to notice that the U_p -value decreases if the air cavity thickness increases. The best incremental is that with 10 cm of air cavity thickness (4.2% going from 5 to 10 cm). In fact the U_p -value of pattern with air cavity thickness of 15 cm is only 2.5% by comparison with the pattern with air cavity thickness of 10 cm. If air cavity thickness reaches 25 cm the U_p -value decreases only of about 10% from the case of a 5 cm air cavity.



7.3.3 Influence of the skin's colour

In order to improve the summer thermal performance of external envelope of buildings appropriate skin's colour is needed. This section highlights the influence of skin's colour for the estimation of the U_p -value of one rainscreen ventilated façade. The rainscreen (only the South façade was analysed) consists of stone cladding tile system with ventilation grills partially open (50% of geometric area) and open joints.

In Figure 7.09 three different patterns for three different absorptance solar coefficients (0.3, 0.6 and 0.9) are depicted. In this analysis only three tone-colours were considered: an absorptance solar coefficient equal to 0.3 for light-tone colours, 0.6 for half-tone colour and finally 0.9 for dark-tone colours. From the Figure 7.09 it is evident that the U_p -value increases for the high value of absorptance solar coefficients. In detail U_p -value for half-tone skin's colour ($0.746 \text{ Wm}^{-2}\text{K}^{-1}$) increases about 40% than those with light-tone colour ($0.533 \text{ Wm}^{-2}\text{K}^{-1}$) and about 75% for the dark-tone colours ($0.936 \text{ Wm}^{-2}\text{K}^{-1}$).

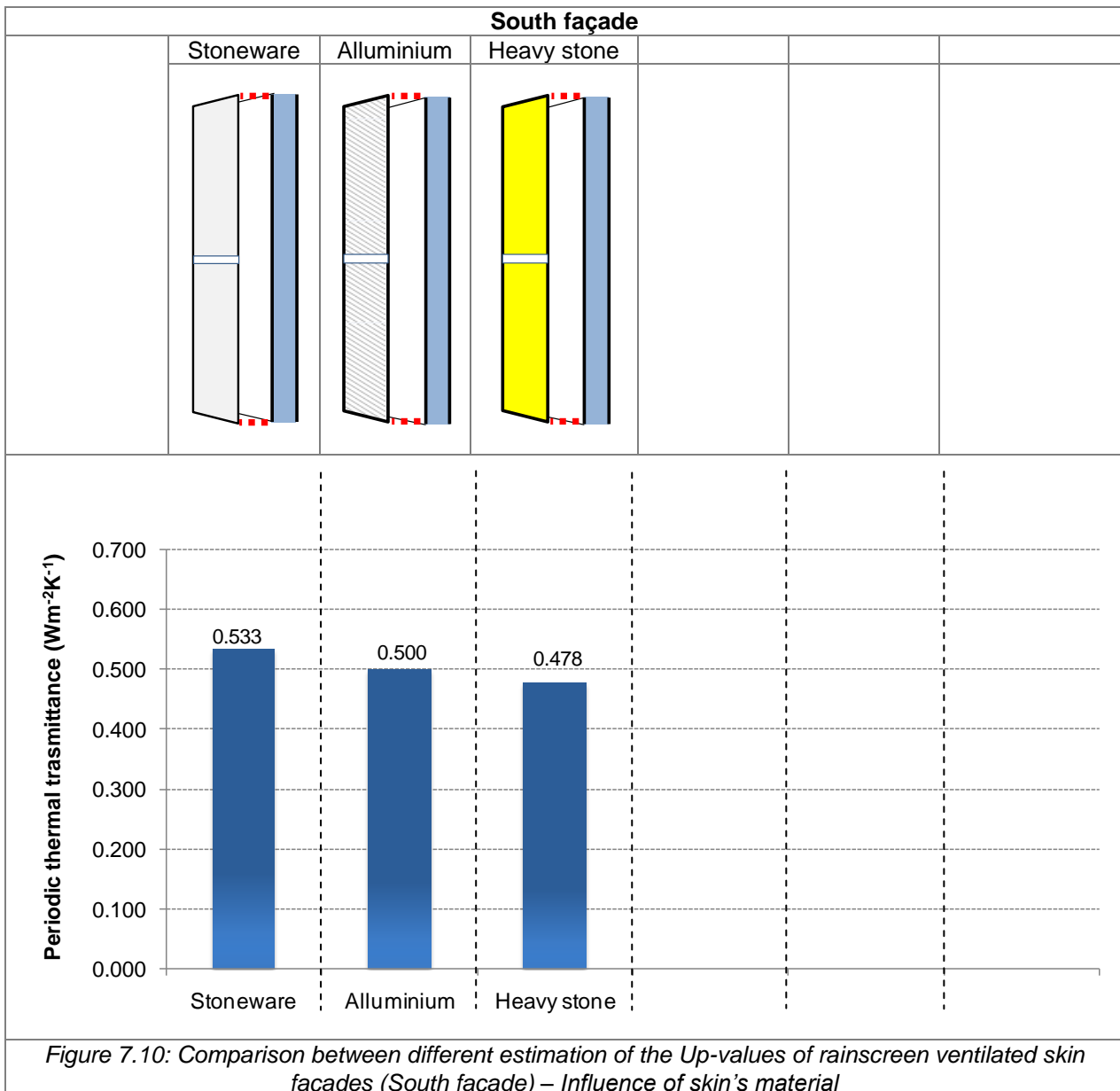


7.3.4 Influence of the skin's material

The configuration setup of the analyzed rainscreen ventilated skin façades is the same on the previous investigations. In particular, only the South orientation was investigated and the rainscreen consists in ventilation grills partially open (50% of geometric area) and open joints. Only three types of material were studied: stoneware skin (10 mm of thickness), aluminium skin (5 mm of thickness) and finally a heavy stone skin (30 mm of thickness). In Table 7.01 the significant thermo-physical properties of the skin's layer are reported.

Table 7.01: Thermal properties of the externals skin

Layer	Thickness (mm)	Thermal conductivity ($W m^{-1} K^{-1}$)	Density ($kg m^{-3}$)	Specific Heat ($J kg^{-1} K^{-1}$)	Emissivity (-)	Absorptance solar (-)
Stoneware	10	1.30	2300	840	0.90	0.3
Alluminium	5	160	2800	840	0.22	0.3
Heavy stone	30	2.80	2700	1000	0.90	0.3



In Figure 7.10 it possible to notice that the periodic thermal transmittance of the patterns with aluminium skin and heavy stone skin appears smaller than that of the pattern with stoneware skin. In Figure 7.11 it possible to notice how the heat flow rate of internal surface of the pattern with aluminium skin (4.9 Wm^{-2}) was lower than that of stoneware skin (5.2 Wm^{-2}). It is also interesting to observe the heat flow rate of pattern with heavy stone skin by comparison with patterns with different materials. The maximum and minimum heat flow of pattern of heavy stone skin is respectively 3.1 and -1.6 Wm^{-2} and the heat flow rate is lower (4.7 Wm^{-2}) than other patterns. From Figure 7.11 it possible to notice that the trend of heat flow of heavy stone skin is shifted with regards to the other two trends. It is evident that a time lag of about 2 hours exists in the former pattern.

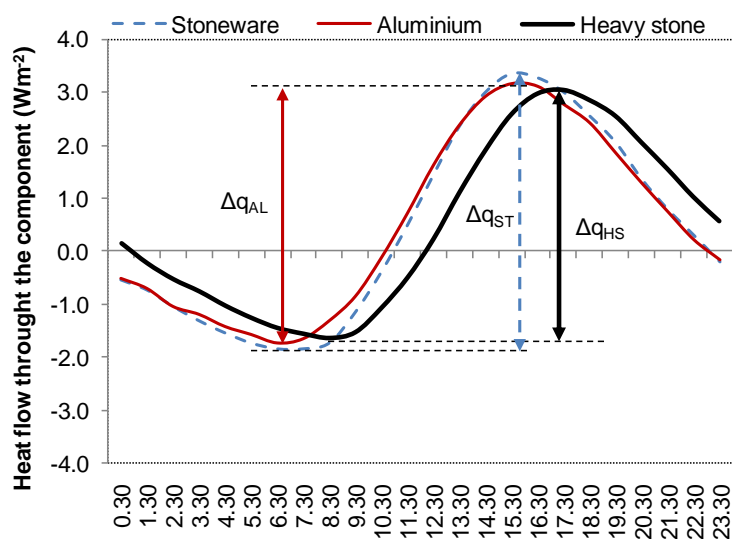
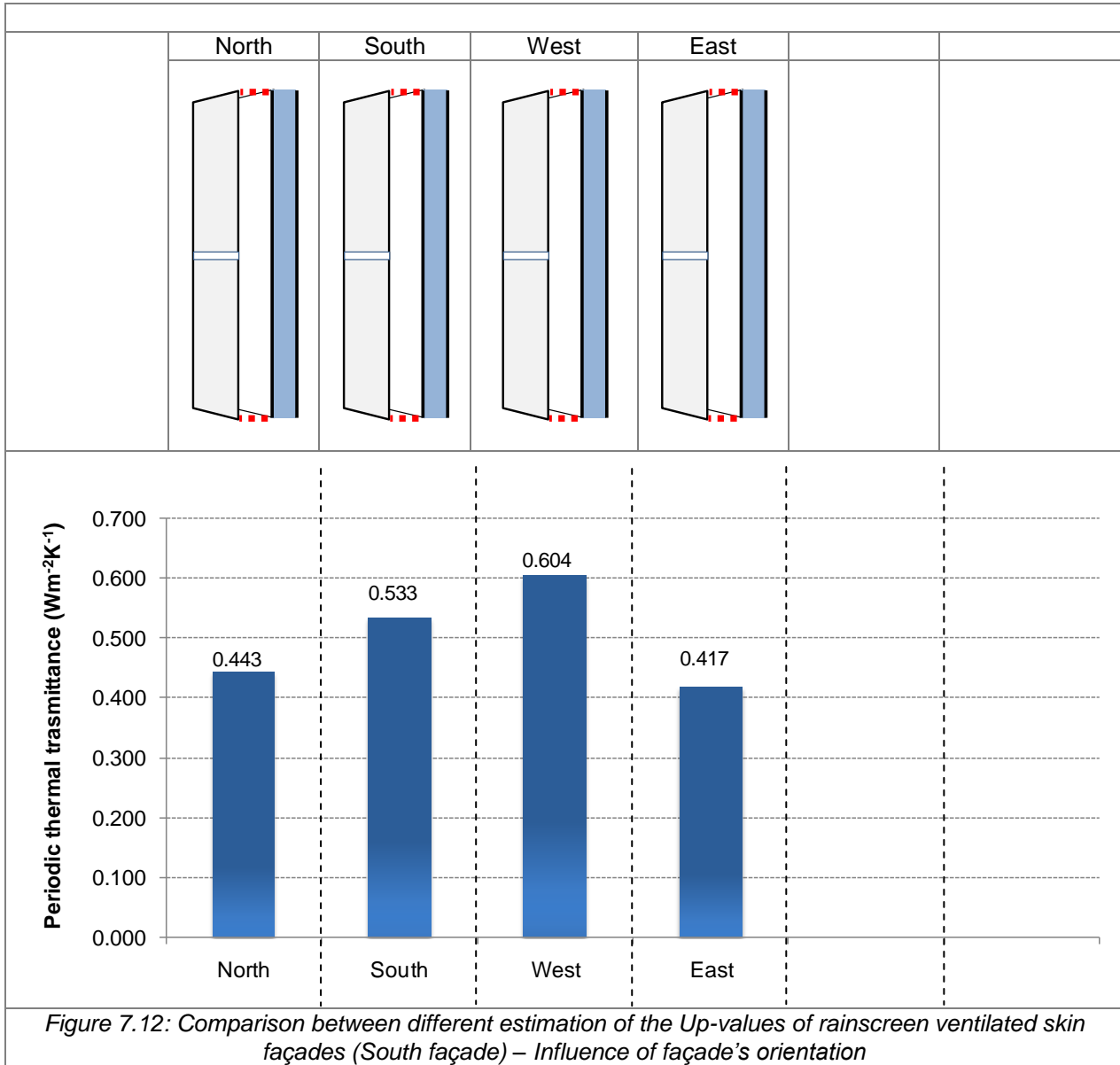


Figure 7.11: Comparison between different trends of heat flow rate through the internal surface of the component for three skin material (South façade)

7.3.5 Influence of the façade's orientation

It is known that the orientation of the building façade is very important for the energy performance of buildings. In this section the value of periodic thermal transmittance as function of the orientation façade will be investigate. The analyzed patterns consist of stoneware tile system (bright finish) with ventilation grills partially open (50% of geometric area) and open joints.



In Figure 7.12 Up-values of the rainscreen pattern mentioned above are depicted for every orientation. It is interesting to notice that the smallest value was for the East façade and North façade. It is evident that the heat flow rate through the internal surface of the component was smaller than those for the other orientation as is also depicted in Figure 7.12. The highest value of periodic thermal transmittance was for both the West and South façades.

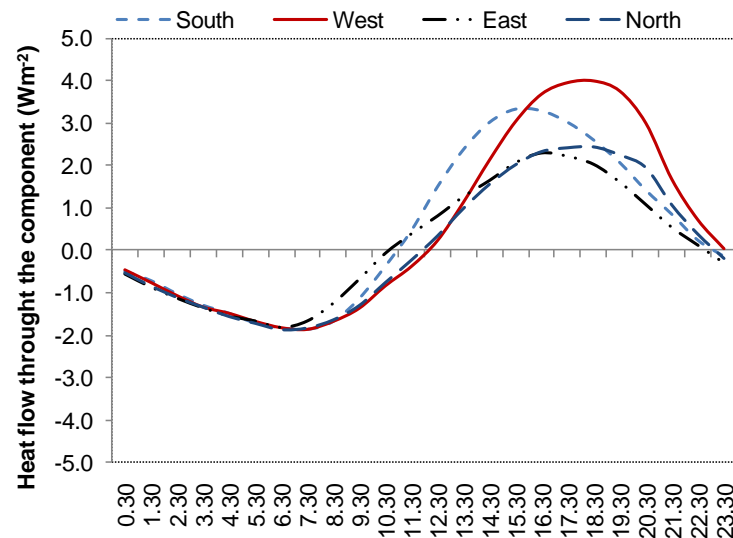


Figure 7.13: Comparison between different trends of heat flow rate through the internal surface of the component for every orientation

Figure 7.13 shows that the highest value of heat flow rate was shifted in the afternoons while the highest morning heat flow (from 6:30 to 11:30) was that for the East façade.

7.4 Conclusions

The analysis of this chapter shows that the thermal performance strongly depends both on the configuration and orientation of the façade used. No single parameter capable of evaluating the summer performance of the façade exists. In this chapter the dynamic thermal transmittance in according to EN ISO 13786 [2007] expressed by the ambient temperature was used. An alternative method with sol-air temperature instead of ambient temperature overpredicts the dynamic thermal transmittance. Easily, the Up-values, the best configuration of rainscreen ventilated skin façade with stone cladding is the S0 pattern for the South façade and is the W0 and W2 patterns for the West façade.

The performance of the aluminium skin appears worst than those of stone cladding skin but as demonstrated in Section 7.3.4 this depends of the heat flow during the night.

In order to investigate the best summer thermal performance of rainscreen ventilated skin façade a study by means of the dynamic thermal performance for different configuration setup of rainscreen walls was made. In particular, influences of ventilation grills, air cavity thickness, skin colour, skin material, orientation of façade were investigated. It is difficult to obtain an optimum configuration to improve the summer thermal performance of the external envelope but some technical consideration was expressed in this chapter. In summary the best summer thermal performance of rainscreen ventilated façade can be obtained by combination of a well ventilated channel (at least 25% of geometric area of ventilation grills with joints opened), an air cavity thickness of at least of 10 cm, an external skin with bright finish and heavy material with low emissivity. However, patterns with skin with low external surface emissivity (such some aluminium) require more detailed thermal performance information. As a consequence of the diversity of the results, designers should be aware that ventilated skin façades do not necessarily improve the energy efficiency of their designs.

This chapter has highlighted the importance of many factors in calculating the periodic thermal transmittance. For example, the exterior colour of the wall as well as a badly ventilation in the ventilated walls decreases thermal performance in the summer period. In order to evaluate the

summer thermal performance, the periodic thermal transmittance determined with the sol-air temperature instead ambient temperature is not suitable for these aim because it increases the thermal performance of walls with dark finish.

CHAPTER 8

ENERGY PERFORMANCE: A CASE STUDY

8.1 Introduction

In the previous chapters the thermal performance of different configurations of ventilated walls were analysed. As a benchmark the periodic thermal transmittance parameter in accordance with Standard EN ISO 13786 [2007] was used. This chapter will assess the energy performance of some walls described in the previous chapter a whole building.

The building energy simulation program ESP-r (see Chapter 3) is used to study the energy performance of four types of envelope façades. Two traditional Italian masonry (with and without thermal insulation) and two Rainscreen Ventilated Façade (RVF) are studied.

The RVF is selected on the basis of the results obtained in the previous chapter.

The following two sections discuss the influence of RVF on the net sensible energy demand for space heating and cooling of office buildings.

In general, the energy performance of the buildings depends on the type of external envelope as well as on other important factors, which include internal gains. In order to assess the influence of some of these factors on the results, two kinds of investigations are carried out.

First, simulations of the building without windows are carried out. The results are compared with a traditional façade solution. Then, the influence of system settings on the whole building (changing RVF orientation, skin material, skin colour and location) and the influence of modelling assumptions are studied.

Finally, some considerations on the comparison between the ventilated and non-ventilated solution (based on energy terms) of a virtual building will be presented.

8.2 Simulation

In this Section, the energy performance of RVF is studied and compared to that of a traditional wall system. The net sensible heating and cooling demand of a single room is discussed, then, the results are extrapolated to a whole ideal building.

8.2.1 Simulation results for a single room

The simulated building consists of three floors on top of each other with a squared base. The single room measures 3.0x3.0x3.5 m (width x depth x height). The overall internal height of the building is 10.5 m. The internal air room temperature was considered floating freely both in winter and summer while the hourly weather condition was referred to the city of Bologna (Italy) [Italian Climate Data Set Gianni de Giorgio].

In this analysis doors and windows are not considered. Internal gains due to occupancy, lighting and office appliances are in accordance with the Italian Standard UNI/TS 11300-1 [2008] and are summarised in Table 8.01.

The lights are supposed to work continuously during office hours. During night-time, the internal gains are set back to about 10% of the daytime values.

The heating and cooling demands of each zone are determined by the internal gains and the hygienic ventilation needs. The hygienic ventilation requirements of all zones are taken in accordance with the Italian Standard UNI 10339 [2005]. In the daytime of weekdays the hygienic ventilation rate is equal to $36 \text{ m}^3\text{h}^{-1}$ per person and in the rest of time it is considered equal to 0.2 ACH (air volume change per hour). A time-step of 15 minutes was used in the simulation.

Table 8.01: Sensible internal gains

days	hours	Occupancy + lighting + office appliances (Wm^{-2})
Weekdays	7-17	28
	17-23	3
	23-7	3
Saturday-Sunday	7-17	3
	17-23	3
	23-7	3

In order to investigate the thermal performance of a single façade only the South wall and the roof were exposed to weather conditions. The rest of building components (West, East and Nord façades and ground floor) were considered thermally adiabatic.

The energy demand of the following façades is studied:

- Envelope of clay brick blocks, called “A” ($U = 0.61 \text{ Wm}^{-2}\text{K}^{-1}$).
- Envelope of clay brick blocks with RVF, called “A+RVF” ($U = 0.58 \text{ Wm}^{-2}\text{K}^{-1}$).
- Envelope of clay brick blocks with external insulation ($U = 0.34 \text{ Wm}^{-2}\text{K}^{-1}$), called “B”.
- Envelope of clay brick blocks with external insulation with RVF ($U = 0.33 \text{ Wm}^{-2}\text{K}^{-1}$), called “B+RVF”

Thermal transmittance values labelled with “U” in brackets are calculated in accordance to Standard EN ISO 6946 [2007]. In Table 8.02 the thermophysical properties of layers for the above-mentioned four walls (A, A+RVF, B and B+RVF) and the rest of building components (roof, ground floor and internal floors) are listed.

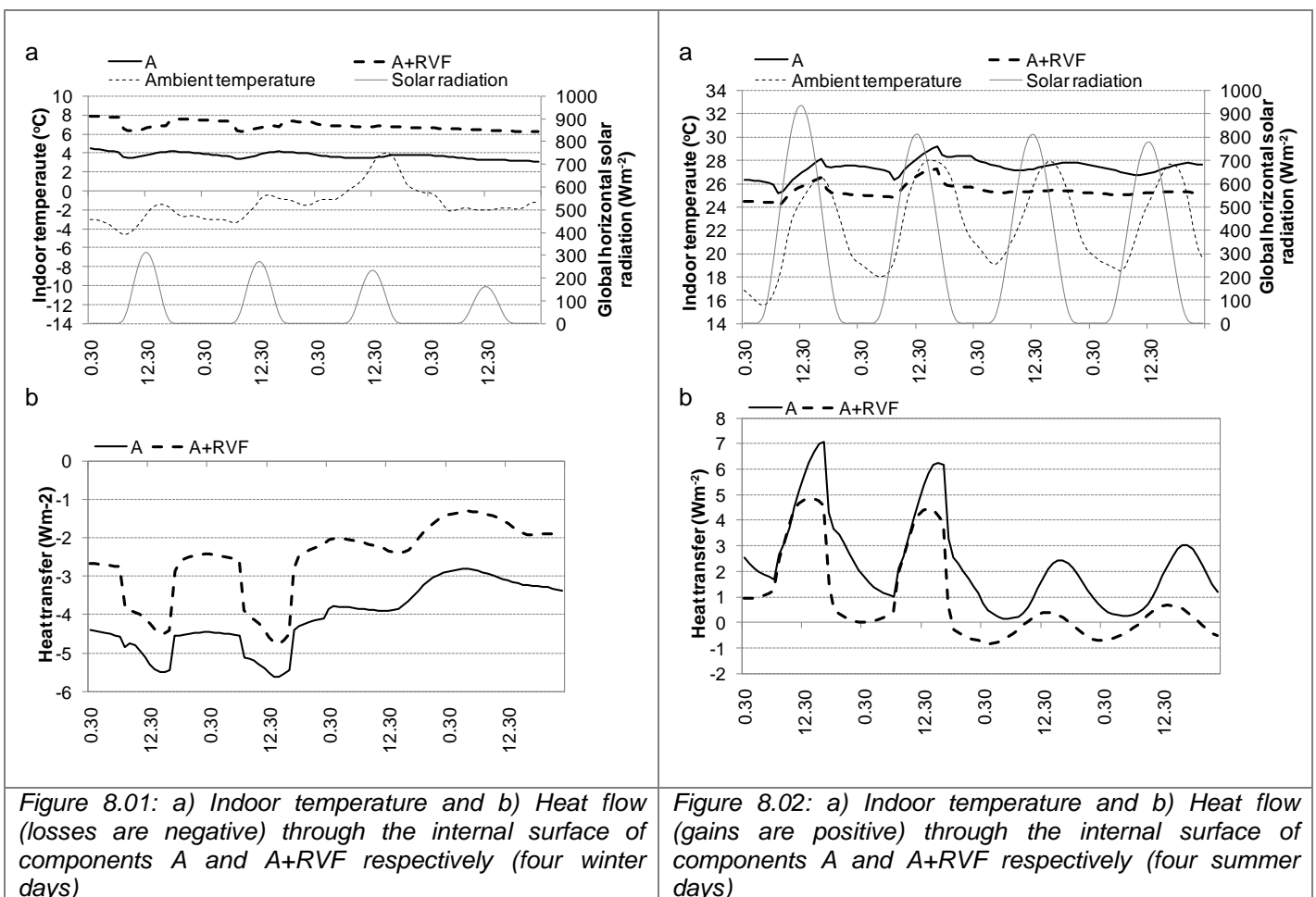
Table 8.02: Thermal properties of the layers of the building components

	Layer	Thickness (cm)	Thermal conductivity ($\text{W m}^{-1} \text{K}^{-1}$)	Density (kg m^{-3})	Specific Heat ($\text{J kg}^{-1} \text{K}^{-1}$)	Thermal resistance ($\text{m}^2\text{K W}^{-1}$)
A	Internal plaster	0.015	0.90	1800	910	-
	Clay brick block	0.300	-	800	840	1.44
	External plaster	0.015	0.90	1800	910	-
A+RVF	Internal plaster	0.015	0.90	1800	910	-
	Clay brick block	0.300	-	800	840	1.44
	External plaster	0.015	0.90	1800	910	-
	Air cavity	0.100	-	-	-	-
	Stone cladding	0.010	1.3	2300	840	-
B	Internal plaster	0.015	0.90	1800	910	-
	Clay brick block	0.200	-	800	840	0.47
	Thermal insulation	0.100	0.044	60	1000	-
	External plaster	0.015	0.90	1800	910	-
B+RVF	Internal plaster	0.015	0.90	1800	910	-
	Clay brick block	0.200	-	800	840	0.47

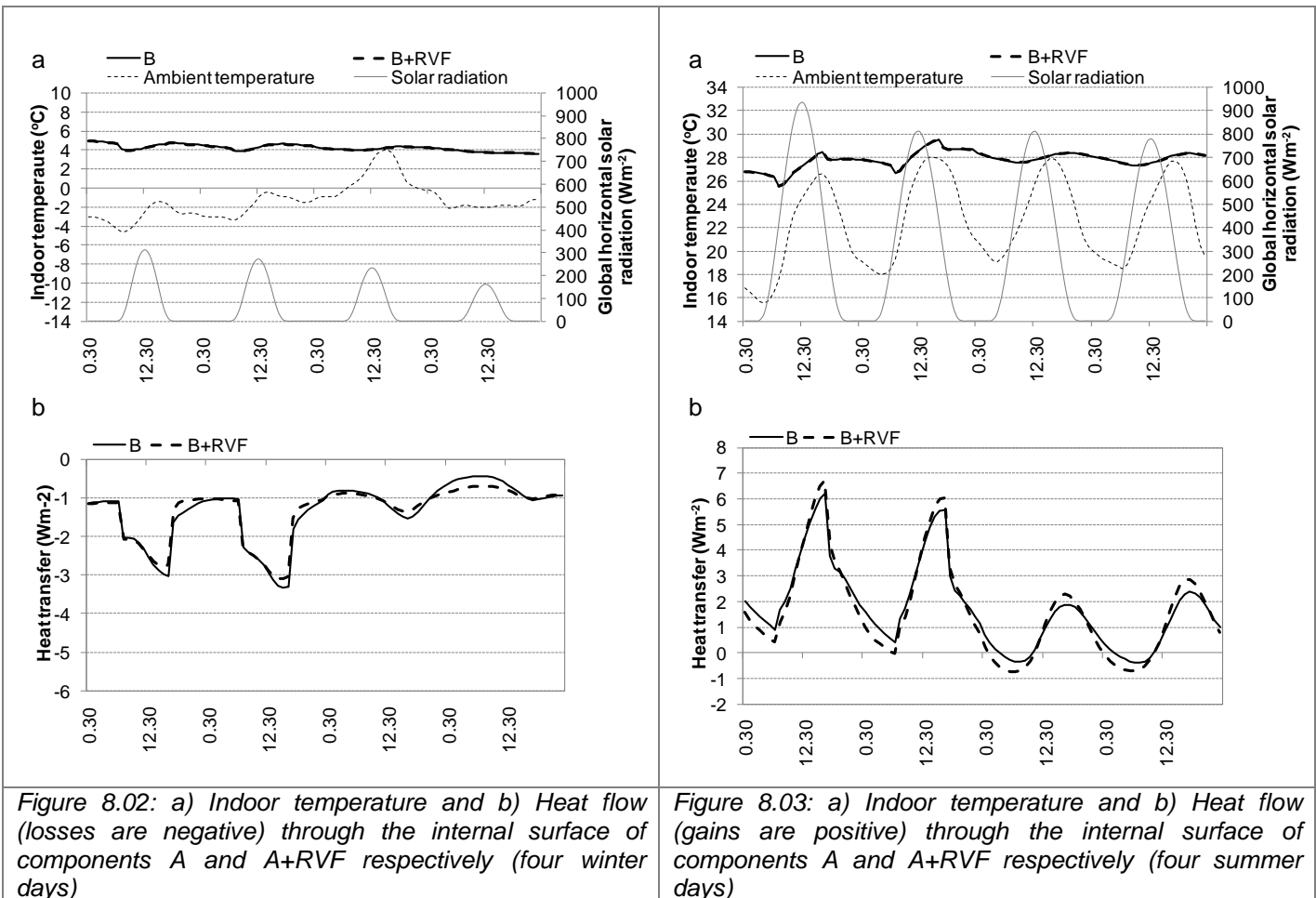
	Thermal insulation	0.100	0.044	60	1000	-
	Air cavity	0.100	-	-	-	-
	Stone cladding	0.010	1.3	2300	840	-
Roof	Internal plaster	0.015	0.90	1800	910	-
	Brick concrete slab	0.300	-	1050	920	0.41
	External covering	0.005	0.23	1100	1000	-
Internal floor	Internal plaster	0.015	0.90	1800	910	-
	Brick concrete slab	0.300	-	1050	920	0.41
	Air cavity	0.128	-	-	-	-
	Gypsum plasterboard	0.012	0.21	900	910	-
Ground floor	Internal tiles	0.010	1.00	2300	840	-
	Concrete	0.050	0.25	800	1000	-
	Thermal insulation	0.040	0.044	60	1000	-
	Concrete slab	0.200	1.15	1800	1000	-
	Sand and gravel	0.300	2.00	1700	910	-

Figure 8.01 presents the indoor temperature and also the inside heat transfer through every wall configuration analysed (A, A+RVF, B and B+RVF) for the only vertical façade exposed (South façade) to weather effects.

Walls labelled with A and B respectively are not supplied with a ventilation system while walls labelled respectively with A+RVF and B+RVF are ventilated façade systems.



In Figures 8.01 and 8.02 it possible to notice the trends of indoor temperature (a) and the heat transfer (b) through the surface of the component for the two different façade types (A and A+RVF) for the winter and summer periods (four days for each season). Ambient temperature and solar radiation are also depicted. It is interesting to observe that the indoor temperature of configurations setup with RVF (A+RVF) always stays higher than the traditional setup (A) in this winter period while it is a little lower in the four summer days. The indoor temperature decreases about 2° C from walls A to A+RVF in the summer period. Walls with RVF appear more performant in the winter period too. This aspect is also reflected in the heat transfer trends in Figure 8.01b and 8.02b. Analogous considerations can be made for configurations B and B+RVF.



Figures 8.02 and 8.03 show the trends of indoor temperature (a) and heat transfer (b) through the surface of the component for two different façade types (B and B+RVF) for the same periods of the previous analysis. In this case, the configuration B consists of a brick block and an external layer of thermal insulation. The presence of the insulation increases the indoor temperature both in the winter and in summer periods in comparison with the configuration without it. The trends (indoor temperature and heat transfer) are very similar; there is no difference between the setup with RVF (B+RVF) and that traditional (B). It is evident that the thermal insulation reduces benefits of the ventilation in the channel.

These analyses of only the indoor temperatures and heat flows are not sufficient to describe the performance of the ventilated walls. For example, the information that can be extracted by the heat flows trends are restricted to a short time only and also is not possible to fully observe solar gains effects through walls. Further, the presence of an extra layer and an extra façade layer increase the total thermal resistance but could decrease solar gains in the winter period. For this reason an extended annual analysis is necessary to understand the real performance of this kind of walls.

Nonetheless, this analysis suffices to assess the thermal performance of walls with RVF in comparison to walls without RVF for a simple room without windows. Under such conditions, the thermal performances of RVF are higher than those of traditional walls. In the next section the energy performance of a RVF virtual building is studied.

8.2.2 Simulation results for a whole building

Building description

The building is a virtual office building and is not a real one; it was constructed only for the purpose of the following energy analysis. In this Section, the energy performance of whole building equipped with construction typologies explained above (Table 8.02) is simulated.

The set-point temperature for heating is 20°C with a night setback to 16°C. The set-point temperature for cooling is 26°C. Cooling and heating are only allowed during office hours (from 7 a.m. to 5 p.m.) of workdays. The internal gains and the hygienic ventilation of the building are the same as those used in the previous simulation examples. In the analysis, the load or energy demand of the whole building is defined as the energy needed to keep the office temperature between the set-points.

The building consists of three floors (open spaces) and the external dimensions of the building are 20.66 x 10.66 x 12 m (width x depth x height) with a gross volume equal to 2643 m³. It is oriented in such a way that the largest façade faces south and every side is considered exposed to weather conditions. Its form is a parallelepiped with symmetric faces (Figure 8.04).

Materials of the building components are the same as those used in the previous simulation examples. The conditioned area of each floor is 200 m² and the floor to floor height is 3.5 m.

The transparent surface is about 48 m² and has a glass to wall ratio of about of 10%. Windows are double pane with a U-value of transparent surface of 1.70 Wm⁻²K⁻¹. A time-step of 15 minutes was used in this simulation.

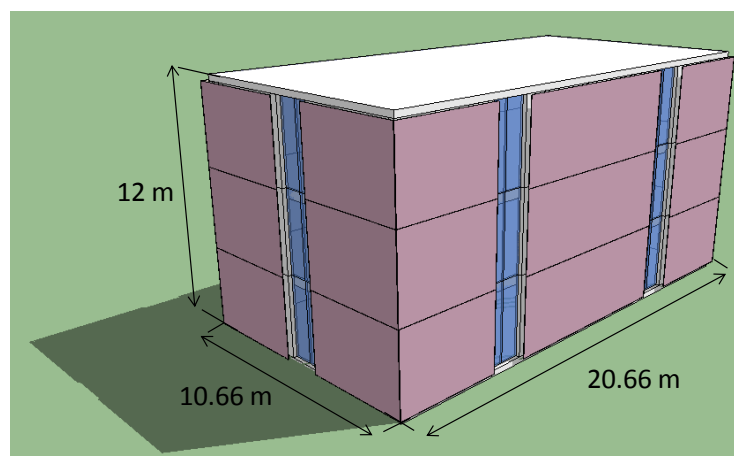


Figure 8.04: View of simulated office building with dimensions.

Energy objectives

During both the heating and the cooling season, the same four systems of the previous single room are investigated. Clearly, the energy efficiency objectives depend on the envelope typology and also on the RV-façade orientation. For this reason several simulations were carried out in order to evaluate the influence of façade orientation on the energy performance of the building.

Figure 8.05 shows four building envelopes which were used to investigate the energy demand of the building. The RVF for Figures 8.05b and 8.05d consists of stone cladding (bright finish) with upper and lower ventilation grills completely opened and open joints.

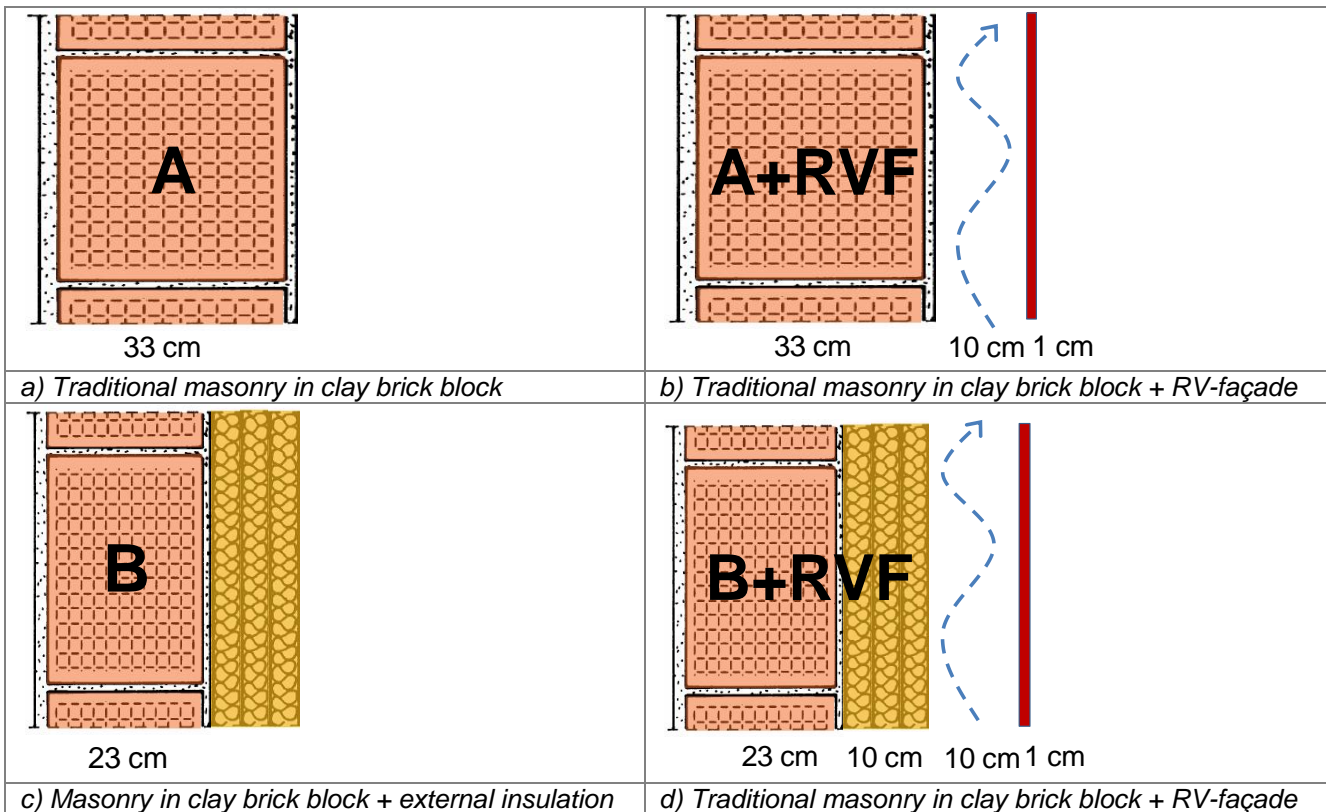


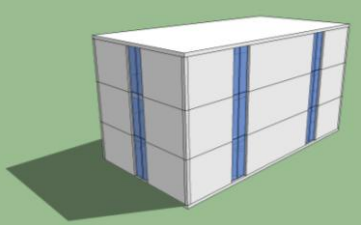
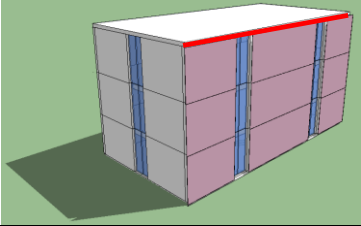
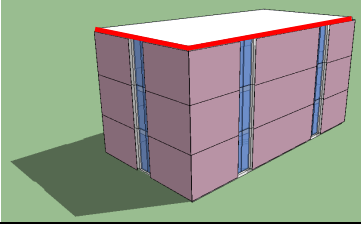
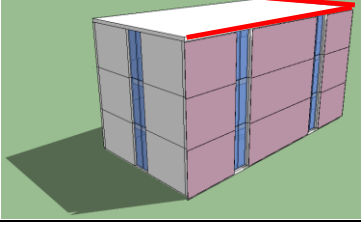
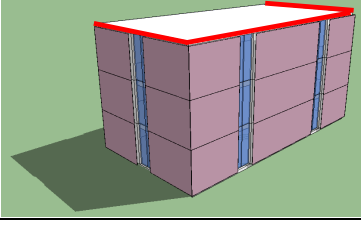
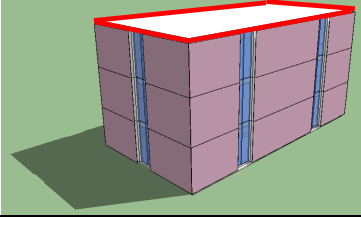
Figure 8.05: Simulated building envelope for virtual office building.

Six different configurations are treated for each envelope:

- No RVFs on any side of the building. This simulation is called “Basic”.
- Only the South façade has a RVF. This simulation is called “Basic+South”.
- Both South and West façade have RVFs. This simulation is called “Basic+South+West”.
- Both South and East façade have RVFs. This simulation is called “Basic+South+East”.
- South, West and East façades have RVFs. This simulation is called “Basic+South+West+East”.
- Every wall has RVF. This simulation is called “Basic+South+West+East+North”.

In Table 8.03 the energy delivered, E (kWh) to configurations A and A+RVF for heating and cooling during for winter and summer are reported. In the last column of Table 8.03 the differences from the energy demand for the Basic configuration are also indicated.

Table 8.03: Energy demand for heating and cooling of the simulated building (A and A+RVF envelopes)

A and A+RVF envelopes	simulation	period	E (kWh)	Energy difference from Basic configuration
	Basic	Winter	75648	-
		Summer	-16005	-
	Basic+ South	Winter	76714	+1.4%
		Summer	-15415	-3.7%
	Basic+ South+ West	Winter	76633	+1.3%
		Summer	-15367	-4.0%
	Basic+ South+ East	Winter	76604	+1.3%
		Summer	-15391	-3.8%
	Basic+ South+ West+ East	Winter	76513	+1.1%
		Summer	-15343	-4.1%
	Basic+ South+ West+ East+ North	Winter	76231	+0.8%
		Summer	-15364	-4.0%

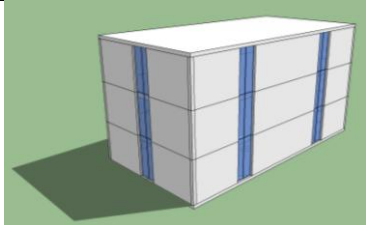
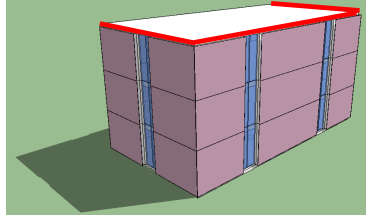
The energy difference mentioned above range from 3.7 to 4.1% in the summer period and from 1.1 to 1.4% in the winter period. It is interesting to notice that these percentage differences are reductions for the cooling energy and increments for heating demands, which confirms the cooling effect of the rainscreen façades. The energy increments in winter period could be due to the ventilation in the channel and the less solar gains. The air ventilation in the channel could increase the heat loss of the building envelope and an extra heating power would be necessary to keep the indoor temperature at 20° C.

Moreover, the energy demand depends on the orientation of RVF. The best configuration in order to obtain the maximum cooling energy reduction from the basic solution is that with RVFs on all sides except the northern one.

Now, the energy demand of configurations with thermal insulation is evaluated.

In Table 8.04 the energy delivered, to configurations B and B+RVF for heating and cooling of the simulated building during winter and summer are reported.

Table 8.04: Energy demand for heating and cooling of the simulated building (B and B+RVF envelopes)

B and B+RVF envelopes	simulation	period	E (kWh)	Energy difference from Basic configuration
	Basic	Winter	72827	-
		Summer	-16374	-
Stoneware				
	Basic+ South+ West+ East	Winter	72759	-0.1%
		Summer	-16244	-0.8%

In this case, benefits are minimal (1% in summer) for a strongly thermally insulated, ventilated wall solution. As stated before, the presence of a thick thermal insulation decreases the benefits of the air cavity ventilation on the reduction of external summer loads.

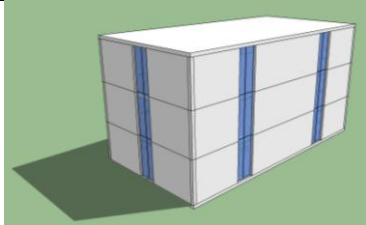
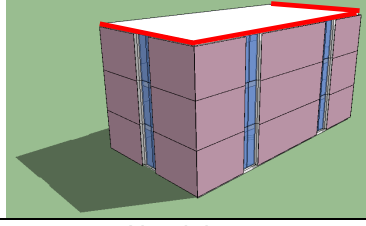
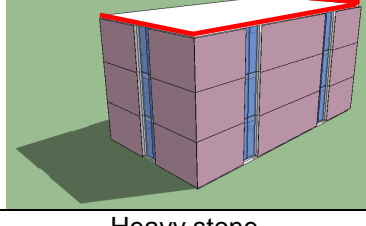
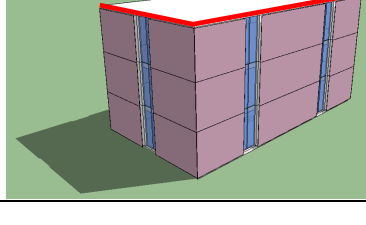
The analysis now focuses on the influence of various elements of the building; to this purpose, only the “Basic + South + East +West” solution to assess the energy performance of RVF (A+RVF) is used.

First the different external skin material will be analysed.

The RVF has a bright finish surface with upper and lower ventilation grills completely opened and open joints. The analysed material skins are the same of Chapter 7 and their main thermal characteristics are reported in Table 7.01

In Table 8.05 the energy results for the new solutions are listed.

Table 8.05: Energy demand for heating and cooling of the simulated building (A and A+RVF envelopes) – different skin materials.

A and A+RVF envelopes	simulation	period	E (kWh)	Energy difference from Basic configuration
 Stoneware	Basic	Winter	75648	-
		Summer	-16005	-
 Aluminium	Basic+ South+ West+ East	Winter	76513	+1.1%
		Summer	-15343	-4.1%
 Heavy stone	Basic+ South+ West+ East	Winter	75656	+0.0%
		Summer	-15675	-2.1%
 Heavy stone	Basic+ South+ West+ East	Winter	76505	+1.1%
		Summer	-15326	-4.2%

The energy savings of heavy stone (4.2%) and aluminium (2.1%) skins are comparable with that of stoneware (4.1%). These benefits are small also when heavy stone is considered as external skin material (3 cm) instead of stoneware (1 cm). Besides, the aluminium skin brings a smaller improvement than the other patterns in summer. There are no energy benefits for all patterns in the winter period. The heating energy demand increases to about 1 % more than that for the Basic solution.

Another important factor that influences the energy performance of the whole building is the external colour of the envelope. For this analysis, only the pattern with stoneware is taken into account while the colour of the skin is changed. The analysed skin colours are:

- light corresponding to an solar absorption coefficient of 0.3;
- soft corresponding to an solar absorption coefficient of 0.6;
- dark corresponding to an solar absorption coefficient of 0.9.

In Table 8.06 results for the three configurations with different skin colour of the building envelope are listed.

Each configuration A+RVF is compared with the corresponding simulated non ventilated solution (labelled with "A") with the same external colour. Percentage changes of benefits compared to a traditional non-ventilated solution are also reported.

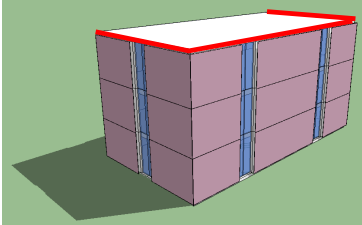
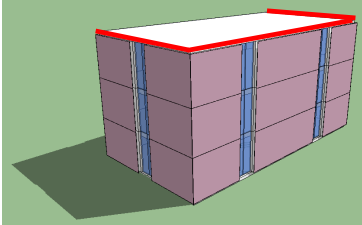
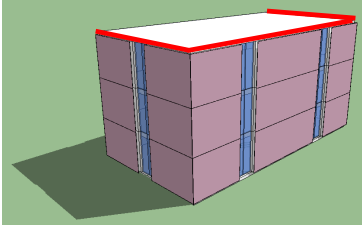
Table 8.06: Energy demand for heating and cooling of the simulated building (A and A+RVF envelopes) – different skin colour.

A and A+RVF envelopes	configuration	period	E (kWh) A	E (kWh) A+RVF	Energy difference between A and A+RVf
Stoneware (light skin colour)	Basic+ South+ West+ East	Winter	75648	76513	+1.1%
		Summer	-16005	-15343	-4.1%
Stoneware (soft skin colour)	Basic+ South+ West+ East	Winter	74439	75855	+1.9%
		Summer	-17435	-16058	-7.9%
Stoneware (dark skin colour)	Basic+ South+ West+ East	Winter	73293	75250	+2.7%
		Summer	-18946	-16753	-11.6%

The skin colour is a very important aspect for the summer thermal performance of this particular rainscreen ventilated façade. The energy saving of the ventilated solution with a soft skin colour is about 8% in comparison to a traditional, non-ventilated solution with the same colour. A benefit of 12% with a dark finish for the external skin is obtained. It is interesting to notice that the energy saving of the ventilated solution with a soft skin colour (16058 kWh) is the same of that the traditional with a light colour (16005 kWh). The increment of heating energy demand ranged from 1 to 3% from the traditional solution. The choice of the skin colour for the RVF is very important to assess the energy performance of buildings.

Finally, in Table 8.06 heating and cooling energy demand results of three different Italian locations are listed: Bologna (northern Italy), Rome (central Italy) and Palermo (southern Italy). For each simulation the results for the traditional (non-ventilated) and the RVF solution respectively with soft colour of external skin were compared. It is interesting to see different benefits for the three locations both in winter and summer. Regarding the cooling demand the improvements with a RVF solution are 5%, 3% and 8% for Palermo, Rome and Bologna respectively. On the contrary, regarding the heating demand, the RVF solution decreases only for Rome; the increment of the heating energy demand are 3% and 2% respectively for Palermo and Bologna.

Table 8.07: Energy demand for heating and cooling of the simulated building (A and A+RVF envelopes) – different locations.

A and A+RVF envelopes	period	Energy demand (Basic solution) (kWh)	Energy demand (Basic+South+West+East) (kWh)	Energy difference from Basic configuration
(Bologna)				
	Winter	74439	75855	+1.9%
	Summer	-17435	-16058	-7.9%
(Rome)				
	Winter	33252	33091	-0.5%
	Summer	-18854	-18257	-3.2%
(Palermo)				
	Winter	14272	14707	+3.0%
	Summer	-24364	-23169	-4.9%

In Figures 8.06 and 8.07 results of the last three configurations (VF) are compared with the simulated non ventilated solution (labelled with "NOT VF"). Percentage changes of benefits compared to a traditional non-ventilated solution are also reported.

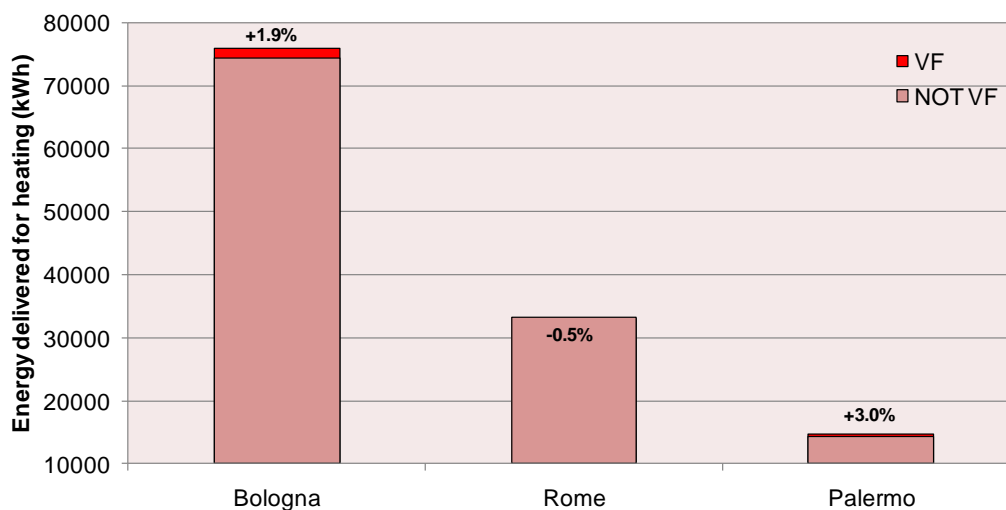


Figure 8.06: Energy demand for heating for the three ventilated wall solution (VF) compared with a non ventilated solution (Not VF).

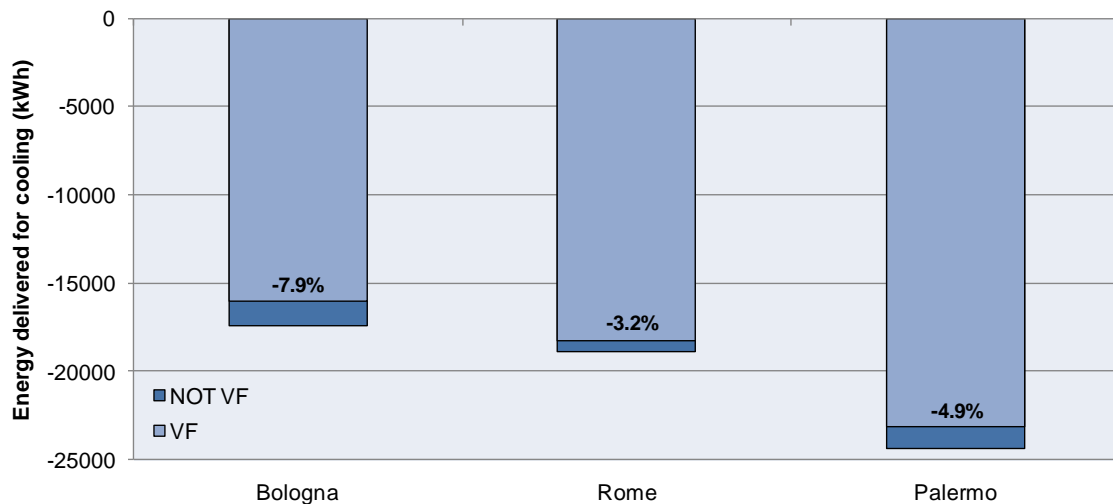


Figure 8.07: Energy demand for cooling for the three ventilated wall solution (VF) compared with a non ventilated solution (Not VF).

A recent work [Naboni, 2007] reported about the same energy considerations on energy demands by utilizing dynamic simulation software [EnergyPlus]. This study covered only one type of ventilated façade for an ideal residential building located in some Italian localities. The energy benefits were about 6-8% when comparing a ventilated wall solution with a non-ventilated wall solution.

This analysis has highlighted the small improvement of the ventilated wall over a non-ventilated solution. Reasons of this small difference may lie in the amount of internal loads, location and shape of building, surface area of windows, the overheating of the air cavity and its small natural expulsion of the air heated by solar radiation in the channel.

However for dark finish on the external skin it possible to obtain a sensible energy saving (12%) in comparison with a traditional solution with the same colour. It was also highlighted that the presence of a screen on the outside of the wall may increase the thermal resistance of the entire wall. This may decrease the heat removal capabilities when ambient temperatures are lower than the indoor temperature. The absence of solar radiation and the lack of influence of wind may support stack effects in increasing the thermal resistance of the entire wall during the night.

8.3 Conclusions

In this Chapter energy simulations by means ESP-r software for one simple room and a whole virtual building are presented. An annual energy simulation of four types of envelope façades under one Italian weather conditions was carried out. Results were discussed and compared to a traditional wall system with and without external thermal insulation. Results depend mainly on the choice of envelope typology, internal gains and also façade orientation. Simulations show that by using an RVF it is possible to improve energy performance of some components of the overall building's in terms of energy demand. The heating and cooling loads are small if compared to traditional walls (walls without RVF). In general terms the obtained energy saving for combined cooling and heating is in the range 2-12% range.

The cooling energy advantages of the analysed RVF in this work depend by many factors. The most important are good ventilation in the channel, ventilated façade orientation, skin material, skin colour, internal gains and the location. In this work an optimal solution of the envelope solution consists of stone cladding (soft finish) with upper and lower ventilation grills completely opened

and open joints; the thickness of air cavity is 10 cm and the South, West and East façades have RVFs. Under such conditions, the energy performances of RVF are 8% higher than those of traditional walls.

For the cases studied, the overall building energy improvement is limited to the envelopes. Only by combining typologies or changing the system settings according to the particular situation, an overall improvement over the traditionally insulated wall and window glazing unit with exterior shading is possible, but this is not the aim of this work.

As a consequence of the diversity of the results, designers should be aware that RVFs do not necessarily improve the energy efficiency of their designs. On the contrary, in most cases, the net sensible energy demand of a traditional but performing solution is not outperformed by RVFs.

CONCLUSIONS

Ventilated façades have gained an increased popularity among architects and principals, whose desire is to design energy-conscious, sustainable office buildings. The work at hand presents a contribution to assess the energy performance of a rainscreen ventilated skin façade.

In this final chapter, the main achievements and conclusions are summarised and perspectives for future research are outlined.

Main results and conclusions

In this work, the potential of ventilated façades to lower the net sensible energy demand in buildings is studied with a coupled experimental and numerical approach. It is shown that although some type of rainscreen ventilated façade typologies are capable of lowering the cooling energy demand of a few percent points, a general recommendation to apply these envelopes on the basis of their energy performance cannot be defended. The main steps and achievements that led to this conclusion are summarised below.

Experimental evaluation

Experimental work was done on a type of naturally ventilated façade on a test building located in Italy, San Mauro Pascoli - Forlì Cesena. The temperature profiles as well as the cavity air velocity were continuously measured during the winter and the summer periods. The measurements are used to better understand the complexity of ventilated skin façade, to relate the data to energy objectives, to evaluate energy modelling assumptions and to derive some parameters and relationships. Analysis of the temperature profiles shows that the surface and cavity temperature are determined not only by the presence of openings such as ventilation grills and open joints, but also by the air cavity thickness and the finish of the external skin of the ventilated façade.

In the winter period, the ventilated façade cavity was quite warmer than the ambient temperature in a typical sunny day. In the summer period, the cavity temperature was becomes rather hot and very hot with dark skin finish and in absence of the ventilation in the channel.

A limited experimental evaluation of two correlations for the convective heat transfer coefficient is presented. The spread on the results, however, shows that obtaining a reliable expression for the heat transfer coefficient is very difficult. As consequence a simply correlation to estimate the convective heat transfer coefficient for energetic purposes was used.

Further, another experimental evaluation for the steady-state thermal transmittance of rainscreen ventilated façade was given. In winter period the measured steady-state thermal transmittance of rainscreen ventilated façade was agrees with the value estimated by Standard EN ISO 6946 [2007].

Dynamic simulation

The modelling of the test building was made using ESP-r software. The program is based on the numerical discretization and on simultaneous solution of heat-balance methods. Three different multi-zone models were defined for each ventilated façade and comparison with the experimental results was used in order to select the best ESP-r air flow network for the modelling of this kind of envelope component. The temperature of each cavity control volume is represented by a bulk temperature and the convective heat transfer is estimated by heat transfer coefficients.

The default convection heat transfer used for internal surface nodes is given by the Alamdari-Hammond correlations and it is also used for the analyzed rainscreen ventilated skin façades. Most ventilation components (ventilation grills and joints) were modelled as a standard airflow orifices. The air mass flux between nodes was be calculated by using the pressure difference existing between nodes.

The main results obtained can be summarized as follows:

- If the thermal model of the ventilated wall does not include the open grills at the bottom and at the top wall and the presence of the open joints on the external rainscreen surface, the numerical results exhibit, as expected, a large disagreement with the experimental results. In this case, the agreement with the experimental data is strongly influenced by the orientation of the ventilated wall considered and the temperature increases for walls exposed to large amounts of the solar radiation. The air circulation within the cavity is due to the temperature difference between the cavity walls and the air only and this difference increases with the incident solar radiation.
- In the modelling of the rainscreen ventilated façades the presence of the external open joints can be ignored without decreasing the accuracy of the numerical results significantly. Conversely, by ignoring the open joints, the airflow network model becomes simpler and the numerical solution of the balance equations is faster. For this reason, this kind of model can be suggested as more appropriate for long-term dynamic simulations in which CPU time saving can be important.
- The ESP-r model of this component underestimates the external rainscreen surface temperature during the night when solar radiation is absent; on the contrary, in the presence of high levels of solar radiation, when the effect of this parameter becomes predominant with respect to the effects due to the ambient temperature and to the wind, the agreement with the experimental data is very good.
- The typical air cavity velocities predicted by the ESP-r model are very low (less than 0.12 ms^{-1}) and these values are confirmed the experimental data. The low velocity is due to the large thickness of the air cavity adopted in this ventilated façade (24 cm).
- It was shown that the model of the whole building could predict the trend of the indoor air temperature during the winter period in which the heating plant of the tower was turned off, although the ESP-r simulation overpredicts the degree of thermal insulation and the thermal inertia of the building, probably due to uncertainties in thermophysical properties of the materials involved in the structural elements of the building.

The dynamic thermal behaviour of the ventilated façade is strongly influenced by weather conditions (i.e. solar radiation on the external surface, ambient temperature and wind speed and direction), thermal and geometrical properties (i. e. different materials, different thickness of the air cavity, different opening of ventilation grills and joints and also different colour of the outer surface

of the external skin). Comparisons between predicted and measured data demonstrate that the model of the ventilated façade is able to take into account the combined effects of these quantities.

Thermal and energy performance assessment

The analysis shows that the thermal performance strongly depends both on the configuration and orientation of the façade studied. No single parameter capable of evaluating the summer performance of the façade exists. The dynamic thermal transmittance in accordance with EN ISO 13786 [2007] expressed by the ambient temperature was used.

In order to investigate the best summer thermal performance of rainscreen ventilated skin façade a study for different setups of rainscreen walls was made. In particular, influences of ventilation grills, air cavity thickness, skin colour, skin material, orientation of façade were investigated. It is difficult to obtain an optimum configuration to improve the summer thermal performance of the external envelope but some technical considerations were expressed. In summary the best summer thermal performance of rainscreen ventilated façade can be obtained by combination of a well ventilated channel (at least 25% of the projected area of ventilation grills with open joints), an air cavity thickness of at least of 10 cm, an external skin with bright finish and a heavy material with low emissivity. However, patterns with skin with low external surface emissivity (such as some aluminium surfaces) require more detailed thermal performance evaluation.

Energy simulations show that by using rainscreen ventilated skin façade is possible to improve the energy performance of some components of the overall building and thus energy usage.

Unfortunately, most typologies are incapable of lowering the heating and cooling demand simultaneously. The improved heating and cooling demands are small by comparison with traditional walls (walls without RVF). In general terms the obtained energy savings both for cooling and heating are in the 2-12% range.

The cooling energy advantages of the analysed RVF in this work depend by many factors. The most important are good ventilation in the channel, ventilated façade orientation, skin material, skin colour, internal gains and the location. In this work an optimal solution of the envelope solution consists of stone cladding (soft finish) with upper and lower ventilation grills completely opened and open joints; the thickness of air cavity is 10 cm and the South, West and East façades have RVFs. Under such conditions, the energy performances of RVF are 8% higher than those of traditional walls.

For the cases studied, the overall building energy improvement is limited to the envelopes. Only by combining typologies or changing the system settings according to the particular situation, an overall improvement over the traditionally insulated wall and window glazing unit with exterior shading is possible, but this is not the aim of this work.

In order to correctly evaluate the energy efficiency of the rainscreen ventilated skin façades, it is imperative not only to study the transmission gains and losses but also to take into account the enthalpy change of the cavity air.

In conclusion, the diversity of the outcomes – resulting from the diversity of typologies, system settings and system parameters – suggest that designers should realise that the rainscreen ventilated skin façades not necessarily improve the energy efficiency of their buildings. On the contrary, in most cases, the net sensible energy demand of a traditional, but well performing solution, was not ameliorated by using a ventilated façade.

Recommendations for further research

In this work, a small but meaningful step towards an overall energy performance assessment of rainscreen ventilated façades was made. Unfortunately, a considerable amount of work is needed before an exhaustive evaluation of the influence of ventilated façade on the overall building energy use is possible. A first and important move towards an overall energy performance assessment is the integration of ventilated skin façade models into a whole building energy simulation tool that includes the HVAC-plant. Furthermore, it is a necessary step towards an energy life cycle analysis, which is the ultimate tool to assess the impact of ventilated skin façade on a global scale. In addition to a whole building simulation, energy measurements on ventilated skin façades and on office buildings in general are highly recommendable. Building energy consumption measurements make it also possible to position the energy performance of buildings with ventilated skin façades in a broader perspective and to compare them to buildings with traditional, but well-proven technologies.

Another recommendation concerns the extension of the simulation to other typologies (i.e. ventilated façades and the phase change materials) and climatic conditions. Experiments are necessary to find out whether it is still appropriate to model the airflow in a simplified way. It requires the knowledge of pressure distribution in the cavity in order to calculate the mass and heat transfer.

The above recommendations and the numerous hypotheses and simplifications that were applied in the presented model justify the third opportunity for further research: model refinement. Radiation and conduction are relatively well-known. Convective heat transfer and airflow modelling are not. Computational Fluid Dynamics (CFD) offers an attractive, yet complex analysis tool to address these short-comings.

LIST OF PUBLICATIONS

Journal papers

Marinosci, C.; Strachan, P.; Semprini, G.; and Morini, G. L., 2010, Empirical validation and modelling of a naturally ventilated rainscreen façade building, *Energy and Buildings* 43 853–863

Conference papers

Marinosci, C; Morini, G. L.; Semprini, G.; and Lorenzini M., 2011, Field measurement data and modelling of a rainscreen ventilated façade in the winter and summer periods, CLIMAMED 2011, VI Mediterranean Congress Of Climatization, Madrid (submitted).

Marinosci, C; Morini, G. L.; and Semprini, G., 2010, Experimental benchmark of the modelling of a rainscreen ventilated façade, DYNASTEE workshop on Dynamic Methods for Building Energy Assessment, Brussels.

Cocchi, A.; Semprini, G.; and Marinosci, C., 2010, An integrated system for saving thermal energy in buildings: a case history, in: Proceedings of the 10th REHVA World Congress “Sustainable Energy Use in Buildings” – Clima 2010, Antalya, Turkey, Paper R1-TS41-PP09.

Semprini, G.; Barbaresi L.; and Marinosci, C., 2010, Acoustic and thermal properties of Italian masonry walls, in Proceedings of the 39th International Congress and Exposition on Noise Control Engineering – Intern-Noise 2010,

Semprini, G.; and Marinosci, C., 2009, Influence of the external air flow rate on the Energy efficiency of residential buildings, International Congress AICARR “Systems, Energy and Built Environment toward a Sustainable Comfort, Tivoli 2009.

Semprini, G.; and Marinosci, C., 2009, Prestazioni energetiche invernali ed estive: analisi e confronti su un edificio campione, Atti del Convegno AICARR “Prestazioni energetiche del sistema edificio–impianto: Software per la diagnosi energetica ed il calcolo in regime invernale, Bologna (in Italian).

Semprini, G.; and Marinosci, C., 2008, Effetti dell’inerzia termica dei componenti edilizi in ambienti non climatizzati nel periodo estivo”. Atti del 63° Congresso Nazionale ATI, Palermo (in Italian).

CONCLUSIONS

- Semprini, G.; Marinosci, C.; Barbaresi, L.; and Falcioni S., 2008, Valutazioni delle prestazioni igrotermiche dei componenti edilizi secondo la UNI EN ISO 13788-2003: analisi e confronti, Atti del Convegno AICARR "Certificazione energetica: normative e modelli di calcolo per il sistema edificio-impianto posti a confronto (in Italian).
- Semprini, G.; Cocchi, A.; and Marinosci C., 2008, Possible correlation between acoustic and thermal performances of building structures, Conference Acoustics'08, Paris 2008.
- Semprini, G.; and Marinosci, C., 2007, Requisiti prestazionali degli edifici ed aspetti energetici", Atti del Convegno AICARR "L'impiantistica di fronte alle nuove disposizioni sul risparmio energetico", Bologna (in Italian).
- Semprini, G.; Falcioni, S.; and Marinosci C., 2006, Valutazione dell'inerzia termica delle strutture edilizie", Atti del Convegno AIA "Prestazioni Termo-Acustiche dei componenti edilizi di facciata - Rumore degli impianti nelle costruzioni civili", Bologna (in Italian).

REFERENCES

- Acocella, A., 2000, Stratigrafia parietale. *Materia*. 31, 10-21. Milano: Ed. Motta, (in Italian).
- Afonso, C.; and Oliveira, A., 2000. Solar chimneys: simulation and experiment. *Energy and Buildings* 32, 71–79.
- Ayres, J.M.; and Stamper, E., 1995, Historical Development of Building Energy Calculations, *ASHRAE Journal*, pp. 47-53.
- Alamdari, F.; and Hammond, G.P., 1983, Improved data correlations for buoyancy driven convection in rooms, *Building Services Engineering Research & Technology* 4 pp.106-112.
- Al-Homoud, M.S., 2001, Computer-aided building energy analysis techniques, *Building and Environment*, vol. 36, pp. 421-433.
- Asan, H.2006, Numerical computation of time lags and decrement factors for different building materials *Building and Environment* 41, pp. 615–620.
- Asan, H. ; and Sancaktar, Y.S., 1998, Effects of Wall's thermophysical properties on time lag and decrement factor, *Energy and Buildings* 28, pp. 159-166.
- ASHRAE, 1997, 1997 ASHRAE Handbook - Fundamentals, Atlanta: American Society of Heating, Refrigerating, and Air-Conditioning Engineers, Inc.
- ASHRAE Handbook , 2005, Fundamentals volume of the ASHRAE Handbook, ASHRAE, Inc., Atlanta, GA, USA,
- ASTM E1933 - 99a, 2010, Standard Test Methods for Measuring and Compensating for Emissivity Using Infrared Imaging Radiometers
- ASTM C1242-00, 2000, Standard Guide for Design, Selection, and Installation of Stone Anchors and Anchoring Systems
- ASTM C1354, 1996, Strength of individual stone anchorages in dimension stone.
- Aung, W., 1972, Fully developed laminar free convection between vertical plates heated asymmetrically, *International Journal of Heat and Mass Transfer*, vol. 15, pp. 1577-1580.
- Balocco, C., 2002, A simple model to study ventilated façades energy performance, *Energy and Buildings* 34, pp. 469-475.
- Balocco, C., 2004, A non-dimensional analysis of a ventilated double façade energy performance, *Energy and Buildings* 36, pp. 35-40.
- Bansal, N.K.; Mathur, R.; and Bhandari, M.S., 1993. Solar chimney for enhanced stack ventilation. *Building and environment* 28, 373–377.
- Bansal, N.K.; Mathur, R.; and Bhandari, M.S., 1994, Study of solar chimney assisted wind tower system for natural ventilation in buildings, *Building and Environment* 29 (4), pp. 4950–5000.

REFERENCES

- Barozzi, G.S.; Imbabi, M.S.E.; Nobile, E.; and Sousa, A.C.M., 1992, Physical and numerical modelling of a solar chimney-based ventilation system for buildings, *Building and Environment* 27 (4), pp. 433–445.
- Bartoli, C.; Ciampi, M.; and Tuoni, G., 1997 Ventilated walls: air-space positioning and energy performance. *Proceedings of the 3rd International Thermal Energy & Environment Congress*. II, 528-533. Marrakesh: Ed. El Watanya.
- Bartoli, C.; Ciampi, M.; Leccese, F.; and Tuoni, G., 1998, Sulla distribuzione di strati resistivi e capacitivi in pareti multistrato. *Atti del XVI° Congresso Nazionale sulla Trasmissione del Calore UIT*. II, 719-732. Pisa: Ed. ETS.
- Bassett, M.R.; and S. McNeil. 2005a. Drained and vented cavity walls – measured ventilation rates. IRHACE Conference Institution of Refrigeration, Heating and Air Conditioning Engineers. Nelson, New Zealand.
- Bassett, M.R.; and S. McNeil. 2005b. The theory of ventilation drying applied to New Zealand cavity walls. IRHACE Conference Institution of Refrigeration, Heating and Air Conditioning Engineers. Nelson, New Zealand.
- Beausoleil-Morrison, I., 2000, The adaptive coupling of heat and airflow modelling within dynamic whole building simulation, Ph.D. Thesis, Glasgow: University of Strathclyde.
- Bejan, A., 1993, *Heat transfer*, New York: Wiley.
- Bejan, A.; and Lage, J.L., 1990, The Prandtl number effect on the transition in natural convection along a vertical surface, *ASME Journal of Heat Transfer*, vol. 112, pp. 787-790
- Berdahl, P.; and Martin, M., 1984, Characteristic of infrared sky radiation in the United States, *Solar Energy*, vol. 33, pp. 321 - 326.
- Berkovsky, B. M.; and Polevikov, V. K., 1977, Numerical study of problems of high-intensive free convection. In: *Heat Transfer and Turbulent Buoyant Convection* (ed. Spalding, D. B.; and Afghan, H.), Hemisphere.
- Biwole, P.H., Woloszyn, M.; Pompeo C., 2008, Heat transfers in a double-skin roof ventilated by natural convection in summer time. *Energy and Buildings*, 40, pp. 1487 – 1497.
- Bliss, R. W., 1961, Atmospheric radiation near the surface of the ground, *Solar Energy*, vol. 5, pp. 103-120.
- Bodoia, J.R.; and Osterle, J.F., 1962, The development of free convection between heated vertical plates, *Journal of Heat Transfer*, vol. 84, pp. 40-44.
- Bondielli, G.G., 2000, La facciata ventilata. *Materia*. 31, 76-83. Milano: Ed. Motta, (in Italian).
- Borgers, T.R.; and Akbari, H., 1984, Free convective turbulent flow with the Trombe wall channel, *Solar Energy* 33 (3–4), pp. 253–264.
- Černe, B.; and Medved, S., 2005, The dynamic thermal characteristics of lightweight building elements with a forced ventilated cavity and radiation barriers *Energy and Buildings* 37 (2005) 972–981
- Bouchair, A., 1984, Solar chimney for promoting cooling ventilation in southern Algeria, *Building Services Engineering Research and Technology* 15 (2), pp. 81–93.
- Brinkworth, B.J.; Marshall, R.H.; and Ibrarrahim. Z., 2000, A validated model of naturally ventilated PV cladding. *Solar Energy*. 69, 67-81. Oxford: Ed. Elsevier Science.
- Bronson, D.; Hinchey, S.B.; Haberl, J.S.; and O’Neal, D.L., 1992, A procedure for calibrating the DOE-2 simulation program to non-weather-dependent measured loads, *ASHRAE Transactions* 98, pp.636-652.

- Brunello, P.; and Peron, F., 1996 Modelli per l'analisi del comportamento fluidodinamico delle facciate ventilate. Atti del 51° Congresso Nazionale ATI. I, 313-324. Padova: Ed. SGE, (in Italian).
- BS 8298, 1994, Natural stone cladding and lining. Code of practice for design and installation of.
- BS 8298, 1994, Code of practice for design and installation of natural stone cladding and lining
- Carslaw, H.S.; and Jaeger, J.C., 1959, Conduction of Heat in Solids, second ed. Oxford University Press.
- Catton, I., 1979, Natural convection in enclosures, Proceedings of the 6th Heat Transfer Conference, Toronto, vol. 6, pp. 13-43.
- Çengel, Y. A., 1997, Introduction to Thermodynamics and heat transfer, Mc-graw Hill Companies
- Chaturvedi, S.K.; Chen, D.T.; and Mohieldin, T.O., 1992, Ventilation characteristics of a Trombe wall thermosyphon loop, in: Proceedings of the International Symposium on Room Air Conditioning and Ventilation Effectiveness, Tokyo, Japan, July 22–24, pp. 624–631.
- Churchill, S.W.; and Ozoe, H., 1973, Correlations for forced convection with uniform heating in flow over a plate and in developing and fully developed flow in a tube, Journal of Heat Transfer, vol. 95, pp. 78-84.
- Ciampi, M.; and Tuoni, G., 1998, Sul comportamento delle pareti ventilate in regime termico periodico. La Termotecnica. 11, 79-87. Milano: Ed. Bias, (in Italian).
- Ciampi, M.; and Tuoni G., 1995 Sulle prestazioni energetiche delle pareti ventilate. La Termotecnica. 3, 75-85. Milano: Ed. Bias, (in Italian).
- Ciampi, M.; Leccese, F.; and Tuoni, G., 2003, Ventilated façades energy performance in summer cooling of buildings, Solar Energy 75, pp. 491–502.
- Clarke, J.A., 2001, Energy Simulation in Building Design, Oxford.
- Clarke, J.A.; and Maver, T. W., 1991, Advanced Design Tools for Energy Conscious Building Design: Development and Dissemination, Building and Environment, vol. 26, nr. 1, pp. 25-34.
- Cole, R., 1976, The longwave radiative environment around buildings, Building and Environment, vol. 11, pp. 3-13.
- Corrado, V.; and Paduos, S., 2009, Prestazione termica dinamica dei componenti edilizi in regime di sollecitazione dinamica: modelli di calcolo a confronto, 64° Congresso Nazionale ATI, (in Italian)
- Corrado, V.; and Paduos, S., 2010, Il progetto termico dinamico dell'involucro opaco: componenti tradizionali ed innovativi a confronto , 65° Congresso Nazionale ATI, (in Italian)
- Coussirat, M.; Guardo, A.; Jou, E.; Egusquiza, E.; Cuerva, E.; and Alavedra, P., 2008, Performance and influence of numerical sub-models on the CFD simulation of free and forced convection in double-glazed ventilated façades, Energy and Buildings 40, pp. 1781-1789.
- Costola, D.; Blocken, B. ;and Hensen, J.L.M., 2009, Overview of pressure coefficient data in building energy simulation and air flow network programs, Building and Environment 44, pp. 2027-2036.
- CSTB, 1999, Regles generales de conception et de mise en oeuvre de l'ossature metallique et de l'insolation thermique des bardages rapportes.
- Davies, M. G., 2004, Bulding heat transfer, Wiley.

REFERENCES

- Davenport, A.G.; and Hui, H.Y.L., 1982, External and internal wind pressures on cladding of buildings. Ontario: Boundary Layer Wind Tunnel Laboratory, University of Western Ontario.
- Davidovic, D.; Srebric, J.; and Burnett, E.F.P., 2006, Modeling convective drying of ventilated wall chambers in building enclosures, *International Journal of Thermal Sciences* 45, pp.180-189.
- Davis, B.L.; and Ekern, M.W., 1977, Wind Fabric Diagrams and Their Application to Wind Energy Analysis, *J. Appl. Meteor.*, 16, pp. 552-531.
- Di Maio, F.; and van Paassen, A.H.C., 2000, Simulation of temperature and air flow in a second skin facade, in: *Proceedings of the Roomvent 2000—Seventh International Conference on Air Distribution in Rooms*, Reading, UK, 9– 12 July, pp. 943–949.
- DIN 18515-1, 1998, Design and installation of tile or stone cladding
- DIN 18516 (Part 3), 1990, Back-ventilated, non-loadbearing, external enclosures of buildings, made from natural stone. Design and installation.
- Dyer, J.R., 1978, Natural-convective flow through a vertical duct with a restricted entry, *International Journal of Heat and Mass Transfer*, vol. 21, pp. 1341-1354.
- Duffie, J.A.; and Beckman, W.A., 1991, *Solar Engineering of Thermal Processes*, Wiley, New York.
- Duffin R.J., 1984, A passive wall design to minimize building temperature swings. *Solar Energy*;33(3/4):337–42.
- Eicker, U.; Fux, V.; Infield, D.; Mei, L.; and Vollmer, K., 1999, Thermal performance of building integrated ventilated PV facades, in: *Proceedings of the International Solar Energy Conference*, Jerusalem, Israel, July 4–9, pp. 613–616.
- EISherbiny, S. M.; Raithby, G.D.; and Hollands, K.G.T., 1982, Heat Transfer by Natural Convection Across Vertical and Inclined Air Layers, *Journal of Heat Transfer*, nr 104, pp. 96-102.
- EN ISO 6946, 2007, Building components and building elements: Thermal resistance and thermal transmittance-Calculation method.
- EN ISO 13792, 1995, Thermal performance of buildings – Calculation of internal temperatures of a room in summer without mechanical cooling – Simplified methods
- EnergyPlus: the official building simulation program of the United States Department of Energy, EnergyPlus Manual.
- Faggembauu, D.; Costa, M.; Soria, M.; and Oliva, A.,2003, Numerical analysis of the thermal behaviour of ventilated glazed façades in Mediterranean climates. Part I: development and validation of a numerical model *Solar Energy* 75, pp. 217–228.
- Faggembauu, D.; Costa, M.; Soria, M.; and Oliva, A.,2003, Numerical analysis of the thermal behaviour of glazed ventilated façades in Mediterranean climates. Part II: applications and analysis of results *Solar Energy* 75, pp. 229–239.
- Fazio, P.; and Kontopidis, T., 1988, Cavity pressure in rain screen walls *Building and Environment* 23 pp.137-143.
- Feustel, H.E.; and Dieris, J., 1992, A Survey of Airflow Models for Multizone Structures, *Energy and Buildings*, vol. 18, pp. 79-100.
- Ferrario, P.; and Gregato, G., 2001, Facciate ventilate. *Materiali Edili.* 38, 34-45. Milano: Ed. Alberto Greco (in Italian).

- Fracastoro, G.V.; Giai, L.; and Perino, M., 1999, Analisi del comportamento termico di coperture di edifici con intercapedine d'aria. Atti del XV° Congresso sulla Trasmissione del Calore UIT. I, 337-348. Pisa: Ed. ETS, (in Italian).
- Gan, G., 1998, A parametric study of Trombe walls for passive cooling of buildings, *Energy and Building* 27 pp.37-43.
- Gan, G.; and Riffat, S.B., 1998, A numerical study of solar chimney for natural ventilation of buildings with heat recovery, *Applied Thermal Engineering* 18 (12), pp. 1171–1187.
- Gratia E; and Herde AD, 2007, Guidelines for improving natural daytime ventilation in an office building with a double-skin façade. *Solar Energy* 81, pp. 435–48.
- Gratia E; and Herde AD, 2007, Greenhouse effect in double-skin façade. *Energy and Buildings* 39, pp. 199–211.
- Hazleden, D., 2001, Envelope drying rates experiment final report. Research Highlights, Canada Mortgage and House Cooperation.
- Hensen, J.L.M.; Bartak, M.; and Drkal, F., 2002, Modelling and simulation of doubleskin façade systems, *ASHRAE Transactions* 108 (2), pp. 1251–1258.
- Hansen, M., Nicolajsen, A., and Stang, B. 2002. On the influence of ventilation on moisture content in timber framed walls. *Proceedings of the 6th Symposium on Building Physics in the Nordic Countries*.
- Holmes, J.D., 1986, Wind loads on low rise buildings, in: *The structural and environmental effects of wind on buildings and structures*, Melbourne: Faculty of Engineering, Monash University.
- Hottel, H.C., 1954, Radiant Heat Transmission, in: McAdams, W.H. (ed.), *Heat Transmission*, New York: McGraw-Hill.
- Hung, Y.H.; and Shiau, W.M., 1988, Local steady-state natural convection heat transfer in vertical plates with a rectangular rib, *International Journal of Heat and Mass Transfer*, vol. 31, pp. 1279-1288.
- Incropera, F.P.; and De Witt, D.P., 1981, *Fundamentals of heat transfer*, New York, John Wiley and Sons.
- Inoue, T.; Matsuo, Y.; and Ibamoto, T., 1985, Study on the thermal performance of ventilation window, *Proceedings of the International Symposium on Thermal Application of Solar Energy*, Hakone, pp. 221-226.
- ISO 9869, 1994, In situ measurement of thermal resistance and thermal transmittance.
- Italian Climate Data Set Gianni de Giorgio,
http://apps1.eere.energy.gov/buildings/energyplus/cfm/weather_data.cfm
- Ito, N.; Kimura, K.; and Oka, J., 1972, A field experiment study on the convective heat transfer coefficient on the exterior surface of a building, *ASHRAE Transactions*, vol. 78 (2), pp. 184-191.
- Janssen, H., 2002, The influence of soil moisture transfer on building heat loss via the ground, Ph.D. Thesis, Leuven: KU Leuven, Laboratory for Building Physics.
- Kairys, L.; and Karbauskaite, J., 2003, Solar radiation influence to the thermo physical parameters of thermal wave that penetrates through the lightweight buildings partitions, in: *Proceedings of the Conference on Dynamic Analysis and Modelling Techniques for Energy in Buildings*, Ispra, Italy, pp. 105–113.
- Kalema, T, 1992, Thermal analysis of buildings – Verification and further development of the TASE program, Ph.D. Thesis, Tampere: Tampere University of Technology.
- Kasten, F.; and Czeplak, G., 1980, Solar and terrestrial radiation dependent on the amount and type of cloud, *Solar Energy*, vol. 24, pp. 177-189.

REFERENCES

- Khalifa, A.J.N, 1989, Heat transfer processes in buildings, Ph.D. Thesis, Cardiff: University of Wales, College of Cardiff.
- Khedari, J.; Boonsri, B.; and Hirunlabh, J., 1999. Ventilation impact of a solar chimney on indoor temperature fluctuation and air change in a school building. *Energy and Buildings* 32, 89–93.
- Kimura, R.I., 1977, Scientific basis of air conditioning, *Applied Science* pp.175-186.
- Kusuda, T., 1976, NBSLD: The Computer Program for Heating and Cooling Loads in Buildings, NBS Building Science Series nr. 69, Washington: National Bureau of Standards.
- Leal, V.; Maldonado, E.; Erell, E.; and Etzion, Y., 2003, Modeling a reversible ventilated window for simulation within ESP-r - The Solvent case, in: Eighth International IBPSA Conference, Eindhoven, Netherlands, pp.713-720.
- Liddament, M.W., 1996, A guide to energy efficient ventilation, Warwick: Air Infiltration and Ventilation Centre.
- Loomans, M., 1998, The measurement and simulation of indoor airflow, Ph.D. Thesis, Eindhoven: Technical University Eindhoven.
- Loveday, D.L.; and Taki, A.H., 1996, Convective heat transfer coefficients at a plane surface on a full-scale building façade, *International Journal of Heat and Mass Transfer*, vol. 39, pp. 1729-1742.
- Manz, H., 2003, Numerical simulation of heat transfer by natural convection in cavities of façade elements *Energy and Buildings* 35, pp. 305–311.
- Manz, H.; and Frank, T., 2005, Thermal simulation of buildings with double-skin façades, *Energy and Buildings* 37 pp.1114-1121.
- Marinosci, C.; Strachan, P.; Semprini, G.; and Morini, G. L., 2010, Empirical validation and modelling of a naturally ventilated rainscreen façade building, *Energy and Buildings* 43 853–863.
- Marinosci C.; Morini G. L.; and Semprini G., Experimental benchmark of the modelling of a rainscreen ventilated façade, DYNASTEE workshop on Dynamic Methods for Building Energy Assessment, Brussels 2010.
- Maver, T.W.; and Clarke, J.A., 1984, Major Extensions to the ESP System, Final Report for Science and Engineering Research Council Grant GR/C/2283.7, Glasgow: University of Strathclyde.
- Mitalas, G.P., 1978, Comments on the Z-Transfer Function Method for Calculating Heat Transfer in Buildings, *ASHRAE Transactions*, vol. 84, part 1, pp. 667-676.
- Mootz, F.; and Bezia, J.-J.1996, Numerical study of a ventilated façade panel, *Solar Energy* 57 pp.29-36.
- Murakami, S.; and Mochida, A., 1988, 3-D numerical simulation of airflow around a cubic model by means of the k- ϵ model, *Journal of Wind Engineering and Industrial Aerodynamics*, vol. 31, pp. 283-303.
- Naboni, E., 2007, Ventilated opaque walls - a performance simulation method and assessment of simulated performance, PhD thesis- Politecnico di Milano Building Environment Science and Technology.
- Negrão, C.O.R., 1995, Conflation of Computational Fluid Dynamics and Building Thermal Simulation, Ph.D. Thesis, Glasgow: University of Strathclyde.
- Nielsen, P.V., 1974, Flow in Air Conditioned Rooms, Ph.D. Thesis, Copenhagen: Technical University of Denmark.

- Nore, K.; Blocken, B.; and Thue, J.V. 2010, On CFD simulation of wind-induced airflow in narrow ventilated façade cavities: Coupled and decoupled simulations and modelling limitations, *Building and Environment* 45, pp. 1834-1846.
- Ong, K. S., 2003, A mathematical model of a solar chimney, *Renewable Energy* 28, pp.1047-1060.
- Ong, K.S.; and Chow, C.C., 2003. Performance of solar chimney. *Solar Energy* 74, 1–17.
- Onysko, M. D., 2000, Drying of walls with ventilation: a parametric analysis. Research report-Housing Technology Series, Canada Mortgage and Housing Corporation. Thermal buoyancy is the principal mechanism for air flow in these open cavities. The performance of such cavities has been extensively studied mostly for passive solar heating.
- Pitts, A.C.; and Craigen, S., 1996, A technique for controlling air flow through modified Trombe walls, in: *Proceedings of the 17th AIVC Conference on Optimum Ventilation and Air Flow Control in Buildings*, vol. 2, Gothenberg, Sweden, September 17–20, pp. 477–485.
- Park, S.D.; Suh, H.S.; and Cho, S.H., 1989, The Analysis of Thermal Performance in an Airflow Window System Model, *Proceedings of the ASHRAE/DOE/BTECC/CIBSE Conference, Thermal Performance of the Exterior Envelopes of Buildings IV*, Clearwater Beach, pp. 361-375.
- Patania, F., Gagliano, A., Nocera, F., Ferlito, A.; Galesi, A., 2010, Thermofluid-dynamic analysis of ventilated façades *Energy and Buildings* 42, pp. 1148–1155.
- Pedrini, A.; Westphal, F. S.; and Lamberts, R., 2002, A methodology for building energy modelling and calibration in warm climates, *Building and Environment* 37, pp.903-912.
- Poirazis, H., 2006, Double-skin façades for office buildings-literature review, in: *Report ECBCS Annex 43*, Division of Energy and Building Design, Department of Construction and Architecture, Lund Institute of Technology, Sweden.
- Rodrigues, A.M.; Canha da Piedade, A.; Lahellec, A.; and Grandpeix, J.Y., 2000, Modelling natural convection in a heated vertical channel for room ventilation, *Building and Environment* 35, pp. 455–469.
- Rohsenow, W.M.; Harnett, J.P.; and Ganic, E.P., 1985, *Handbook of Heat Transfer Fundamentals*, New York: McGraw-Hill.
- Said, S.A.M.; and Krane, R.J., 1990, An analytical and experimental investigation of natural convection heat transfer in vertical channels with a single obstruction, *International Journal of Heat and Mass Transfer*, vol. 33, pp. 1121-1134.
- Saelens D., 2002, Energy performance assessment of single storey multiple-skin-façades, Ph.D. Thesis, Katholieke Universiteit Leuven.
- Serra, V.; Zanghirella, F.; and Perino, M., 2010, Experimental evaluation of a climate façade: Energy efficiency and thermal comfort performance, *Energy and Buildings* 42, pp. 50-62.
- Sharples, S., 1984, Full-scale measurements of convective energy losses from exterior building surfaces, *Building and Environment*, vol. 19, pp. 31-39.
- Smolec, W.; and Thomas, A., 1991, Some aspects of Trombe wall heat transfer models, *Energy Conversion and Management* 32 pp.269-277.
- Sobel, N.; Landis, F., and Mueller, W.K., 1966, Natural convection heat transfer in short vertical channels including the effects of stagger, *Proceedings International Heat Transfer Conference*, pp. 121-125.
- Stec, W.J.; van Paassen, A.H.C.; and Maziarz, A, 2005, Modelling the double skin façade with plants, *Energy and Buildings* 37 (5), pp. 419–427.

REFERENCES

- Stephenson, D.G.; and Mitalas, G.P., 1971, Calculation of Heat Conduction Transfer Functions for Multi-Layer Slabs, ASHRAE Transactions, vol. 77, part 2, pp. 117-126.
- Stovall, T.K.; and Karagiozis, A.N., 2004, Airflow in the ventilation space behind a rain screen wall. In: Proceedings of thermal performance of the exterior envelopes of buildings IX, ASHRAE Buildings IX, Clearwater Beach, FL, USA.
- Strachan, P.A., 2008, Simulation support for performance assessment of building components, Building and Environment 43 pp.228-236.
- Strachan, P.A.; and Vandaele, L., 2008, Case studies of outdoor testing and analysis of building components, Building and Environment 43 pp.129-142.
- Straube, J.F.; and Burnett, E.F.P., 1995, Vents, Ventilation Drying, and Pressure Moderation. Building Engineering Research Report for Canada Mortgage and Housing Corp.:Ottawa.
- Straube, J.F.; and Burnett, E.F.P., 1997, In-Servise Performance of Enclosure Walls. Volume 1: Summary Final Report. Building Engineering Research Report: University of Waterloo.
- Straube, J.F.; and Burnett, E.F.P., 1997, Field Testing of Filled –Cavity Wall System, Proceedings of Int. Conf. Building Envelope Science and Tech. '97, Bath, UK, April 15-17.
- Straube, J.F.; and Burnett, E.F.P., 1998, Field Measurement of Masonry Veneer Exposure Conditions, Eighth Canadian Masonry Symposium, Jasper, Alta., Canada, May 31-June 3.
- Straube, J.; VanStraaten, R.; Burnett, E. and Schumacher. C., 2004, Review of literature and theory – report#1 final report. ASHRAE 1091-Development of Design Strategies for Rainscreen and Sheathing Membrane Performance in Wood Frame Walls.
- Tanda, G., 1997, Natural convection heat transfer in vertical channels with and without transverse square ribs, International Journal of Heat and Mass Transfer, vol. 40, nr. 9, pp. 2173 - 2185.
- Threlkeld, J.L., 1998, Thermal Environmental Engineering, Prentice-Hall, Englewood Cliffs, NJ.
- Torricelli, M.C., Del Nord, R.; and Felli, P., 2001, Materiali e tecnologie dell'architettura. Bari: Ed. Laterza, (in Italian).
- Torricelli, M.C., 2000, Caldo d'inverno e fresco d'estate. Costruire in Laterizio. 77, 56-67. Faenza: Ed. Faenza, (in Italian).
- Tsuchiya, M.; Murakami, S.; Mochida, A.; Kondo, K.; and Isjida, Y., 1997, Development of a new k- ϵ model for flow and pressure fields around a bluff body, Journal of Wind Engineering and Industrial Aerodynamics, vol. 67&68, pp. 169-182.
- UNI/TS 11300-1, 2008, Prestazioni energetiche degli edifici: Parte 1: Determinazione del fabbisogno di energia termica dell'edificio per la climatizzazione estiva ed invernale.
- UNI 7959, 1988, Edilizia. Pareti perimetrali verticali. Analisi dei requisiti.
- UNI 8178, 1980, Edilizia. Coperture. Analisi degli elementi e strati funzionali.
- UNI EN 12670, 2003, Pietre naturali - Terminologia
- UNI 8627, 1984, Edilizia. Sistemi di copertura. Definizione e classificazione degli schemi funzionali, soluzioni conformi e soluzioni tecnologiche.
- UNI 8979, 1987, Edilizia. Pareti perimetrali verticali. Analisi degli strati funzionali.

- UNI 9460, 2008, Coperture discontinue - Istruzioni per la progettazione, l'esecuzione e la manutenzione di coperture realizzate con tegole di laterizio o calcestruzzo
- UNI EN 12057, 2005, Prodotti di pietra naturale - Marmette modulari - Requisiti
- UNI EN 12058, 2005, Prodotti di pietra naturale - Lastre per pavimentazioni e per scale - Requisiti
- UNI 9811, 1991, Opere di ingegneria civile. Ancoranti metallici ad espansione. Criteri di accettazione.
- UNI 10372, 2004, Coperture discontinue - Istruzioni per la progettazione, l'esecuzione e la manutenzione di coperture realizzate con elementi metallici in lastre
- UNI EN 14411, 2007, Piastrelle di ceramica - Definizioni, classificazione, caratteristiche e marcatura
- UNI EN ISO 10545-1, 2000, Piastrelle di ceramica - Campionamento e criteri di accettazione
- UNI 11018, 2003, Rivestimenti e sistemi di ancoraggio per facciate ventilate a montaggio meccanico. Istruzioni per la progettazione, l'esecuzione e la manutenzione.
- UNI 8178, Classificazione degli strati funzionali per le pareti esterne verticali.
- van Paassen, A.H.C.; and Stec, W., 2000, Controlled double façade for preheating ventilation, in: Proceedings of the 21st Annual AIVC Conference on Innovations in Ventilation Technology, The Hague, the Netherlands, September 26–29, p. 13.
- Warrington, R.O.; and Ameer, T.A., 1995, Experimental studies of natural convection in partitioned enclosures with a Trombe wall geometry, *Solar Energy Engineering* 117, pp. 16–21.
- Zannoni, G., 1996, Aria alle tegole. Modulo. 219, 162-168. Milano: Ed. BE-MA (in Italian).
- Zhou, Y.S.; and Stathopoulos, T., 1996, Application of two-layer methods for the evaluation of wind effects on a cubic building, *ASHRAE Transactions*, vol. 102, pp. 754-764.